THE SEARCH FOR MEV-SCALE NEUTRINOS IN TEMPORAL COINCIDENCE WITH O4 GRAVITATIONAL WAVE EVENTS USING THE SNO+ EXPERIMENT

Amanda Bacon

A DISSERTATION

in

Physics and Astronomy

Presented to the Faculties of the University of Pennsylvania

in

Partial Fulfillment of the Requirements for the

Degree of Doctor of Philosophy

2026

Supervisor of Dissertation

Joshua Klein, Professor of Physics and Astronomy, Edmund J. and Louise W. Kahn Term Professor

Graduate Group Chairperson

Cullen Blake, Associate Professor of Physics and Astronomy

Dissertation Committee

Christopher Mauger, Associate Professor of Physics and Astronomy
Evelyn Thomson, Professor of Physics and Astronomy
Cullen Blake, Associate Professor of Physics and Astronomy
Gary Bernstein, Reese W. Flower Professor of Astronomy and Astrophysics

THE SEARCH FOR MEV-SCALE NEUTRINOS IN TEMPORAL COINCIDENCE WITH O4 GRAVITATIONAL WAVE EVENTS USING THE SNO+ EXPERIMENT

COPYRIGHT

2026

Amanda Bacon

ACKNOWLEDGEMENT

I was going to delete this page because that would have been easier than writing notes to the people who stood beside me through the worst mistake of my life... But here it is. And I was right. Deleting this page would have been easier, but I can't leave without saying goodbye (...again).

To Josh Klein, my advisor and friend through these long seven-ish years. Actually, longer, if I'm being pedantic. You were my introduction to particle physics, starting with MiniCLEAN and ending up on SNO+. It's been a journey I wouldn't change for a second. Thank you for your patience, guidance, and willingness to let me figure things out on my own, even when I was plain wrong most of the time. You never made me feel stupid... even when I should have known the answer. Meeting you has been one of the highlights of my life.

I never would have made it this far without my incredible undergraduate advisor, Hugh Crowl. I'm sorry I broke your heart and chose to pursue physics. Just know astronomy always has a special place in my heart. I'm also sorry I didn't win the Nobel Prize. I did get the Ph.D., though (hopefully). To Andrew McIntyre, you always rooted for me. For that, I am truly thankful. Math has never been as fun or as interesting as it was under your guidance. To Joyce Church and Deb Matte, thank you for being my rocks throughout undergrad. I will always cherish our chicken finger + apple sauce dinners. Thank you for caring for and believing in me.

To MiniCLEAN's own Steve Linden, you have to be 50 now, right? You made the grueling day-to-day (really, it was every day of the week) of MiniCLEAN underground trips amusing. You're also the reason I learned how to drive in the snow without snow tires. I almost died, but I lived.

To the Penn group, both past and present, I really couldn't have done it without any of you. Eric Marzec, you were the first face I saw in the wintry wasteland of Sudbury, ON. Thank you for helping me get the hover-over crate/card text working on the Minard N100/N20 display... even though I was there for MiniCLEAN. I still don't like C++ though. Tanner Kaptanoglu, the next victim. I wish we overlapped at Penn longer, but it was an honor working with you on light yield and

dichroic filter characterizations. My love for hands-on experimentation was further cemented with these projects. Thank you also for your careful review of this dissertation analysis. I only hope to be half the researcher you are in the future. Logan Lebanowski, thank you for all things C++, RAT, and ROOT during my first graduate analysis on SNO+ charge windows. I also show everyone the "Chicken Attack" video whenever I can. Tony (fast) Zummo, my guide to SNO+ electronics. I only hope I trained Ravi half as well as you trained me. Tereza Kroupová, I still don't understand your need to wear blue-tinted glasses when you have 20/20 vision. It feels like a personal attack. You were my rock throughout the charge and dissertation analyses. Thank you for reading over this monster. Sam Naugle, the office was never the same after you left. It's been very fun getting to know you. You always believed in me and I only hope I made you (somewhat) proud. Thank you for being my partner on the CTC baseline work and patiently answering my RAT questions. Ben Harris, I will forever remember the proverb "There's a window in every wall." I was an honor to co-mentor with you on the LAPPD analysis. You're a hardware wizard and I know you'll do great things in the future. James Shen, I think I'll be very hesitant on any cluster I'm a part of in the future because of the PTSD from your reprimands on nubar. Thank you for being an endless source of knowledge on all things SLURM, nubar, and just about everything else... alongside being a great friend. If you ever end up missing me, try looping one song for months on end. Ravi Pitelka, thank you for introducing me to Merlin and being a true friend. Your bird photos never fail to amaze me, and I look forward to every new one that appears in the future. You'll do a great job spearheading SNO+ electronics debugging... May God have mercy on your soul. Max Dubnowski, it was fun helping you set up for EOS PMT + dichroicon testing in the darkbox. I hope you have as much fun with this project as I did with dichroic filter characterizations. I also hope I never hear "Based" or "Chat, what do we think of this?" again. To David Drobner, resident roboshifter progenitor, it was fun attending Neutrino2026 with you. I won't miss having to strain my neck looking up at you though.

To Matt Depatie and Mark Ward, SNO+'s resident electronics experts, it has been an honor working with both of you over the years. You kept the detector running through countless challenges. Here's hoping it continues for many years to come.

Finally, none of this would have been possible without family. To the Miller, Arii, and Cooper families, thank you for supporting me, encouraging me, and loving me throughout this journey. I could never adequately express how much that has meant to me, and I'll never be able to thank you enough.

To Renee and Dale, thank you for welcoming me into your family and making me feel like I belonged from the very beginning. To Jesse, thank you for always being the life of the party and for providing the muscle during the move to Texas. To Cheyenne and Coop, thank you for all the laughs and the chaos. To Bryce, thank you for being a fun friend, and for sharing Corrie with me.

To Tatum, Raya, and Palmer, thank you for bringing never-ending joy and laughter into my life. The best gift in life is being your aunt.

And finally, to Corrie, my lighthouse, my person. Thank you for standing beside me through every high and every low of this journey. Your love and support carried me through the hardest moments of graduate school, and I would not be here without you.

Auntie Dr. Amanda Bacon (hopefully that isn't preemptive), signing off.

ABSTRACT

THE SEARCH FOR MEV-SCALE NEUTRINOS IN TEMPORAL COINCIDENCE WITH O4 GRAVITATIONAL WAVE EVENTS USING THE SNO+ EXPERIMENT

Amanda Bacon

Joshua Klein

This dissertation presents a search for low-energy neutrinos in temporal coincidence with gravitational wave events reported by the LIGO-Virgo-KAGRA collaboration during the fourth observing run (O4), using 499.0 days of data collected during the liquid scintillator phase of the SNO+ experiment. The search uses inverse beta decay (IBD), which is primarily sensitive to electron antineutrinos, and neutrino-proton elastic scattering, a complementary neutral current channel providing sensitivity to all neutrino flavors.

Candidate events were identified using optimized reconstruction and event-selection criteria developed with Monte Carlo simulations and validated with background-only data. The IBD background rate was measured directly from data, naturally incorporating reactor antineutrinos, geoneutrinos, radioactive backgrounds, cosmogenic backgrounds, and accidental coincidences present during detector operation. A model-independent framework was developed using flat spectrum neutrino Monte Carlo samples, allowing the detector response to be evaluated as a function of neutrino energy and applied to different theoretical emission models.

As part of this work, improvements were made to the SNO+ Monte Carlo simulation, including modifications to the IBD generator to produce a true flat neutrino spectrum and corrections to the implementation of the neutrino-proton elastic scattering cross section. Detector characterization studies, including measurements of the deployed scintillator light yield and investigations of detector timing and electronics performance, were also performed to validate the detector response used throughout the analysis.

The final gravitational wave-coincident dataset contained 143 candidates overlapping stable SNO+

data-taking periods. After excluding candidates classified as terrestrial or unknown by the LIGO-Virgo-KAGRA collaboration, the final astrophysical sample used for compact binary merger fluence limits contained 126 gravitational wave candidates. No statistically significant neutrino excess was observed in either the IBD or neutrino-proton elastic scattering channels.

The IBD search observed no coincident candidates in the final astrophysical gravitational wave sample, consistent with an expected background of 1.25 ± 0.09 events. The corresponding Feldman-Cousins 90% confidence level upper limit is $N_{90}^{\text{stack}} = 1.47$ signal events. Stacked average (per gravitational wave) upper limits on the electron antineutrino fluence were derived for both monoenergetic neutrino emission and model-dependent spectra, including thermal neutrino and core-collapse supernova-inspired models used as detector sensitivity benchmarks.

The neutrino-proton elastic scattering search represents the first application of this all-flavor channel to a gravitational wave-coincident neutrino search. Using an optimized ± 50 s coincidence window, 108424 candidate events were observed, consistent with the expected background of 108345 ± 786 events estimated from local sidebands. The observed 0.24σ fluctuation is consistent with the background-only hypothesis. For the final astrophysical gravitational wave sample, the Feldman-Cousins method gives a 90% confidence level upper limit of $N_{90}^{\text{stack}} = 1479.6$ signal events. These results are used to derive the first all-flavor neutrino-proton elastic scattering fluence limits associated with compact binary merger candidates.

The resulting SNO+ IBD fluence limits improve upon previous liquid scintillator gravitational wave-neutrino searches by approximately an order of magnitude in the few-MeV energy region, primarily due to the larger fiducial target mass, increased gravitational wave sample size, and low background rate achieved in SNO+. The neutrino-proton elastic scattering results establish the first all-flavor MeV neutrino search through this interaction channel in coincidence with gravitational wave events. Together, these analyses extend previous multi-messenger searches performed by Borexino, KamLAND, and Super-Kamiokande and demonstrate the capability of SNO+ to search for weak neutrino signals associated with astrophysical transients.

TABLE OF CONTENTS

ACKNOWLEDGEMENT iii

ABSTRACT vi

LIST OF TABLES xi

LIST OF ILLUSTRATIONS xiv

CHAPTER 1 : INTRODUCTION 1

CHAPTER 2 : THE HISTORY OF THE NEUTRINO 3

2.1 The Proposal of the Neutrino 3

2.2 The Discovery of the Neutrino 4

2.3 Neutrinos in the Standard Model 5

2.4 Neutrino Oscillation 7

2.5 Neutrino Decoherence 16

2.6 Neutrino Mass 21

2.7 Neutrinoless Double Beta Decay 25

2.8 Neutrino Sources and Experiments 27

CHAPTER 3 : THE SNO+ DETECTOR 37

3.1 SNO+ 38

3.2 Phases of SNO+ 40

3.3 PMTs, Electronics, and DAQ 51

3.4 Electronics Upgrades 61

3.5 Electronics Calibration 77

3.6 Absolute Timing and GPS Synchronization 78

CHAPTER 4 : SIMULATION AND RECONSTRUCTION 86

4.1 Event Generation 87
4.2 Event Reconstruction 88

CHAPTER 5 : GRAVITATIONAL WAVES 94
5.1 A Brief History of Gravitational Waves 95
5.2 Gravitational Wave Detectors 95
5.3 Observing Catalogs 102
5.4 Open Data 104
5.5 Gravitational Wave Sources 104
5.6 Multi-Messenger Astronomy 108
5.7 Neutrinos from Gravitational Wave Mergers 109
5.8 Motivation for the SNO+ Search 112

CHAPTER 6 : A SEARCH FOR NEUTRINOS IN TEMPORAL COINCIDENCE WITH GRAVITATIONAL WAVES IN SNO+ 114
6.1 Overview 114
6.2 Data Sets 116
6.3 Analysis Strategy 121
6.4 Monte Carlo Simulation 123
6.5 GW Coincidence Analysis Framework 130
6.6 Signal Channels 133
6.7 IBD Analysis 143
6.8 IBD Results 157
6.9 Neutrino-Proton ES Analysis 175
6.10 Neutrino-Proton ES Results 179
6.11 Summary 183

CHAPTER 7 : CONCLUSIONS 186
7.1 Future Work 188

APPENDIX A : BACKGROUND IBD CANDIDATE LISTS 191

APPENDIX B : GW-COINCIDENT CANDIDATE LISTS 200

BIBLIOGRAPHY 209

LIST OF TABLES

TABLE 2.1 Typical mass pattern for nuclei that undergo double beta decay. 27

TABLE 2.2 List of eight isotopes known to undergo double beta decay. Isotopes with a higher Q-value (total kinetic energy released) and longer $2\nu\beta\beta$ half-life are most desirable as they allow detectors to achieve lower backgrounds. Additionally, higher isotopic abundance means larger isotope mass can be deployed without requiring expensive enrichment. Information for this table was partially taken from [1]. 27

TABLE 3.1 Parameters for the two-exponential fit. Adapted from [2]. 50

TABLE 3.2 Table of the bis-MSB run, number of data points with GPS timing, and the offset/drift of the 10 MHz clock relative to the MTC/D clock per hour. 84

TABLE 5.1 Representative neutrino production mechanisms in hot, dense neutron-rich matter relevant to binary neutron star mergers. Here $\ell = e, \mu, \tau$ and N denotes a nucleon. 109

TABLE 6.1 Reduction of the LVK O4 candidate list to the final astrophysical GW sample used for fluence limits. The largest reductions arise from excluding GW candidates during the bisMSB loading period and from detector run selection requirements. The intermediate GW sample contains all candidates passing detector requirements, while the final astrophysical sample excludes terrestrial and unknown classifications. 120

TABLE 6.2 Comparison of detector livetimes calculated using the 10 MHz and 50 MHz clock systems. 132

TABLE 6.3 Interaction channels for supernova neutrinos in liquid scintillator with corresponding event yields estimated based on a CCSN at 10 kpc observed in SNO+, adapted from [3] and [4]. The errors on the event yields are derived from the uncertainties of the interaction cross sections. Note that the uncertainties of the electron scattering cross sections arising from Standard Model calculations are less than 1%, and are neglected in the yield count. 134

TABLE 6.4 IBD selection criteria applied to both data and MC analyses. 143

TABLE 6.5 Livetime loss associated with the muon veto in the IBD analysis. 145

TABLE 6.6 Approximate composition of the IBD-like background expected in the GW coincidence windows, estimated by scaling the SNO+ reactor antineutrino background model to the total GW search livetime. The final background normalization used in this analysis is determined directly from the data-driven background measurement. 151

TABLE 6.7 Summary of the data-driven IBD background estimate for the PPO+BHT and bisMSB scintillator phases. The expected background is calculated from the measured IBD candidate rate in the background-only dataset and scaled to the total livetime contained within the ±1000 s GW coincidence windows. Uncertainties correspond to the statistical uncertainty from the number of IBD candidates observed in the background-only datasets. 152

TABLE 6.8 Summary of the final astrophysical GW candidate IBD unblinding results. The expected background is calculated using the data-driven IBD background rates scaled to the total GW coincidence livetime. The combined Feldman–Cousins 90% confidence level upper limit on the number of signal events is $N_{90} = 1.47$. . 162
TABLE 6.9 Mean spectrum-weighted IBD pair selection efficiencies and 90% confidence level fluence upper limits for the stacked analysis using all 126 GW candidates and for the individual GW candidate `S250206dm` (SNO+ run 366227). The stacked (average per-GW) common-fluence limits are calculated by summing the run-dependent sensitivities of all 126 GW candidates under the assumption of a common neutrino fluence at Earth, using $N_{90}^{\mathrm{stack}} = 1.47$. The individual-GW limits use the single-window Feldman-Cousins upper limit of $N_{90} = 2.44$. The efficiency uncertainties include only MC statistical uncertainties. 164
TABLE 6.10 Selected monoenergetic IBD common-fluence upper limits for the stacked sample of 126 GW candidates. The listed efficiencies are the mean run-dependent pair selection efficiencies obtained from the flat spectrum MC simulation, whereas the stacked fluence limits use the summed sensitivity of all 126 GW candidates. The final column gives the individual-GW fluence limits for the GW candidate `S250206dm` (SNO+ run 366227), calculated using the single-window Feldman-Cousins upper limit of $N_{90} = 2.44$. The quoted efficiency uncertainties correspond to the binomial MC statistical uncertainty. 165
TABLE 6.11 Observed IBD candidate counts, expected backgrounds, and 90% confidence level Feldman-Cousins signal upper limits for the full GW sample and the merger-classification subsets. The background expectations are calculated separately for the PPO+BHT and bisMSB detector phases and then summed within each merger class. 165
TABLE 6.12 Upper limits on the isotropic-equivalent energy emitted in electron antineutrinos for the stacked GW samples under the GKVM and Fermi-Dirac spectral assumptions. The normalized effective distance is calculated using Equation 6.64, and the emitted-energy limits are obtained using Equation 6.65. 173
TABLE 6.13 Individual-GW fluence and isotropic-equivalent emitted-energy upper limits for the NS-BH candidate `S250206dm` (SNO+ run 366227, $d = 349$ Mpc). 174
TABLE 6.14 Neutrino-proton ES selection criteria applied to both data and MC analyses. . . 176
TABLE 6.15 Neutrino-proton ES unblinding results comparing the observed candidates counts in the GW coincidence windows with the expected background estimated from the local sidebands. The ON-window corresponds to the optimized ±50 s GW coincidence windows, while the OFF-window corresponds to the local sideband regions used to estimate the background. 179

TABLE A.1 Summary of background-only IBD candidates identified in the LAB+PPO+BHT phase. The GW neutrino analysis selection is compared with the independent reactor antineutrino analysis. Green indicates candidates found by both analyses, magenta indicates candidates removed by reactor antineutrino vetoes, blue indicates candidates retained only by the GW/solar analyses due to the extended prompt energy range ($E_{\mathrm{prompt}} > 9$ MeV), and white indicates runs not included in the reactor antineutrino dataset. 191

TABLE A.2 Summary of background-only IBD candidates identified in the LAB+PPO+BHT+bisMSB phase. Candidates are compared with the independent reactor antineutrino analysis. Green/yellow candidates represent agreement between analyses, while magenta candidates are rejected by reactor antineutrino vetoes. Differences arise from analysis-specific vetoes and selection criteria. 191
TABLE A.3 Full list of background-only IBD candidates in the LAB + 2.2 g/L PPO + 6.5 mg/L BHT phase. The table compares the GW IBD selection with the independent reactor antineutrino candidate list. Green/yellow entries indicate agreement with the reactor antineutrino lists, magenta tag cells indicate candidates removed by reactor antineutrino vetoes, blue marks the GW/solar prompt energy extension, and white entries indicate candidates not included in the reactor antineutrino comparison dataset. 192
TABLE A.4 Full list of background-only IBD candidates in the LAB+ 2.2 g/L PPO + 6.5 mg/L BHT + 2.2 mg/L bisMSB phase. The table compares the GW IBD selection with the independent reactor antineutrino candidate lists. Green/yellow entries indicate agreement with the reactor antineutrino lists, magenta tag cells indicate candidates removed by reactor antineutrino vetoes, and orange indicates candidates removed due to pedestal-cut. 193

TABLE B.1 O4a GW candidates used in the SNO+ coincidence search. The GW trigger time, corresponding SNO+ run, run duration, and GW GPS trigger time are shown. 201
TABLE B.2 O4b GW candidates used in the SNO+ coincidence search. The GW trigger time, corresponding SNO+ run, run duration, and GW GPS trigger time are shown. 203
TABLE B.3 O4c GW candidates used in the SNO+ coincidence search. The GW trigger time, corresponding SNO+ run, run duration, and GW GPS trigger time are shown. 207

LIST OF ILLUSTRATIONS

FIGURE 2.1 Beta particle's continuous energy spectrum with endpoint energy noted as the expected observation [5]. 4
FIGURE 2.2 Reines and Cowan's initial proposal to detect the neutrino using a nuclear explosion [6]. 5
FIGURE 2.3 Diagram of the elementary particles in the Standard Model [7]. 6
FIGURE 2.4 Diagrams of the normal hierarchy (left) and inverted hierarchy (right). The colors show the relationships between the flavor eigenstates and the mass eigenstates. Δm^2_{atm} corresponds to Δm^2_{32}, where "atm" traditionally denotes measurements using atmospheric neutrinos. Δm^2_{sol} corresponds to Δm^2_{21}, where "sol" traditionally denotes measurements using solar neutrinos [8]. 22
FIGURE 2.5 Feynman diagrams of double beta decay (left) and neutrinoless double beta decay (right) [9]. 26
FIGURE 2.6 Predicted solar neutrino energy spectra for the various components of the *pp* chain and CNO cycle [10]. 30
FIGURE 2.7 Results from SNO showing the measured ^{8}B solar neutrino flux decomposed into electron neutrino (ϕ_e) and non-electron neutrino ($\phi_{\mu,\tau}$) components and compared with the SSM prediction [11]. 30
FIGURE 2.8 Energy spectra of antineutrinos emitted in the decay chains of ^{238}U, ^{235}U, ^{232}Th, and ^{40}K [12]. 32
FIGURE 2.9 Neutrino signal from SN1987A at IMB, Kam-II, BUST, and LSD [13]. 35

FIGURE 3.1 An illustration of the SNO+ detector modified from [14]. 39
FIGURE 3.2 A schematic of the SNO+ experiment depicting the hold-up ropes and belly plates (left). The same experiment, but with the inclusion of the PSUP in green, the AV in blue, the hold-up ropes in pink, and the hold-down ropes in red (right). Adapted from [15] and [4]. 40
FIGURE 3.3 An illustration of the SNO+ detector phases. This analysis uses data from the scintillator phase. 41
FIGURE 3.4 Absorption and emission spectra for the PPO and bisMSB components in the SNO+ scintillator cocktail. The left y-axis shows the probability of emission, the right y-axis corresponds to the sparse dotted lines showing absorption in units of mm^{-1}. The black fine dotted line shows the R1408 Hamamatsu PMT measured total detection efficiency (divided by 10 to fit on the graph). Plot adapted from [16]. 44
FIGURE 3.5 Experimental setup used for the light yield measurements. The UVT acrylic cube containing the scintillator sample is optically coupled to a Hamamatsu R7600-U200 trigger PMT. A Hamamatsu R1408 SNO PMT is positioned approximately 0.5 cm away to detect the scintillation light. The ^{90}Sr source is mounted beneath the acrylic cube and is not visible in the photograph. 47
FIGURE 3.6 Decay scheme of the ^{90}Sr source used in the light yield measurements. 48

FIGURE 3.7 Relative light yield of prepared LAB+PPO samples (red circles) and SNO+ scintillator (gold stars) as a function of PPO concentration. Published measurements from Brookhaven National Laboratory are shown in blue for comparison. Adapted from [2]. 50
FIGURE 3.8 Double beta decay isotopes. Plot adapted from [17]. 51
FIGURE 3.9 A schematic of the Hamamatsu R1408 PMT and its waterproof enclosure (left). The same PMT mounted in a hexagonal ABS cell, which also forms the housing for the light concentrator. Adapted from [15]. Dimensions are in cm. 53
FIGURE 3.10 A SNO light concentrator imaged in 2019, showing visible aging of the reflective petals. Image adapted from [18]. 54
FIGURE 3.11 Rack 8 containing crates 12 and 13 (left). Timing rack containing the MTC/D, MTC/A+'s, TUB and TUBii, and the CAEN. Both located on the deck above the SNO+ detector. 56
FIGURE 3.12 The SNO+ trigger system adapted from [18]. 56
FIGURE 3.13 A picture of the SNO XL1 (left) and XL2 (right) boards. Adapted from [19]. . 62
FIGURE 3.14 A picture of the SNO+ XL3 with ML403 and Ethernet cable. 62
FIGURE 3.15 Diagram of the signals input to the triggering logic on the MTC/A+. Figure adapted from [20]. 65
FIGURE 3.16 Schematic and picture of low-pass RC filter circuit connected to the CTC's N20 and N100 outputs. 70
FIGURE 3.17 N20 (left) and N100 (right) CTC output signals with and without the filter. . 71
FIGURE 3.18 N20 (left) and N100 (right) CTC output signals with and without the battery simulating a baseline shift. 72
FIGURE 3.19 Project box containing low-pass RC filter circuit that will be attached to the CTC's. 73
FIGURE 3.20 Diagram of the low pass filter circuit project boxes connected to N20 and N100 trigger outputs on the CTC. 73
FIGURE 3.21 Crate 0 baseline monitor measurements of N20 and N100 trigger signals. . . . 75
FIGURE 3.22 Image of SNO+ rack 8 with crates 12 and 13. The N100 and N20 baseline monitor project boxes are visibly horizontal and connected to the CTCs (black cards on the far left). 76
FIGURE 3.23 A screenshot of the slow control's page depicting a baseline shift in crate 17's N100 trigger signal. 77
FIGURE 3.24 GPS schematic adapted from [21]. 79
FIGURE 3.25 Plots of the GPS offset in the PPO phase. Scatter plot version (left) and histogram version (right) depicting nominal offset of ∼0.092 ms. 82
FIGURE 3.26 Plots of the GPS offset in the bisMSB phase. Scatter plot version (left) and histogram version (right) depicting nominal offset of ∼0.092 ms. 83
FIGURE 3.27 Plot of the bis-MSB runs that depict the offset increasing linearly with time. . 85

FIGURE 4.1 Scintillator emission time profile as modeled in RAT. Models for both full fill (2.2 g/L β Model) and partial fill (0.6 g/L β Model) are shown. Adapted from [22]. 89

FIGURE 4.2 The number of triggered PMTs (N_{Hit}) as a function of energy (blue) for electrons simulated at the center of the detector. At higher energies, the probability of more than one hit increases, and so too does the departure from linearity. A linear energy estimator H is depicted in orange. Adapted from [23]. 92

FIGURE 5.1 A skymap depicting GW170817 source localizations. Adapted from [24] 98
FIGURE 5.2 Simplified schematic of an Advanced LIGO detector. Adapted from [25]. . . . 100
FIGURE 5.3 LIGO 40 kg test mass suspended from an upper reaction mass by four fused-silica fibers. Adapted from [26]. 101
FIGURE 5.4 LVK Observing Timeline. Adapted from [27] 102
FIGURE 5.5 Diagram of the four types of gravitational wave producers. Adapted from [28]. 105
FIGURE 5.6 Diagram of the merger cycle from inspiral to merger to ringdown. Adapted from [29]. 106

FIGURE 6.1 An illustration of the SNO+ scintillator phases. 118
FIGURE 6.2 The ±1000 s coincidence window highlighted by the pink rectangle defines the signal region used to search for neutrinos temporally coincident with GW events.123
FIGURE 6.3 Comparison of generated electron antineutrino energy distributions using the standard IBD generator (top) and the modified flat spectrum IBD generator developed for this analysis (bottom). 126
FIGURE 6.4 RAT801 GW MC production with run 310048 (PPO–top) and run 355014 (bisMSB–bottom), reweighted using the reactor antineutrino spectrum (blue). Overlaying this with the analysis script using RAT801 SNO+ PPO MC production for the reactor IBD spectrum with the same runs (black). 128
FIGURE 6.5 Differential neutrino-proton ES cross section calculated using the analytic expression of Dasgupta and Beacom [30] for representative neutrino energies. . . 130
FIGURE 6.6 Differential neutrino-proton ES cross section implemented in the original RAT `ProtonESgen.cc` event generator. 131
FIGURE 6.7 The "Wrong Cross Section" curve corresponds to the original RAT implementation, while the "Corrected Cross Section" curve uses the locally updated implementation matching the analytic expression from Dasgupta and Beacom [30]. 131
FIGURE 6.8 GKVM CCSN fluence as a function of neutrino energy for all flavors (left) and the cross sections of the IBD and neutrino-proton ES channels, alongside another IBD cross section from SNOwGLoBES in orange (right). 142
FIGURE 6.9 Reconstructed energy distributions of prompt (top) and delayed (bottom) IBD candidates. The dashed distributions correspond to IBD candidates identified in the background-only dataset, while the solid distributions correspond to candidates found within the ±1000 s GW coincidence windows. No IBD candidates were observed in the GW-coincident sample. 160
FIGURE 6.10 Singles distribution of events in the PPO+BHT (blue) and bisMSB (red) phases. The dashed distributions correspond to the background-only dataset, while the solid distributions show events within the ±1000 s GW coincidence windows. 161

FIGURE 6.11 SNO+ 90% confidence level monoenergetic IBD stacked common-fluence upper limit obtained using all 126 GW candidates (red), compared with the stacked Borexino result using 74 GW candidates (black). Both analyses report stacked average (per-GW) fluence limits under the assumption that every GW candidate produces the same neutrino fluence at Earth. 166
FIGURE 6.12 SNO+ 90% confidence level monoenergetic IBD stacked common-fluence upper limits separated by LVK merger classification. The BBH result combines 122 GW candidates and uses $N_{90}^{\mathrm{BBH}} = 1.49$, while the NS-BH result combines four candidates and uses $N_{90}^{\mathrm{NSBH}} = 2.40$. 167
FIGURE 6.13 Comparison of 90% confidence level monoenergetic $\bar{\nu}_e$ fluence upper limits. The SNO+ result (red) is the stacked common-fluence limit from 126 GW candidates, and the Borexino result (black) is the corresponding stacked limit from 74 candidates. The SNO+ individual-GW result (magenta) is shown together with the published individual-event limits from Borexino (cyan), KamLAND (slate gray and orange), and Super-Kamiokande (blue). 168
FIGURE 6.14 Effect of different possible unblinding outcomes on the SNO+ 90% confidence level IBD fluence upper limits. Curves correspond to different assumed numbers of observed events in the GW coincidence windows, with the upper limits calculated using the Feldman-Cousins approach. 170
FIGURE 6.15 Normalized effective distances used to convert the stacked common-fluence limits into isotropic-equivalent emitted-energy constraints. The values are calculated using $D_{\mathrm{eff}}^2 = N_{\mathrm{GW}} / \sum_i d_i^{-2}$ for the full GW sample ("All", $N = 126$), the BBH sample ($N = 122$), and the NS-BH sample ($N = 4$). The relatively small NS-BH effective distance reflects the proximity of the four NS-BH candidates compared with the BBH population. 172
FIGURE 6.16 Upper limits on the common isotropic-equivalent energy emitted in electron antineutrinos for the full, BBH, and NS-BH stacked GW samples under the GKVM and Fermi-Dirac spectral assumptions. The limits use the stacked common-fluence constraints and the normalized effective distances defined in Equation 6.64. 174
FIGURE 6.17 Simulated neutrino-proton ES reconstructed energy as a function of incident neutrino energy after applying the analysis energy range. The low reconstructed visible energies arise from ionization quenching of proton recoils in liquid scintillator. 178
FIGURE 6.18 Reconstructed energy distribution of neutrino-proton ES candidates in the optimized ± 50 s GW coincidence windows compared with the scaled sideband background prediction. Both distributions are summed over the GW candidates and scintillator phases. Error bars show the statistical uncertainties on the GW-coincident and scaled sideband samples. 180
FIGURE 6.19 Combined SNO+ 90% confidence level stacked (average per-GW) monoenergetic neutrino-proton ES fluence upper limits using the final 126 astrophysical GW candidates. The limits assume a common neutrino fluence at Earth for every GW candidate and are reported using the same per-GW normalization convention as the IBD analysis. 182

FIGURE 6.20 SNO+ 90% confidence level monoenergetic neutrino-proton ES fluence upper limits separated by GW merger classification. 183

CHAPTER 1

INTRODUCTION

"It's not a question, but a lesson learned in time"

— "Good Riddance (Time of Your Life)," Green Day

The direct detection of gravitational waves in 2015 opened a new observational window on the Universe and established gravitational wave astronomy as a major branch of modern astrophysics. The subsequent discovery of the binary neutron star merger GW170817 and its associated electromagnetic counterpart demonstrated the power of multi-messenger observations for studying compact binary mergers. Despite these successes, no statistically significant detection of MeV neutrinos in temporal coincidence with gravitational wave events has been reported to date.

The LIGO-Virgo-KAGRA collaboration has reported approximately 302 candidate gravitational wave events during the joint fourth observing run (O4), the longest observing campaign to date, spanning from May 24, 2023 to November 18, 2025.

This dissertation presents a search for MeV neutrinos in temporal coincidence with gravitational wave events using data from the SNO+ experiment. The analysis considers two complementary interaction channels: inverse beta decay (IBD), which is primarily sensitive to electron antineutrinos, and neutrino-proton elastic scattering (ES), which is sensitive to neutrinos of all flavors through the neutral current interaction. By searching for neutrino signals associated with gravitational wave events, this work probes models predicting low-energy neutrino emission from compact binary mergers and contributes to the growing field of multi-messenger astronomy.

In addition to the physics analysis, this dissertation includes several detector and software developments that improved the SNO+ experiment. These include measurements of the deployed scintillator light yield, implementation and testing of an electronics baseline monitoring system, characterization of the detector's absolute timing for gravitational wave coincidence studies, improvements to the IBD Monte Carlo generator, and the correction of the neutrino-proton elastic

scattering cross section used in the detector simulation.

Chapter 2 reviews the history of the neutrino and its role within the Standard Model of particle physics. Topics include neutrino oscillations, propagation decoherence, neutrino masses, and the principal natural and artificial sources of neutrinos.

Chapter 3 presents a detailed description of the SNO+ experiment, including the detector design, photomultiplier tubes, electronics, data acquisition system, and calibration methods. Detector characterization studies performed as part of this dissertation are also presented, including measurements of the deployed scintillator light yield, studies of the electronics baseline monitoring system, and characterization of the detector's absolute timing for gravitational wave coincidence analyses.

Chapter 4 discusses the SNO+ simulation and analysis tools. This includes a description of the `RAT` software package and the reconstruction methods used to infer the properties of events in the detector. Modifications to the IBD event generator and corrections to the neutrino-proton elastic scattering cross section for this work are described in Chapter 6.

Chapter 5 provides an overview of gravitational wave physics and modern gravitational wave detectors. The chapter reviews compact binary mergers, multi-messenger astronomy, the expected production of MeV neutrinos from gravitational wave sources, and previous experimental searches for neutrinos coincident with gravitational wave events.

Chapter 6 presents the search for neutrinos in temporal coincidence with gravitational wave events. The chapter describes the data sets, event selection criteria, signal efficiencies, background estimation, statistical methodology, and the resulting upper limits on the neutrino fluence from compact binary mergers.

No statistically significant neutrino signal was observed in temporal coincidence with gravitational wave events. Consequently, new upper limits on the MeV neutrino fluence from compact binary mergers are established using the SNO+ detector.

CHAPTER 2

THE HISTORY OF THE NEUTRINO

"Wish we could turn back time to the good old days

When our mama sang us to sleep, but now we're stressed out

We're stressed out"
— "Stressed Out," Twenty One Pilots

The neutrino has a rich history, from its initial postulation to the present day, as physicists continue to investigate its fundamental properties. It has been the subject of extensive theoretical and experimental study for many decades. Its elusive nature, resulting from its weak interaction with matter, makes its detection and full understanding challenging. The following sections describe the development of neutrino physics, from its conception and eventual discovery to the many questions and challenges that remain today.

2.1 The Proposal of the Neutrino

The history of the neutrino begins not with the neutrino itself, but with a radioactive process known as beta decay. Beta decay is the process by which an unstable nucleus releases energy through the emission of an electron or a positron, while converting a neutron into a proton (or a proton into a neutron) as depicted in Equations 2.1 and 2.2. In both cases of β^- (Eq. 2.1) and β^+ (Eq. 2.2) decay, however, the emitted electron or positron does not exhibit a well-defined energy. Instead, it displays a continuous energy spectrum, shown in Figure 2.1, which appeared to violate the law of conservation of energy.

$$n \rightarrow p + e^- + \bar{\nu}_e \tag{2.1}$$

$$p \rightarrow n + e^+ + \nu_e \tag{2.2}$$

A solution to this apparent violation was proposed in 1930 by Wolfgang Pauli. After considering the problem, Pauli suggested a radical explanation. Perhaps the beta particle (electron/positron) was not the only particle emitted in beta decay. This tertiary particle would have to be extremely

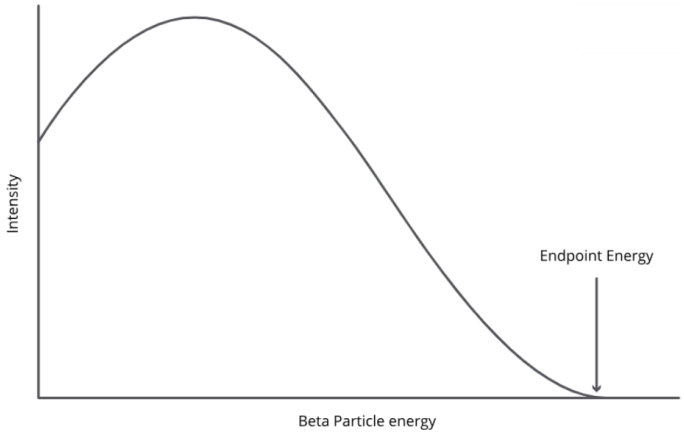


Figure 2.1: Beta particle's continuous energy spectrum with endpoint energy noted as the expected observation [5].

elusive, as it had not been observed experimentally. Pauli proposed that this particle would have no electric charge, be nearly massless, and interact only weakly with matter [31]. With the inclusion of this particle, the continuous energy spectrum observed in beta decay could be explained.

Pauli initially referred to this hypothetical particle as a "neutron," at least until 1932, when the neutral counterpart to the proton was discovered and given that name. The particle proposed by Pauli was later renamed the "neutrino" by Enrico Fermi, who developed a comprehensive theory of beta decay in 1934 [32]. At the time, Pauli believed the neutrino would be impossible to detect.

From the 1930s to the 1950s, Pauli's assertion held true: the neutrino remained undetected.

2.2 The Discovery of the Neutrino

It was not until 26 years after Pauli's proposal that the neutrino was experimentally observed for the first time. Frederick Reines and Clyde Cowan undertook one of the most challenging tasks in experimental physics: detecting the neutrino. As nuclear physicists, their initial idea involved placing a detector in free fall down a shaft as a bomb was detonated, as depicted in Figure 2.2. This approach was ultimately deemed impractical, and they instead turned to a more controlled and sustained source: the Savannah River nuclear reactor.

Although a nuclear reactor produces a neutrino flux approximately 1,000 times weaker than that

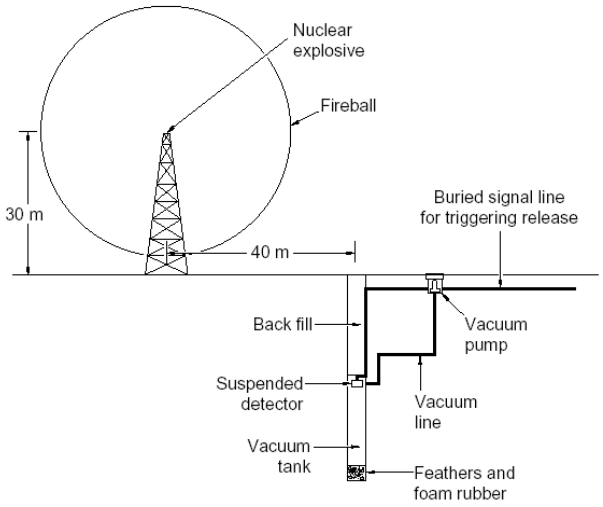


Figure 2.2: Reines and Cowan's initial proposal to detect the neutrino using a nuclear explosion [6].

of a nuclear bomb [33], it offers the key advantage of providing a continuous and stable source over extended periods, making detection feasible.

Using antineutrinos emitted from the Savannah River nuclear reactor, Reines and Cowan successfully achieved the first experimental detection of the neutrino, as reported in their paper titled "The Neutrino" [34].

Their experiment used a cadmium-doped water target placed between two liquid scintillator detectors just outside a nuclear reactor core. Detection relied on observing the coincidence between the positron produced in inverse beta decay (see Subsection 2.8.4) and the γ rays emitted during neutron capture.

2.3 Neutrinos in the Standard Model

The Standard Model of particle physics was developed in the 1960s and 1970s to classify all known elementary particles and describe their interactions. It includes three of the four fundamental forces of nature: electromagnetism, the strong force, and the weak force. Gravity is not included in the Standard Model. In addition, the Standard Model succeeds in categorizing the known elementary particles according to their intrinsic spin and the interactions in which they participate. A summary of the Standard Model, including the known elementary particles and force-carrier bosons, is shown

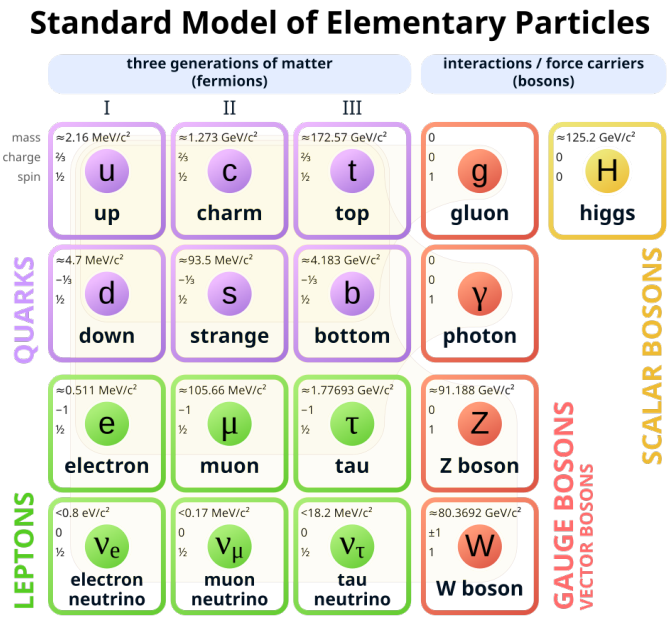


Figure 2.3: Diagram of the elementary particles in the Standard Model [7].

in Figure 2.3.

A large number of measurements have been performed testing the accuracy of the Standard Model, nearly all of which have been found to agree with its predictions to high precision. However, there are still a few observations that cannot be explained by the Standard Model. Several of these unresolved questions involve neutrinos. In the Standard Model, neutrinos are neutral leptons with three different flavor states (ν_e, ν_μ, ν_τ), which only interact via the weak force and gravity. As a result, neutrino cross sections are small and their interactions are rare. The detection and study of neutrinos are challenging, which leaves many open questions about their fundamental properties.

For example, neutrinos produced as one flavor can later be detected as another flavor. This phenomenon is referred to as neutrino oscillation (see Section 2.4) and implies that neutrinos have mass. This feature is not included in the Standard Model, which describes neutrinos and antineutrinos as massless neutral fermions, with only left-handed neutrinos and right-handed antineutrinos participating in weak interactions. Many experiments over the years have set out to measure the mass of the neutrino. Current experiments have established that neutrino masses are extremely small, but

the absolute value remains unknown. The mechanism that governs how neutrinos obtain their mass is also unknown. The following sections discuss the properties of neutrinos in more detail.

2.4 Neutrino Oscillation

Unless otherwise stated, this section uses natural units ($\hbar = c = 1$). In these units, energy, momentum, and mass are expressed in electronvolts (eV) and their derived units, while length and time have units of inverse energy. SI forms of commonly used oscillation formulas are provided where appropriate

2.4.1 Oscillations in Vacuum

Neutrinos are produced through weak interactions in one of three flavors, known as flavor eigenstates, $|\nu_{e,\mu,\tau}\rangle$ and propagate according to their three mass eigenstates $|\nu_{1,2,3}\rangle$. The relationship between these eigenstates is described by Equation 2.3:

$$|\nu_\alpha\rangle = \sum_{i=1}^{3} U^*_{\alpha i}|\nu_i\rangle, \quad \alpha = e, \mu, \tau \tag{2.3}$$

where α is the flavor states (e, μ, τ) and i is the mass eigenstates (1,2,3). The flavor states are superpositions of the mass eigenstates, and only mass eigenstates propagate simply. $U_{\alpha,i}$ are the elements of a 3×3 unitary matrix referred to as the Pontecorvo-Maki-Nakagawa-Sakata (PMNS) matrix. The PMNS matrix (Equation 2.4) is parameterized by the following three mixing angles: θ_{12}, θ_{13}, and θ_{23}, along with a charge-parity (CP) violating phase δ_{CP}:

$$U = \begin{pmatrix} c_{12}c_{13} & s_{12}c_{13} & s_{13}e^{-i\delta_{CP}} \\ -s_{12}c_{23} - c_{12}s_{23}s_{13}e^{i\delta_{CP}} & c_{12}c_{23} - s_{12}s_{23}s_{13}e^{i\delta_{CP}} & s_{23}c_{13} \\ s_{12}s_{23} - c_{12}c_{23}s_{13}e^{i\delta_{CP}} & -c_{12}s_{23} - s_{12}c_{23}s_{13}e^{i\delta_{CP}} & c_{23}c_{13} \end{pmatrix} \tag{2.4}$$

where $c_{ij} = \cos\theta_{ij}$ and $s_{ij} = \sin\theta_{ij}$. If U was diagonal (i.e., θ_{12}, θ_{13}, and $\theta_{23} = 0$), the flavor eigenstates would map directly to the mass eigenstates. The PMNS matrix could be written into a product of three matrices (under three separate rotations) involving only one mixing angle θ_{ij} each, as shown in Equation 2.5.

$$U = \begin{pmatrix} 1 & 0 & 0 \\ 0 & c_{23} & s_{23} \\ 0 & -s_{23} & c_{23} \end{pmatrix} \begin{pmatrix} c_{13} & 0 & s_{13}e^{-i\delta_{CP}} \\ 0 & 1 & 0 \\ -s_{13}e^{-i\delta_{CP}} & 0 & c_{13} \end{pmatrix} \begin{pmatrix} c_{12} & s_{12} & 0 \\ -s_{12} & c_{12} & 0 \\ 0 & 0 & 1 \end{pmatrix} \tag{2.5}$$

Each angle controls mixing between one pair of mass states, where θ_{12} is traditionally referred to as the solar sector, θ_{13} connects 1 and 3 and allows CP phase effects, and θ_{23} is traditionally referred to as the atmospheric sector. The propagation of the neutrino is governed by the time-dependent Schrödinger equation:

$$i\frac{d}{dt}|\nu_i(t)\rangle = H|\nu_i(t)\rangle \tag{2.6}$$

For neutrinos in vacuum, the mass eigenstates are energy eigenstates of the free Hamiltonian:

$$H|\nu_i\rangle = E_i|\nu_i\rangle \tag{2.7}$$

Schrödinger's equation (Equation 2.6) can be solved knowing that for a mass eigenstate, since Equation 2.7 is true, a time-dependent state can be written as:

$$|\nu_i(t)\rangle = f_i(t)|\nu_i\rangle \tag{2.8}$$

where $f_i(t)$ is a complex-valued function that describes the time evolution of the mass eigenstate and $|\nu_i\rangle$ is now used as the time-independent eigenstate at $t = 0$. Substituting this expression into Equation 2.6 gives:

$$i\frac{d}{dt}(f_i(t)|\nu_i\rangle) = H(f_i(t)|\nu_i\rangle) \tag{2.9}$$

Because the mass eigenstate $|\nu_i\rangle$ is time-independent, the time derivative acts only on $f_i(t)$, yielding:

$$i\frac{d}{dt}(f_i(t)|\nu_i\rangle) = f_i(t)H|\nu_i\rangle \tag{2.10}$$

Applying Equation 2.7, the Hamiltonian acting on the mass eigenstate produces a factor of E_i. Since $|\nu_i\rangle$ appears on both sides of the equation, it can be divided out, resulting in:

$$i\frac{df_i(t)}{dt} = E_i f_i(t) \tag{2.11}$$

Rearranging this expression gives:

$$\frac{df_i(t)}{dt} = -iE_i f_i(t) \tag{2.12}$$

The solution to this first-order differential equation is:

$$f_i(t) = e^{-iE_i t} \tag{2.13}$$

Substituting this result back into Equation 2.6 yields the time evolution of a mass eigenstate:

$$|\nu_i(t)\rangle = e^{-iE_i t}|\nu_i\rangle \tag{2.14}$$

A neutrino produced as a flavor eigenstate is a superposition of mass eigenstates, each of which evolves according to Equation 2.3. The time-dependent flavor state is therefore given by:

$$|\nu_\alpha(t)\rangle = \sum_i U^*_{\alpha i} e^{-iE_i t}|\nu_i\rangle \tag{2.15}$$

The amplitude for a neutrino produced in flavor state α to be detected later as flavor state β is obtained by projecting the evolved state onto $\langle\nu_\beta|$:

$$A_{\alpha\to\beta}(t) = \langle\nu_\beta|\nu_\alpha(t)\rangle \tag{2.16}$$

with

$$|\nu_\beta\rangle = \sum_j U^*_{\beta j}|\nu_j\rangle \tag{2.17}$$

Taking the Hermitian conjugate gives:

$$\langle \nu_\beta | = \sum_j U_{\beta j} \langle \nu_j | \tag{2.18}$$

Substituting these expressions into Equation 2.16 gives:

$$A_{\alpha\to\beta}(t) = \Big(\sum_j U_{\beta j}\langle \nu_j|\Big)\Big(\sum_i U^*_{\alpha i} e^{-iE_i t}|\nu_i\rangle\Big) \tag{2.19}$$

Expanding the sums yields:

$$A_{\alpha\to\beta}(t) = \sum_{i,j} U_{\beta j} U^*_{\alpha i} e^{-iE_i t}\langle \nu_j|\nu_i\rangle \tag{2.20}$$

where the orthonormality of mass eigenstates is:

$$\langle \nu_j|\nu_i\rangle = \delta_{ji} \tag{2.21}$$

Using the orthonormality of the mass eigenstates, only terms with $j = i$ survive, resulting in:

$$A_{\alpha\to\beta}(t) = \sum_i U_{\beta i} U^*_{\alpha i} e^{-iE_i t} \tag{2.22}$$

The transition probability is given by the modulus squared of the amplitude:

$$P_{\nu_\alpha\to\nu_\beta}(t) = |A_{\alpha\to\beta}(t)|^2 = \left|\sum_i U_{\beta i} U^*_{\alpha i} e^{-iE_i t}\right|^2 \tag{2.23}$$

This expression can be written explicitly as the product of the amplitude and its complex conjugate:

$$P_{\nu_\alpha\to\nu_\beta}(t) = \Big(\sum_i U_{\beta i} U^*_{\alpha i} e^{-iE_i t}\Big)\Big(\sum_j U^*_{\beta j} U_{\alpha j} e^{+iE_j t}\Big) \tag{2.24}$$

Multiplying the sums and combining the exponential factors gives:

$$P_{\nu_\alpha \to \nu_\beta}(t) = \sum_{i,j} U_{\beta i} U^*_{\alpha i} U^*_{\beta j} U_{\alpha j} e^{-iE_i t} e^{+iE_j t} \tag{2.25}$$

Thus, the probability that a neutrino produced in flavor eigenstate α is later detected as flavor eigenstate β is:

$$P_{\nu_\alpha \to \nu_\beta}(t) = \sum_{i,j} U^*_{\alpha i} U_{\beta i} U_{\alpha j} U^*_{\beta j} e^{-i(E_i - E_j)t} \tag{2.26}$$

This probability being non-zero for $\alpha \neq \beta$ is known as neutrino oscillation. Equation 2.3 showed that if U were diagonal, each flavor state would correspond to a unique mass eigenstate. In that case, $U_{\alpha i} = \delta_{\alpha i}$, and the off-diagonal terms ($\alpha \neq \beta$) vanish identically. Therefore, $P_{\nu_\alpha \to \nu_\beta} = 0$ for $\alpha \neq \beta$, and neutrino oscillations would not occur.

To obtain a more useful form of the oscillation probability, several approximations can be made. Assuming the neutrino is highly relativistic and using natural units ($c = \hbar = 1$), the energy of the i^{th} mass eigenstate may be expanded as

$$E_i = \sqrt{p_i^2 + m_i^2} \approx p + \frac{m_i^2}{2p} \tag{2.27}$$

where the neutrino masses are small compared with their momenta and all mass eigenstates are assumed to have approximately the same momentum p. For relativistic neutrinos, $p \simeq E$, giving

$$E_i - E_j \approx \frac{\Delta m_{ij}^2}{2E} \tag{2.28}$$

where the mass-squared differences are defined as $\Delta m_{ij}^2 = m_i^2 - m_j^2$. Since relativistic neutrinos travel at approximately the speed of light ($v \approx c$), the propagation time and distance are related

by $t \approx L$[1]. Substituting Equation 2.28 into Equation 2.26 yields

$$P_{\nu_\alpha \to \nu_\beta}(L, E) = \sum_{i,j} U^*_{\alpha i} U_{\beta i} U_{\alpha j} U^*_{\beta j} e^{-i \frac{\Delta m^2_{ij} L}{2E}} \tag{2.29}$$

From Equation 2.29, it can be seen that the magnitude of the transition probability depends entirely on the elements of U, while the phase depends on the mass-squared differences (Δm^2_{ij}), the distance traveled by the neutrino (L), and the energy of the neutrino (E). The real and imaginary parts can be separated as:

$$\begin{aligned} P_{\nu_\alpha \to \nu_\beta}(L, E) = \delta_{\alpha\beta} &- 4 \sum_{i<j} \mathrm{Re}\left[U_{\alpha i} U^*_{\beta i} U^*_{\alpha j} U_{\beta j}\right] \sin^2\left(\frac{\Delta m^2_{ij} L}{4E}\right) \\ &+ 2 \sum_{i<j} \mathrm{Im}\left[U_{\alpha i} U^*_{\beta i} U^*_{\alpha j} U_{\beta j}\right] \sin\left(\frac{\Delta m^2_{ij} L}{2E}\right) \end{aligned} \tag{2.30}$$

For massless neutrinos, which make up the Standard Model, $\Delta m^2_{ij} = 0$ and the sine terms in Equation 2.30 are zero. Thus, oscillation requires massive neutrinos (as well as mixing). Also of note is that the oscillation probability depends only on the mass-squared differences of the neutrino masses. Despite requiring massive neutrinos, oscillation cannot be used to determine the absolute neutrino masses.

The same derivations can be performed for antineutrinos, but with the relationship between the flavor and mass eigenstates defined by the complex conjugate of U. Equation 2.4 shows that the only way to obtain a non-zero, imaginary component for any $U_{\alpha i}$ is through a non-zero value for δ_{CP}. The difference between U and U^*, and therefore the difference between neutrino and antineutrino oscillation (in vacuum), is determined by δ_{CP}.

The simplified two-neutrino case is also shown as an example for comparison to the more complicated

[1] In natural units, L is measured in inverse energy (eV^{-1}). Restoring SI units gives the commonly used oscillation phase $1.27\,\Delta m^2_{ij}[\mathrm{eV}^2] L[\mathrm{m}]/E[\mathrm{MeV}]$.

result accounting for matter effects. The mixing matrix for this case is given by:

$$U = \begin{pmatrix} \cos(\theta) & \sin(\theta) \\ -\sin(\theta) & \cos(\theta) \end{pmatrix} \tag{2.31}$$

and the oscillation probability is given by:

$$P_{\nu_e \to \nu_\mu}(L, E) = \sin^2(2\theta)\, \sin^2\left(\frac{\Delta m^2 L}{4E}\right) \tag{2.32}$$

2.4.2 Oscillations in Matter

In addition to neutrino propagation in vacuum, it is important to understand how neutrinos oscillate while traveling through matter. As neutrinos propagate through matter, they undergo both neutral current (NC) and charged current (CC) interactions with electrons (e^-), protons (p), and neutrons (n). NC interactions affect all three neutrino flavors equally and therefore do not alter the oscillation probabilities. CC interactions occur only for electron neutrinos (ν_e) interacting with electrons (e^-). This additional interaction introduces a flavor-dependent potential that modifies the oscillation probabilities.

The effective matter potential arising from CC interactions of ν_e is given by:

$$V_{CC} = \pm\sqrt{2} G_F n_e \tag{2.33}$$

where G_F is the Fermi constant and n_e is the electron number density of the medium. The potential is positive (+) for neutrinos and negative (-) for antineutrinos. Electron neutrinos experience both CC and NC interactions with electrons, whereas muon neutrinos and tau neutrinos experience only NC interactions. For antineutrinos, the CC contribution changes sign, producing an effective matter potential of opposite sign. Since NC interactions contribute equally to all active flavors, they cancel from the oscillation probabilities.

In the flavor basis, the total Hamiltonian is the sum of the vacuum and matter contributions:

$$H = H_{vacuum} + H_{matter} \tag{2.34}$$

The matter contribution can be written in the matrix form as:

$$A = \begin{pmatrix} A_{CC} & 0 & 0 \\ 0 & 0 & 0 \\ 0 & 0 & 0 \end{pmatrix} \tag{2.35}$$

with $A_{CC} = 2EV_{CC}$.

In the mass basis, it is the matrix M:

$$M = \begin{pmatrix} 0 & 0 & 0 \\ 0 & \Delta m^2_{21} & 0 \\ 0 & 0 & \Delta m^2_{31} \end{pmatrix} \tag{2.36}$$

Converting to the flavor basis can be done using:

$$H_{vacuum} = \frac{1}{2E} U M U^{\dagger} \tag{2.37}$$

The full Hamiltonian in the flavor basis can therefore be written as:

$$H = \frac{1}{2E}(U M U^{\dagger} + A) \tag{2.38}$$

For simplicity, two-flavor mixing between ν_e and ν_μ is considered to illustrate the essential features

of matter-enhanced oscillations. In this approximation, the vacuum Hamiltonian is:

$$H_{vacuum} = \frac{\Delta m^2}{4E} \begin{pmatrix} -\cos(2\theta) & \sin(2\theta) \\ \sin(2\theta) & \cos(2\theta) \end{pmatrix} \tag{2.39}$$

The corresponding matter contribution is:

$$H_{matter} = \frac{1}{2E} \begin{pmatrix} A_{CC} & 0 \\ 0 & 0 \end{pmatrix} \tag{2.40}$$

Combining the vacuum and matter terms yields the evolution equation:

$$i\frac{d}{dt} \begin{pmatrix} \psi_{ee} \\ \psi_{e\mu} \end{pmatrix} = \frac{1}{4E} \begin{pmatrix} -\Delta m^2 \cos(2\theta) + A_{CC} & \Delta m^2 \sin(2\theta) \\ \Delta m^2 \sin(2\theta) & \Delta m^2 \cos(2\theta) - A_{CC} \end{pmatrix} \begin{pmatrix} \psi_{ee} \\ \psi_{e\mu} \end{pmatrix} \tag{2.41}$$

Diagonalizing this Hamiltonian gives:

$$\mathcal{H} = \frac{1}{4E} \begin{pmatrix} -\Delta m^2_{\text{eff}} & 0 \\ 0 & \Delta m^2_{\text{eff}} \end{pmatrix} \tag{2.42}$$

This defines the effective mass-squared difference, Δm^2_{eff}. The transformation to the diagonal basis is accomplished using the effective mixing matrix:

$$U_{matter} = \begin{pmatrix} \cos(\theta_{\text{eff}}) & \sin(\theta_{\text{eff}}) \\ -\sin(\theta_{\text{eff}}) & \cos(\theta_{\text{eff}}) \end{pmatrix} \tag{2.43}$$

Comparing the matrix elements yields the effective mixing angle:

$$\sin^2(2\theta_{\text{eff}}) = \frac{\sin^2(2\theta)}{\left(\cos 2\theta - A_{CC}/\Delta m^2\right)^2 + \sin^2(2\theta)} \tag{2.44}$$

Because the matter potential changes sign for antineutrinos, the effective mixing parameters differ between neutrinos and antineutrinos. The oscillation probability in matter is then:

$$P_{\nu_e \to \nu_\mu}(L, E) = \sin^2(2\theta_{\text{eff}}) \sin^2\left(\frac{\Delta m^2_{\text{eff}} L}{4E}\right) \tag{2.45}$$

This expression has the same form as the vacuum oscillation probability (Equation 2.32), but with the vacuum mixing angle and mass-squared difference replaced by their effective values in matter. An analogous calculation can be performed for the three-neutrino case, which results in a similar substitution of effective mixing angles and mass-squared differences (as shown in [35]).

A notable feature of matter-enhanced oscillation is that $\sin^2(2\theta_{\text{eff}}) = 1$ when $\cos 2\theta - A_{CC}/\Delta m^2 = 0$. Under this resonance condition, oscillations become maximal even when the vacuum mixing angle (determined by $\sin^2(2\theta)$) is small. For neutrinos, this occurs at a specific electron density or neutrino energy:

$$n_e = \frac{\Delta m^2 \cos 2\theta}{2\sqrt{2}\, E G_F} \quad \text{or} \quad E = \frac{\Delta m^2 \cos 2\theta}{2\sqrt{2}\, n_e G_F} \tag{2.46}$$

This resonant enhancement of neutrino oscillations is known as the Mikheyev-Smirnov-Wolfenstein (MSW) effect and plays a central role in the flavor conversion of solar neutrinos. As solar neutrinos propagate from the dense core toward the lower-density surface, the electron density changes continuously. Consequently, the effective mixing angle evolves continuously until the neutrinos emerge into vacuum.

2.5 Neutrino Decoherence

As discussed in the previous section, neutrino flavor eigenstates are quantum mechanical superpositions of the three mass eigenstates,

$$|\nu_\alpha\rangle = \sum_{i=1}^{3} U_{\alpha i} |\nu_i\rangle \tag{2.47}$$

During coherent propagation, the probability of a flavor transition is given by Equation 2.23. The

oscillation probability arises from interference between the different mass eigenstates and depends upon the relative phase accumulated during propagation.

The relative phase between two mass eigenstates is

$$\Delta\phi_{ij} = \frac{\Delta m_{ij}^2 L}{2E} \tag{2.48}$$

where

$$\Delta m_{ij}^2 = m_i^2 - m_j^2 \tag{2.49}$$

One complete oscillation occurs when the relative phase advances by 2π. Setting Equation 2.48 equal to 2π gives the oscillation length,

$$L_{\text{osc}} = \frac{4\pi E}{\Delta m_{ij}^2} \tag{2.50}$$

For a representative neutrino energy of $E = 10$ MeV and the atmospheric mass splitting $\Delta m_{32}^2 \approx 2.5 \times 10^{-3}$ eV^2,

$$L_{\text{osc}} \approx 10 \text{ km} \tag{2.51}$$

Compact binary mergers detected through gravitational waves typically occur at distances of hundreds of Mpc. Consequently, MeV neutrinos from these sources undergo approximately

$$N_{\text{osc}} \sim \frac{L}{L_{\text{osc}}} \sim 10^{20} \tag{2.52}$$

oscillation cycles before reaching Earth. Since neither the neutrino source nor the detector possesses sufficient energy resolution to resolve individual oscillations over such enormous baselines, the oscillatory interference terms average to zero.

$$\left\langle e^{-i\frac{\Delta m_{ij}^2}{2E}L} \right\rangle \to 0 \tag{2.53}$$

Equation 2.23 therefore reduces to the oscillation-averaged probability

$$P^{\text{avg}}_{\nu_\alpha \to \nu_\beta} = \sum_i \left|U_{\beta i}\right|^2 \left|U_{\alpha i}\right|^2 \tag{2.54}$$

which is the practical limit for astrophysical distances. The oscillation-averaged probability accurately describes essentially all astrophysical neutrino observations. In practice, the oscillatory terms are first washed out by the finite energy resolution of the detector together with the intrinsic energy spread of the emitted neutrinos. Over sufficiently long propagation distances, however, the loss of coherence becomes physical as the individual mass eigenstate wave packets separate in space. Once the wave packets no longer overlap, quantum interference is no longer possible. Unlike coherent oscillations, the oscillation-averaged probability no longer depends explicitly on the propagation distance or the oscillation phase.

For an electron neutrino produced at the source, the probabilities that the electron neutrino occupies each mass eigenstate is

$$|U_{e1}|^2 \approx 0.67 \tag{2.55}$$

$$|U_{e2}|^2 \approx 0.30 \tag{2.56}$$

$$|U_{e3}|^2 \approx 0.02 \tag{2.57}$$

Thus, an electron neutrino is produced predominantly as ν_1, with smaller contributions from ν_2, and only a few percent in ν_3. After oscillations have averaged out, these fractions remain constant with distance because the three mass eigenstates propagate independently.

In natural units ($c = 1$), the group velocity of mass eigenstate i is

$$v_i \simeq 1 - \frac{m_i^2}{2E^2} \tag{2.58}$$

The spatial separation between two mass eigenstates after propagating a distance L is

$$\Delta x_{ij} \simeq \Delta v_{ij} L \simeq \frac{\left|\Delta m_{ij}^2\right|}{2E^2} L \tag{2.59}$$

Decoherence occurs when this separation exceeds the wave packet spatial width σ_x:

$$\Delta x_{ij} \gtrsim \sigma_x \tag{2.60}$$

Combining Equations 2.59 and 2.60 gives the order-of-magnitude coherence length

$$L_{\mathrm{coh},ij} \sim \frac{2E^2 \sigma_x}{\left|\Delta m_{ij}^2\right|} \tag{2.61}$$

More generally, this may be written as

$$L_{\mathrm{coh},ij} \sim \kappa \frac{E^2 \sigma_x}{\left|\Delta m_{ij}^2\right|} \tag{2.62}$$

where κ is a numerical factor of order unity whose precise value depends on the definition and shape of the wave packet.

For a 10 MeV neutrino propagating over a distance of 1 Mpc, assuming $\Delta m_{31}^2 = 2.5 \times 10^{-3}$ eV^2 and $\Delta m_{21}^2 = 7.5 \times 10^{-5}$ eV^2, Equation 2.59 gives

$$\Delta x_{31} \approx 385.7 \text{ km} \tag{2.63}$$

$$\Delta x_{21} \approx 11.6 \text{ km} \tag{2.64}$$

Maintaining coherence over this distance would therefore require emitted neutrino wave packets with spatial widths of tens to hundreds of kilometers, far larger than expected for realistic production processes. The mass eigenstate wave packets are consequently expected to separate well before reaching Earth. Neutrinos produced in supernovae and compact binary mergers therefore arrive at

Earth as an incoherent mixture of mass eigenstates.

The same velocity differences responsible for wave packet separation also produce measurable arrival-time delays. To express these delays in conventional SI units, the factors of c are restored in the following equations. Starting from the relativistic energy relation,

$$E^2 = p^2c^2 + m^2c^4 \tag{2.65}$$

the neutrino velocity for $m \ll E$ is

$$v \simeq c\left(1 - \frac{m^2c^4}{2E^2}\right) \tag{2.66}$$

The resulting arrival-time delay relative to a massless particle is

$$\Delta t \simeq \frac{Lm^2c^3}{2E^2} \tag{2.67}$$

For astrophysical sources, it is convenient to denote the propagation distance by D, emphasizing that it corresponds to the distance from the source to Earth. The arrival-time delay may then be written as

$$\Delta t = 5.14 \text{ ms} \left(\frac{m}{1 \text{ eV}}\right)^2 \left(\frac{10 \text{ MeV}}{E}\right)^2 \left(\frac{D}{10 \text{ kpc}}\right) \tag{2.68}$$

For a representative binary black hole merger located at $D = 410$ Mpc, an emitted neutrino energy of $E = 10$ MeV, and adopting the current direct limit $m_\nu < 0.45$ eV [36], the maximum expected arrival-time delay is

$$\Delta t < 43 \text{ s} \tag{2.69}$$

This delay is significantly smaller than the ± 50 s and ± 1000 s coincidence windows used in this dissertation, ensuring that all three mass eigenstates would remain within the search window even for neutrino masses near the current experimental upper limit. This also demonstrates that neutrino arrival times can, in principle, probe the absolute neutrino mass over cosmological baselines.

The different mass eigenstates therefore also arrive at slightly different times,

$$\Delta t_{ij} = \frac{D\Delta m_{ij}^2}{2E^2 c} \tag{2.70}$$

where Δm_{ij}^2 is the experimentally measured mass-squared difference, conventionally quoted in units of eV^2 (equivalently $(mc^2)^2$).

For the same representative source,

$$\Delta t_{21} \approx 16 \text{ ms} \tag{2.71}$$

$$\Delta t_{32} \approx 0.5 \text{ s} \tag{2.72}$$

These arrival-time differences reflect the same velocity differences that produce wave packet separation. Over cosmological baselines, the individual mass eigenstate wave packets are therefore expected to arrive independently at Earth rather than as a coherent quantum superposition.

Although no coincident neutrino events were observed in the present analysis, a future high-statistics observation of MeV neutrinos coincident with gravitational waves could provide a unique probe of neutrino propagation over cosmological distances. Measurements of the relative arrival times of the detected neutrinos and the associated gravitational wave signal could constrain the absolute neutrino mass, test wave packet decoherence, and potentially distinguish between the normal and inverted neutrino mass orderings, described in Subsection 2.6.1.

2.6 Neutrino Mass

2.6.1 Neutrino Mass Hierarchy

Section 2.4 described neutrino interactions and neutrino oscillations in both vacuum and matter. Neutrino oscillations in vacuum depend only on the magnitudes of the mass-squared differences between the neutrino mass eigenstates, not on their signs. Matter effects within the Sun have allowed solar neutrino experiments to determine that Δm_{21}^2 is positive. The magnitude of Δm_{32}^2 has been measured to be significantly larger than that of Δm_{21}^2. At the time of writing, the sign of

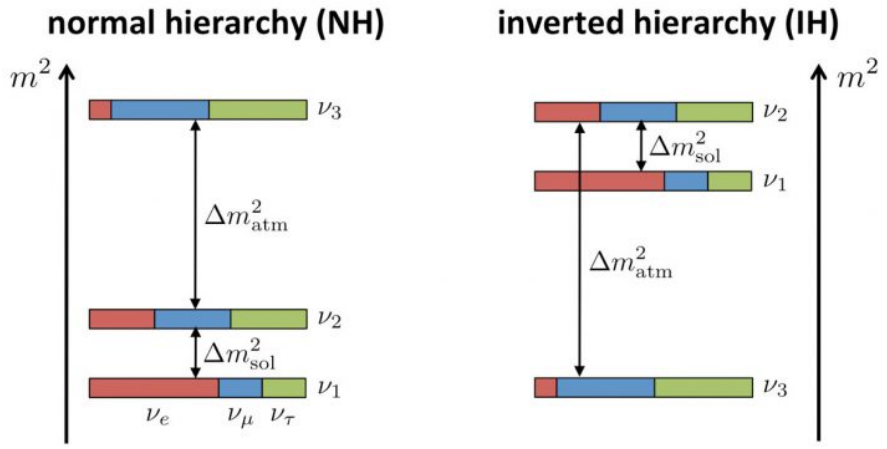


Figure 2.4: Diagrams of the normal hierarchy (left) and inverted hierarchy (right). The colors show the relationships between the flavor eigenstates and the mass eigenstates. Δm^2_{atm} corresponds to Δm^2_{32}, where "atm" traditionally denotes measurements using atmospheric neutrinos. Δm^2_{sol} corresponds to Δm^2_{21}, where "sol" traditionally denotes measurements using solar neutrinos [8].

Δm^2_{32} has not yet been determined. As a result, two possible mass orderings remain: $m_1 < m_2 \ll m_3$ or $m_3 \ll m_1 < m_2$. These scenarios are known as the Normal Hierarchy and the Inverted Hierarchy and are illustrated in Figure 2.4.

2.6.2 Absolute Neutrino Mass

As discussed in Section 2.4, neutrino oscillations depend only on the mass-squared differences between the neutrino mass eigenstates and not on their absolute masses. As a result, oscillation experiments provide little information about the absolute neutrino masses; only lower limits can be placed under the assumption that the lightest mass eigenstate is massless.

The absolute neutrino masses have not yet been measured directly, despite extensive experimental efforts. Several experiments have attempted to determine the neutrino mass through precise measurements of the β decay energy spectrum. One such experiment, KATRIN, currently provides the world's leading direct upper limit on the neutrino mass, with $m_\nu < 0.45$ eV at 90% confidence level (CL) [36]. Indirect constraints on the sum of the neutrino masses have also been obtained from cosmological observations. Several analyses place limits of $\sum m_\nu < \sim$0.1 eV [37–40], although these constraints depend strongly on the underlying cosmological model.

2.6.3 Neutrino Mass Mechanism

As discussed in Section 2.3, neutrinos are massless in the Standard Model. One way to generate neutrino masses is to apply the same mechanism used for the other fermions in the Standard Model: the Higgs mechanism. In this approach, a Dirac mass term is added to the Lagrangian:

$$\mathcal{L} = -m_D \left(\bar{\psi}_L \psi_R + \bar{\psi}_R \psi_L\right) \tag{2.73}$$

where ψ_L and ψ_R represent the left and right chiral states of the neutrino. The Higgs mechanism is given in:

$$m_D = \frac{y_i^\nu V}{\sqrt{2}} \tag{2.74}$$

where V is the Higgs vacuum expectation value and y_i^ν is the Yukawa coupling of the neutrino to the Higgs field. This expression gives the Dirac mass of the neutrino. Although this mechanism can generate neutrino masses, it is unsatisfactory for several reasons.

First, Equation 2.73 implies the existence of both left- and right-handed chiral states for neutrinos and antineutrinos. In the Standard Model, only left-handed neutrinos and right-handed antineutrinos couple to the weak force. However, only left-handed neutrinos and right-handed antineutrinos have been observed experimentally. As a result, this mechanism requires the introduction of a right-handed neutrino field for each generation. These states are sterile with respect to the Standard Model gauge interactions and therefore do not participate in the weak interaction.

Second, current limits on neutrino masses are much smaller than the mass of the electron, the lightest charged fermion. If neutrinos obtain mass through the Standard Model Higgs mechanism, their Yukawa couplings would need to be at least six orders of magnitude smaller than the electron Yukawa coupling, making them by far the smallest Yukawa couplings in the Standard Model.

Because neutrinos are electrically neutral, they may acquire mass through a different mechanism. Majorana's proposal that the neutrino is its own antiparticle implies that $\psi^C = \psi$. The mass term

in the Lagrangian becomes:

$$\mathcal{L} = -m_L \left(\bar{\psi}_L^C \psi_L + \bar{\psi}_L \psi_L^C\right) \tag{2.75}$$

This Majorana mass term addresses the two shortcomings of the Dirac mass term. However, the existence of a Majorana mass term does not exclude the presence of a Dirac mass term. Including both contributions in the Lagrangian gives:

$$\mathcal{L} = -m_L \left(\bar{\psi}_L^C \psi_L + \bar{\psi}_L \psi_L^C\right) - m_R \left(\bar{\psi}_R^C \psi_R + \bar{\psi}_R \psi_R^C\right) - m_D \left(\bar{\psi}_L \psi_R + \bar{\psi}_R \psi_L\right) \tag{2.76}$$

Diagonalizing the resulting mass matrix yields two mass eigenvalues. An important limiting case is the Type-I "seesaw" mechanism, which explains the smallness of the observed neutrino masses and occurs when $m_L = 0$ and $m_R >> m_D$. Other realizations of the seesaw mechanism exist, including Type-II and Type-III seesaw models. In this limit, the mass eigenvalues become:

$$m_{\text{light}} \approx \frac{m_D^2}{m_R}, \qquad m_{\text{heavy}} \approx m_R \tag{2.77}$$

The Type-I seesaw mechanism yields one light and one heavy neutrino mass eigenstate. The seesaw is a ratio where the higher the mass of the right-handed neutrino, the lower the mass of the left-handed neutrino. These metaphorical right-handed neutrinos would be massive. In the Type-I seesaw mechanism, the heavy mass eigenstate is predominantly composed of the right-handed neutrino field and is Majorana in nature when the Majorana mass term m_R is present. Because the heavy neutrino states are expected to have masses far above current experimental energies and mix only weakly with the active neutrinos, they have not yet been observed experimentally.

If neutrinos are Majorana particles, two important consequences follow. First, neutrinos have a lepton number of 1 and antineutrinos have a lepton number of -1. If neutrinos are their own antiparticles, total lepton number is no longer conserved. In addition, the PMNS matrix would

acquire two additional Majorana phases. These phases can be represented by the matrix:

$$P_M = \begin{pmatrix} e^{i\alpha_1} & 0 & 0 \\ 0 & e^{i\alpha_2} & 0 \\ 0 & 0 & 1 \end{pmatrix} \tag{2.78}$$

which multiplies the PMNS matrix on the right, as shown in Equations 2.4 and 2.5. These phases do not affect neutrino oscillation probabilities and appear only in lepton number violating processes. Searching for these lepton number violating processes is a test of the Majorana nature of neutrinos. The most prominent example of such a process is neutrinoless double beta decay.

2.7 Neutrinoless Double Beta Decay

The Dirac and Majorana parameterizations of the PMNS matrix cannot be distinguished through neutrino oscillation experiments. The most direct way to determine whether neutrinos are Dirac or Majorana particles is to search for lepton number violating processes. If neutrinos are Majorana particles, the virtual neutrino emitted at one weak-interaction vertex can be absorbed at the second vertex. Because a non-zero neutrino mass allows the required helicity flip during propagation, the process can proceed without neutrinos appearing in the final state, giving rise to neutrinoless double beta decay ($0\nu\beta\beta$).

Beta decay occurs when a nucleus lowers its energy by changing its atomic number by $\Delta Z = \pm 1$, where a neutron is converted into a proton (or a proton is converted into a neutron. See Equations 2.1 and 2.2). For some nuclei, changing Z by only ± 1 raises its energy due to the difference between even and odd pairing energies. In some nuclei, a change of $\Delta Z = \pm 2$ leads to a more stable, lower-energy configuration, allowing double beta decay ($2\nu\beta\beta$) to occur, though it is a rare process. For β^- decay, the double beta decay process is:

$$(Z, A) \rightarrow (Z \pm 2, A) + 2e^- + 2\nu_e \tag{2.79}$$

The only readily detectable products are the emitted electrons (or positrons), since the nuclear recoil

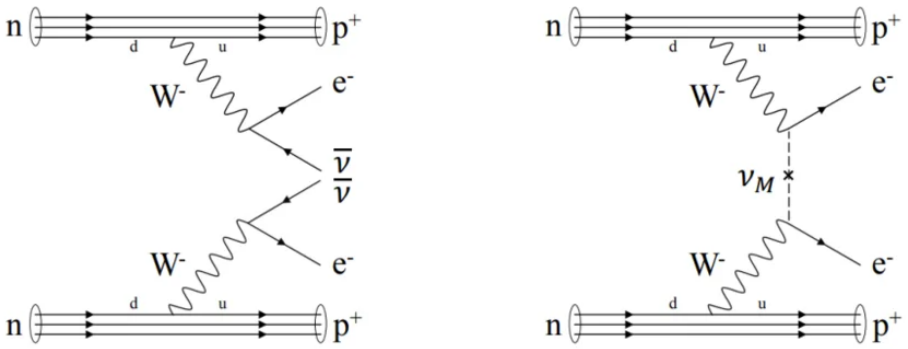


Figure 2.5: Feynman diagrams of double beta decay (left) and neutrinoless double beta decay (right) [9].

is negligible and the neutrinos escape undetected. The electrons (or positrons) exhibit a continuous energy spectrum dependent on the energy taken away by the neutrinos. If neutrinos are Majorana particles, the two virtual neutrinos exchanged in this process can effectively cancel, as illustrated in Figure 2.5.

In $0\nu\beta\beta$ decay (Equation 2.80), essentially all of the released energy is carried by the two electrons (or positrons). As a result, the summed electron energy forms a monoenergetic peak at the endpoint of the $2\nu\beta\beta$ spectrum.

$$(Z, A) \rightarrow (Z + 2, A) + 2e^{-} \tag{2.80}$$

For double beta decay to occur, the isotope must satisfy two conditions: 1) The initial nucleus and final nucleus differ by two units of charge ($Z \rightarrow Z + 2$). 2) The intermediate nucleus with charge $Z + 1$ must be energetically forbidden or strongly suppressed from undergoing ordinary single beta decay. If the nucleus could undergo a fast one-step beta decay, then the double beta decay mode would be irrelevant because the nucleus would decay predominantly through the faster first-order weak process.

Nuclei that undergo double beta decay typically exhibit the mass pattern summarized in Table 2.1.

Thus, $(Z, A) \rightarrow (Z+1, A)$ is energetically forbidden or strongly suppressed and $(Z, A) \rightarrow (Z+2, A)$

Nucleus	Type	Relative Mass
Parent (Z, A)	even-even	low
Intermediate $(Z+1, A)$	odd-odd	high
Final $(Z+2, A)$	even-even	lower

Table 2.1: Typical mass pattern for nuclei that undergo double beta decay.

is energetically allowed. This makes double beta decay the only viable decay path. To date, 20 isotopes have been observed to undergo $2\nu\beta\beta$ decay [1], of which the eight most relevant are listed in Table 2.2. Because of its high natural abundance, ^{130}Te was selected as the double beta decay isotope for SNO+. The dominant decay mode is:

$$^{130}\text{Te} \rightarrow ^{130}\text{Xe} + 2e^- + 2\nu_e \tag{2.81}$$

The intermediate nucleus, ^{130}I, is not accessible through a favorable single beta transition, so ordinary beta decay does not dominate. As a result, ^{130}Te can only decay through the much rarer double beta process. With ^{130}Te, a low energy detection threshold, high energy resolution, and low backgrounds are required to measure the 2.5 MeV decays.

Nuclide	Q-value (MeV)	Isotopic Abundance (%)	Half-life (10^{21} years)
^{48}Ca	4.27	0.187	0.064
^{76}Ge	2.04	7.8	1.93
^{82}Se	3.00	9.2	0.096
^{100}Mo	3.03	9.6	0.69
^{116}Cd	2.81	7.5	0.028
^{130}Te	2.53	34.1	0.82
^{136}Xe	2.46	8.9	2.17
^{150}Nd	3.37	5.6	0.11

Table 2.2: List of eight isotopes known to undergo double beta decay. Isotopes with a higher Q-value (total kinetic energy released) and longer $2\nu\beta\beta$ half-life are most desirable as they allow detectors to achieve lower backgrounds. Additionally, higher isotopic abundance means larger isotope mass can be deployed without requiring expensive enrichment. Information for this table was partially taken from [1].

2.8 Neutrino Sources and Experiments

Neutrino experiments have detected neutrinos from six primary sources: the Sun, the atmosphere, human-made beams, nuclear reactors, radioactivity within the Earth's crust, and supernovae. Most

of these sources and the experiments used to study them are discussed in the following subsections. The sources most relevant to this dissertation are described in Subsections 2.8.4 and 2.8.5. Beam neutrinos are not discussed in this dissertation.

2.8.1 Solar Neutrinos

Following the discovery of the neutrino by Reines and Cowan (see Section 2.2), efforts to understand the fundamental properties of neutrinos accelerated, leading to the construction of increasingly sophisticated neutrino experiments. The Sun is a natural fusion reactor and therefore produces an enormous flux of neutrinos. Solar neutrinos are generated through two sets of thermonuclear reactions: the proton-proton (*pp*) chain and the carbon-nitrogen-oxygen (CNO) cycle. These reactions produce neutrinos with energies extending up to approximately 10-20 MeV. The predicted energy spectra and fluxes of these neutrinos are shown in Figure 2.6.

One of the most successful theories in modern astrophysics is the Standard Solar Model (SSM), which accurately predicts the Sun's luminosity, radius, and surface heavy-element-to-hydrogen ratio [41]. In the late 1960s, the Homestake experiment in Lead, South Dakota, detected only about one-third of the solar neutrino flux predicted by the SSM. Similar results were later obtained by the Kamiokande experiment in 1988. This discrepancy became known as the Solar Neutrino Problem (SNP) and remained one of the major unresolved problems in particle physics and astrophysics for several decades. The deficit was subsequently confirmed by other experiments, including SAGE [42], GALLEX [43], and GNO [44].

The solution to the SNP was established experimentally by the Super-Kamiokande and Sudbury Neutrino Observatory (SNO) experiments in 1998 and 2001, respectively. SNO provided the most definitive evidence that neutrino oscillations were responsible for the observed deficit by using heavy water (D_2O) to measure solar neutrinos through CC, NC, and elastic scattering (ES) interactions [11]:

$$\text{CC} : \nu_e + d \rightarrow e^- + p + p \tag{2.82}$$

$$\text{NC} : \nu_x + d \rightarrow \nu_x + n + p \tag{2.83}$$

$$\text{ES} : \nu_e + e^- \rightarrow \nu_x + e^- \tag{2.84}$$

where $x = (e, \mu, \tau)$.

The Sun produces only electron neutrinos (ν_e), so the detection of ν_μ and ν_τ provides direct evidence for neutrino flavor transformation. The CC interaction on deuterium is sensitive exclusively to ν_e and provides a direct measurement of the electron neutrino flux. The NC interaction is equally sensitive to all neutrino flavors and therefore provides a model-independent measurement of the total solar neutrino flux. The ES interaction is sensitive to all flavors, but the cross section for ν_e is approximately six times larger than that for ν_μ and ν_τ.

SNO measured a ratio of CC to NC fluxes, ϕ_{CC}/ϕ_{NC}, of approximately 0.34, indicating that only about one-third of the original solar electron neutrinos remained as ν_e upon reaching Earth. At the same time, the total flux measured through the NC channel was consistent with the prediction of the SSM. Figure 2.7 summarizes the SNO results, where the flux is decomposed into electron neutrino (ϕ_e) and non-electron neutrino ($\phi_{\mu,\tau}$) components and compared with the SSM prediction. These measurements provided compelling evidence that neutrinos oscillate and therefore possess non-zero mass.

2.8.2 Atmospheric Neutrinos

Cosmic rays are highly energetic particles, composed primarily of protons and atomic nuclei, that originate from the Sun and other astrophysical sources. When these particles strike the Earth's atmosphere, they interact with nuclei in the upper atmosphere and produce cascades of secondary particles. Atmospheric neutrinos are generated predominantly through the decay of mesons, such as pions (π) and kaons (K), produced in these interactions. The principal decay chains responsible for atmospheric neutrino production are:

$$\pi^\pm \rightarrow \mu^\pm + \nu_\mu(\bar{\nu}_\mu) \tag{2.85}$$

$$K^\pm \rightarrow \mu^\pm + \nu_\mu(\bar{\nu}_\mu) \tag{2.86}$$

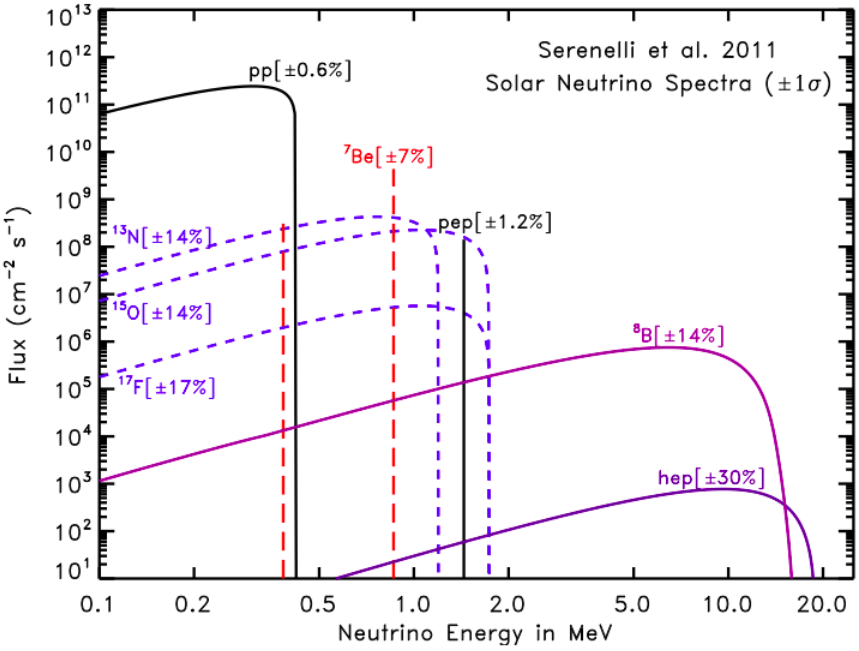


Figure 2.6: Predicted solar neutrino energy spectra for the various components of the *pp* chain and CNO cycle [10].

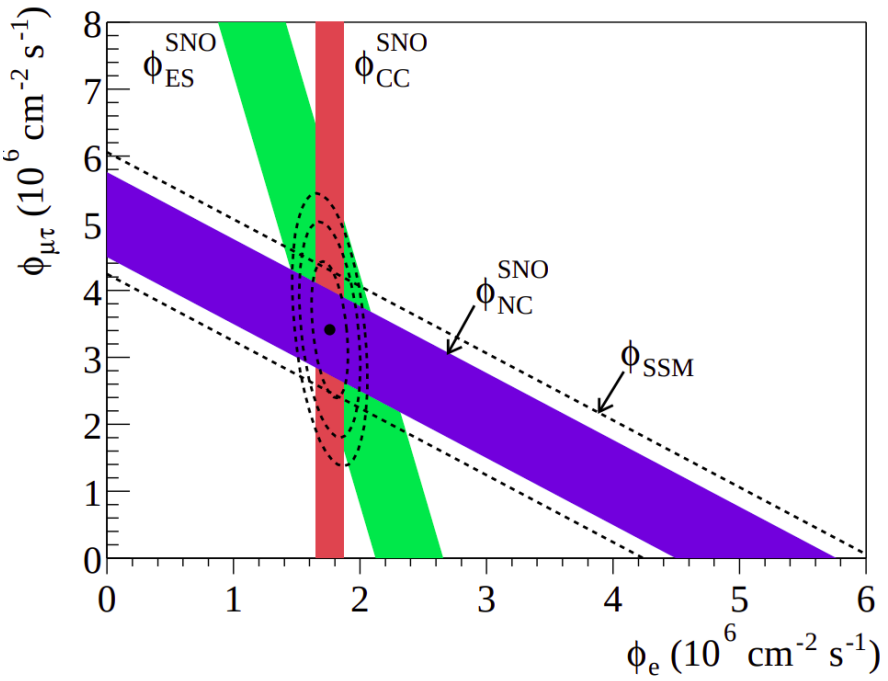


Figure 2.7: Results from SNO showing the measured ^{8}B solar neutrino flux decomposed into electron neutrino (ϕ_e) and non-electron neutrino ($\phi_{\mu,\tau}$) components and compared with the SSM prediction [11].

$$\mu^+ \rightarrow e^+ + \nu_e + \bar{\nu}_\mu \tag{2.87}$$

The corresponding charge-conjugate process for μ^- decay produces $\bar{\nu}_e$ and ν_μ. As a result, atmospheric neutrinos consist primarily of muon and electron neutrinos and antineutrinos. Their energies typically range from approximately 100 MeV to 10 GeV, although higher-energy atmospheric neutrinos are also observed.

In 1986, the Kamiokande experiment measured atmospheric neutrinos and found that the ratio of CC ν_μ to ν_e interactions was significantly smaller than predicted [45]. The observed ratio of the measured to expected muon-to-electron neutrino interaction rates was:

$$R_{\mu/e} = 0.60^{+0.06}_{-0.05} \tag{2.88}$$

This deficit indicated that a substantial fraction of muon neutrinos disappeared before reaching the detector. The most natural explanation is neutrino oscillation, primarily through the transformation $\nu_\mu \rightarrow \nu_\tau$. This interpretation was confirmed conclusively by the Super-Kamiokande (Super-K) experiment in 1998 [46], providing some of the first compelling evidence for atmospheric neutrino oscillations.

2.8.3 Geoneutrinos

Geoneutrinos are electron antineutrinos produced within the Earth by radioactive decays that contribute to the planet's radiogenic heat. They originate primarily from the β^- decay chains of long-lived isotopes with half-lives comparable to or longer than the age of the Earth, most notably ^{238}U, ^{232}Th, and ^{40}K. The total energy released in these decay chains is:

$$^{238}\mathrm{U} \rightarrow ^{206}\mathrm{Pb} + 8\alpha + 6e^- + 6\bar{\nu}_e + 51.698\ \mathrm{MeV} \tag{2.89}$$

$$^{232}\mathrm{Th} \rightarrow ^{208}\mathrm{Pb} + 6\alpha + 4e^- + 4\bar{\nu}_e + 42.652\ \mathrm{MeV} \tag{2.90}$$

$$^{40}\mathrm{K} \rightarrow ^{40}\mathrm{Ca} + e^- + \bar{\nu}_e + 1.311\ \mathrm{MeV} \tag{2.91}$$

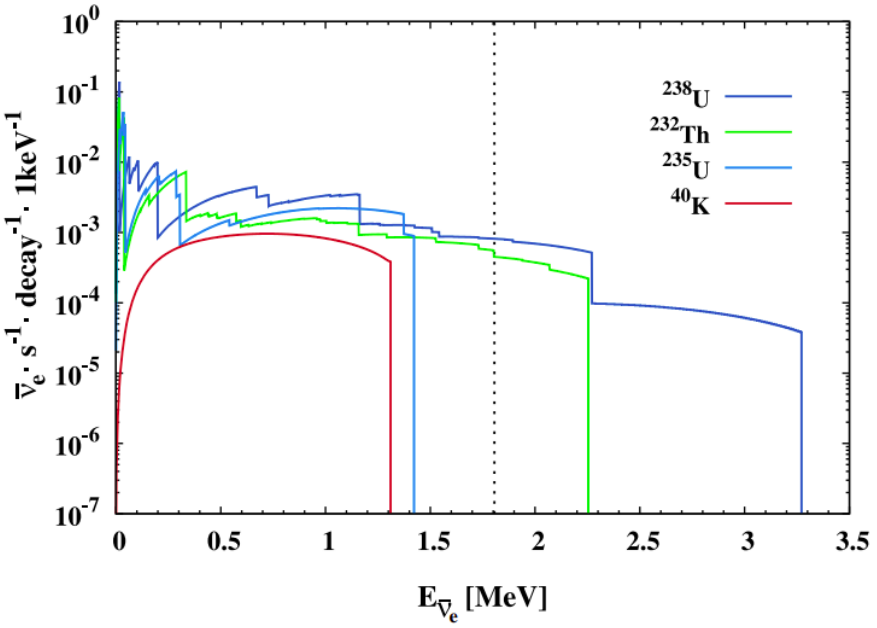


Figure 2.8: Energy spectra of antineutrinos emitted in the decay chains of ^{238}U, ^{235}U, ^{232}Th, and ^{40}K [12].

Only geoneutrinos from the ^{238}U and ^{232}Th decay chains can be detected through inverse beta decay, since some of their emitted antineutrinos have energies above the 1.8 MeV threshold. In contrast, antineutrinos from ^{40}K decay are below this threshold and are therefore inaccessible to this detection channel. Inverse beta decay is discussed in more detail in Chapter 6.

As shown in Figure 2.8, geoneutrinos have relatively low energies, and only a small fraction of the ^{238}U and ^{232}Th spectra lie above the inverse beta decay threshold. Consequently, geoneutrinos are challenging to detect. Assuming a representative geological model, approximately 30 geoneutrino events are expected to be observed in SNO+ each year [47].

Reactor antineutrinos, discussed in the next subsection, constitute the dominant background in geoneutrino searches.

2.8.4 Reactor Neutrinos

Nuclear reactors provided the source of antineutrinos used in the first experimental detection of the neutrino by Reines and Cowan (see Section 2.2). They also constitute one of the dominant

backgrounds in the primary analysis presented in this dissertation.

Nuclear reactors produce enormous fluxes of electron antineutrinos ($\bar{\nu}_e$) with energies extending up to approximately 10 MeV. These antineutrinos are produced in the beta decays of neutron-rich fission fragments generated during the fission of isotopes such as ^{235}U, ^{238}U, ^{239}Pu, and ^{241}Pu. Reactor antineutrinos are most commonly detected through the inverse beta decay (IBD) interaction:

$$\bar{\nu}_e + p \rightarrow e^+ + n \tag{2.92}$$

In this process, an electron antineutrino ($\bar{\nu}_e$) interacts with a free proton (p) (a hydrogen nucleus) in the detector, producing a positron (e^+) and a neutron (n). The positron deposits its kinetic energy and subsequently annihilates with an electron, creating a prompt signal. The neutron thermalizes and is captured after a characteristic delay, producing a delayed signal. This prompt-delayed coincidence provides a distinctive signature that is widely used to identify reactor antineutrino interactions.

Reactor antineutrino experiments have played a central role in measuring neutrino oscillation parameters by observing the disappearance of $\bar{\nu}_e$ as they propagate from the reactor core to the detector. This disappearance occurs because $\bar{\nu}_e$ oscillate into $\bar{\nu}_\mu$ and $\bar{\nu}_\tau$, which do not produce CC interactions at reactor antineutrino energies. Using the currently measured oscillation parameters, the expected rate of reactor IBD events in SNO+ is approximately 100 events per year [47].

Geoneutrinos constitute an important background in reactor antineutrino measurements, while both reactor antineutrinos and geoneutrinos are backgrounds in the analysis presented in Chapter 6.

2.8.5 Supernovae & Exotics

In January 1987, the Kamiokande-II experiment began routine observations of solar neutrinos. Just one month later, on February 23, 1987, Kamiokande-II detected a burst of neutrinos from Supernova 1987A (SN1987A) [48], located in the Large Magellanic Cloud at a distance of approximately 50 kpc from Earth. This observation marked the first detection of neutrinos from an astrophysical

source beyond the Solar System and provided the first direct evidence that core-collapse supernovae (CCSN) release a substantial fraction of their gravitational binding energy in the form of neutrinos.

The neutrino burst from SN1987A, shown in Figure 2.9, was also observed by the Irvine-Michigan-Brookhaven (IMB) [49], Baksan Scintillator Underground Telescope (BUST) [50], and Liquid Scintillator Detector (LSD) [51] experiments. In total, fewer than 25 neutrino interactions were recorded over a period of approximately 13 s, yet these events confirmed the basic theoretical picture of CCSN. In this picture, the collapsing core of a massive star forms a proto-neutron star (PNS) and releases approximately 10^{53} erg of gravitational binding energy, of which roughly 99% is emitted as neutrinos and antineutrinos of all flavors over a timescale of several seconds [13]. Although CCSN emit neutrinos and antineutrinos of all flavors, the SN1987A detectors were primarily sensitive to electron antineutrinos via IBD.

The detection of SN1987A demonstrated that neutrinos can be observed from distant astrophysical sources and established neutrino astronomy as a powerful tool for studying extreme environments in the Universe. Since neutrinos escape from dense regions that are opaque to electromagnetic radiation, they provide a unique probe of the physical processes occurring deep within stellar cores. SNO+, among other neutrino detectors, are waiting for another supernova.

The field of neutrino astronomy has since expanded beyond the MeV regime. The IceCube Neutrino Observatory, a cubic-kilometer Cherenkov detector embedded in the Antarctic ice, is primarily sensitive to neutrinos with energies from several GeV to beyond the PeV scale. IceCube has observed a diffuse astrophysical flux of high-energy neutrinos and identified individual astrophysical neutrino sources, establishing high-energy neutrino astronomy as a complementary branch of multi-messenger astrophysics. Although IceCube is optimized for high-energy neutrinos rather than individual MeV interactions, it is also sensitive to a Galactic core-collapse supernova through a collective increase in photomultiplier counting rates, complementing dedicated low-energy detectors such as SNO+, Super-Kamiokande, KamLAND, and Borexino.

In addition to supernovae, many other astrophysical and exotic phenomena have been proposed

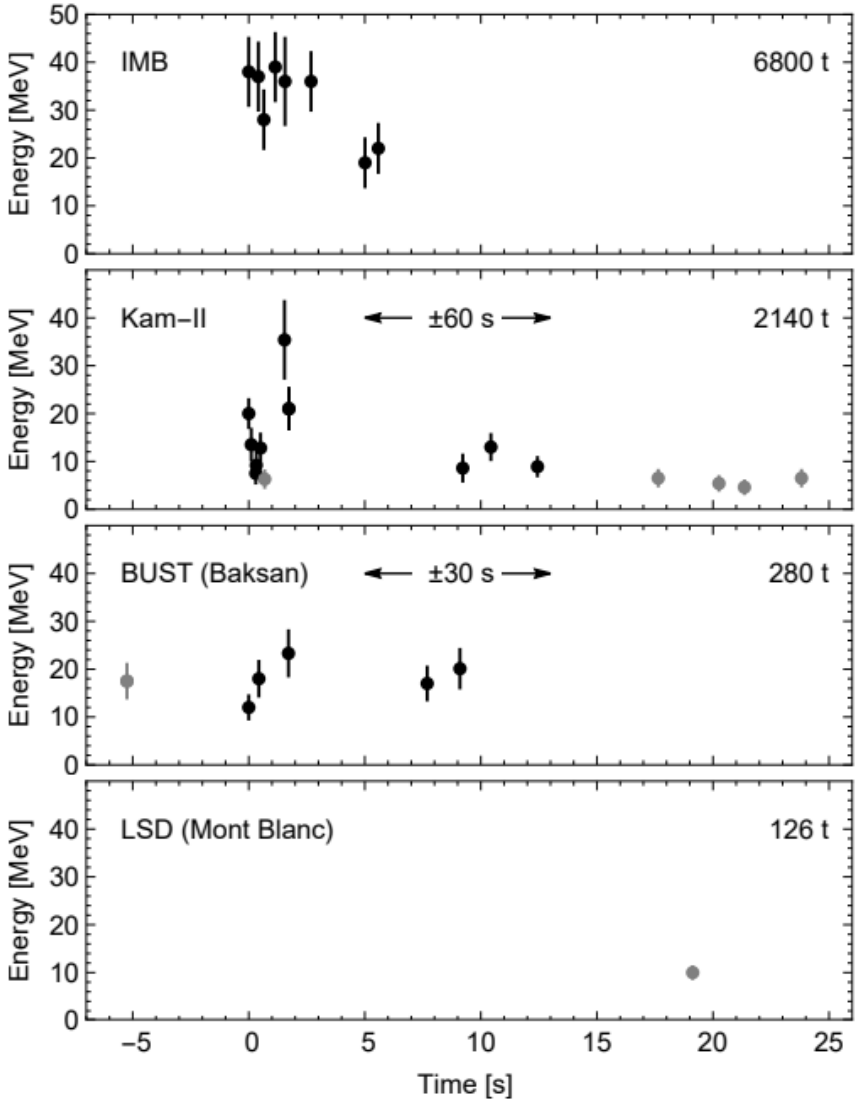


Figure 2.9: Neutrino signal from SN1987A at IMB, Kam-II, BUST, and LSD [13].

as potential sources of neutrinos. These include neutron star mergers, black hole accretion disks, gamma-ray bursts, and other transient events associated with the emission of gravitational waves. If such sources produce detectable neutrino bursts, coincident observations of neutrinos and gravitational waves would provide a powerful multi-messenger probe of the underlying astrophysical mechanisms.

Although no neutrino counterpart has yet been conclusively associated with a gravitational wave event, many of the systems observed through gravitational waves are expected to produce neutrinos through radioactive decays, thermal processes in hot dense matter, and particle interactions in relativistic outflows. Searches for neutrinos in temporal coincidence with gravitational wave events therefore provide a promising multi-messenger probe of these sources and motivate the analysis presented in Chapter 6.

CHAPTER 3

THE SNO+ DETECTOR

"Ain't lookin' for nothin' but a good time and it don't get better than this"

— "Nothin' but a Good Time," Poison

As detailed in Section 2.8.1, the Sudbury Neutrino Observatory (SNO) was a heavy water Cherenkov detector operating from April 1999 to November 2006 [15]. The purpose of SNO was to study the mass and mixing parameters of neutrinos. It primarily detected neutrinos produced by fusion reactions in the Sun. At the time, several neutrino experiments measured solar neutrinos and found that the observed flux was too low; indicating that far fewer neutrinos were detected than expected based on the known energy output of the Sun. This discrepancy became known as the Solar Neutrino Problem (SNP).

SNO's heavy water target uniquely enabled the simultaneous measurement of charged current (CC), neutral current (NC), and elastic scattering (ES) interactions. The CC interaction is sensitive only to electron neutrinos, while the NC interaction is equally sensitive to all neutrino flavors. By comparing these interaction rates, SNO demonstrated that electron neutrinos produced in the Sun transform into muon and tau neutrinos during propagation to Earth. The measurement of ^{8}B solar neutrinos provided definitive evidence for neutrino flavor oscillations and resolved the SNP. This work ultimately led to the 2015 Nobel Prize in Physics being awarded to Arthur McDonald (SNO) and Takaaki Kajita (Super-Kamiokande) [52].

The SNO+ experiment builds upon the infrastructure of SNO, described in detail in [15], with the primary goal of searching for neutrinoless double beta decay. The following sections describe the detector, the phases of data taking, and the goals of the experiment. In addition to providing an overview of the detector, this chapter presents several detector characterization and calibration studies performed as part of this dissertation. Subsection 3.2.3 describes a measurement of the deployed scintillator light yield, Section 3.4 describes the development and implementation of an electronics

baseline monitoring system, and Section 3.6 describes the characterization of the detector's absolute timing and the timing corrections implemented for this analysis.

3.1 SNO+

The SNO+ experiment is an optical neutrino detector located at SNOLAB, a Class 2000 clean room facility 2 km underground in Creighton Mine near Sudbury, Ontario, Canada. The site has a rock overburden of 5890 meters water equivalent (m.w.e.), resulting in a very low muon flux of 0.27 muons/m^2/day [53], which corresponds to approximately 3 muons per hour in the detector volume. The combination of a clean environment and a low cosmic ray flux makes SNOLAB an excellent location for low background experiments such as SNO+.

An artist's depiction of the detector is shown in Figure 3.1. A 20 m diameter cavity containing approximately 5.3 ktonnes of ultra-pure water (UPW) acts as a massive shield against radioactivity from the surrounding norite rock. Around 9300 photomultiplier tubes (PMTs) are mounted on a stainless steel geodesic sphere, approximately 9 m in radius, called the PMT Support Structure (PSUP). The PMTs face inward towards the acrylic vessel (AV). There are approximately 90 outward-looking (OWL) PMTs used as a veto to reject events originating in the outer volume.

Between the PSUP and the AV is an additional 1.7 ktonnes of UPW, which provides further shielding from radioactivity originating in the surrounding PMTs. The AV is 5 cm thick, has a radius of 6 m, and holds the target volume of 780 tonnes of liquid scintillator.

The AV is held in place by Tensylon "hold-up" and "hold-down" ropes to counteract gravity and buoyant forces arising from the density difference between scintillator and UPW. The hold-up ropes are secured at the top of the cavity and at the "belly plates" on the AV. The belly plates are acrylic slabs bonded to the AV at equidistant intervals around the equator, with a U-shaped groove machined into each to secure the rope. The hold-down ropes are anchored at the bottom of the cavity and wrap around the top of the AV at the neck. The belly plates and hold-up and hold-down ropes are shown in Figure 3.2.

The neck is a 7 m tall cylindrical structure extending upward to the deck above, allowing access to

the inner AV volume. The deck houses the electronics and calibration systems for the experiment. Also located on the deck, within a clean room, is an interface that provides access to the detector volume for calibration source deployment. A sealed cover-gas system protects the detector from radon ingress through this interface.

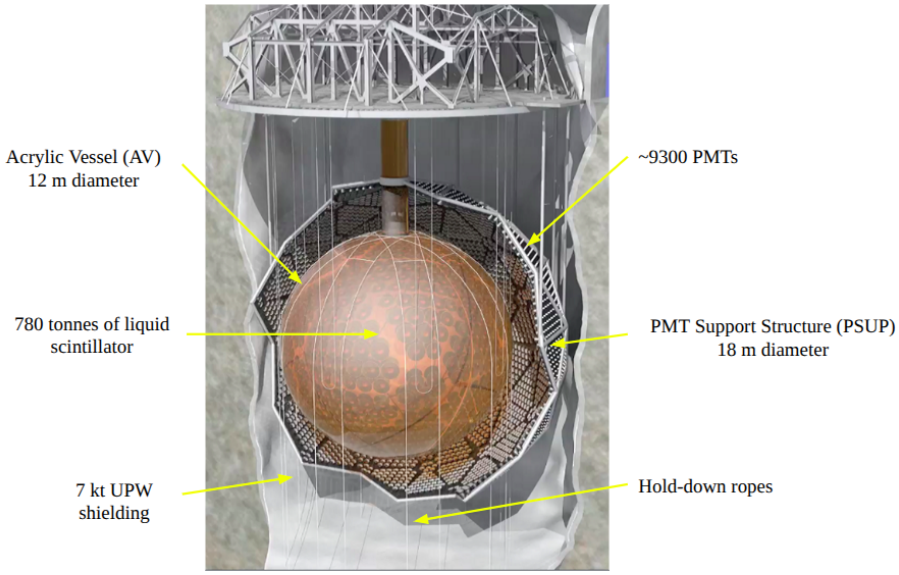
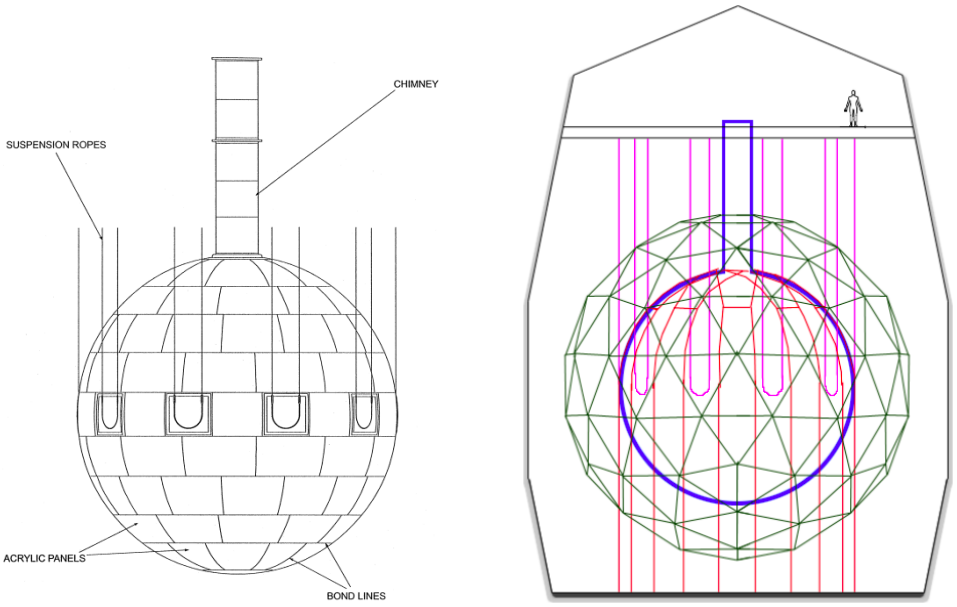


Figure 3.1: An illustration of the SNO+ detector modified from [14].

SNO+ has taken a phased approach to deploying the target medium inside the AV. As a result, several processing plants are used for the purification, deployment, and recirculation of the liquid media filling the detector. The water plant was inherited from SNO, while the scintillator and tellurium plants were constructed specifically for SNO+. The scintillator plant has been commissioned and used to fill the detector, while commissioning of the tellurium plant is ongoing at the time of writing.

At the time of the writing of this thesis, the detector was filled with liquid scintillator in two stages (corresponding to the addition of two fluors). The analysis presented in this thesis uses data taken during the scintillator-filled phase.



(a) Hold-up ropes and belly plates

(b) Hold-down ropes

Figure 3.2: A schematic of the SNO+ experiment depicting the hold-up ropes and belly plates (left). The same experiment, but with the inclusion of the PSUP in green, the AV in blue, the hold-up ropes in pink, and the hold-down ropes in red (right). Adapted from [15] and [4].

3.2 Phases of SNO+

SNO+ is a multi-purpose detector that will operate in four distinct phases, enabling the study of different physics topics in each configuration. The first phase employed UPW as the target medium. During the COVID-19 pandemic, the filling of liquid scintillator was temporarily suspended after approximately 365 tonnes had been deployed, resulting in a partial fill scintillator phase. The third phase employs a full liquid scintillator target, enabling a broad neutrino physics program. The final phase will load ^{130}Te into the scintillator to search for neutrinoless double beta decay. The following subsections describe the underlying physics principles and goals of each phase. The detector configurations and corresponding timelines are summarized in Figure 3.3

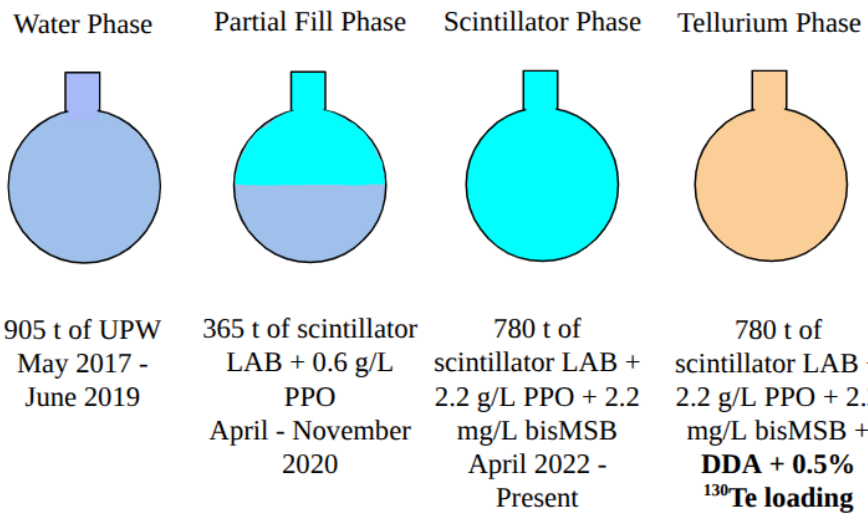


Figure 3.3: An illustration of the SNO+ detector phases. This analysis uses data from the scintillator phase.

3.2.1 Water Phase

The first phase of SNO+ was the water phase. During this phase, the AV was filled with 905 tonnes of UPW, and data were collected from May 2017 to June 2019. The primary goals of the water phase were to commission the electronics and data acquisition (DAQ) system, calibrate the detector response, and measure backgrounds.

In water Cherenkov detectors, interactions are detected via Cherenkov radiation, which is observed by the PMTs. Cherenkov radiation is produced when a charged particle travels through a medium at a speed greater than light in that medium, $\frac{c}{n}$. The corresponding kinetic energy threshold for electrons in water is 265 keV. There are several useful properties of Cherenkov light that SNO+ uses to reconstruct an event's position, direction, and energy.

Cherenkov light is emitted along a cone in the direction of the particle's motion. The majority of the light travels directly to the PMTs. The timing of the light reaching the PMTs can be used to determine the position of the event.

Since the light is emitted along a cone, the half-angle of this emission cone is given by:

$$\cos\theta_c = \frac{1}{n\beta} \tag{3.1}$$

where n is the index of refraction of the medium and $\beta = \frac{v}{c}$. For relativistic particles in water, $\beta \approx 1$ and $n = 1.33$, resulting in a Cherenkov angle of $\theta_c \approx 41°$ in water. This emission angle is used to reconstruct the direction of travel of the particle.

The amount of Cherenkov photons produced in an interaction scales approximately linearly with energy. The number of detected photons will, thus, be approximately proportional to energy. In the water phase, roughly 7 photons are detected per MeV of deposited energy.

Several calibration sources were deployed during the water phase: ^{16}N, which provides a tagged 6 MeV γ, Americium-Beryllium (AmBe), which produces 4.4 MeV γ's and neutrons, and several LED/lasers with intensity controlled by trained operators. Analyses completed with these sources include the energy, position, and direction reconstruction calibration using the ^{16}N source [54], a measurement of the neutron capture cross section and neutron detection efficiency with the AmBe source [55], and a calibration of the water attenuation, effective attenuation of the acrylic vessel, and the angular response of the PMTs across various wavelengths with the laser calibration source [56].

SNO+ published several physics results using the water phase data. Alongside the calibration analyses above, a measurement of the ^{8}B solar neutrino flux [57] and the first ever detection of reactor antineutrinos in a water Cherenkov detector [58].

As briefly mentioned previously, an important aspect of Cherenkov light is the directionality of the photons created in the interaction. This is contrasted in the next subsection in the discussion of the isotropically emitted scintillation light. The Cherenkov spectrum is proportional to $1/\lambda^2$, meaning that the majority of the light is emitted in the ultraviolet (UV) spectrum, but with a significant fraction emitted in the visible spectrum between 350 nm and 600 nm. Because the UV light is often absorbed by the detector medium, the visible light is critical to detect with a high efficiency.

Cherenkov light is emitted in scintillator as well, it is just saturated by the scintillation light, which is orders of magnitude more intense.

3.2.2 Partial Scintillator Fill Phase

The COVID-19 pandemic forced a temporary pause in filling operations after 365 tonnes of scintillator had been deployed. As a result, several months of stable data taking were collected from April to November 2020. This dataset enabled analyses and background measurements relevant to both the pure scintillator phase and future tellurium-loaded phase of SNO+. A measurement of Δm^2_{21} with limited sensitivity was performed during the partial fill phase using reactor antineutrinos [59, 60].

3.2.3 Scintillator Phase

The next phase of SNO+ involved replacing the 905 tonne UPW target with 780 tonnes of liquid scintillator. Scintillator filling began in late 2019 and continued until the detector was fully filled in 2022. After filling was completed, additional compounds were added to the scintillator cocktail to increase the light yield.

Liquid Scintillator

In the scintillator phase, interactions are detected using the isotropically emitted scintillation light produced by charged particles. The process is as follows: a charged particle interacts with the surrounding medium, which excites the surrounding molecules to a continuum state by ionizing radiation. Upon de-excitation to the ground state, the molecule fluoresces, emitting a relatively large number of photons. The wavelength distribution of the emitted photons is determined by the chemical structure of the scintillator.

In the case of SNO+, the primary solvent is linear alkylbenzene (LAB), which does not fluoresce on its own and requires a fluorophore (fluor). When an LAB molecule becomes excited, the purpose of a fluor is to allow non-radiative energy to transfer from LAB to the fluor before the fluorescence occurs for the LAB molecule. The primary fluor in the SNO+ cocktail is 2,5-diphenyloxazole (PPO). PPO shifts the emitted distribution to wavelengths more optimal for detection. A secondary fluor, 1,4-bis(2-methylstyryl) benzene (bisMSB), was added in July 2023. This further shifts the wavelength

closer to the quantum efficiency (QE) of the PMTs and improves the light yield. Figure 3.4 shows the emission spectra of PPO and bisMSB and the SNO PMT efficiency curve is also included. The bisMSB emission spectrum has better overlap with the PMT efficiency compared to the PPO emission.

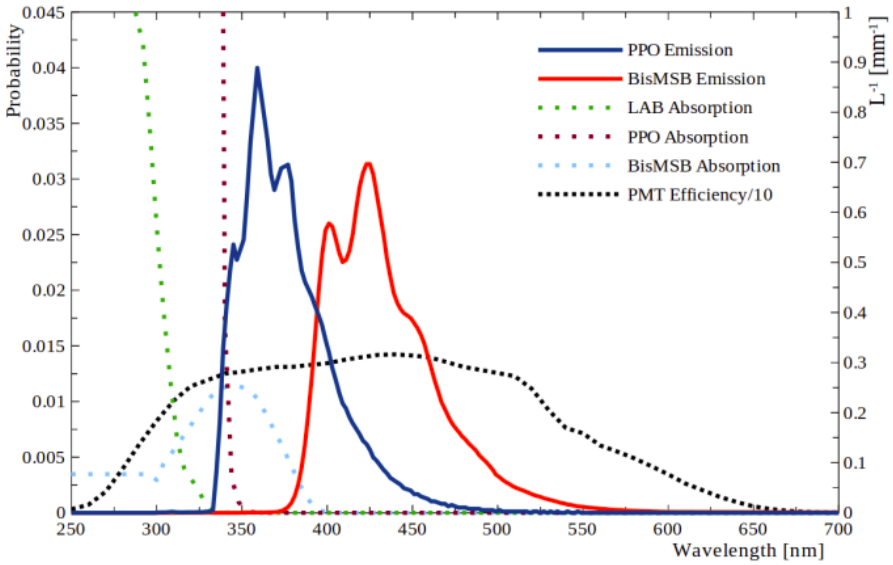


Figure 3.4: Absorption and emission spectra for the PPO and bisMSB components in the SNO+ scintillator cocktail. The left y-axis shows the probability of emission, the right y-axis corresponds to the sparse dotted lines showing absorption in units of mm^{-1}. The black fine dotted line shows the R1408 Hamamatsu PMT measured total detection efficiency (divided by 10 to fit on the graph). Plot adapted from [16].

The amount of scintillation light produced by an interaction is much larger than the amount of Cherenkov light produced. Scintillation light has ∼50 times more detected photons per MeV. Aside from the intensity of light produced in scintillator, the time profile of the emission is on the order of tens to hundreds of nanoseconds. Cherenkov light emission is on the order of picoseconds.

A charged particle interacting with the scintillator will create scintillation and Cherenkov light. The most common particles SNO+ detects are α's, β's, γ's, protons (p), and neutrons (n). Different particles of the same energy can produce different amounts of photons; this is known as quenching. Quenching is the reduction of light output per unit of deposited energy. In an interaction, a particle deposits energy E. A naive expectation is for the number of photons produced to be proportional

to E. In reality, heavily ionizing particles produce less light than expected because some of the excitation energy is lost through non-radiative processes instead of producing scintillation photons.

Low ionization density particles like electrons (e^-), positrons (e^+), and γ-induced electrons, produce excitations that are relatively spread out due to their light masses. These interactions produce predominantly scintillation light, and the light yield is nearly linear with deposited energy. Highly ionizing particles, such as protons, nuclear recoils, and α particles, by contrast produce excitations that are closely packed together due to their heavier masses (i.e., they move more slowly for the same kinetic energy). Because they move more slowly, they deposit their energy over a much shorter distance, producing a much larger stopping power (dE/dx).

The reduction in scintillation light due to quenching is described empirically by Birks' law:

$$\frac{dL}{dx} = S\frac{dE/dx}{1 + k_B\, dE/dx} \tag{3.2}$$

where L is the total number of photons produced, S is the scintillation efficiency (in units of photons per unit energy), k_B is Birks' constant, an empirical parameter describing the quenching response of the scintillator, dL/dx is the light output per unit distance, and dE/dx is the energy deposited per unit distance.

As shown by Equation 3.2, particles with larger values of dE/dx, such as protons and α particles, produce proportionally less scintillation light. Notably, α particles produce approximately ten times fewer photons than β particles of the same energy.

For different particles that produce the same amount of light, the scintillation time profiles also differ. The time profile of an α particle, for example, tends to be broader than that of a β particle. This difference provides an additional means of particle identification.

SNO+ Scintillator Cocktail

As discussed above, the primary solvent in the SNO+ scintillator cocktail is LAB. LAB was chosen due to its high light yield and its lack of naturally occurring radioactive contaminants (such

as Uranium, Thorium, and Potassium) within the material, otherwise known as radiopurity, its compatibility with the SNO+ acrylic, and its reasonable cost. The chemical structure of LAB consists of a benzene ring connected to a long hydrocarbon chain. It has a chemical composition of $C_6H_5C_nH_{2n+1}$, where n ranges from 9 to 13.

PPO is used as the primary fluor and has a chemical composition of $C_{15}H_{11}NO$. In April 2022, PPO was loaded into the detector at a concentration of 2.2 g/L in April 2022, increasing the scintillation light yield relative to lower PPO concentrations.

BisMSB is used as a secondary fluor to shift the wavelength of the scintillation light, improving detection efficiency and further improving the light yield. The final concentration of 2.2 mg/L of bisMSB was added into the detector in December 2024. This addition resulted in an increase in the light yield by ∼50%.

Light Yield Measurements

The light yield, scintillation time profile, and optical properties of the SNO+ scintillator cocktail directly determine the detector's energy resolution, particle identification capabilities, and overall sensitivity. The SNO+ collaboration has performed extensive measurements to characterize these properties. As part of this detector characterization program, I performed a measurement of the light yield of the deployed LAB + 2.2 g/L PPO scintillator. The measured light yield was used to validate the scintillation model employed throughout this dissertation.

Experimental Setup

The light yield measurements were performed using a benchtop setup consisting of a UV-transparent (UVT) acrylic cube containing the scintillator sample and a 0.1 μCi ^{90}Sr button source. The acrylic cube was fabricated from the same UVT acrylic used for the SNO acrylic vessel and contained a cylindrical cavity filled with approximately 15 mL of scintillator. The ^{90}Sr source was mounted beneath the cavity so that the emitted β particles traversed the scintillator volume.

The acrylic cube was optically coupled to a 1-inch square Hamamatsu R7600-U200 PMT, which served as the trigger PMT. A Hamamatsu R1408 8-inch SNO PMT was positioned approximately

0.5 cm from the cube to detect the scintillation light. The trigger PMT has a transit time spread (TTS) of approximately 250 ps, making its contribution to the overall timing resolution negligible. A photograph of the setup is shown in Figure 3.5.

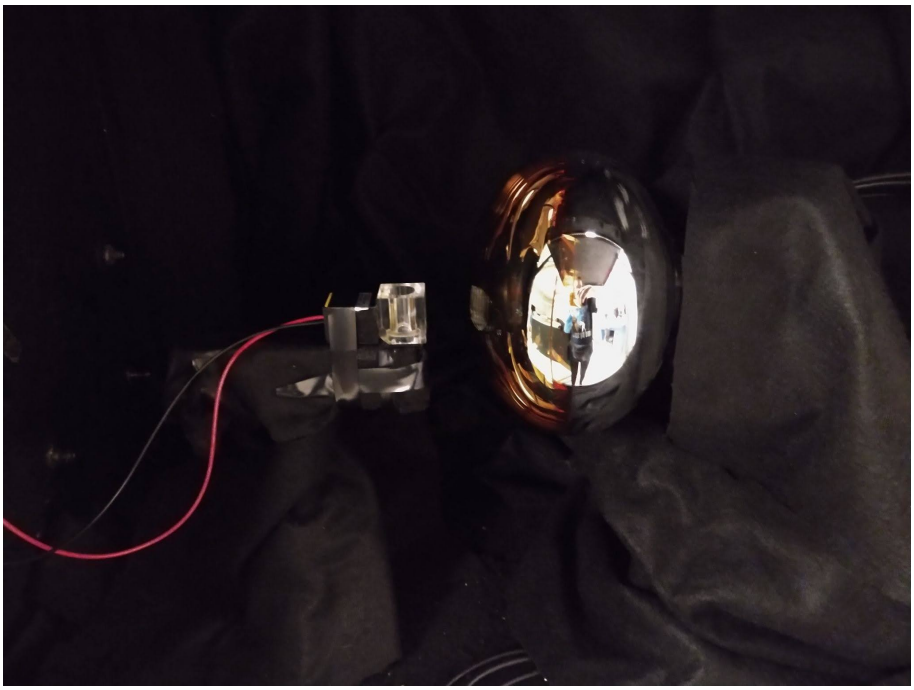


Figure 3.5: Experimental setup used for the light yield measurements. The UVT acrylic cube containing the scintillator sample is optically coupled to a Hamamatsu R7600-U200 trigger PMT. A Hamamatsu R1408 SNO PMT is positioned approximately 0.5 cm away to detect the scintillation light. The ^{90}Sr source is mounted beneath the acrylic cube and is not visible in the photograph.

The ^{90}Sr source undergoes β decay to ^{90}Y with a half-life of 28.9 years. The daughter nucleus subsequently decays to stable ^{90}Zr with a half-life of 64.1 hours. The decay scheme is shown in Figure 3.6. Electrons emitted in both decays produce scintillation light within the liquid scintillator as well as a small amount of Cherenkov light. The Cherenkov emission provides a prompt optical signal with a well-understood wavelength spectrum that assists in characterizing the detector response.

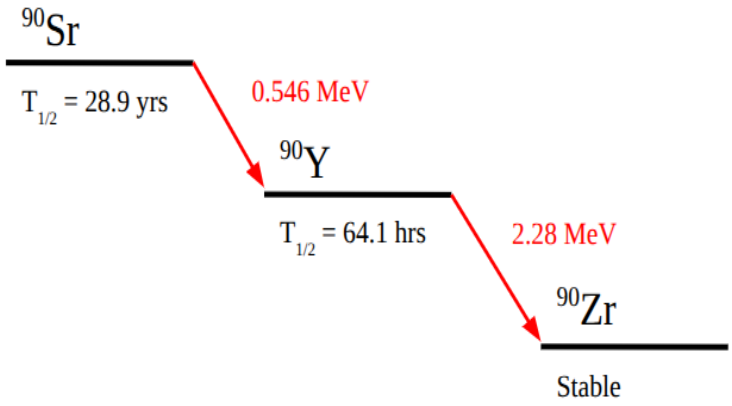


Figure 3.6: Decay scheme of the ^{90}Sr source used in the light yield measurements.

The setup was housed inside a light-tight dark box lined with Finemet magnetic shielding to reduce the influence of the Earth's magnetic field. Black felt was used to suppress stray optical reflections. High voltage was supplied to the PMTs using an ISEG NHS six-channel NIM module [61]. The trigger and SNO PMTs were operated at -800 V and 2000 V, respectively.

Signals from both PMTs were digitized using a Teledyne LeCroy WaveSurfer 4104HD oscilloscope [62]. The trigger PMT initiated the oscilloscope readout, and waveforms with a duration of 200.2 ns were recorded using 400 ps sampling intervals. The 12-bit digitized waveforms were acquired using the `LeCrunch` software package [63], which also stored the data in `hdf5` format for offline analysis.

Measurement Procedure

Prior to each measurement, the scintillator sample was stripped with nitrogen gas for approximately 30 minutes to remove dissolved oxygen, which quenches scintillation light and reduces the measured light yield. The deoxygenated scintillator was then transferred into the acrylic cube by filling along the wall of the cavity to minimize trapped air bubbles before being sealed with a microscope coverslip.

To account for long-term variations in the detector response, a standard LAB + 2.0 g/L PPO scintillator sample was measured immediately before the 2.2 g/L PPO sample. Using a reference

sample measured on the same day minimizes systematic effects associated with gradual changes in the electronics, PMT response, and experimental setup. The relative light yield of the 2.2 g/L PPO scintillator was determined by comparing its measured response to that of the contemporaneous 2.0 g/L PPO reference sample.

Approximately 10^5 waveforms were recorded for each scintillator sample. The charge collected by the SNO PMT was integrated event-by-event to produce a charge spectrum. The relative light yield was determined from the charge-weighted integral of this spectrum relative to that obtained from the reference scintillator.

Results

Figure 3.7 shows the measured relative light yields for prepared LAB+PPO samples (red circles) and the siphoned SNO+ AV scintillator (gold stars). The measurements are normalized to a 2.0 g/L PPO reference sample, previously determined to have an absolute light yield of 11920 ± 630 photons/MeV through comparison with Geant4-based RAT simulations. Also shown are published measurements from Brookhaven National Laboratory (blue) [64], normalized to the same 2.0 g/L PPO reference concentration.

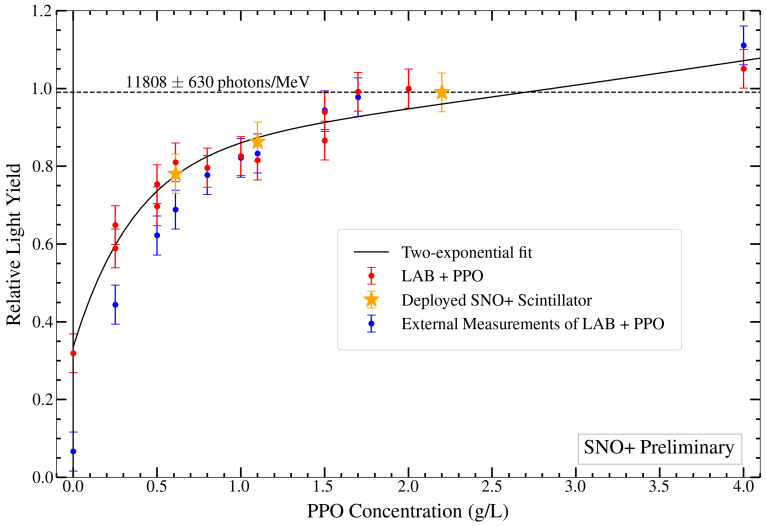


Figure 3.7: Relative light yield of prepared LAB+PPO samples (red circles) and SNO+ scintillator (gold stars) as a function of PPO concentration. Published measurements from Brookhaven National Laboratory are shown in blue for comparison. Adapted from [2].

A two-exponential fit of $L_R = ae^{b\times C_B} + ce^{d\times C_B}$ was performed on the measurements of LAB+PPO, where C_B is the PPO concentration and L_R is the relative light yield normalized to $C_B = 2.0$. The resulting fit parameters and χ^2 value are listed in Table 3.1.

a	b	c	d	χ^2
0.8419	0.0603	-0.5063	-2.696	0.02647

Table 3.1: Parameters for the two-exponential fit. Adapted from [2].

The measured relative light yield of the LAB + 2.2 g/L PPO scintillator was

$$L_{\text{rel}} = 0.9906 \tag{3.3}$$

corresponding to a light yield of

$$11808 \pm 630 \text{ photons/MeV} \tag{3.4}$$

This measured value is consistent with previous measurements of LAB+PPO scintillators and con-

firms that the deployed SNO+ scintillator achieved the expected optical performance. The measured light yield was subsequently incorporated into the detector simulation, improving the agreement between Monte Carlo predictions and the detector response.

3.2.4 Tellurium Phase

In late 2027, the SNO+ collaboration expects to be in the final phase of scintillator. The 780 tonne liquid scintillator target will be loaded with 1.3 tonnes of ^{130}Te. The primary goal of this phase is to search for neutrinoless double beta decay ($0\nu\beta\beta$). Figure 3.8 shows the Q-value of 10 double beta decay isotopes. Emphasis should be placed on ^{130}Te, which has a Q-value of 2.5 MeV. SNO+ aims to reach a sensitivity to the ^{130}Te ($0\nu\beta\beta$) half-life of 2 $\times 10^{26}$ years in 3 years of data taking.

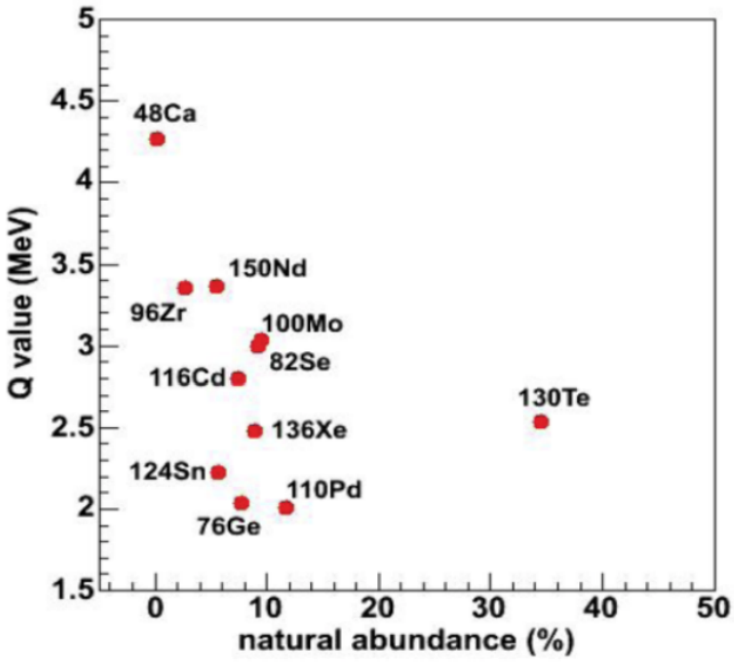


Figure 3.8: Double beta decay isotopes. Plot adapted from [17].

3.3 PMTs, Electronics, and DAQ

Particle interactions produce photons. Although the mechanisms of photon production differs between the various phases of SNO+, the underlying method of photon detection remains the same. The detection of these photons by the PMTs allows information about the processes that produced the light to be inferred. A custom electronics chain is used to digitize and read out the signals from

the PMTs. This process is described in the following subsections.

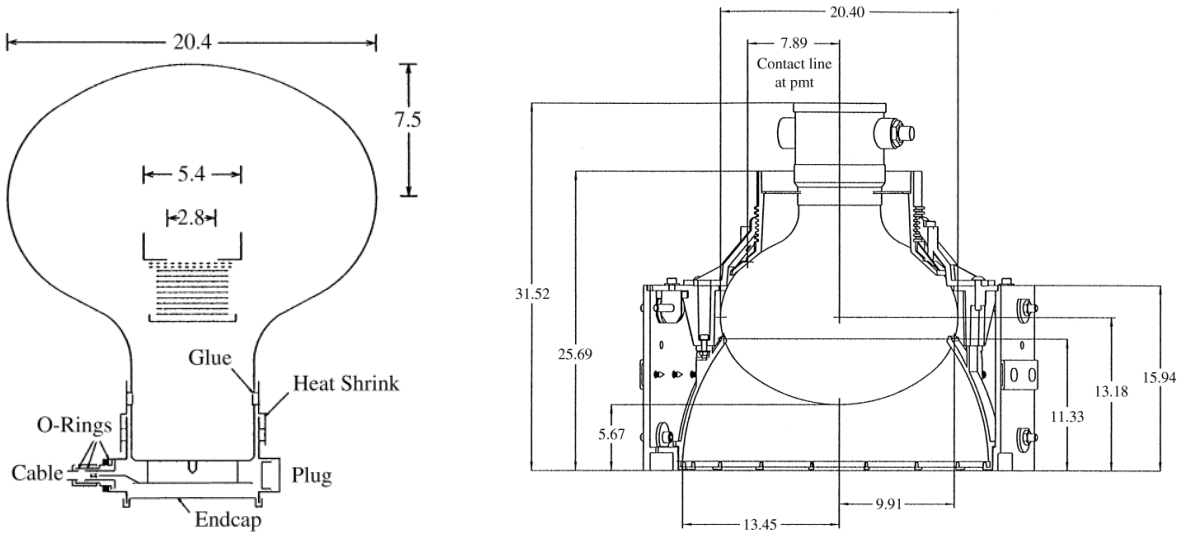
3.3.1 Photomultiplier Tubes

Photon detection can be accomplished using various types of photodetectors, SNO+ uses PMTs. PMTs have a glass tube that is coated with a metallic film called a photocathode. When a photon reaches the photocathode, it may produce a photoelectron (p.e.) via the photoelectric effect. A voltage of approximately 2000 V is applied across the PMT, which accelerates the p.e. to several layers of dynodes which when struck, emit more electrons. This process amplifies the signal from the initial photon to a detectable current of electrons often referred to as a "hit."

The SNO+ detector utilizes approximately 9300 8-inch Hamamatsu R1408 PMTs, which were also used in the original SNO detector. Between the end of SNO operations and the start of SNO+ data taking, PMTs that were no longer operational were removed. The removed PMTs had their bases repaired or replaced and were then reinstalled in the detector. Several hundred working PMTs were recovered for use in SNO+ as a result.

The SNO PMTs were originally selected due to their relatively low dark rate (approximately 500 Hz at 16° C), reasonable charge resolution, and relatively good timing. At the time of writing this thesis, advances in photodetector technology have produced improved PMTs as well as alternative devices such as Silicon Photomultipliers (SiPMs) and Large Area Picosecond Photodetectors (LAPPDs).

The PMT base distributes high voltage (HV) to the dynode stack, which must be protected from the surrounding environment to operate reliably. Because the PMTs are submerged in UPW, a waterproof housing was developed using silicone gel encapsulation. The Hamamatsu R1408 PMT with this waterproof housing is shown in Figure 3.9.



(a) R1408 PMT (b) Hexcell

Figure 3.9: A schematic of the Hamamatsu R1408 PMT and its waterproof enclosure (left). The same PMT mounted in a hexagonal ABS cell, which also forms the housing for the light concentrator. Adapted from [15]. Dimensions are in cm.

The PMTs are mounted within 27 cm diameter light concentrators, shown in Figure 3.10, with schematics provided in Figure 3.9. The light concentrators consist of reflective, aluminum-coated petals arranged in the shape of a Winston cone, an ideal non-imaging light collector [65]. These concentrators increase the effective photocathode coverage by redirecting photons that would otherwise miss the PMT photocathode. Over the operational lifetime of SNO and SNO+, the concentrator petals have aged and dulled, reducing their overall reflectivity. During SNO data taking, the effective photocathode coverage, including the enhancement provided by the concentrators, was 54%. The effective coverage in SNO+ is slightly lower due to the reduced reflectivity of the aging concentrator petals.

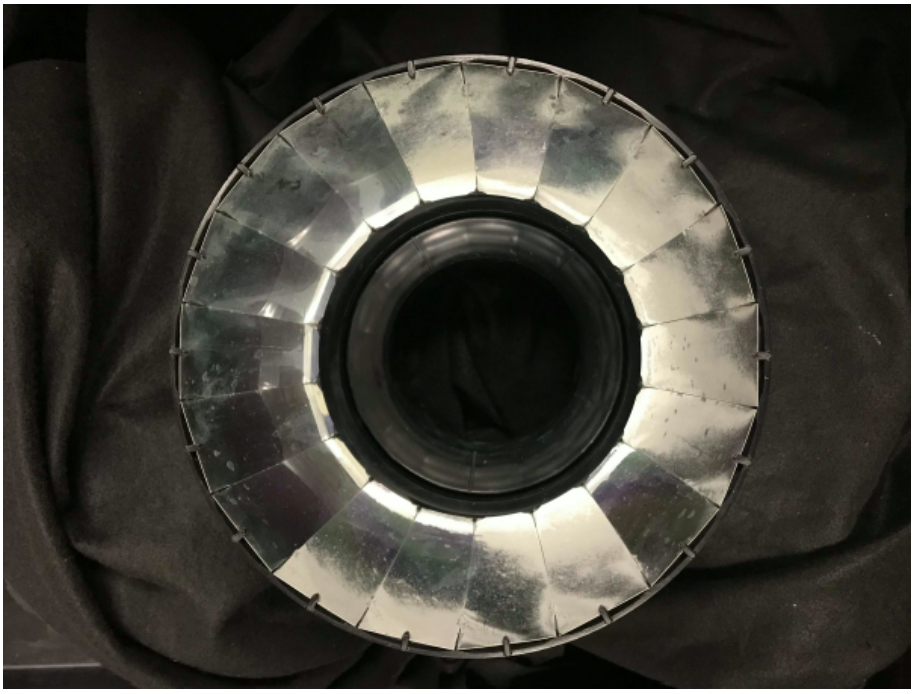


Figure 3.10: A SNO light concentrator imaged in 2019, showing visible aging of the reflective petals. Image adapted from [18].

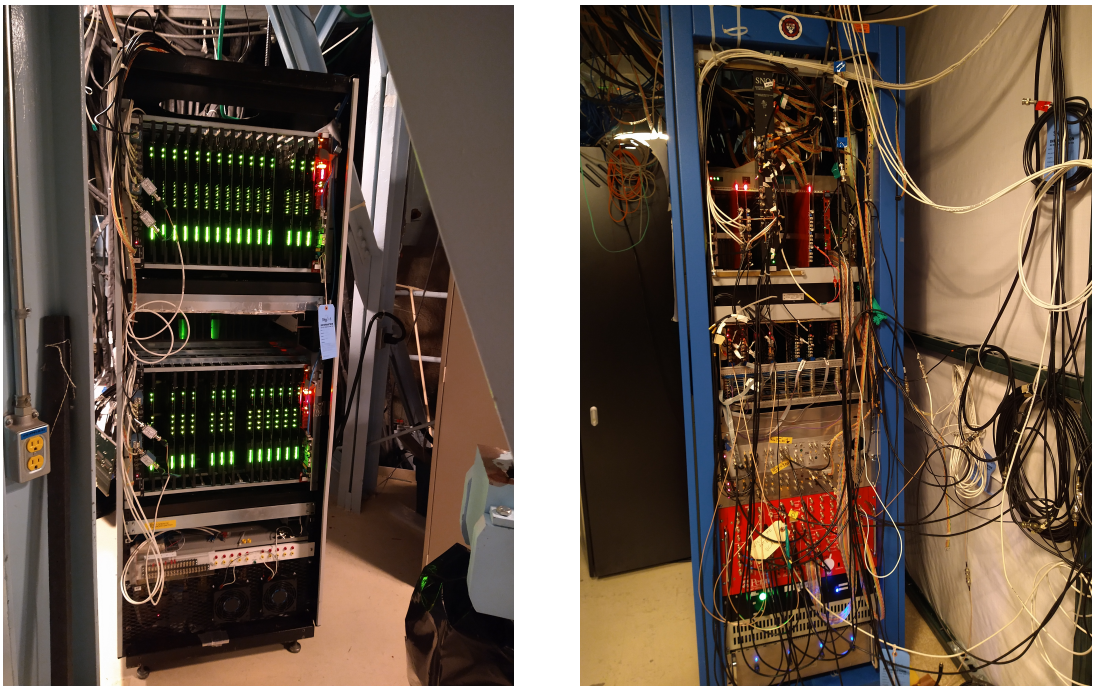
Of the "normal" inward-facing PMTs, 49 have the last dynode tapped to provide a second, low-gain readout channel. These low-gain channels extend the dynamic range of SNO+ at high light intensities by approximately a factor of 100 [15]. There are approximately 90 OWL PMTs, which are not equipped with concentrators and are mounted facing outward to detect light from muons and other sources in the region exterior to the PSUP. Four High Quantum Efficiency (QE) Hamamatsu R5912 PMTs were installed to better understand the performance of future SNO+ phases. In addition, four neck PMTs are located in the gas volume above the neck of the AV. These PMTs are used to identify and reject events caused by static electrical discharge in the gas region above the detector [66].

Accurate measurement of the properties of PMT hits is necessary to reconstruct information about the events. PMTs must efficiently detect when a photon reaches the photocathode, and accurately measure the time the hit occurred and the charge deposited. The SNO+ PMTs have timing resolution of approximately 1.5 ns.

3.3.2 Electronics and DAQ

After a photon produces a signal in a PMT, the signal is converted into usable data through the custom electronics chain designed to read out and trigger on signals from the PMT array. Together, these electronics form the data acquisition (DAQ) system. The system was built by Penn and inherited from SNO, with several notable upgrades, described in Section 3.4, to handle the higher rates associated with the increased light in the liquid scintillator phase. The electronics measure the time and charge of each PMT that detects a photon and packages these measurements into "events," consisting of all hits occurring within an approximately 420 ns window.

The SNO+ electronics system consists of 19 crates (numbered 0-18; crate 19 is known as the test stand). Each crate contains 16 Front End Cards (FECs), 16 PMT Interface Cards (PMTICs) (numbered 0-15), one Crate Trigger Card (CTC), and one XL3, as well as high and low voltage backplanes. Each FEC contains four daughterboards (DBs), for a total of 64 DBs per crate. The DBs contain custom integrated circuits that perform signal processing for eight PMT channels each. Thus, each crate is responsible for the analog processing and trigger generation of 512 PMT signals. The entire electronics chain services approximately 9730 PMT channels. High and low voltage power supplies provide the necessary voltages for the PMTs and electronics in each crate. All crates are housed in electronics racks on the deck above the detector, with most racks holding two crates. An image of a rack containing two crates is shown in Figure 3.11. In addition, a central (timing) electronics rack reads out global event information and receives inputs from each crate to determine when data should be saved. The timing rack consists of seven Master Trigger Cards/Analog (MTC/A+), one Master Trigger Card/Digital (MTC/D), one Trigger Latch board, two Trigger Utility Boards (TUB and TUBii), and one CAEN v1720 digitizer. An image of the timing rack is shown in Figure 3.11 and a schematic of the full trigger system is shown in Figure 3.12.



(a) Crates (b) Timing Rack

Figure 3.11: Rack 8 containing crates 12 and 13 (left). Timing rack containing the MTC/D, MTC/A+'s, TUB and TUBii, and the CAEN. Both located on the deck above the SNO+ detector.

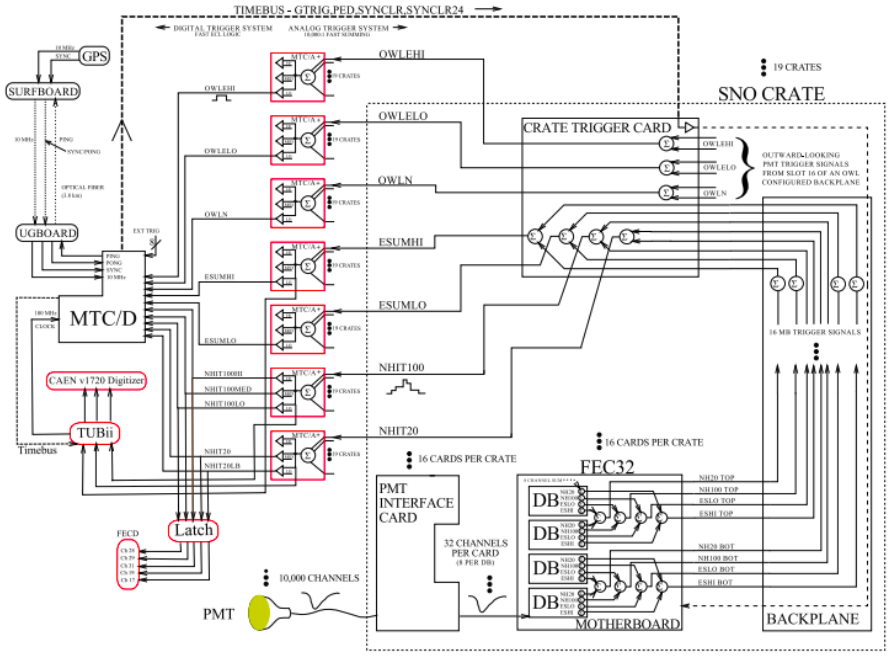


Figure 3.12: The SNO+ trigger system adapted from [18].

The PMTs in each crate are powered by a single HV supply, which provides approximately 60 mA of current across the 512 channels. The HV supply connects directly to the SNO+ HV backplane, which distributes HV to the PMTICs. Each PMTIC contains four Paddle Cards (PCs). There are 32 75Ω waterproof RG51 coaxial cables (grouped in sets of eight on each PC) that connect the PMTICs to the PMTs. These cables travel approximately 32 m down to the PMTs, carrying HV to the PMT base, where it is distributed to the dynode stack. Approximately 2000 V is supplied to the PMTs, though the operating voltage varies from 1800 V to 2350 V across the crates.

When an interaction in the detector produces light, the resulting analog PMT signal travels back along the same cables to the PMTICs, where an HV-blocking capacitor removes the DC component. The PMTIC also provides additional features, including disconnect relays that allow experts to disconnect eight channels at a time, as well as overvoltage and breakdown protection diodes. Flexible feed-through resistors allow tunable HV adjustments for each PMT. The HV setting at the supply and the values of the feed resistors are tuned such that the gain of the PMTs on the crate is close to 1×10^7. The mapping from HV to gain for each PMT was measured in dedicated setup at Queen's University, which characterized more than 9800 PMTs for SNO [67].

The signal from the PMT is then passed directly from the PMTIC onto the FEC via two 90-pin connectors, bypassing the HV and low voltage (LV) backplanes. On the FEC, the signals are distributed to one of the four DBs, depending on the location of the PMT connection. On the DBs, the signals are passed into two four-channel custom discriminators (SNOD), where each channel is compared against programmable thresholds. Typically, these "channel thresholds" are set to correspond to approximately one-quarter of the peak voltage of an average single photoelectron (SPE) signal. For channels that cross threshold, a PMT "hit" is created. The total number of PMT hits in a triggered event is often referred to as the N_{Hit} of the event.

Each PMT signal that crosses threshold is passed to two custom integrator (SNOINT) chips, where the signal is integrated along three paths to produce three charge values. These correspond to: charge integrated under high gain over a long integration window (approximately 400 ns, capturing pulses due to late light, reflections, and scattering) (QHL); charge integrated under high gain over

a short integration window (approximately 60 ns) (QHS); and low gain, short integration (QLS). The low gain path can also operate with long integral (QLL); nominally, this path is referred to as QLX. The SNOINT also shapes the input PMT signal and outputs two versions with different gains for triggering: ESUMH (high gain) and ESUML (low gain), which are basically copies of the PMT pulse along the high and low gain paths.

Simultaneously, on custom CMOS chips (eight single-channel chips per DB), a time-to-amplitude converter (TAC) is started on the leading edge of the SNOD signal. The TAC is stopped by a centrally generated global trigger (GT). The CMOS chip also creates two fixed-current square pulses used for triggering: one approximately 100 ns long (N100) and one approximately 20 ns long (N20). The N100 and N20 can be disabled at the channel level for broken channels. The CMOS chip also provides 16 analog memory cells per measurement per DB for storage. If these cells fill before being read out, a missed count flag is set high in the PMT bundle.

The time from the TAC, the three charge values, the crate number, FEC slot number, channel number, cell number, and associated error flags constitute the entirety of the analog-processing information stored by the SNO electronics. A direct map of the crate/card/channel/cell to PMT location is stored in a database and used to identify the physical origin of each signal.

The N100, N20, and ESUM signals represent the primary trigger signals for the detector. Separate trigger signals exist for the OWL PMTs that are handled equivalently. Each trigger signal generated on the DBs is passed to the FECs, where the bottom and top 16 channels are summed and sent onto the LV backplane. The LV backplane provides a path to the CTC, where each trigger signal is summed separately for the entire crate. Thus, each crate produces crate-level sums of N100, N20, ESUMH, and ESUML.

The signals for the seven triggers (N100, N20, ESUMH, ESUML, OWLEHI, OWLELO, and OWLN) from each of the 19 CTCs are then passed to the MTC/A+ boards in the central timing rack. Each MTC/A+ performs a detector-wide analog sum of its trigger signal with three different gain paths, each compared against a programmable threshold. When a trigger sum crosses threshold, a 20 ns

digital "raw trigger" is produced. Details about the MTC/A+ are described in Subsection 3.4.2. There are a seven MTC/A+'s in total, one for each trigger type. In principle, all MTC/A+'s are identical. The high gain path is referred to as the N100L or N20L, where "L" is for low-threshold. The medium gain path is N100M or N20M, and the low gain path is N100H or N20H.

The raw trigger produced by the MTC/A+'s are created for each individual gain path that crosses threshold. These raw triggers are sent to the MTC/D. The MTC/D has a trigger mask that decides which raw trigger signals to accept as a valid trigger signal. For triggers that are masked in, the MTC/D generates a global trigger (GT), which ends the trigger cycle and indicates that the detector should read out its data.

The GT is fanned out to all crates via ribbon cables connected to each CTC. From there, it is passed down the LV backplane to every channel on the DBs. Simultaneously, the MTC/D generates a lockout (LO) signal lasting 420 ns, during which the MTC/D will not emit another GT. This effectively creates a 420 ns trigger window in which to readout the PMT hits. The MTC/D records the trigger type responsible for the GT (e.g. N100, N20), along with any additional triggers arriving within approximately 20 ns, in a trigger word. A counter called the global trigger ID (GTID) is incremented at the MTC/D for each generated GT. This GTID is used to ensure the entire system remains in sync.

At the crate level, the GT is distributed to each of the channels, which stops the TAC ramps and signals to each channel that it should read out its data (time and charge information). Channels store their data waiting for a GT for a length of time known as GTValid. If a GT does not arrive before GTValid expires, the stored charge and TAC values are cleared. Each channel independently tracks the GTID, which is checked against the master trigger system every 216 GTIDs to ensure the channels are in sync. A CMOS/CGT sync flag is set in the PMT bundle if the channel gets out of sync with the rest.

When a GT arrives within the GTValid window, the channels with valid hits are buffered into FEC memory (4 GB). The data are digitized on the FEC and transferred across the LV backplane to

the XL3. Each crate contains one XL3, an upgraded board for SNO+ (described in Subsection 3.4.1). The XL3 sends the data to the central DAQ computer via Ethernet. The DAQ computer runs several servers that handle data readout and speak to the hardware. The xl3-server and mtc-server handle sending commands to and receiving replies from the XL3 and MTC respectively. The data-server receives PMT data from the XL3s and trigger data from the MTC/D and relays that data to any subscribed clients. The most important client is the SNO+ Event Builder ("Builder"), which uses the GTID stored in the PMT data and the trigger data to combine PMT and trigger data into an "event." Once the builder is satisfied that all PMT hits have been saved to the correct event, the builder writes the data to disk in the custom "zdab" format.

Data are written to a file until it reaches a maximum size of 1 GB, at which point the builder will save it, close the file, then create a new file. Files are indexed by run, typically one hour in duration for Physics data taking. Each run contains metadata such as run number, run type (e.g. Physics, Calibration, Maintenance), and detector activity during the run (e.g. Recirculation, DCR Activity).

The absolute time of each event and the relative timing between events are recorded by two separate clocks. A 10 MHz clock is distributed by a commercial GPS system previously located on surface. As of March 4, 2025, the GPS unit and SURFBOARD are located underground. The 10 MHz clock, synchronized to GPS, is distributed via a 4 km long fibre optic cable and relayed underground through the UGBOARD to the MTC/D. The 10 MHz clock provides a "universal" time and is synced to the GPS once per hour. A 100 MHz clock runs on the TUBii (described in Subsection 3.4.3) and is plugged directly into the MTC/D, where it is converted to 50 MHz. This clock is used for inter-event timing and provides 20 ns resolution.

An auxiliary CAEN v1720 waveform digitizer in the central timing rack digitizes summed trigger signals. The raw triggers from the MTC/A+ are plugged into the MTC/D through a board called the Latch board (described in 3.4.4). Figure 3.12 depicts a detailed schematic of the SNO+ trigger system. The path from the PMT to the MTC/D is shown with the new/upgraded boards from SNO to SNO+ highlighted in red.

The MTC/D also provides a pulser than can generate forced GTs at a fixed rate. This pulse GT (PGT) produces zero-bias triggers used to measure dark noise rates and CMOS dropout rates. In combination with the PGT, the MTC/D can issue pedestal signals to all crates in the crate pedestal mask (set on the MTC/D) that tells the crates to read out the data for any channels in the channel pedestal mask (set by the XL3). This bypasses the discriminators and forces channels to read out their data. These pedestal signals are used for electronics calibration (e.g. ECAL and ECA, described in Subsection 3.5) and by the N_{Hit} monitor for determination of the trigger efficiency.

3.4 Electronics Upgrades

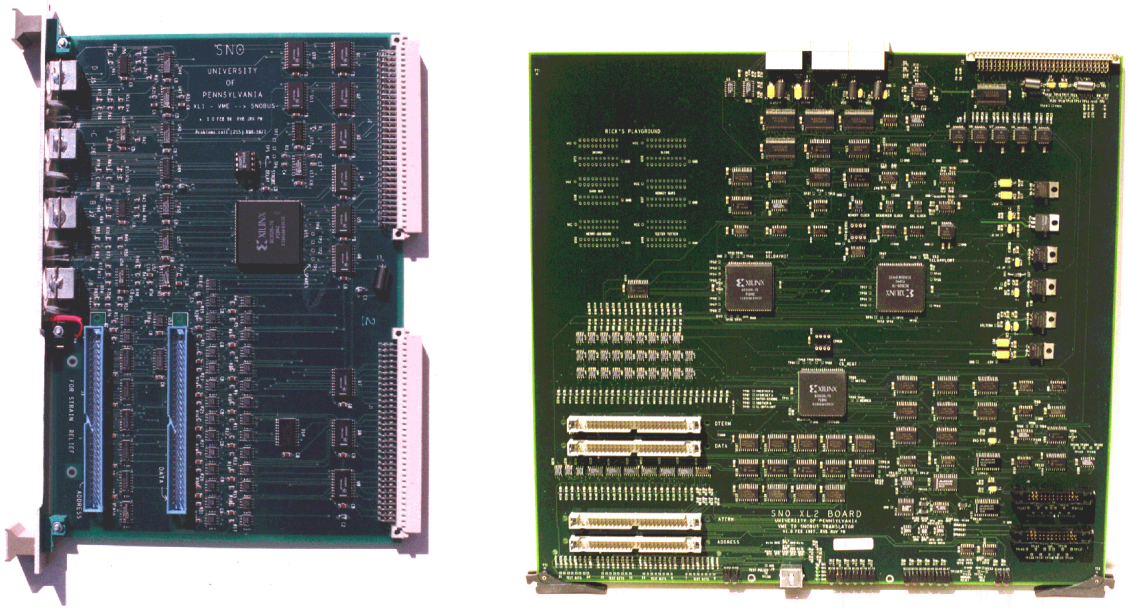
SNO+ required additional boards and upgrades to the electronics chain due to the migration from heavy water (SNO) to liquid scintillator. The updates were required due to the higher trigger rates and expected average PMT occupancy by using liquid scintillator as the target material. The following subsections cover these upgrades.

3.4.1 XL3

The SNO data readout system consisted of XL1s and XL2s, depicted in Figure 3.13, which provided centralized readout of the crates. One caveat of these boards was their limitation to communicate and receive data from one crate at a time at a maximum rate of approximately 250 kB/s. The XL1 and XL2 were replaced by the XL3, shown in Figure 3.14, which does an asynchronous, parallel readout of the crates that drastically increases the readout speed and provides an updated interface for control of the HV supplies that power the PMTs.

Each crate contains one (1) XL3 that provides the readout of the front-end electronics. A Xilinx ML403 board [68] is connected to each XL3. The ML403 contains a Xilinx Vertex-4 FPGA, a PowerPC processor, 64 MB of SDRAM, and a CompactFlash card, which stores the firmware running on the Vertex-4 FPGA and C code that runs on the PowerPC processor. The Vertex-4 FPGA is configured to pull the readout data from the FECs across the backplane. The PowerPC processor C code requests the data from the FPGA and buffers it into local memory. The data is then pushed by the XL3 to a central DAQ computer over Ethernet using standard TCP/IP protocols. This allows each XL3 to readout data at a maximum rate of around 14 MB/s, giving a

detector wide readout rate of 266 MB/s. This is ∼1000x faster than the SNO readout.



(a) XL1 (b) XL2

Figure 3.13: A picture of the SNO XL1 (left) and XL2 (right) boards. Adapted from [19].

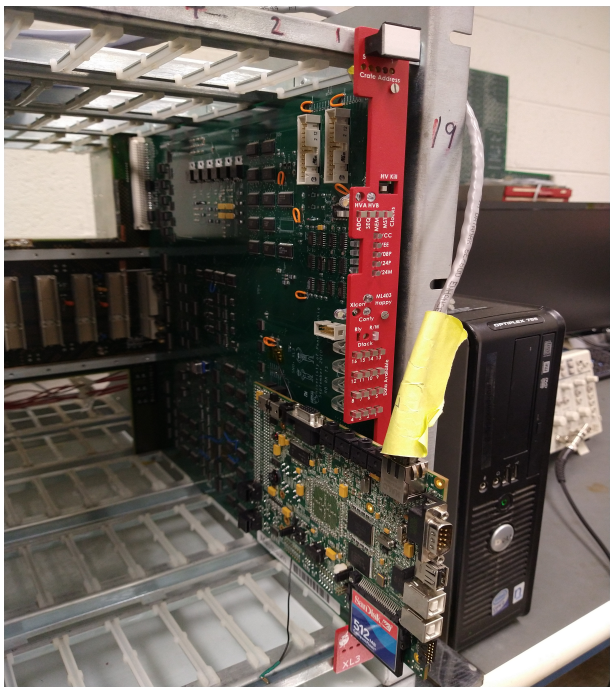


Figure 3.14: A picture of the SNO+ XL3 with ML403 and Ethernet cable.

3.4.2 MTC/A+

Another board that was upgraded from SNO was the MTC/A, which summed the analog trigger signals from each of the CTCs and handled the triggering logic. The motivation for the MTC/A+ is the large number of expected PMT hits as it handles higher hit rates and thus higher currents. Alongside dealing with higher hit rates, it also provides additional trigger functionality and baseline restoration, which was designed to improve stability. The MTC/A+ has 20 inputs, which is enough for all 19 crates and one spare. Each crate's input is connected via a reed relay, which provides the ability to disconnect the signal from the sum in case of instability caused by a single crate. This allows for fast debugging with the trigger signal by identifying the problem crate. These signals are then sent through a series of analog summing stages using operational amplifiers. At this point, the signals are summed and split into three separate gain paths. These gain paths provide different dynamic ranges for the same trigger signal. The final sum output for each of the three gain paths is sent to three places: the baseline restoration functionality, the analog output, and the triggering functionality. The baseline restoration functionality uses an integrating amplifier with a long time constant (of order tens of seconds) to output the average voltage of the final summing stage. This alleviates issues associated with trigger baseline shifts that can be caused by variations in the DC-coupled analog sum baseline. The time constant is slower than the PMT signals, so it does not integrate them. This signal is then fed back to the non-inverting input of the final summing amplifier, removing any long term DC shifts in the baseline of the signal. The MTC/D monitors and reads out the MTC/A+ baselines after the voltage is sent through the TUBii. The analog output is a copy of the analog trigger sum. This is sent through TUBii, copied, and shaped to be sent to the CAEN digitizer, which reads out the waveforms, and sent to an oscilloscope underground (UG) for monitoring purposes. The final place is the trigger functionality, which takes the outputs from the final stage summing amplifiers and inputs each into a comparator with a threshold controlled by a DAC on the MTC/A+. The signal from the comparator being high/low indicates whether the MTC/A+ is above/below the trigger threshold. The output of these three comparators, along with two additional signals, known as lockout and a delayed copy of the global trigger (GT), are then sent to a Xilinx CoolRunner-II CPLD [69]. This allows for customizable logic to be applied to

the five input signals to determine when a trigger should be emitted. The CPLD has three trigger signal outputs, one for each gain path, which are sent to the MTC/D to trigger the detector. The CPLD has standard trigger logic that results in a raw trigger being emitted on the output of the corresponding gain path whenever the trigger signal crosses the comparator threshold for that gain path.

There is additional triggering logic implemented on the CPLD that involves deadtime and retriggering logic.

SNO+ typically records triggered events at a rate of ∼2 kHz, with each event spanning a 420 ns readout window. During detector operation, only events satisfying the trigger conditions are read out and stored. Deadtime refers to periods during which the detector electronics are temporarily unable to accept or record additional events because they are processing a previous trigger. Events occurring during these intervals are not recorded.

The SNO+ trigger system has two types of deadtime:

- Trigger deadtime: A period of time not read out by the detector where a trigger signal is unable to cause a GT.
- Hit deadtime: A period of time where a PMT can be hit, but is unable to be read out as part of an event.

The first type of deadtime exists due to the way lockout (LO) is implemented on the MTC/D. In nominal Physics running, LO is set to 420 ns and no raw trigger signals can create a GT during that time. There is a ∼200 ns delay (primarily due to cable lengths) that is associated with sending the analog trigger signals from the crates to the MTC/A+, the trigger logic on the MTC/A+, and sending the GT back to the crates. As a result, the hits that cause a GT fall in the middle of the 420 ns trigger window with only ∼220 ns of data saved afterward. If an event occurs ∼300 ns after the initial event and produces enough hits to create a raw trigger, the event may not trigger the detector because LO has not yet ended. In addition, its hits will not be read out in the initial event.

Since there is no GT, the information would then be completely lost with no indication that it even occurred.

Hit deadtime exists due to how the readout on the DBs is implemented. When a PMT is hit, a signal known a GTValid is set high and the TAC ramp begins. The signal used to indicate a PMT has a valid hit ready to be read out is GTValid. The TAC ramp is used to measure the time since the hit occurred. The length of the TAC ramp must be longer than GTValid in order to ensure a valid time can be read out for the event. The length of GTValid must be shorter than LO to prevent the same hit from being read out into two events. As a result, there is a small deadtime between when GTValid ends and when the TAC ramp resets. GTValid remains high for the full ∼400 ns after a hit occurs regardless of whether a GT arrives and the channel is read out. This means a channel that is read out <400 ns after a hit occurs is dead for the remaining amount of the 400 ns.

Additional triggering logic is implemented on the CPLD to mitigate deadtime. After the MTC/D emits a GT, LO prevents another GT from being emitted for 420 ns. This additional logic can be used to emit another trigger immediately at the end of LO based on the conditions during LO. This logic is known as "retriggering logic" and the triggers emitted due to this logic are referred to as retriggers. Recall that the CPLD on the MTC/A+ has access to five signals to determine when to trigger the detector: the output of the comparator for each gain path on the MTC/A+, LO from the MTC/D or TUBii, and a delayed copy of the global trigger (DGT) produced by TUBii. A diagram of the system is shown in Figure 3.15.

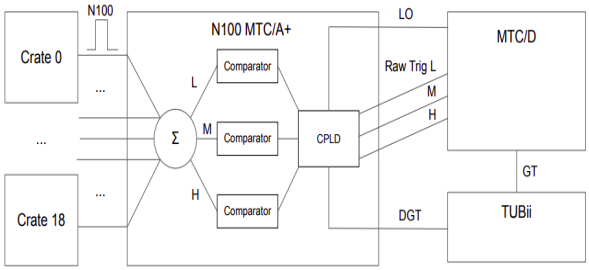


Figure 3.15: Diagram of the signals input to the triggering logic on the MTC/A+. Figure adapted from [20].

The retrigger logic was developed to emit retriggers under these three conditions (plus the standard logic):

- Standard triggers: On the rising edge of the comparator signal, a raw trigger is emitted.
- LO retriggers: If the comparator signal is high at the end of LO, a raw trigger is emitted at the end of LO (immediately).
- DGT retriggers: If a rising edge of the comparator signal occurs during LO, but after DGT, a raw trigger is emitted at the end of LO.
- Automatic retriggers: When a raw trigger caused by any of the propr three conditions is emitted, emit another raw trigger at the end of LO.

On each of the three gain paths, each trigger logic condition can be applied independently. All three gain paths implement the first three conditions and the low gain path implements all four. As a result, the low gain path can be set at a high threshold, ensuring retriggers for all events above that threshold.

This retriggering logic was designed to be as inclusive as possible to ensure no events are lost due to trigger deadtime.

3.4.3 TUBii

The Trigger Utility Board Mk.II (TUBii) replaced the SNO Trigger Utility Board (TUB). TUBii provides additional triggering logic as well as performs the following roles:

- MTC/A+ & CAEN Interface: Analog trigger signals from the MTC/A+ are sent to TUBii, which copies the signal. The -5 V baseline from the MTC/A+ is removed. Once copy of the signal is sent to the oscilloscope (UG), while the other copy is shaped to the correct dynamic range before being sent to the CAEN digitizer. TUBii also provides a measurement of the MTC/A+ baseline values. TUBii sends GT and SYNC signals to the CAEN to read out the waveforms and ensure synchronization with the rest of the detector. TUBii also sends a

delayed copy of the GT signal, mentioned in Subsection 3.4.2, to the MTC/A+ to be used in its triggering logic and buffers the voltage of the baseline restoration on the MTC/A+. This is sent to the MTC/D and read out for monitoring.

- Calibration Interface: (e.g., the laserball, TELLIE, and SMELLIE). It provides synchronization with the trigger system and tunable pulser frequencies used by these systems to control the rate of light pulsing. Additionally, TUBii controls the triggering for calibration systems with a tunable delay and an interface to the asynchronous trigger functionality on the MTC/D.

- Clock Interface: TUBii has its own clock along with a clock input. It can select which clock is sent to the required 50 MHz clock input on the MTC/D. TUBii will automatically fall back to the other clock if it detects the selected clock is not working.

- Logic converters (e.g., ECL to TTL)

- Audio output of the GT rate, which is still used for monitoring in SNO+.

The TUBii triggering logic is designed to use any of the raw trigger signals from the MTC/A+ as input. A GT for the detector can be created from nearly any logical combination of trigger signals. As an example, TUBii can take an N20 raw trigger, where the threshold has been set relatively low, and an N100 raw trigger, where the threshold has been set relatively high, as inputs. The trigger was implemented as method for detecting gamma-rays in the external volume during the scintillator phase, where the low energy decays of ^{14}C make it difficult to measure the events in the external water volume.

3.4.4 Other Upgrades

In SNO, the Analog Measurement Board (AMB) was used to measure the peak, integral, and derivative of the analog trigger sum from the MTC/A. The AMB was replaced by a CAEN v1720 8 channel 12-bit 250 MS/s (rate corresponds to 4 ns bins in the waveform) waveform digitizer with a dynamic range of 2 V in SNO+. As mentioned in Subsection 3.4.3, the analog sums from the MTC/A+ are shaped to the proper dynamic range by TUBii, then sent to the CAEN digitizer.

TUBii also sends the GT and SYNC signals to the CAEN, which ensures synchronization with the rest of the detector. The CAEN reads out N100, N20, and ESUMH trigger signal waveforms during nominal Physics running. There are 8 inputs, which allows for additional signals to be connected and digitized (used in some calibrations to readout an additional PMT signal from the calibration system itself).

The MTC/D records only trigger signals occurring within ∼20 ns of the initial signal in the trigger word. If triggers occur after this time, but still within the 420 ns trigger window, an additional bit known as "Missed trigger" bit is set high. The Latch Board addresses this issue by splitting the most important trigger signals (e.g., N100 and N20 trigger signals) before they reach the MTC/D. It sends the additional copy to a modified FEC called the FEC/D, located in crate 17, slot 15. This modified FEC reads out the digital trigger inputs as hit records and provides additional calibration channels. The FEC/D Latch Board acts as a trigger fan-out for the MTC/A+, taking the three MTC/A+ trigger signals as input and sending two ECL outputs and one negative-going pulse to the FEC/D. Rather than determining which trigger bits fired (information already recorded by the MTC/D trigger word), the latch board records the relative timing of the individual trigger signals. This information is valuable for trigger diagnostics, commissioning, and calibration studies. The FEC/D is read out through the XL3 in the same manner as a standard FEC and is also used for calibration sources, such as the ^{16}N trigger PMT, where it records the timing of the raw MTC/A+ trigger signals.

Baseline Monitoring

Baseline shifts, also referred to as drop-out, occur when the baseline value of a signal changes, effectively lowering the trigger threshold. In extreme cases, the baseline can drop enough that the detector will trigger even when no PMTs were hit by light. This results in a high trigger rate with low number of PMTs hit (N_{Hit}). The baseline restoration implemented on the MTC/A+ corrects these shifts, although only on relatively long timescales. Aside from the baseline restoration, the trigger electronics are DC-coupled.

To further improve system stability, the CTCs were upgraded with heat sinks on the N20 and

N100 transistors to reduce temperature-dependent baseline drift. In addition, a baseline monitoring system was developed to identify crates exhibiting baseline instabilities during detector operation.

Baseline shifts during Physics data taking can lead to significant detector instability. Prior to the implementation of baseline monitoring, identifying the affected crate often required several minutes to days of investigation. The baseline monitoring system identifies the offending crate, substantially reducing the time required to diagnose and resolve these instabilities. The development, testing, and implementation of this monitoring system is described below.

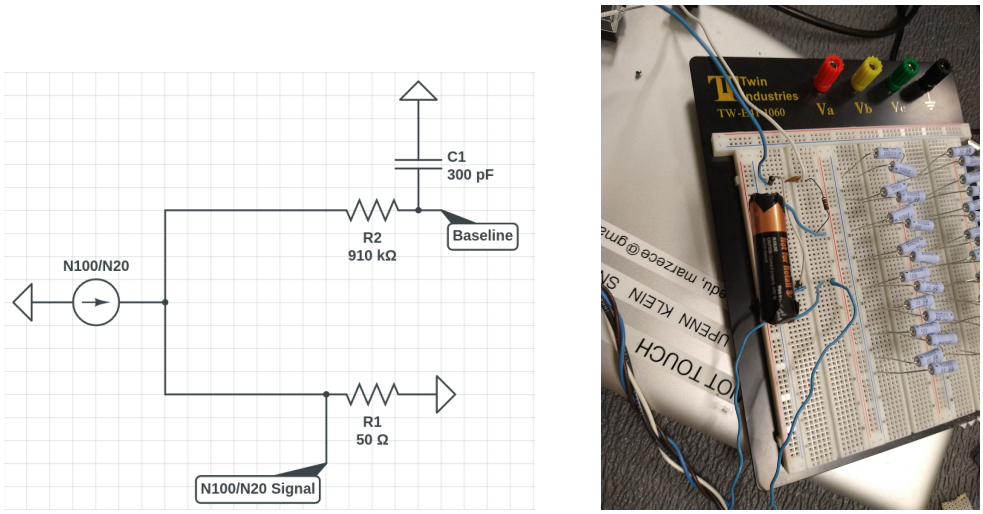
Teststand Validation

Initial testing was performed using the SNO+ electronics teststand (crate 19), which contains a representative MTC/D, CTC, FEC + DBs, XL3, ML403, and LV backplane. The teststand provides an isolated environment for evaluating modifications to the trigger electronics before installation underground.

The baseline monitoring system samples the N20 and N100 trigger outputs from the CTC using passive signal splitters and low-pass RC filter circuits. Before deployment, it was necessary to verify that these additional components did not distort the trigger signals or degrade detector performance.

RC Filter Tests

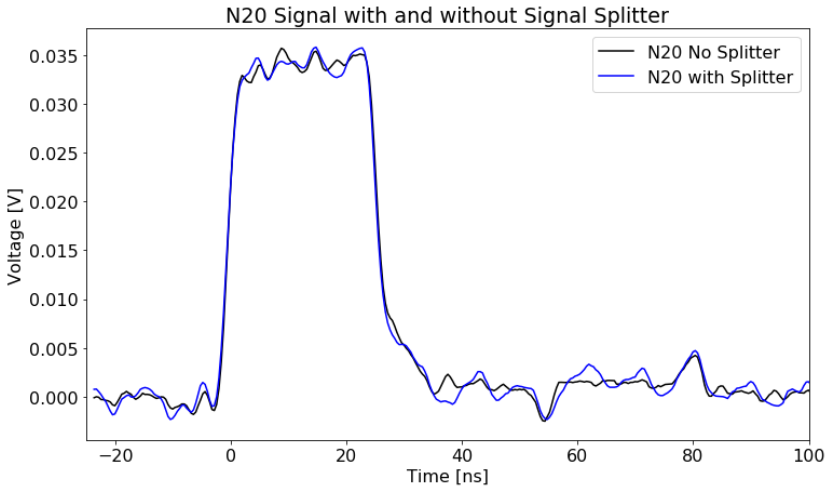
The first study evaluated the effect of inserting a simple low-pass RC filter circuit (910 kΩ, 300 pF), shown in Figure 3.16, into the N20 and N100 trigger outputs. The filter extracts the slowly varying baseline from the fast trigger pulses, which would allow the baseline voltage to be continuously monitored by the detector slow controls system. The RC values were chosen to provide a high-impedance monitor of slow baseline variations while strongly attenuating the fast components of the N20 and N100 trigger signals. A 50 Ω terminator was installed on the trigger output as a precaution to provide the expected load and proper grounding of the CTC output while the monitoring circuit was connected.



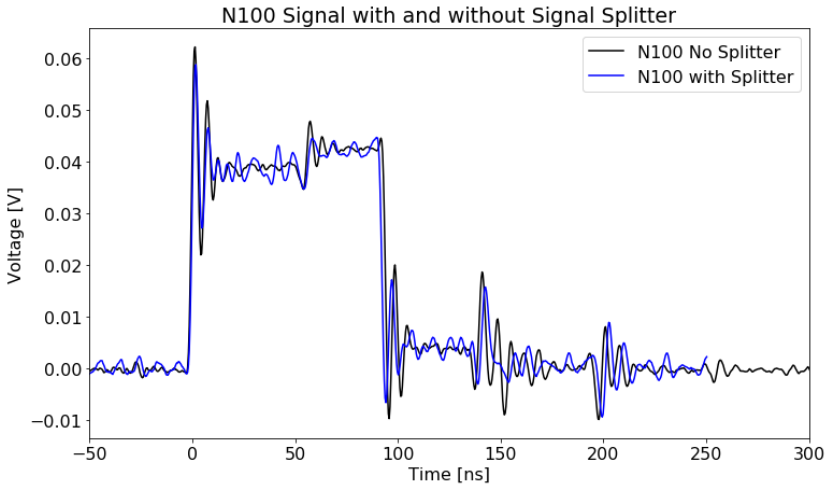
(a) Schematic (b) Circuit

Figure 3.16: Schematic and picture of low-pass RC filter circuit connected to the CTC's N20 and N100 outputs.

Figure 3.17 compares the N20 and N100 trigger pulses before and after inserting the RC filter circuit. The waveforms are nearly indistinguishable, demonstrating that the additional circuitry does not significantly modify the trigger signals. In particular, the pulse amplitudes remain unchanged, no measurable pulse broadening is observed, and no additional ringing or reflections are introduced. These results demonstrate that the monitoring circuit can be connected to the trigger outputs without affecting detector timing or trigger performance.



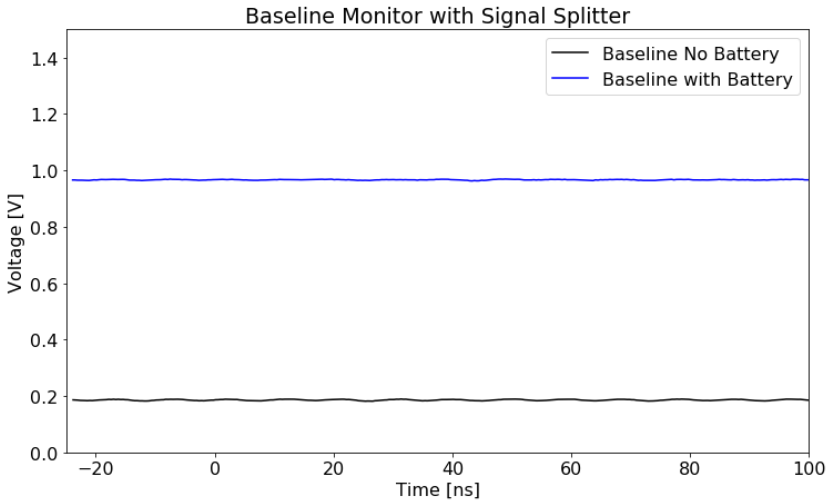
(a) C19 N20



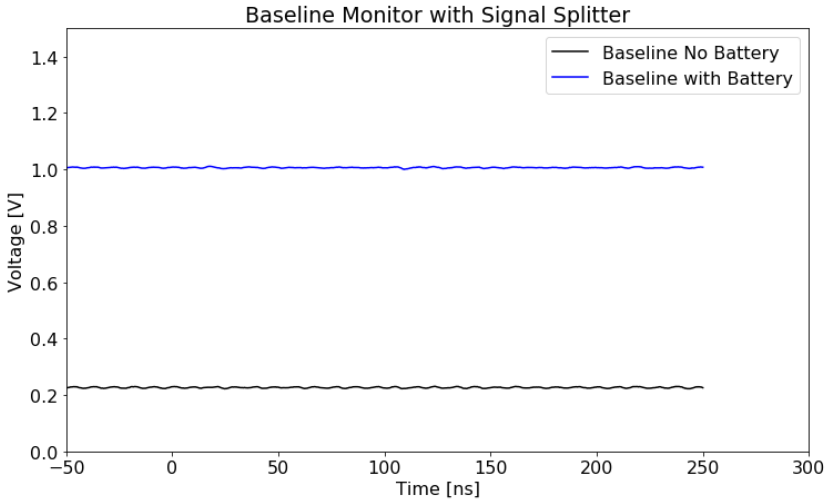
(b) C19 N100

Figure 3.17: N20 (left) and N100 (right) CTC output signals with and without the filter.

To verify its response when a baseline shift occurs, controlled baseline offsets were introduced using a 1.5 V battery connected through the RC filter. Trigger signals were recorded with a Teledyne LeCroy WaveSurfer 4104HD oscilloscope [62] using the 1 MΩ input impedance configuration. Figure 3.18 shows that the applied offset shifted the baseline as expected. The trigger pulses remained unchanged and no measurable increase in electronic noise was observed. These tests demonstrated that the monitoring circuit measures baseline drift without perturbing the trigger signals.



(a) C19 N20



(b) C19 N100

Figure 3.18: N20 (left) and N100 (right) CTC output signals with and without the battery simulating a baseline shift.

Detector Installation

Following successful teststand validation, two baseline monitoring circuits were assembled and installed in rack 1, crate 0's CTC located on the SNO+ deck. The detector was turned off at the time, but power was supplied to a crate to test the circuit boxes. The monitoring units were connected to the N20 and N100 trigger outputs using BNC tee connectors, allowing the trigger signals to continue uninterrupted to the MTC/A+ while simultaneously providing a filtered copy to the slow controls

system. An image of the low-pass RC filter box is shown in Figure 3.19.

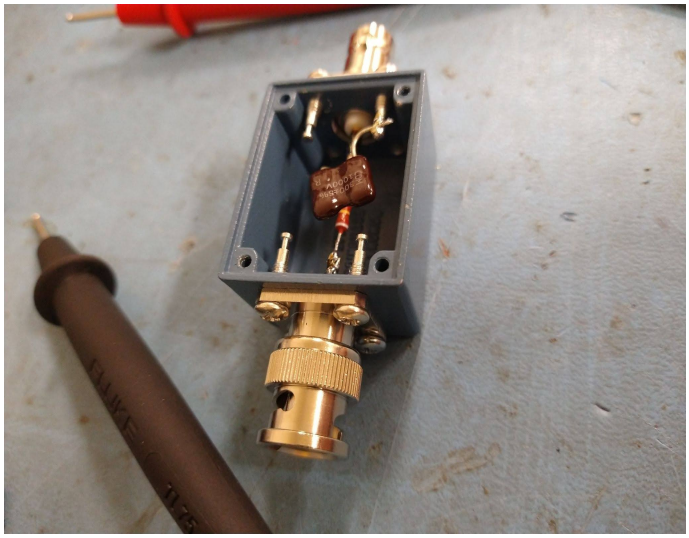


Figure 3.19: Project box containing low-pass RC filter circuit that will be attached to the CTC's.

Figure 3.20 is a diagram of the implementation of the project boxes into the CTC. The CTC has seven trigger BNC outputs, the project boxes use a BNC tee connector so that the N20 and N100 trigger signals pass through the low-pass filter circuit and get passed to the MTC/A+ and the slow controls computer.

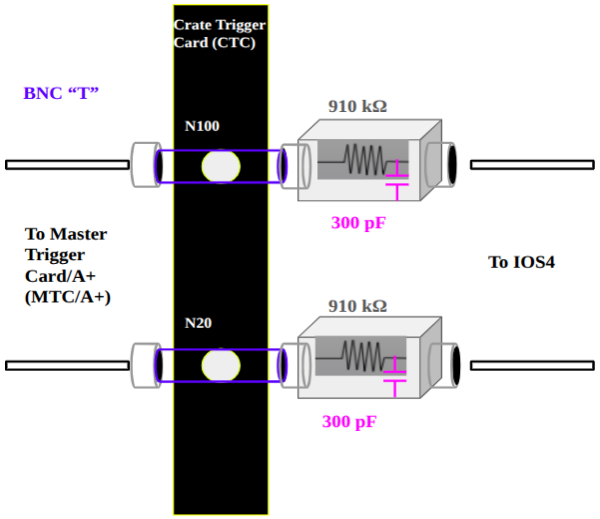
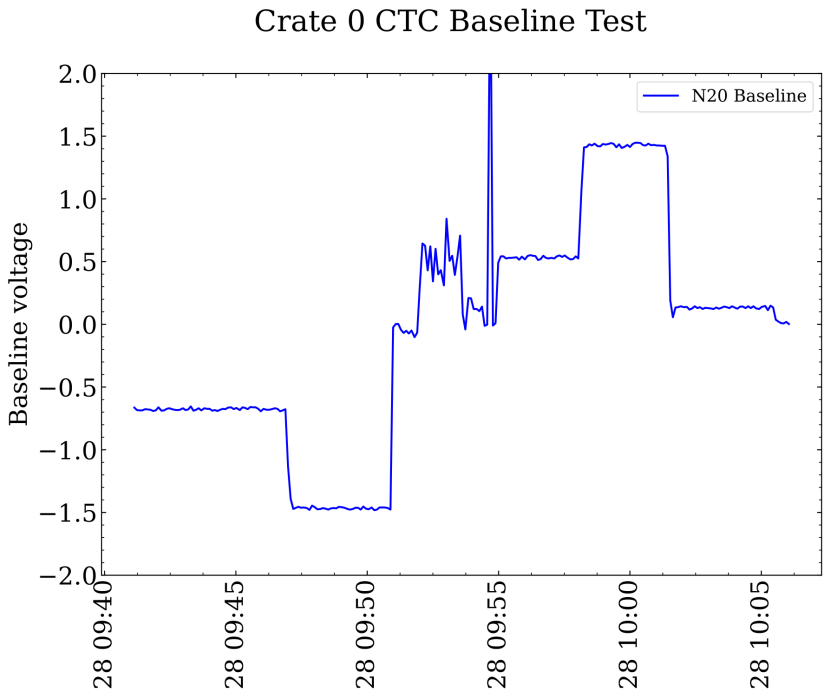
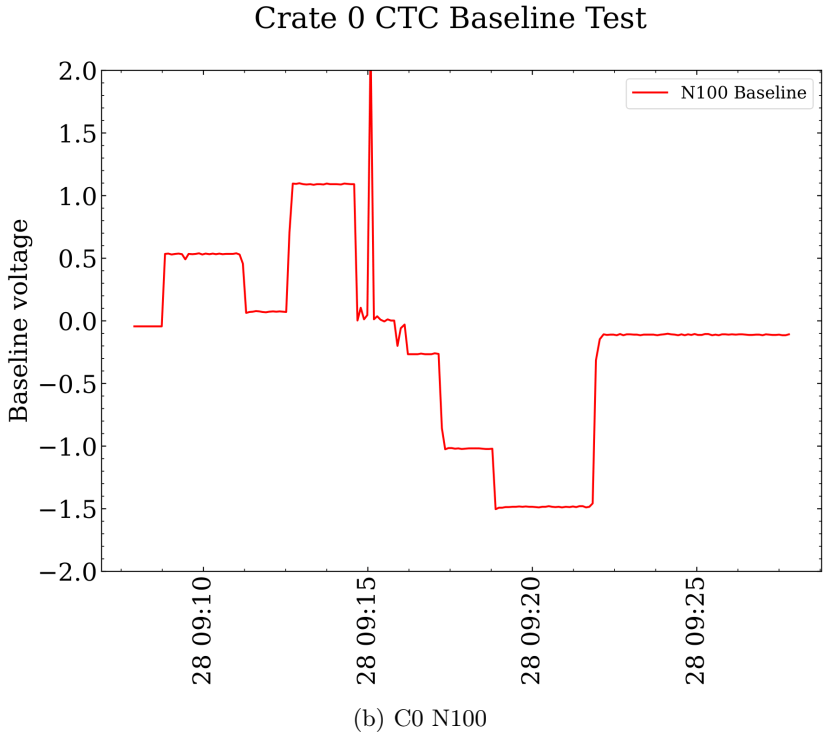


Figure 3.20: Diagram of the low pass filter circuit project boxes connected to N20 and N100 trigger outputs on the CTC.

Figure 3.21 shows the response of the baseline monitor when controlled voltage offsets were applied to the CTC. The discrete steps correspond to changes in the applied test voltage from the auxiliary power supply. For the N20 channel, the applied offsets produced clear positive and negative shifts in the monitored baseline. The large spike near 09:55 is a transient associated with changing the test configuration and does not persist as a stable baseline offset. The N100 channel shows the same behavior: the monitored baseline follows the applied voltage steps, including the sign reversal produced by flipping the test connections. These tests demonstrated that the slow controls readout could identify the affected crate and distinguish baseline shifts on the N20 and N100 trigger outputs.



(a) C0 N20



(b) C0 N100

Figure 3.21: Crate 0 baseline monitor measurements of N20 and N100 trigger signals.

After performing the preliminary tests of a low-pass RC filter with the teststand's CTC and crate 0 on the SNO+ deck, 38 project boxes with low-pass filter circuits were stuffed and sent to site for implementation into the detector.

Operational Performance

The installed baseline monitoring system continuously measures the baseline levels of the N20 and N100 trigger outputs for every crate. During detector operation, developing baseline shifts can now be rapidly associated with individual crates, substantially reducing the time required to diagnose and correct detector instabilities. Prior to implementation, identifying the responsible crate could require several minutes to days of investigation. Figure 3.22 shows the final installation of the baseline monitoring project boxes on the detector electronics racks. Each monitoring unit connects to the N20 and N100 trigger outputs of a CTC through a BNC tee connector, allowing continuous monitoring while leaving the primary trigger path unchanged.

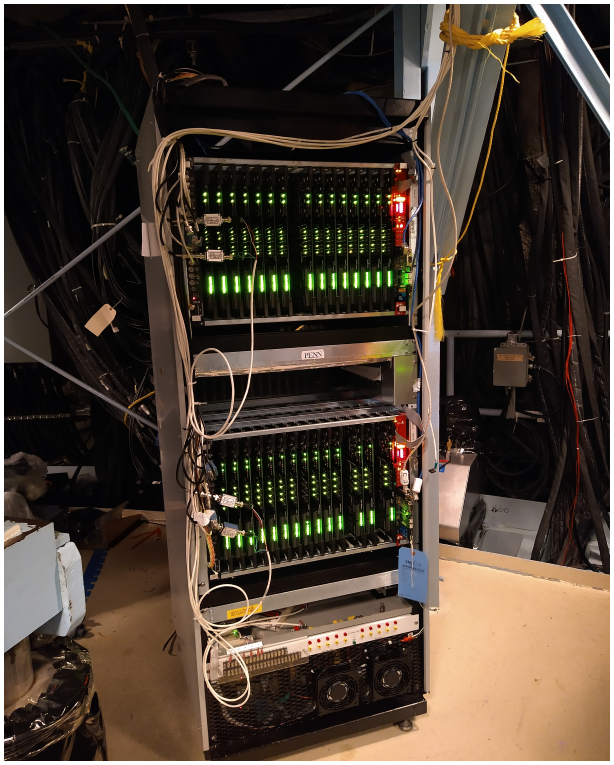


Figure 3.22: Image of SNO+ rack 8 with crates 12 and 13. The N100 and N20 baseline monitor project boxes are visibly horizontal and connected to the CTCs (black cards on the far left).

Figure 3.23 shows a typical slow controls display during detector operation. Each trace corresponds to the monitored baseline voltage for a particular crate. A sudden deviation from the nominal baseline immediately identifies the crate responsible for the instability, allowing operators to diagnose the problem in real time rather than searching crate-by-crate.



Figure 3.23: A screenshot of the slow control's page depicting a baseline shift in crate 17's N100 trigger signal.

3.5 Electronics Calibration

SNO+ performs two types of electronics calibrations: ECALs and ECAs (both short for electronics calibrations, of course). For calibrations, the electronics were designed to produce forced triggers. Forced channel triggers are known as "pedestal" signals. When a pedestal signal is sent to a channel, the channel will behave as if it received a hit even when no PMT pulse was present. Another type of forced trigger is a forced global trigger known as "pulseGT." The MTC/D can directly trigger the detector and readout all of the channels that the pedestal was sent to. These two forced signals allow user controlled triggering and readout to be used for the electronics calibrations.

ECAL is responsible for setting and measuring several hardware settings on the FECs and DBs while minimizing channel-to-channel variations across the detector. The quantities set and calibrated in an ECAL are as follows:

- Discriminator thresholds: The DB discriminator threshold is varied. The location of the baseline and the size of the noise is determined by the trigger rate at each discriminator threshold. The threshold is placed just above the noise level.

- Charge baselines: FEC DACs control the charge readout baseline. These DACs are varied to find a similar baseline for QHS/QHL/QLX across all channels in the detector.

- Charge integration times: FEC DACs also control the slope of several voltage ramps, which determine the length of the QHS and QHL charge integration windows. These DACs are varied to find integration windows of ∼60 ns and ∼400 ns for QHS and QHL, respectively.

- Hit validity window: The length of time in which a hit is valid before being discarded (GTValid). It is determined by the TAC ramp. The slope of the TAC ramp (and thus its length) is controlled by a DAC on the FEC. This DAC is varied to ensure that GTValid is shorter than Lockout (420 ns) for all channels. This ensures that a single PMT hit cannot be read out in two different triggered events.

ECA is responsible for the calibration of baseline values from the measured charges (QHS/QHL/QLX) and the relationship between readout voltage (TAC) and time for each channel. This requires sending pedestals to each channel, then measuring QHS/QHL/QLX. These hits are produced with no charge on the PMT, so the charge readout is the baseline value. To calibrate the time readout, pedestals are sent with a known time delay between the pedestal signal and the GT signal. This time delay is varied with the TAC value measured at each delay. The TAC ramp is approximately linear, so a line is fit to the data for each channel to provide a conversion between TAC and hit time.

3.6 Absolute Timing and GPS Synchronization

Precise absolute timing is essential for searches involving transient astrophysical phenomena, such as supernova neutrinos and neutrinos in temporal coincidence with gravitational wave events. Unlike most detector observables, the event time must be referenced to an external standard so that observations can be compared with those made by other experiments around the world. For SNO+, this reference is provided by the Global Positioning System (GPS), which supplies an accurate absolute time and a stable 10 MHz clock used to synchronize the detector electronics.

Figure 3.24 shows a simplified block diagram of the SNO+ GPS timing system. A commercial GPS

receiver located on the surface provides both an absolute time reference and a continuous 10 MHz clock signal. These signals are transmitted through optical fibers to the underground electronics, where they are distributed to the MTC/D via the Underground Board (UGBOARD). The MTC/D maintains the detector clock, timestamps every trigger, and assigns a unique GTID to each event.

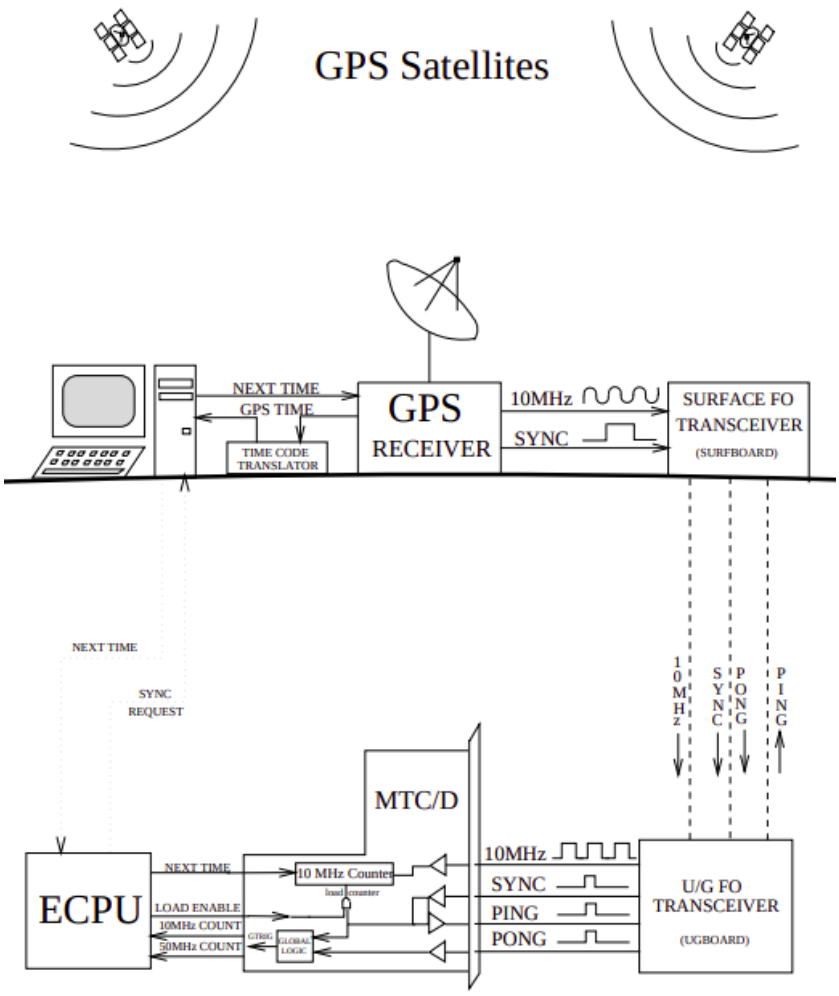


Figure 3.24: GPS schematic adapted from [21].

Two custom interface boards, known as the SURFBOARD and UGBOARD, provide communication between the surface GPS receiver and the underground trigger electronics. The SURFBOARD relays the 10 MHz clock signal and periodic synchronization (SYNC) pulses to the underground electronics, while the UGBOARD distributes these signals to the MTC/D and returns a confirmation (PING/PONG) signal to verify successful synchronization. In addition to relaying timing signals,

both boards provide diagnostic outputs for monitoring the health of the timing system and allow manual synchronization when necessary.

Each trigger recorded by SNO+ is assigned a GPS timestamp. Internally, the detector timing is maintained using a continuously running 10 MHz reference clock that is periodically synchronized to the GPS receiver using a SYNC pulse. Between synchronization pulses, event times are determined by counting successive 10 MHz clock cycles. This design allows the detector to maintain accurate timing even if communication with the GPS receiver is temporarily interrupted, provided the local reference clock remains stable.

During much of the water and scintillator phases, the GPS timing system experienced communication problems between the surface and underground electronics. These issues were not caused by the GPS receiver itself, but rather by failures within the timing distribution system. Contributing factors included damaged optical fibers, power supply failures, hardware modifications associated with relocating components underground, labeling inconsistencies, and failures of passive electronic components on the SURFBOARD and UGBOARD. As a consequence, the detector continued operating using its internal timing reference, but the absolute offset between detector time and GPS time could not always be determined directly.

Following repairs and upgrades, reliable GPS synchronization was restored on November 25, 2025.

Although the detector continued to record events normally during this period, the uncertainty in the absolute timing required careful characterization for analyses relying on external astrophysical triggers. In particular, the search presented in Chapter 6 compares SNO+ event times with gravitational wave trigger times reported by the LIGO-Virgo-KAGRA collaboration. Characterizing the detector's absolute timing offset was therefore necessary to ensure that the coincidence windows were correctly centered on the reported GPS times.

The detector continuously monitors the difference between the detector clock and the GPS reference. Whenever the timing offset exceeds a predefined threshold, the DAQ records a diagnostic message

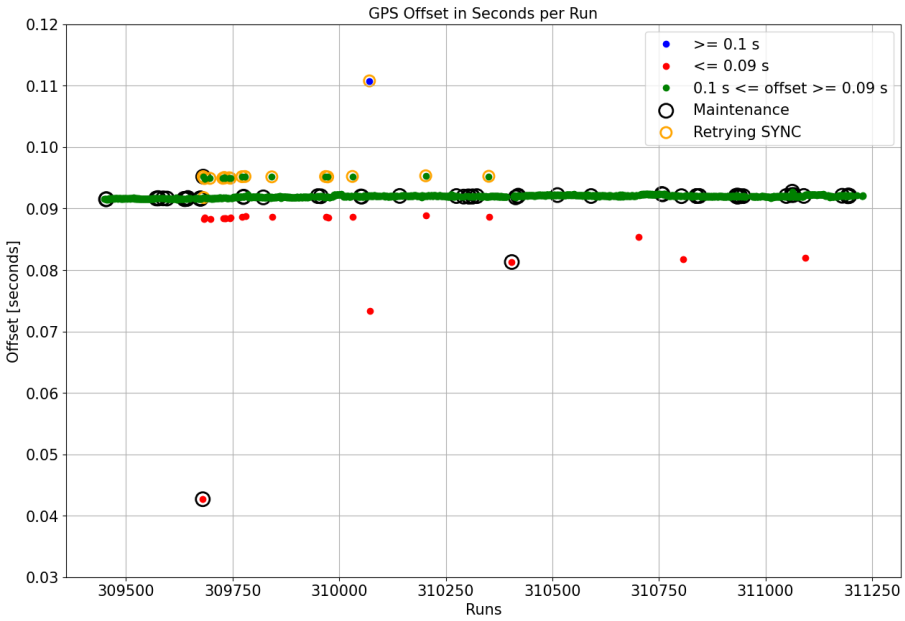
in the run log of the form

```
22 Apr 03:01:02 gps * 10 MHz clock is off by 917270 ticks.
```
(3.5)

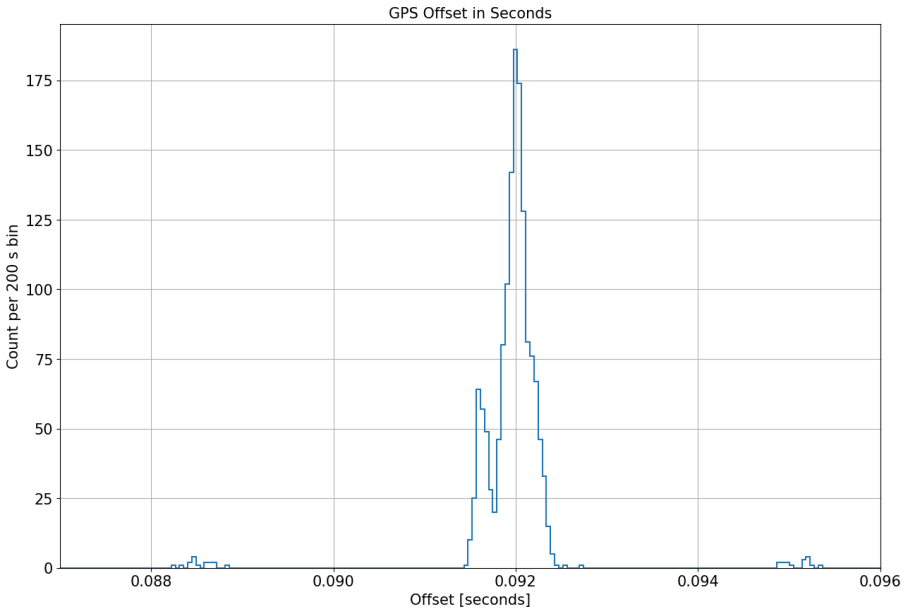
Because the detector clock operates at 10 MHz, one clock tick corresponds to 100 ns. The reported offsets can therefore be converted into an absolute time offset through

$$t_{\text{offset}} = N_{\text{ticks}} \times 100 \text{ ns} \tag{3.6}$$

These offsets were extracted from the DAQ logs for every available run in the scintillator phase and are shown in Figures 3.25 and 3.26.

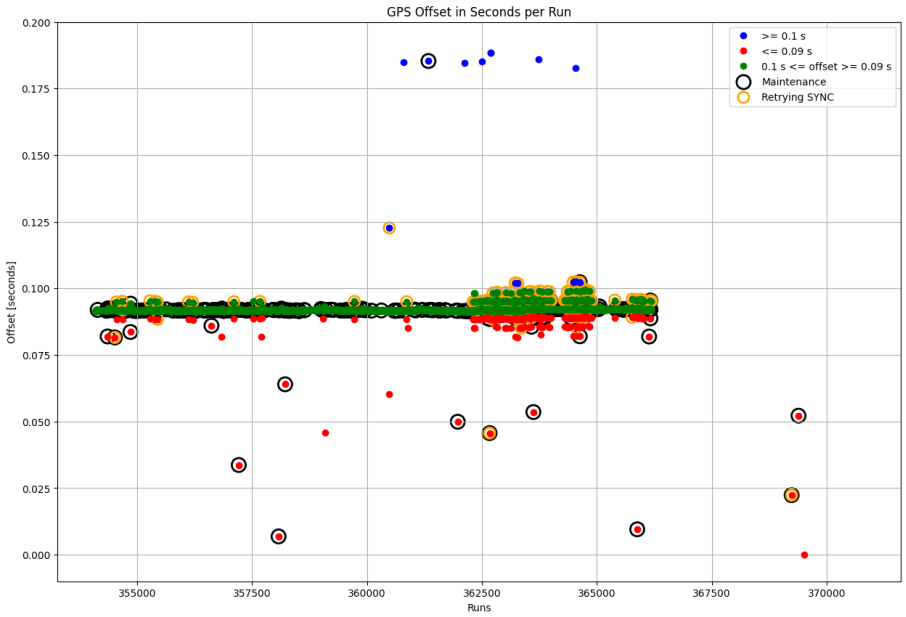


(a) GPS Offset

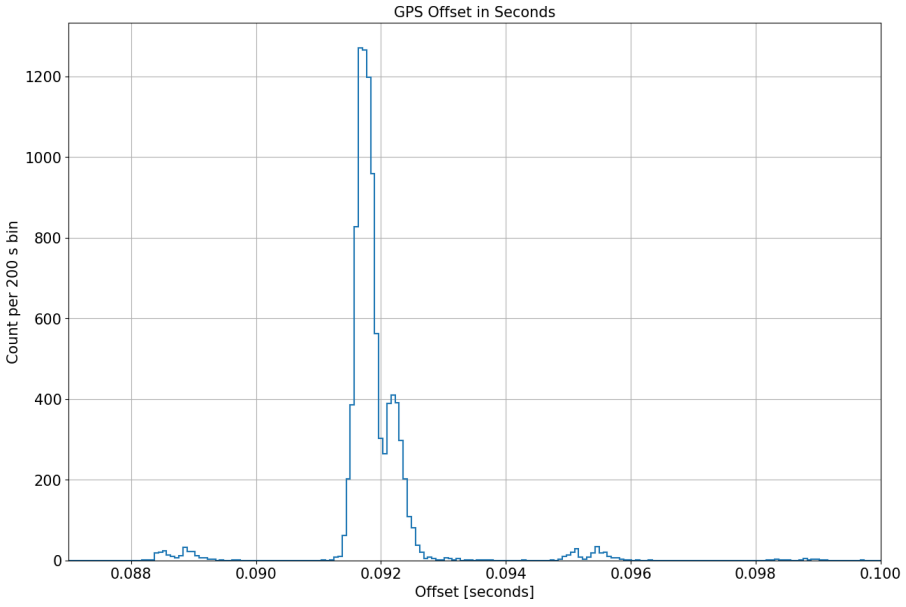


(b) GPS Offset Histogram

Figure 3.25: Plots of the GPS offset in the PPO phase. Scatter plot version (left) and histogram version (right) depicting nominal offset of ∼0.092 ms.



(a) GPS Offset



(b) GPS Offset Histogram

Figure 3.26: Plots of the GPS offset in the bisMSB phase. Scatter plot version (left) and histogram version (right) depicting nominal offset of ∼0.092 ms.

The detector operated with a nearly constant absolute timing offset of approximately 90 ms throughout the PPO and bis-MSB phases. Most runs cluster tightly around this value, indicating stable

detector timing despite the absence of continuous GPS synchronization.

The larger excursions visible correspond to missed synchronization pulses. When a scheduled SYNC pulse is not successfully received, the detector continues operating from its local clock until synchronization is re-established. Once a subsequent SYNC pulse is received, the measured offset returns to its nominal value.

Run	**Number of Points**	**Drift [seconds/hr]**
374856	14	0.09425
374857	44	0.03940
374858	6	0.09419
374859	43	0.09417

Table 3.2: Table of the bis-MSB run, number of data points with GPS timing, and the offset/drift of the 10 MHz clock relative to the MTC/D clock per hour.

To investigate the stability of the detector clock between synchronization events, a dedicated study was performed during the bis-MSB phase (runs 374856-374859). A monitoring script queried the detector every two to three minutes, recording the MTC clock, GPS clock, and their relative offset. The measured offset increased linearly with time, corresponding to a clock drift of approximately 0.0943 s/hr. A table with the results can be found in Table 3.2. The observed linear behavior, as shown in Figure 3.27, demonstrates that the detector timing remained stable and predictable even when operating from the local oscillator.

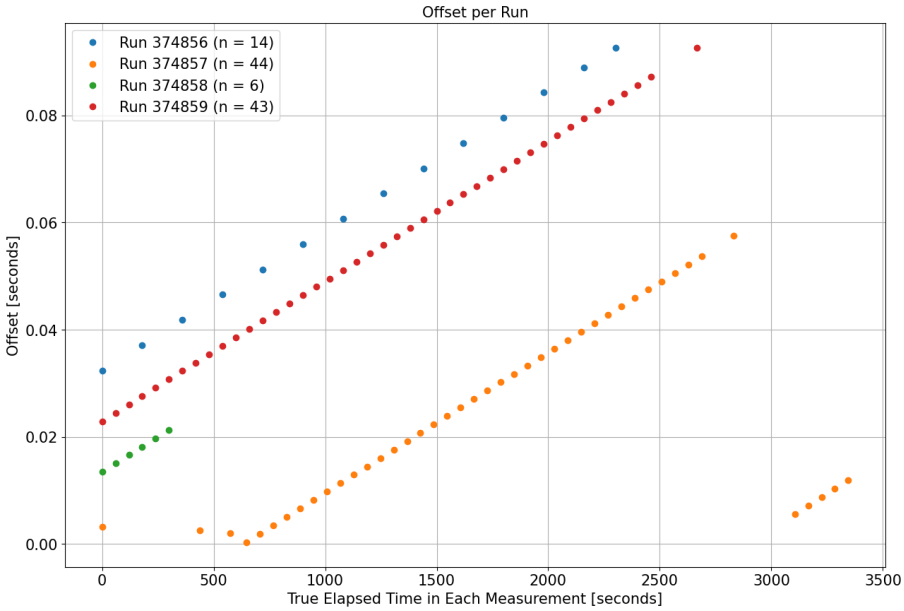


Figure 3.27: Plot of the bis-MSB runs that depict the offset increasing linearly with time.

Event timestamps were reconstructed from the 10 MHz counter, where each clock tick corresponds to 100 ns. For runs in which the detector was operating from the local clock ("NOCLOCK" asserted), a constant correction of +90 ms was applied to the reconstructed timestamps. This value was determined from the GPS timing studies described above and compensates for the measured offset between the detector clock and true GPS time. No correction was applied when the detector was synchronized to the GPS reference.

CHAPTER 4

SIMULATION AND RECONSTRUCTION

"Ticking away
The moments that make up a dull day
You fritter and waste the hours
In an offhand way"
— "Time," Pink Floyd

Monte Carlo (MC) simulations are used to model how particles are produced, propagate, interact with detector materials, and generate detector signals. Simulations are essential because many physical processes cannot be measured directly. In detectors such as SNO+, detailed MC simulations are used to model the production, propagation, and interaction of particles with the detector, as well as the detector response to these interactions. MC simulations provide a connection between the underlying physical processes and experimentally observed quantities, such as PMT hit distributions. By generating large samples of simulated events based on known or hypothesized physical models, MC techniques can be used to predict signal rates, estimate detection efficiencies, characterize backgrounds, optimize event selection criteria, and evaluate sensitivities to potential signals.

The detector does not directly measure the true energy or position of a particle interaction. Reconstruction algorithms are employed to infer properties from interactions, such as energy deposited in the scintillator and the position where the interaction occurred. By comparing simulated truth-level information with reconstructed quantities, MC studies can be used to calibrate reconstruction algorithms, determine energy and position resolutions, evaluate reconstruction biases, and characterize event migration between true and reconstructed parameters. MC simulations and reconstruction are critical for interpreting detector data and for quantifying systematic uncertainties associated with event reconstruction. Finally, calibration data are used to verify that the simulation accurately reproduces the detector response observed in data.

4.1 Event Generation

The primary simulation software used by the SNO+ experiment is RAT (Reactor Analysis Tool), a GEANT4-based [70] simulation and analysis package developed by Stan Seibert and Chris Tunnell [71] for the Braidwood Collaboration.

RAT is written in C++ and uses custom photon tracking and a detailed detector model with full simulation of the PMTs, electronics, and DAQ response. A database known as RATDB stores detector information and configurable parameters, including detector geometry, optical properties, and PMT efficiencies. RATDB contains both static tables, which describe quantities that do not change over time (e.g., PMT locations), and dynamic tables that are updated on a run-by-run basis to reflect the detector state during data taking.

A wide variety of physical processes can be generated in RAT. There are several dedicated event generators created by the SNO+ collaboration to simulate commonly studied events in the detector, such as reactor antineutrinos, solar neutrinos, various radioactive decays, and all of the calibration sources.

Once an event has been generated, GEANT4 handles the propagation and interaction of the primary particles and all daughter particles throughout the detector model. GEANT-4 simulates a complete set of physics processes for interactions of particles in matter over a range of energies. Particle tracking is performed by GEANT4 until an optical photon reaches a PMT, after which the detector response is modeled by RAT.

RAT contains a detailed PMT model that determines whether a photoelectron is produced based on the photon's point of incidence, incident angle, and wavelength. A simulated PMT pulse is generated for each photoelectron. These pulses are then passed to a full simulation of the SNO+ trigger system to determine whether the event would result in a trigger. The pulses for each channel are compared against a discriminator threshold. PMT pulses that pass the discriminator thresholds enter the trigger simulation, where N20, N100, and ESUM trigger signals are generated. This trigger simulation includes many realistic components, such as electronics noise and finite rise-times. The

trigger signals are then summed across the detector and each trigger sum is compared against the corresponding threshold set by the MTC/A+. The trigger simulation also includes important detector effects such as the length of the trigger window and deadtime, set by lockout, and keeps track of the GTID. If the trigger conditions are satisfied, a global trigger (GT) is generated and the event is recorded in the same manner as real detector data. Unlike real data, simulated events contain additional information describing the generated particle properties, such as the generated energy, position, and direction of the simulated particles. This is known as the "MC Truth" information, which describes the true simulated values of these parameters that would not be available in real data.

Events generated in `RAT` are written to custom `ROOT` files using the same event structure as real detector data. This allows the same reconstruction and analysis methods to be applied to both simulation and data. For the analysis presented in this dissertation, flat `ROOT` files known as ntuples are used.

The standard SNO+ simulation framework was used throughout this analysis to generate detector responses and reconstruct simulated events. However, several additions and modifications to the MC framework were required to support the search for neutrinos in temporal coincidence with gravitational wave events. These include the development of a flat-spectrum inverse beta decay event generator for efficient reweighting to arbitrary neutrino emission models, the implementation of supernova-inspired and thermal neutrino spectra, corrections to the neutrino-proton elastic scattering interaction model, and improvements to the simulated retrigger logic. These developments are described in Chapter 6 Subsections 6.4.2 and 6.4.3.

4.2 Event Reconstruction

Event reconstruction involves using the trigger time, the set of PMTs hit (N_{Hit}), the timing of each PMT hit relative to the trigger, and the charge detected by each PMT to infer the physical properties of the particle interaction that produced them. The most important reconstruction quantities in the scintillator phase are the event position, energy, and time. Additional quantities, such as the event time, particle direction, and information related to the underlying interaction process, can also be

reconstructed. The algorithms used to reconstruct these quantities were developed by members of the SNO+ collaboration and are described in more detail in the following subsections.

4.2.1 Position and Time

The position and time of an interaction are reconstructed simultaneously using the "hit time residual," defined as:

$$t_{\text{res}} = t_{\text{hit}} - t_{\text{fit}} - t_{\text{tof}} \tag{4.1}$$

where t_{res} is the hit time residual, t_{hit} is the PMT hit time, t_{fit} is the reconstructed event time, and t_{tof} is the photon time of flight from the reconstructed event position to the hit PMT.

In an idealized scenario (i.e., neglecting optical effects and assuming perfect PMT timing resolution), the hit time residual distribution would match the photon emission time profile when the correct event position and time are chosen. A plot of the scintillator emission time is shown in Figure 4.1.

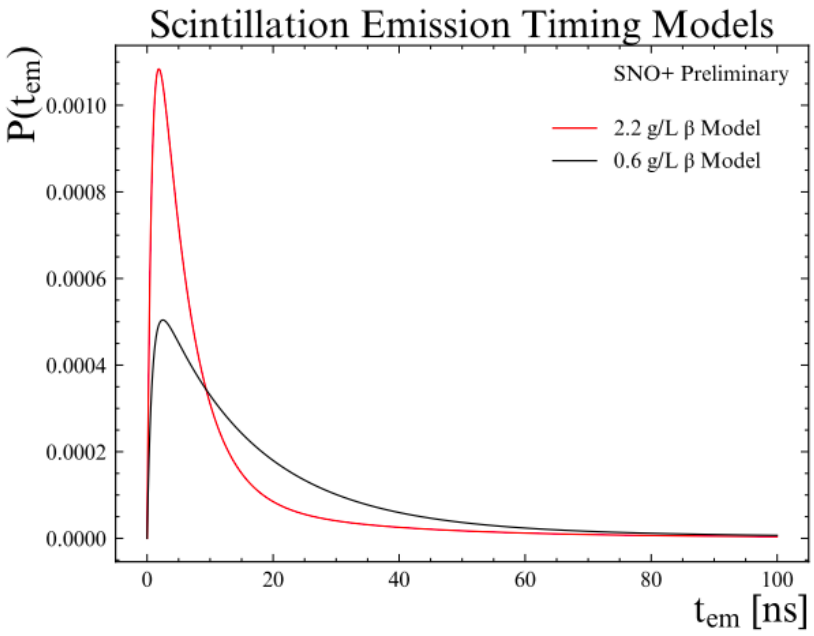


Figure 4.1: Scintillator emission time profile as modeled in RAT. Models for both full fill (2.2 g/L β Model) and partial fill (0.6 g/L β Model) are shown. Adapted from [22].

A likelihood fit is then performed by comparing the observed hit time residual distribution to the

scintillator emission time profile:

$$\log \mathcal{L} = \sum_{i=0}^{N_{\text{Hits}}} \log P\left(t_{\text{res}}^{i}\right) \tag{4.2}$$

where $P(t_{\text{res}}^{i})$ is the probability density associated with the i^{th} hit time residual and N_{Hit} is the total number of PMT hits in the event. The reconstruction algorithm varies the hypothesized event position and time to maximize $\log \mathcal{L}$, yielding the best-fit values for these parameters.

4.2.2 Energy

As discussed in Section 4.2.1, the event position and time are reconstructed using PMT timing information. The event energy is reconstructed independently using the observed PMT occupancy.

As mentioned in Chapter 3, scintillation light is emitted isotropically and the number of detected photoelectrons (p.e.) is roughly linear with energy. For MeV-scale events, the number of scintillation photons produced is such that fewer than one photon is expected to reach a given PMT on average. As a result, N_{Hit} is approximately proportional to the deposited energy. This relationship does not hold for all particle types, as the energy reconstruction algorithm assumes that the event is produced by a single electron. The reconstructed energy of certain particles may differ significantly from their true energies, particularly for heavily ionizing particles such as α particles. Strongly quenched particles, such as α particles, can have reconstructed energies that are approximately an order of magnitude lower than their true energies.

The vast majority of events detected by SNO+ are well modeled by this assumption. A limitation of this approach is that the proportionality begins to break down at higher energies. As the number of photons increases, so too does the likelihood of some PMTs being hit by more than one photon. Events occurring closer to the detector's edge also increase this likelihood as more photons are concentrated onto fewer PMTs. If multiple photons arrive at a PMT within a short time window, the resulting photoelectrons can pile up, causing multiple photons to be recorded as a single hit. As a result, the N_{Hit} of higher energy events can be lower than expectation. In addition, the PMT charge resolution is insufficient to reliably distinguish a single photoelectron from several photoelectrons. The relationship between the PMT hits and energy becomes non-linear as the probability of a PMT

receiving multiple hits increases. An alternative energy estimator that remains linear with energy is therefore required. This is accomplished by dividing the detector into segments of PMTs with approximately equal hit probability. This value is defined as:

$$H = -\sum_{i=1}^{S} N^i_{\mathrm{PMT}} \log\left(1 - \frac{N^i_{\mathrm{Hits}}}{N^i_{\mathrm{PMT}}}\right) \tag{4.3}$$

where S is the number of segments, N^i_{PMT} is the number of PMTs in the segment, and N^i_{Hits} is the number of hit PMTs in the segment.

The segmentation groups PMTs with similar hit probabilities, allowing the average occupancy of each segment to be estimated. The measured occupancy is then converted into the average number of photoelectrons per channel before being scaled by the number of PMTs in the segment, yielding the approximately linear H parameter. Figure 4.2 depicts the number of triggered PMTs ($\mathrm{N_{Hit}}$) as a function of energy for simulated electrons in the SNO+ detector. As the event energy increases, the probability of multiple photons striking the same PMT also increases, leading to deviations from linearity in $\mathrm{N_{Hit}}$.

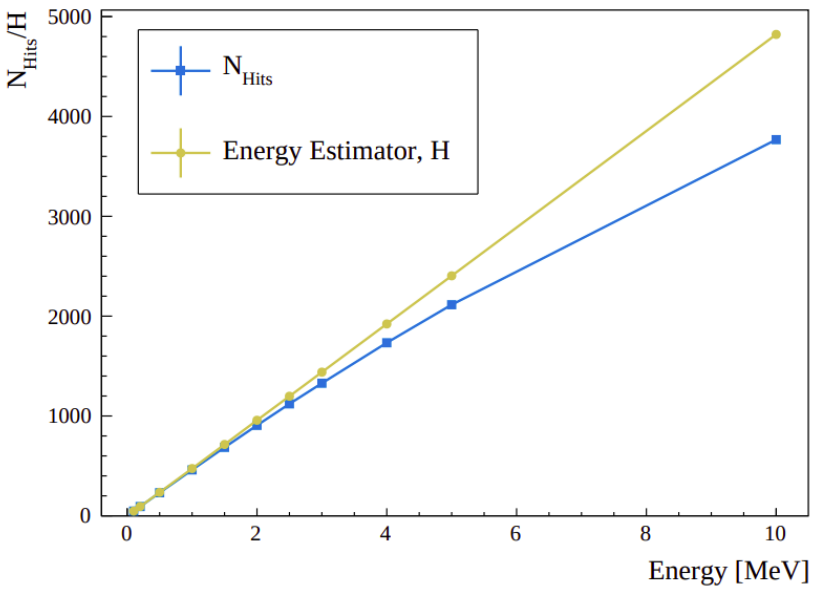


Figure 4.2: The number of triggered PMTs (N_{Hit}) as a function of energy (blue) for electrons simulated at the center of the detector. At higher energies, the probability of more than one hit increases, and so too does the departure from linearity. A linear energy estimator H is depicted in orange. Adapted from [23].

The H parameter is an estimate of the number of detected p.e., which is proportional to energy. The constant of proportionality is determined using simulation and validated with calibration data. One factor that affects this proportionality is the position dependence of the detector response. For example, optical effects such as absorption and scattering depend on the path length traveled by the photons. In addition, total internal reflection can occur for events near the AV boundary, and the PMT detection efficiency depends on the angle of incidence of the photon. These effects are modeled in simulation, and a correction is derived as a function of the reconstructed radius r and polar angle θ [72].

4.2.3 Direction

In addition to scintillation light, Cherenkov light is also produced. Because scintillation light is emitted isotropically, it carries little information about the direction of the originating particle. Cherenkov light, however, is emitted at a characteristic angle relative to the particle's direction of travel and therefore retains directional information.

In the SNO+ water phase, only Cherenkov light is emitted. As a result, directional reconstruction is relatively straightforward. In the scintillator phase, however, the amount of scintillation light is orders of magnitude more intense than Cherenkov light. Recovering directional information therefore requires methods capable of separating the Cherenkov and scintillation light components. SNO+ is the first large-scale liquid scintillator experiment to demonstrate event-by-event direction reconstruction [73]. Directional reconstruction is not used in the analysis presented in this dissertation.

CHAPTER 5

GRAVITATIONAL WAVES

"Time, why you punish me?
Like a wave crashing into the shore
You wash away my dreams
Time, why you walk away?
Like a friend with somewhere to go
You left me crying"
— "Time," Hootie & the Blowfish

On September 14, 2015, the Laser Interferometer Gravitational-wave Observatory (LIGO) detectors made the first direct detection of gravitational waves created by the merger of two black holes approximately 410 Mpc (1.3 billion light years) from Earth [25]. This discovery ended a decades-long effort to directly detect gravitational waves and provided the first direct confirmation of a key prediction of Albert Einstein's theory of general relativity [74], proposed a century earlier. It also marked the beginning of the field of gravitational wave astronomy. The subsequent observation of GW170817 in 2017 [24] established gravitational wave multi-messenger astronomy through the combined detection of gravitational waves and electromagnetic radiation from a binary neutron star merger.

Because this dissertation searches for neutrinos in temporal coincidence with gravitational wave events, the sections most relevant to the present work are Section 5.7, which discusses the physical mechanisms that may produce neutrinos in compact binary mergers, and Section 5.8, which motivates searches for MeV neutrinos from gravitational wave sources.

The remainder of this chapter provides a brief history of gravitational waves, describing how they are generated and detected, and discussing the astrophysical sources that produce perturbations in spacetime. Further details on gravitational wave detector technology can be found in references [75–81], while introductions to general relativity are available in references [82–84].

5.1 A Brief History of Gravitational Waves

The history of gravitational waves (GWs), much like that of the neutrino, begins not with the waves themselves, but with the development of classical electromagnetism and relativity. In 1864, James Clerk Maxwell demonstrated that electricity and magnetism (E&M) could be unified into a single theory that predicted the existence of electromagnetic (EM) waves propagating at the speed of light [85]. Inspired by this analogy, Oliver Heaviside formulated a gravitational counterpart to Maxwell's equations in 1893 and showed that they likewise produce wave-like solutions propagating at a finite speed [86]. Although this description was not the modern theory of gravity, it represented one of the earliest theoretical treatments of GWs. The modern description emerged in 1915 when Albert Einstein published the theory of general relativity (GR) [74], in which gravity is interpreted as the curvature of spacetime.

One of the first indirect pieces of evidence for GWs came in 1974 with the discovery of the first binary pulsar system known as PSR B1913+16 by Russell Hulse and Joseph Taylor Jr. Measurements of the orbital decay of this system showed excellent agreement with the energy loss expected from GW emission predicted by GR [87]. This result provided strong indirect evidence for the existence of gravitational radiation and earned Hulse and Taylor the 1993 Nobel Prize in Physics [88].

The first direct detection of GWs occurred on September 14, 2015, when the Advanced LIGO detectors observed GW150914, a signal originating from the merger of two stellar mass black holes approximately 410 Mpc (1.3 billion light years) from Earth [89].

5.2 Gravitational Wave Detectors

Although resonant-mass detectors are not the focus of this dissertation, the first experimental GW detectors were resonant-mass detectors known as Weber bars [90] in the mid-to-late 1900s. The Weber bar utilized large cylindrical metal alloy bars held under vacuum. When a GW passes through the detector, the bar is excited near its resonant frequency, producing a small mechanical vibration that can be measured by sensitive transducers. Several second-generation resonant-mass detectors were subsequently constructed and operated before the development of large-scale laser

interferometers.

The first generation of laser interferometric GW detectors began operation during the 1990s, including TAMA300 in Japan [91] and GEO600 in Germany [92]. GEO600, while large at the time, has two 600 m long arms of which the light traverses each arm twice giving an effective optical path length of approximately 1200 m. GEO600 is able to detect GWs with a frequency range between 50 Hz and 1.5 kHz. The technologies developed and tested by GEO600 and TAMA300 contributed significantly to the design and operation of later large-scale interferometers, including LIGO, Virgo, and KAGRA.

Detecting GWs requires measuring extremely small transverse distortions of spacetime. Because GWs interact extremely weakly with matter, these distortions are extraordinarily small. Typical astrophysical signals reaching Earth produce strains of order 10^{-21}. The dimensionless strain h represents the fractional change in length produced by a passing GW. The following subsections will briefly detail the main GW detectors in this analysis followed by how they detect perturbations in spacetime.

5.2.1 LIGO

LIGO is the largest and most sensitive GW observatory currently in operation. The observatory consists of two interferometers: LIGO-H located in Hanford, Washington and LIGO-L in Livingston, Louisiana. Each LIGO interferometer consists of two perpendicular 4 km arms, along which the laser beam is split and propagated. LIGO consists of two detectors for three reasons: local vibrations, GW travel time, and source localization.

Local Vibrations

LIGO and other GW detectors are sensitive to extremely small vibrations originating from both natural and anthropogenic sources. Many environmental disturbances can mimic or obscure a GW signal. These include earthquakes, wind, traffic, agricultural activity, low-flying aircraft, lightning, and numerous other environmental disturbances. LIGO-H and LIGO-L are located approximately 3000 km from each other. If they were close, they would sense the same vibrations at essentially

the same time. This would make it difficult to distinguish a GW signal from background/noise. Due to the separation, each detector experiences unique local vibrations. Requiring coincident signals in multiple detectors greatly reduces the probability that a candidate event is caused by local environmental noise.

GW Time Delay

GWs travel at the speed of light. Since LIGO-H and LIGO-L are 3000 km apart, the maximum possible arrival time difference that can elapse between a GW's arrival is approximately 10 ms. This allows for the veto of any similar signal that appears in both detectors more than 10 ms apart since it could not have been caused by a passing GW.

Localization

Placing the two detectors far apart also serves to aid in localizing the source of the GW on the sky. At least three detectors are needed to triangulate a signal, but two can still narrow-down the region of sky containing the source of the signal. Each detector provides independent measurements of the signal arrival time, amplitude, and phase. These measurements are combined to reconstruct the sky position of the source. This skymap is shared with electromagnetic astronomers to perform optical follow up. Additional detectors improve source localization by providing more independent measurements of the arrival time and waveform. The importance of a global detector network was demonstrated by GW170817. LIGO and Virgo collaborated during the second observing catalog and simultaneously detected the first GW (GW170817) from binary neutron stars in August 2017 [24].

For GW170817, LIGO's two detectors and the Virgo detector in Italy were in operation. Simultaneously, the Fermi Gamma-ray Burst Monitor (GBM) and the INTEGRAL satellite detected a coincident short gamma-ray burst. The localization information from each detector was combined to produce a sky map identifying the probable location of the source. This skymap is shown in Figure 5.1. This figure depicts GW170817 source localizations by LIGO alone in the long green band and LIGO + Virgo in the smaller dark green band. The addition of Virgo dramatically reduced the localization region. The light blue band is the time delay between Fermi and INTEGRAL

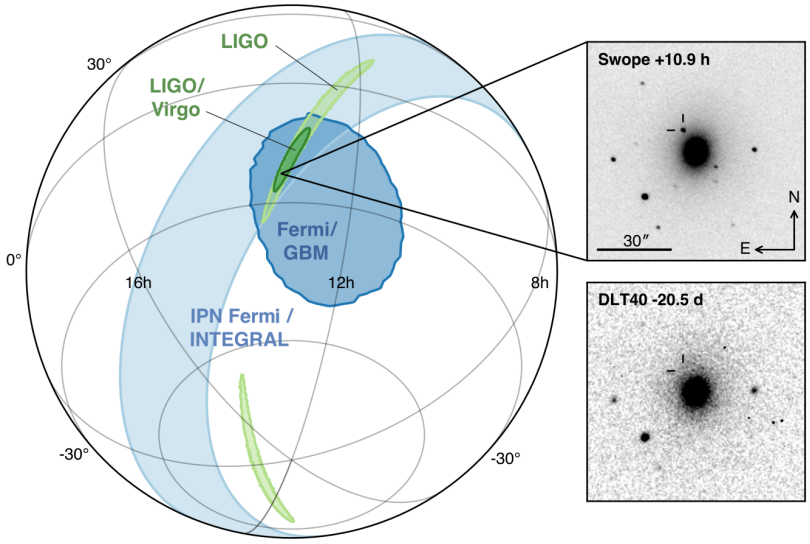


Figure 5.1: A skymap depicting GW170817 source localizations. Adapted from [24]

gamma-ray observatories. The dark blue band is the Fermi-GBM localization. The inset shows the source location in host galaxy NGC 4993. The top image is 10.9 hr after the merger and the bottom is 20.5 days prior to the merger [24].

LIGO Phases

LIGO has done a phased approach from its conception to present day. Initial LIGO operated between 2002 and 2010 [75]. No GWs were detected during this phase. Following Initial LIGO, the detectors underwent a series of upgrades known as Enhanced LIGO, which began after 2010 [93]. Again, no GWs were detected. Another multi-year shutdown occurred during which the detectors were replaced by the improved Advanced LIGO [76]. These upgrades culminated in the first direct detection of gravitational waves on September 14, 2015 [25].

5.2.2 Virgo

The Virgo project was conceived to provide an additional large-scale interferometer capable of operating simultaneously with LIGO, thereby improving detection confidence and source localization. Construction of Virgo began in the late 1990s near Pisa, Italy. The first observations began in 2007. Virgo, like LIGO, underwent upgrades/phases from the initial stage [78] to Advanced Virgo [79]. The upgrades largely targeted the improvement in detection capabilities and occurred from 2009

and completed in 2017.

Advanced Virgo joined the two Advanced LIGO detectors during the O2 observing run (described in Subsection 5.3) in 2017. Virgo and LIGO observed GWs produced by the merger of a binary system of black holes on August 14, 2017. Three days later, they observed the first GWs produced by the merger of a binary system of neutron stars for which a precise sky localization was obtained [24]. The addition of Virgo substantially improved the localization of GW170817, enabling rapid electromagnetic follow-up observations. This event marked the beginning of GW multi-messenger astronomy.

5.2.3 KAGRA

The Japanese Kamioka Gravitational Wave Detector (KAGRA) is a 3 km laser interferometer located underground in the Kamioka mine in Japan. Unlike LIGO and Virgo, KAGRA operates in an underground environment to reduce seismic noise and employs cryogenically cooled test masses to reduce thermal noise. KAGRA joined the global detector network during the O3 observing run (described in Subsection 5.3) and has continued to improve its sensitivity through ongoing commissioning and detector upgrades.

KAGRA is the first large-scale GW detector to combine underground operation with cryogenic test masses [81].

5.2.4 Laser Interferometry

The GW detectors described in Section 5.2 are based on the Michelson interferometer design. The Michelson interferometer was originally developed by Albert Michelson and later used with Edward Morley for their famous 1887 experiment, which attempted to measure the Earth's motion through the hypothetical luminiferous aether. Modern GW detectors employ a modified Michelson interferometer design capable of measuring extremely small changes in distance produced by passing GWs.

Figure 5.2 is a simplified schematic of an Advanced LIGO detector. A GW propagating perpendicular to the detector plane produces alternating stretching and compression of the two 4 km long

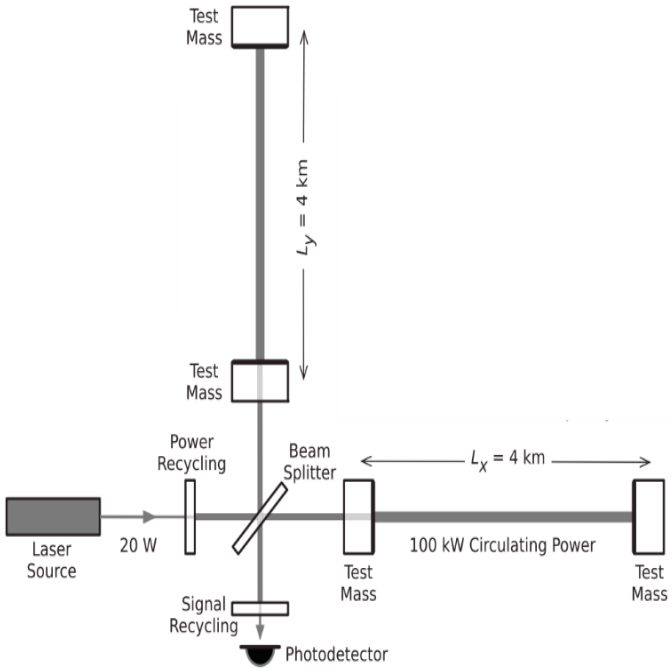


Figure 5.2: Simplified schematic of an Advanced LIGO detector. Adapted from [25].

arms. For a linearly polarized GW aligned with the detector arms, one arm lengthens while the other shortens. Half a cycle later, the effect reverses and the previously stretched arm contracts while the other expands.

A simplified description of the interferometer operation is as follows. A high-power laser beam is directed onto a 50/50 beamsplitter, which divides the light into two perpendicular paths. The beams travel down vacuum arms and reflect from suspended test masses (e.g., mirrors as shown in Figure 5.3) located at the ends of the interferometer. The reflected beams recombine at the beamsplitter and are directed toward a photodetector.

Under normal operating conditions, the arm lengths are adjusted so that the returning laser beams interfere destructively at the photodetector, producing a nearly zero output signal. When a GW passes through the detector, the differential arm length changes slightly. The two beams accumulate different optical phases while traversing the interferometer. Upon recombination, the destructive interference is no longer perfect, resulting in a measurable signal at the photodetector.



Figure 5.3: LIGO 40 kg test mass suspended from an upper reaction mass by four fused-silica fibers. Adapted from [26].

The interferometers measure the dimensionless quantity known as GW strain:

$$h = \frac{\Delta L}{L} \tag{5.1}$$

where L is the arm length and ΔL is the change in length produced by the GW. For the Advanced LIGO detectors, $L = 4$ km and typical astrophysical signals have strains of order

$$h \sim 10^{-21} \tag{5.2}$$

This corresponds to a differential arm-length change of approximately

$$\Delta L \sim hL \sim 4 \times 10^{-18} \text{ m} \tag{5.3}$$

which is approximately one-thousandth of the diameter of a proton. Measuring such extraordinarily small displacements represents one of the most challenging experimental achievements in modern

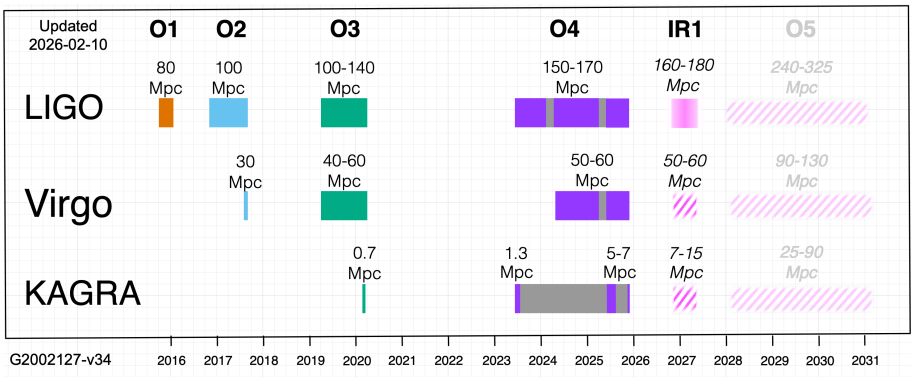


Figure 5.4: LVK Observing Timeline. Adapted from [27]

physics.

To increase sensitivity, Advanced LIGO does not use a simple Michelson interferometer. Instead, Fabry–Perot optical cavities are placed within each arm. These cavities cause the laser light to bounce between the mirrors many times before returning to the beamsplitter, increasing the effective optical path length from 4 km to several hundred kilometers. Additional optical systems, including the power-recycling and signal-recycling cavities, further enhance detector sensitivity by increasing the circulating laser power and shaping the interferometer response to GWs.

During the O4 observing run, the Advanced LIGO detectors were sensitive to GWs in the frequency range from approximately 10 Hz to 5 kHz. This frequency range encompasses many of the expected signals from compact binary mergers, including binary black hole and binary neutron star systems [77]. The binary neutron star detection range during O4 was approximately 150-170 Mpc for each LIGO detector.

5.3 Observing Catalogs

The Advanced LIGO, Advanced Virgo, and KAGRA detectors operate in discrete observing runs separated by commissioning periods and detector upgrades. Figure 5.4 depicts the observing catalogs labeled O1-O5 from 2015 onward. Since the first observing run (O1) in 2015, continual detector upgrades have substantially improved the sensitivities of the interferometers, leading to a dramatic increase in the number of detected GW events.

O1: September 12, 2015 to January 19, 2016

The first Advanced LIGO observing run produced the first direct detection of GWs, GW150914 [25], followed by two additional binary black hole merger candidates, bringing the total number of candidate events in O1 to three, one of which was classified as a low-significance trigger.

O2: November 30, 2016 to August 25, 2017

The second observing run included participation from the Virgo detector and culminated in the landmark detection of GW170817 [24], the first observed binary neutron star merger and the first GW event with an identified electromagnetic counterpart. Alongside this discovery, seven binary black hole merger candidates were also detected, including the most massive and most distant binary black hole merger observed during O2 [94].

O3: April 1, 2019 to March 27, 2020

The third observing run benefited from significant detector upgrades and produced a rapid increase in the number of GW detections (56 total candidates), establishing compact binary mergers as a common astrophysical phenomenon. O3 also marked the first observing run in which all three compact binary merger classes were observed: binary black hole, binary neutron star, and neutron star-black hole mergers.

O4: May 24, 2023 to November 18, 2025

The O4 observing run provides the GW catalog used in this dissertation. O4 began on May 24, 2023 and concluded on November 18, 2025. At the time of writing, the LIGO-Virgo-KAGRA (LVK) collaboration has reported 302 candidate GW events from O4, making it the longest and most sensitive GW observing catalog to date [77].

O4 was divided into three sub-observing runs (O4a, O4b, and O4c) to accommodate detector commissioning, maintenance, and upgrades throughout the observing campaign. LIGO alone observed in O4a (May 24, 2023 to January 16, 2024). KAGRA participated during the first four weeks of O4a before returning to commissioning activities. Shortly afterward, the Noto earthquake on January 1, 2024, caused additional interruptions to KAGRA operations. A commissioning break followed

the completion of O4a. O4b (April 10, 2024 to January 28, 2025) followed O4a with Virgo joining the observing run. KAGRA was offline due to earthquake damage during this sub-catalog. O4c began immediately after O4b (January 28, 2025) and continued until November 18, 2025 with a break from April 1, 2025 to June 11, 2025. KAGRA participated intermittently during O4c after recovering from earthquake-related damage.

5.4 Open Data

Two primary resources provide information on GW candidates: the Gravitational-wave Candidate Event Database (GraceDB) [95] and the Gravitational Wave Open Science Center (GWOSC) [96].

GraceDB is a low-latency system that processes detector data in near real time and rapidly distributes candidate alerts to the broader astronomical community. As a result, it contains candidate events from O4a, O4b, and O4c.

GWOSC serves as the official archival data-release platform for the LVK collaboration. Events appearing in GWOSC have undergone additional offline analyses and validation procedures prior to inclusion in a Gravitational-Wave Transient Catalog (GWTC). At the time of writing, only O4a has been officially released through GWOSC. Consequently, GWOSC lists 129 O4a candidates, whereas GraceDB contains 81 low-latency O4a candidates.

Candidate events included in GWOSC must satisfy additional quality requirements, including an astrophysical probability of $p_{\text{astro}} \geq 0.5$, and must successfully pass event validation procedures [97].

5.5 Gravitational Wave Sources

Current GW searches are generally divided into four source categories. These four categories are depicted in Figure 5.5 and include compact binary coalescence (or compact binary mergers), continuous waves, bursts, and stochastic backgrounds. These categories are described in more detail in the following subsections.

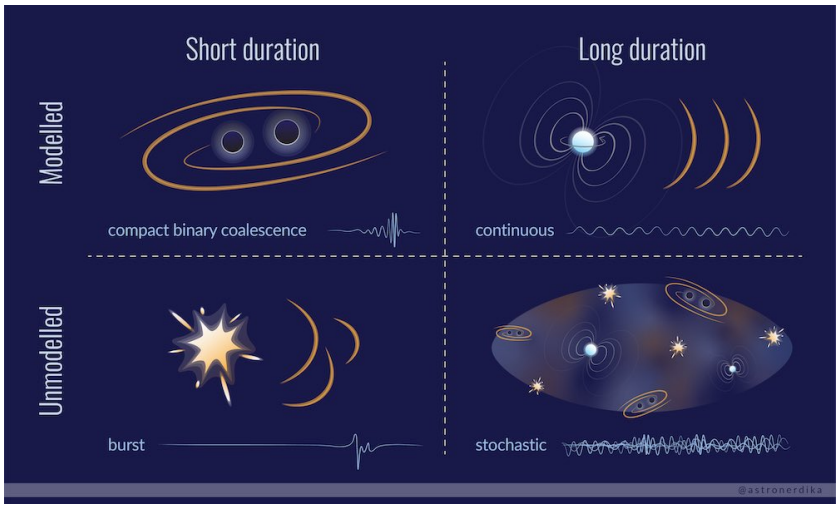


Figure 5.5: Diagram of the four types of gravitational wave producers. Adapted from [28].

5.5.1 Compact Binary Mergers

Compact binary coalescences (CBCs) occur when two compact objects lose orbital energy through the emission of GWs and eventually merge into a single remnant object. Unlike the other GW source categories, the waveforms from CBCs can be accurately modeled using analytical and numerical relativity, making matched-filter searches particularly effective.

The evolution of a compact binary merger is typically divided into three stages: inspiral, merger, and ringdown. During the inspiral phase, GW emission removes orbital energy and angular momentum, causing the orbital separation to decrease. As the objects approach one another, the GW frequency and amplitude increase until the merger occurs. The remnant object subsequently settles into a stable configuration through the emission of GWs during the ringdown phase. Figure 5.6 depicts this inspiral, merger, ringdown scenario and also illustrates the evolution of the GW strain amplitude (discussed in Section 5.2.4).

The following source mergers fall under this category and are briefly described in the bold section below. The neutrino production of each is described in Subsection 5.7.

Binary Black Hole

Binary black hole (BBH) mergers are the most common GW sources detected to date. They produce

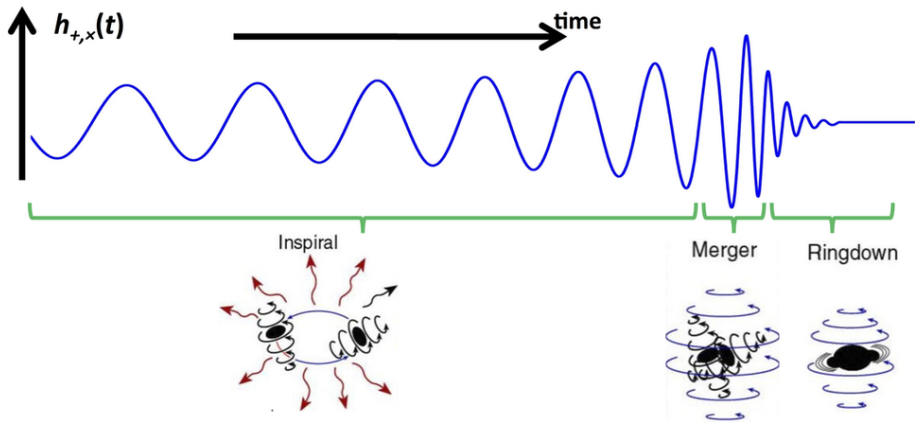


Figure 5.6: Diagram of the merger cycle from inspiral to merger to ringdown. Adapted from [29].

the strongest signals and can be detected from the largest distances from Earth. The first direct detection of a BBH merger is GW150914 in 2015 [25].

Figure 5.6 illustrates the evolution of a BBH merger through the inspiral, merger, and ringdown phases. As the two BHs orbit one another, GW emission carries away orbital energy and angular momentum, causing the orbital separation to decrease and the orbital frequency to increase. The merger produces the peak GW amplitude, after which the newly formed BH settles into a stable configuration through the emission of GWs during the ringdown phase. The production of neutrinos from BBH mergers is discussed in Section 5.7.3.

Binary Neutron Star Mergers

Binary neutron star (BNS) mergers are a rare type of merger detected by GW detectors. The first direct detection of a binary neutron star (BNS) merger is GW170817 [24], which has optical counterparts providing more credence to the BNS classification.

A BNS merger follows a similar structure as a binary black hole merger in Figure 5.6. As the orbit of the BNS system shrinks, the GW luminosity increases, which accelerates the inspiral. Unlike BBH mergers, tidal interactions and the finite size of NS significantly influence the late inspiral and merger. The ringdown phase may describe the remnant as a hypermassive NS that later collapses to a BH or, depending on the total mass of the system, a BH formed promptly after merger. The

production of neutrinos from BNS mergers is discussed in Section 5.7.1.

Neutron Star–Black Hole Mergers

Neutron star-black hole (NS-BH) mergers are rarer than BNS and BBH mergers. NS-BH mergers evolve through the same inspiral, merger, and ringdown phases as other compact binaries. However, the unequal masses and tidal disruption of the NS can produce significantly different observational signatures. The unequal component masses lead to inspiral dynamics that differ from those of equal-mass compact binaries. Whether the NS is tidally disrupted before reaching the BH depends on the masses, spins, and NS equation of state (EOS). If tidal disruption occurs outside the BH event horizon, an accretion disk may form, potentially powering electromagnetic and neutrino emission. Otherwise, the NS is swallowed directly by the BH with little matter remaining outside the event horizon. Following the merger, the remnant BH emits a rapidly damped ringdown signal as it settles into a stable Kerr BH. The production of neutrinos from NS-BH mergers is discussed in Section 5.7.2.

5.5.2 Continuous Wave Sources

Continuous-wave sources include rapidly rotating NS with non-axisymmetric mass distributions, such as asymmetric pulsars. These sources emit nearly monochromatic GWs over long timescales, producing signals that are much weaker than CBCs but persist for months to years.

5.5.3 Burst Sources

The third source category refers to short-duration transient events that are not well modeled. Examples include core-collapse supernovae (CCSN), magnetar flares [98], pulsar glitches [99], cosmic-string cusps [100], and other unknown transient phenomena.

5.5.4 Stochastic Background

The final GW source category is the stochastic GW background (SGWB), which consists of the superposition of many unresolved GW sources, analogous to the cosmic microwave background (CMB) or diffuse supernova background (DSNB) in that it permeates the Universe. Potential contributions include unresolved CBCs, rapidly rotating NSs, cosmic strings, phase transitions in

the early Universe, inflationary GWs, and other cosmological or astrophysical populations.

5.6 Multi-Messenger Astronomy

For centuries, astronomy relied almost exclusively on electromagnetic observations across the radio, infrared, optical, ultraviolet, X-ray, and gamma-ray bands. The addition of neutrinos, GWs, and cosmic rays has transformed this traditional picture into multi-messenger astronomy, where information from multiple types of astrophysical messengers is combined to study the same source. Each messenger probes different physical processes within an astrophysical object. Electromagnetic radiation primarily reveals the outer, optically visible regions, neutrinos probe dense interiors where photons cannot readily escape, and GWs directly trace the bulk motion of massive objects and the dynamics of spacetime itself.

Although SN1987A marked the first observation of an astrophysical source using both neutrinos and electromagnetic radiation [48], GW170817 was the first GW event to be observed through multiple messengers [24]. The BNS merger occurred at a distance of approximately 40^{+8}_{-14} Mpc and was, at the time of its discovery, the closest and best-localized GW source. Approximately 1.7 s after the merger, the Fermi Gamma-ray Burst Monitor (GBM) detected the short gamma-ray burst GRB 170817A, providing the first direct observational connection between BNS mergers and short gamma-ray bursts (SGRBs). Follow-up observations across the electromagnetic spectrum subsequently identified the kilonova, a remnant of an explosive BNS or NS-BH event, AT2017gfo [101] in the same host galaxy, confirming the NS merger interpretation.

The combined GW and electromagnetic observations of GW170817 provided unprecedented insight into CBCs, the production of heavy elements through the r-process, the origin of SGRBs, and the expansion rate of the Universe. This event demonstrated the power of multi-messenger astronomy and established the scientific motivation for coordinated searches for additional messengers, including neutrinos in temporal coincidence with GW events.

5.7 Neutrinos from Gravitational Wave Mergers

The detection of GW170817 demonstrated that GWs can be observed in coincidence with electromagnetic emission from CBCs. At the time of writing, however, no neutrino signal has been conclusively associated with a GW event. Searches for such signals are well motivated since CBCs involving NS are expected to produce hot, dense, neutron-rich matter in which neutrinos are generated efficiently. This section describes the physical mechanisms that can produce neutrinos in CBCs, with particular emphasis on binary neutron star (BNS), neutron star-black hole (NS-BH), and binary black hole (BBH) mergers.

5.7.1 BNS Neutrinos

BNS mergers involve the coalescence of two compact objects composed of extremely dense, neutron-rich matter. During the merger, tidal disruption, shock heating, and compression produce matter with temperatures of order $T \sim$ 10-100 MeV. Under these conditions, weak interactions and thermal processes produce large fluxes of neutrinos and antineutrinos. These neutrinos play an important role in cooling the merger remnant, modifying the electron fraction of the ejecta, and influencing the r-process nucleosynthesis that produces the heavy nuclei whose radioactive decay powers the associated kilonova. Depending on the total binary mass, mass ratio, and NS EOS, the merger remnant may be a promptly formed BH, a hypermassive NS, a supramassive NS, or, in some cases, a stable NS [102]. The dominant electron-flavor neutrino production channels are charged-current (CC) beta processes involving free nucleons, while additional thermal processes produce neutrino-antineutrino pairs of all flavors. Table 5.1 summarizes the principal neutrino production mechanisms expected in the hot, dense matter created during a binary neutron star merger.

Process	Neutrino production channel
Electron capture	$e^- + p \to n + \nu_e$
Positron capture	$e^+ + n \to p + \bar{\nu}_e$
Pair annihilation	$e^- + e^+ \to \nu_\ell + \bar{\nu}_\ell$
Nucleon-nucleon bremsstrahlung	$N + N \to N + N + \nu_\ell + \bar{\nu}_\ell$
Electron-nucleus bremsstrahlung	$e^- + (A, Z) \to e^- + (A, Z) + \nu_\ell + \bar{\nu}_\ell$

Table 5.1: Representative neutrino production mechanisms in hot, dense neutron-rich matter relevant to binary neutron star mergers. Here $\ell = e, \mu, \tau$ and N denotes a nucleon.

Electron capture on protons produces electron neutrinos, while positron capture on neutrons produces electron antineutrinos. Because the merger environment is neutron rich, the relative rates of these processes are sensitive to the local temperature, density, and electron fraction.

Additional thermal processes can produce neutrino-antineutrino pairs of all flavors. These include electron-positron pair annihilation,

$$e^- + e^+ \rightarrow \nu_\ell + \bar{\nu}_\ell \tag{5.4}$$

and nucleon-nucleon bremsstrahlung,

$$N + N \rightarrow N + N + \nu_\ell + \bar{\nu}_\ell \tag{5.5}$$

where $\ell = e, \mu, \tau$ and N denotes a nucleon. Electron-positron pair annihilation is expected to dominate in the hot, low-density regions above the merger remnant and accretion disk, whereas bremsstrahlung becomes increasingly important in the dense nuclear matter of the remnant itself. Together, these processes produce an intense burst of MeV-scale neutrinos over timescales of milliseconds to seconds following the merger.

The neutrino emission from a BNS merger depends strongly on the fate of the remnant. If the merger promptly forms a BH, the neutrino luminosity is expected to be shorter lived and dominated by emission from any remaining accretion disk. If a hypermassive or supramassive NS survives for a longer period before collapse, neutrino emission can persist for longer and may be enhanced by continued thermal cooling of the remnant. In either case, the emitted neutrinos affect the composition of the ejecta by changing the neutron-to-proton ratio, thereby influencing the production of heavy elements through the rapid neutron-capture process (r-process).

The electromagnetic counterpart to a BNS merger, known as a kilonova, is powered by the radioactive decay of freshly synthesized heavy nuclei in the neutron-rich ejecta. These radioactive decays also produce neutrinos through the β-decays of the newly synthesized nuclei. However, at the distances of the GW sources considered in this dissertation, this neutrino component is expected to be negligible. Neutrinos do not directly power the kilonova, but they can alter the electron fraction

of the ejecta and therefore affect the final abundance pattern and opacity of the material. For this reason, a coincident detection of MeV neutrinos from a BNS merger would provide information about the remnant, disk, ejecta composition, and weak-interaction physics that cannot be obtained from GW or electromagnetic observations alone.

5.7.2 NS-BH Neutrinos

NS-BH mergers involve many of the same neutrino production mechanisms as BNS mergers. However, unlike BNS mergers, the amount of neutrino emission depends strongly on whether the NS is tidally disrupted before crossing the BH event horizon.

If the NS is swallowed directly by the BH, little matter remains outside the event horizon to produce significant neutrino emission. In this scenario, only a weak or negligible neutrino signal is expected. Conversely, if tidal disruption occurs outside the event horizon, a hot accretion disk forms around the BH. Temperatures within the accretion disk can reach tens of MeV, creating conditions similar to those found in the remnants of BNS mergers.

Under these conditions, neutrinos are produced primarily through CC beta processes involving free nucleons,

$$e^- + p \rightarrow n + \nu_e \tag{5.6}$$

$$e^+ + n \rightarrow p + \bar{\nu}_e \tag{5.7}$$

as well as thermal pair production and nucleon-nucleon bremsstrahlung. These interactions generate an intense burst of MeV neutrinos that efficiently cools the accretion disk by carrying away thermal energy. This process, known as *neutrino cooling*, regulates the temperature and composition of the disk while modifying the neutron-to-proton ratio of the outflowing ejecta.

As in BNS mergers, neutrino irradiation of the ejecta alters the electron fraction and therefore influences the production of heavy elements through r-process nucleosynthesis. If sufficient neutron-rich material is ejected during the merger, the radioactive decay of freshly synthesized r-process nuclei powers the electromagnetic emission from the kilonova. Consequently, the neutrino luminosity

from an NS-BH merger depends primarily on the amount of material remaining outside the BH after merger, which is determined by the binary masses, the BH spin, and the NS EOS. Regardless of the merger dynamics, the final compact remnant is always a BH.

5.7.3 BBH Neutrinos

Unlike BNS and NS-BH mergers, BBH mergers are not generally expected to produce significant neutrino emission. In the standard astrophysical picture, BBH mergers occur in vacuum and contain essentially no baryonic matter. Since neutrino production requires hot, dense matter, there is no established mechanism capable of generating an observable burst of MeV neutrinos during the merger.

Nevertheless, several theoretical models have proposed that BBH mergers could produce neutrinos if they occur within matter-rich environments. These include mergers embedded in active galactic nucleus (AGN) accretion disks, the remnants of massive stellar collapse, or other dense gaseous environments. In such scenarios, gas surrounding the BHs may be shock heated or accreted during the merger, producing temperatures sufficiently high for weak interactions to generate neutrinos. The dominant production mechanisms are expected to be similar to those discussed for BNS and NS-BH mergers, including CC beta processes, electron-positron pair annihilation, and thermal emission from the hot accretion flow.

Although these scenarios remain speculative and are considerably more uncertain than those for BNS or NS-BH mergers, they motivate searches for neutrino counterparts to all classes of CBCs.

5.8 Motivation for the SNO+ Search

The searches performed by Borexino, KamLAND, and Super-Kamiokande demonstrate that large underground neutrino detectors are capable of searching for MeV neutrinos in temporal coincidence with GW events. Although no statistically significant signal has yet been observed, these experiments have placed increasingly stringent upper limits on the neutrino fluence from CBCs, providing valuable constraints on theoretical models.

SNO+ complements these previous searches through its large liquid scintillator target, excellent

radiopurity, low energy threshold, and sensitivity to MeV neutrinos through inverse beta decay and neutrino-proton elastic scattering (among other channels). These characteristics make SNO+ well suited to searches for low-energy neutrinos associated with CBCs.

The analysis presented in Chapter 6 searches for MeV neutrinos in temporal coincidence with GW candidates from the O4 observing run of the LIGO-Virgo-KAGRA collaboration. In the absence of a detected signal, upper limits on the neutrino fluence constrain models of neutrino emission from compact binary mergers. However, the motivation for these searches extends beyond setting increasingly stringent limits. Theoretical predictions for MeV neutrino emission from compact binary mergers remain uncertain, and the emission may be anisotropic or depend strongly on the merger geometry, remnant evolution, and viewing angle. Even a single nearby or favorably oriented event could produce an observable neutrino signal. A coincident detection would provide unique information on the merger environment while simultaneously probing neutrino propagation over cosmological baselines through measurements of time-of-flight delays, wave packet decoherence, and potentially the neutrino mass ordering. Continued searches are therefore well motivated, despite the expected rarity of detectable signals.

CHAPTER 6

A SEARCH FOR NEUTRINOS IN TEMPORAL COINCIDENCE WITH GRAVITATIONAL WAVES IN SNO+

"*Talking about confidence in GPS location data* Is it guaranteed so that
when the guillotine falls, you're going to move your neck at the right time?
I don't know..."
— "On the Absolute Timing of SNO+," Joshua Klein

This chapter presents the first SNO+ search for neutrinos in temporal coincidence with gravitational wave events. No coincident low-energy neutrino signal associated with gravitational wave events has been observed to date. This chapter provides an overview of the datasets, event selection, reconstruction, background estimation, statistical analysis, and resulting constraints on the neutrino fluence associated with compact binary mergers.

6.1 Overview

This analysis targets MeV-scale neutrino emission associated with compact binary mergers detected through gravitational waves (GW). A coincident detection would represent the first observation of MeV-scale neutrinos from compact binary mergers and would provide a new probe of the physical conditions surrounding the merger environment.

Unlike photons, neutrinos escape from dense astrophysical environments with minimal scattering, carrying information from regions that may be optically inaccessible. The relative arrival times of neutrinos and GWs could probe neutrino properties, including constraints on the absolute neutrino mass through propagation-induced time delays over cosmological distances. In addition, detecting MeV neutrinos from compact mergers would provide insight into the thermal evolution of the merger environments, including accretion disk formation, remnant cooling, and energy transport in dense matter.

Since GW candidates are detected at distances of hundreds to thousands of Mpc, an observed

MeV neutrino counterpart would also represent the detection of a particle messenger that has propagated across cosmological distances, providing a unique probe of particle propagation through the intergalactic medium and large-scale gravitational potentials. In the absence of a statistically significant signal, 90% confidence level upper limits are placed on the neutrino fluence at Earth.

Two interaction channels are investigated in this search. The inverse beta decay (IBD) channel,

$$\bar{\nu}_e + p \rightarrow e^+ + n \tag{6.1}$$

provides the most distinctive experimental signature due to the coincidence between the prompt positron signal and delayed neutron capture, and is primarily sensitive to electron antineutrinos. The neutrino-proton elastic scattering (ES) channel,

$$\nu + p \rightarrow \nu + p \tag{6.2}$$

is sensitive to neutrinos of all flavors through the neutral current (NC) interaction and provides complementary sensitivity to the IBD search. This is the first time this channel has been used in such a search, and is made possible by SNO+'s depth and size.

The analysis uses candidate GW events reported during the fourth observing run (O4) of the LIGO-Virgo-KAGRA (LVK) collaboration, spanning May 24, 2023 to November 18, 2025. This observing period overlaps with the scintillator phase of SNO+, specifically the latter portion of the LAB + 2.2 g/L PPO phase, including data taken after the addition of the antioxidant butylated hydroxytoluene (BHT), and the subsequent LAB + 2.2 g/L PPO + 6.5 mg/L BHT + 2.2 mg/L bisMSB phase.

The addition of BHT was introduced to improve the long-term stability of the scintillator by suppressing chemical degradation. Since the addition of BHT did not produce a significant change in the measured scintillator light yield or optical response, the LAB + PPO and LAB + PPO + BHT data are treated as a single detector configuration throughout this analysis. The addition of

bisMSB, however, significantly modifies the optical properties of the scintillator and therefore defines a separate detector phase. Figure 3.3 summarizes the scintillator timeline used in this analysis.

The full LAB + PPO dataset corresponds to 245 days of livetime (0.52 ktonne-years), while the bisMSB dataset corresponds to 453 days (0.97 ktonne-years). Since this analysis only considers data overlapping LVK O4 and satisfying all analysis requirements, the final datasets are reduced to 49 days of LAB + PPO + BHT data and 450 days of bisMSB data.

The search was performed as a blind analysis [103]. GW events from the LVK O4 catalog were first matched to periods of stable SNO+ data taking, and runs containing coincident GWs were removed while the analysis procedure was developed. Event selection criteria, background estimation methods, reconstruction performance studies, and Monte Carlo (MC) simulations were finalized using independent background datasets and dedicated validation studies. Signal MC simulations were used to determine the detection efficiencies for the IBD and neutrino-proton ES channels and to optimize the event selections prior to unblinding. Once the analysis procedure was finalized, the GW-coincident runs were unblinded and the observed event rates were compared with the expected background. In the absence of a statistically significant excess, 90% confidence level upper limits were placed on the neutrino fluence associated with compact binary mergers.

6.2 Data Sets

6.2.1 LIGO-Virgo-KAGRA O4 Catalog

The fourth joint observing run (O4) of the LVK collaboration spanned from May 24, 2023 to November 18, 2025. As described in Chapter 5, Section 5.3, O4 is the longest observing run to date, contains the largest number of GW candidate events, and achieved the highest detector sensitivity to compact binary mergers among LVK observing runs. O4 is divided into three sub-catalogs: O4a, O4b, and O4c. O4a spans May 24, 2023 to January 16, 2024, O4b spans April 10, 2024 to January 28, 2025, and O4c spans January 28, 2025 to November 18, 2025. At the time of this analysis, the public O4 datasets contained 129, 105, and 68 candidate events in O4a, O4b, and O4c, respectively, for a total of 302 candidate GW events [95, 96].

Each candidate event is assigned probabilities describing its most likely astrophysical origin. Rather than assigning a single discrete classification, LVK reports posterior probabilities for each source class based on the reconstructed source properties, including component masses, spins, signal morphology, and astrophysical population models. The class with the highest probability is used throughout this dissertation when referring to the astrophysical origin of a candidate. Candidate events are classified as binary black hole (BBH), binary neutron star (BNS), neutron star–black hole (NS-BH), terrestrial, or unknown. The terrestrial classification indicates that the trigger is most likely produced by instrumental or environmental noise rather than an astrophysical source, while unknown denotes events that cannot be confidently assigned to one of the compact binary classes. No candidates in the O4 public alerts used for this analysis were classified as BNS mergers.

The treatment of terrestrial and unknown candidates was defined prior to unblinding. All GW candidates passing detector selection requirements were retained during the blind search procedure, including events classified by LVK as terrestrial or unknown, because a statistically significant neutrino counterpart could provide independent evidence supporting the astrophysical origin of a low-significance GW candidate. In the absence of a coincident neutrino excess, these candidates are excluded from the final compact binary merger fluence limits.

6.2.2 SNO+ Data Set

As described in Chapter 3, Section 3.2, SNO+ operates in a phased approach. Figure 3.3 provides an overview of the phases and associated timelines. This analysis uses data acquired during the scintillator phase. For the purposes of this analysis, the scintillator data are divided into two detector configurations: a preliminary LAB + 2.2 g/L PPO + 6.5 mg/L BHT configuration (April 2022-July 2023) and an enhanced LAB + 2.2 g/L PPO + 6.5 mg/L BHT + 2.2 mg/L bisMSB configuration (December 2023-present). Figure 6.1 illustrates these detector configurations.

These detector configurations are treated separately because the detector light yield, optical model, and energy response differ significantly between them. In the preliminary scintillator phase, henceforth known as the PPO+BHT phase, the collected scintillation light yield was measured to be approximately 210 clean PMT hits/MeV. The clean hit definition removes contributions from elec-

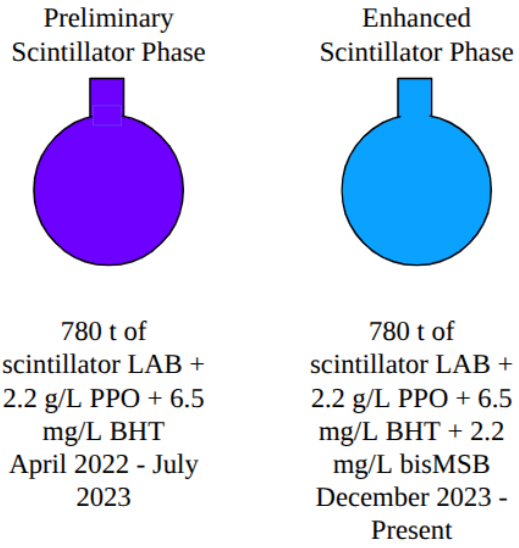


Figure 6.1: An illustration of the SNO+ scintillator phases.

tronic noise and excludes channels that do not satisfy charge and timing calibration requirements. The exact light yield depends on detector conditions, including the number of active PMT channels. The trigger threshold for this dataset was approximately 20 PMT hits, corresponding to about 0.09 MeV, well below the visible energies relevant for the neutrino signals considered in this analysis [104]. In the enhanced scintillator phase, referred to as the bisMSB phase, the light yield was measured to be about 320 PMT hits/MeV [47]. This increase in light yield is due to the addition of bisMSB, a wavelength shifter, which improves the energy resolution.

The PPO+BHT and bisMSB detector configurations are analyzed independently due to their different optical responses. The results from both phases are combined after applying the corresponding detector efficiencies.

6.2.3 Matching GW Candidates with SNO+ Runs

Candidate GW events were matched to periods of stable SNO+ physics data taking using the detector run and run selection databases [105, 106] and the corrected GPS timing described in Section 3.6.

The O4 observing period overlaps the final portion of the PPO detector configuration, the BHT

addition period, the bisMSB loading period, and the final bisMSB detector configuration. The PPO dataset corresponds to runs 300000–310637; however, because O4 began on May 24, 2023, only runs 309448–310637 contribute to this analysis. During the subsequent addition of BHT (runs 310643-311144), the detector optical response remained unchanged. These runs are therefore grouped with the PPO detector configuration throughout this analysis. The bisMSB loading period began during run 350000, with the final detector configuration established at run 354099. Because the detector response evolved continuously during loading, only runs acquired after the final bisMSB concentration was reached are included.

The SNO+ collaboration assigns each physics run a data-quality classification of Gold, Silver, Bronze, or Nickel, with Gold corresponding to the most stringent detector-quality requirements and Nickel the least restrictive. Because this search targets an extremely rare signal and uses event-level quality selections, all four categories are considered, provided the runs satisfy the detector-quality requirements relevant to this analysis.

Because SNO+ is sensitive to low-energy signals, it also records non-physics events arising from electronics, PMTs, and detector operations. Consequently, all data undergo data cleaning followed by run selection before physics analyses are performed.

Data cleaning consists of a series of checks to flag any events that are clearly not physics events, which are run during the processing of recorded data. In particular, data cleaning identifies detector "instrumentals," such as PMT flashers produced by static discharge within a high-voltage PMT, together with other classes of non-physics events. Unwanted physics events can also be flagged, such as muons. Events identified by these criteria are flagged and can be removed or treated separately during physics analyses.

Run-level quantities, including detector status, clock synchronization, PMT coverage, electronics performance, and detector activity, are evaluated automatically. Human activity on deck, detector maintenance, or abnormal operating conditions can also cause runs to be excluded.

Applying the detector availability and data-quality requirements substantially reduces the number

of candidate GW events available for analysis. The dominant losses arise from four sources:

- GW candidates occurring during the bisMSB loading period, for which no stable optics model is available and detector response is not sufficiently well characterized for this analysis
- Runs rejected by the SNO+ run selection criteria or unavailable due to processing failures
- Runs not yet included in the validated processed dataset (after run 371216–July 25, 2025)
- GW candidates for which the required coincidence window is not fully covered by valid SNO+ physics data, including periods when the detector was offline.

Table 6.1 summarizes the reduction from the initial LVK candidate list to the final astrophysical GW sample used in this analysis.

Selection	O4a	O4b	O4c	Total
Initial LVK candidates	129	105	68	302
Remove bisMSB loading phase	−57	—	—	−57
Remove run selection / processing losses	−29	−21	−4	−54
Remove incomplete coincidence windows	−6	−5	−12	−23
Remove post-run 371216 (not processed)	—	—	−25	−25
Final GW sample	37	79	27	143
Remove Terrestrial / Unknown	−14	−2	−1	−17
Final astrophysical GW sample	**23**	**77**	**26**	**126**

Table 6.1: Reduction of the LVK O4 candidate list to the final astrophysical GW sample used for fluence limits. The largest reductions arise from excluding GW candidates during the bisMSB loading period and from detector run selection requirements. The intermediate GW sample contains all candidates passing detector requirements, while the final astrophysical sample excludes terrestrial and unknown classifications.

After detector availability, run selection, and processing requirements are applied, 143 GW candidates remain for the coincidence search. This sample includes 17 candidates classified as terrestrial or unknown by LVK. These candidates are retained during the event search and unblinding procedure, but are excluded from the final astrophysical fluence limit calculation in the absence of a coincident neutrino excess. The final compact binary merger sample used for fluence limits contains

126 GW candidates. These 126 candidates correspond to 123 unique SNO+ runs, since three runs contain more than one GW candidate.

The final sample of 126 GW candidates is larger than those used in previous low-energy neutrino coincidence searches. For comparison, Borexino analyzed 74 GW candidates from O1–O3 [107], KamLAND analyzed 60 candidates from O2–O3 [108], and Super-Kamiokande analyzed 36 candidates from the first half of O3 [109]. The increased number of GW candidates relative to previous searches improves the sensitivity of this analysis by increasing the total exposure to potential neutrino-emitting mergers.

Appendix B contains the list of GW candidates coincident with SNO+ runs.

6.3 Analysis Strategy

The objective of this analysis is to search for neutrinos emitted in coincidence with compact binary mergers detected through GWs. Rather than searching continuously for an excess of neutrino events, the precisely measured GPS trigger times reported by the LVK collaboration are used to define short time windows during which a neutrino signal is expected. Restricting the search to these coincidence windows substantially reduces the expected background while maintaining sensitivity to any prompt neutrino emission associated with the merger.

The analysis is performed as a counting experiment within predefined coincidence windows around each GW trigger time. The number of observed neutrino candidates is compared with the expected background rate determined from independent SNO+ data. In the absence of a statistically significant excess, the observed counts, expected background, detection efficiency, and number of interaction targets are used to calculate upper limits on the neutrino fluence.

Previous searches for neutrinos associated with GW events have adopted coincidence windows ranging from ± 10 s to ± 1000 s. A ± 10 s window is comparable to the duration of neutrino emission from a core-collapse supernova (CCSN), while the ± 500 s window adopted by Baret et al. is motivated by gamma-ray burst models of neutrino emission [110]. The ± 1000 s window has become the standard conservative choice and is adopted for the IBD search presented here. The neutrino-proton

ES search instead uses a ± 50 s window, which improves sensitivity by reducing the background while remaining longer than both the characteristic ~ 10 s timescale expected for thermal MeV neutrino emission and the possible propagation delay expected for a massive neutrino, ensuring potential signals are not excluded. As discussed in Chapter 2, Section 2.5, over cosmological distances neutrino propagation is expected to become decoherent, with the mass eigenstates propagating independently. A measured time difference between coincident GW and neutrino signals could therefore provide constraints on the absolute neutrino mass by comparing the propagation times of massive neutrinos with the effectively massless GW signal.

The dominant backgrounds depend on the neutrino interaction channel being considered. For the IBD search, the delayed-coincidence signature strongly suppresses single-event radioactive backgrounds. After the delayed-coincidence selection, the remaining backgrounds include accidental coincidences between unrelated events, reactor antineutrinos, geoneutrinos, and cosmogenic or atmospheric neutrino interactions. The relative contribution of each component depends on the selected energy range and coincidence requirements.

For the neutrino-proton ES search, which uses a single-event signature, the expected background rate is significantly higher. The dominant backgrounds arise from radioactive decays within the detector materials and scintillator, solar neutrino interactions, and cosmogenic backgrounds.

The combined contribution from these backgrounds is determined directly from SNO+ data outside the GW coincidence windows.

Estimating the accidental background within the coincidence windows is a critical component of the analysis. Rather than relying solely on MC simulations of radioactive and cosmogenic backgrounds, the background expectation is determined directly from SNO+ data. A data-driven background estimate naturally incorporates detector effects, temporal variations, and backgrounds that are difficult to model accurately in simulation. Signal MC is used to determine detection efficiencies, optimize event selections, and calculate the detector response to different assumed neutrino spectra, while the expected background is obtained directly from data.

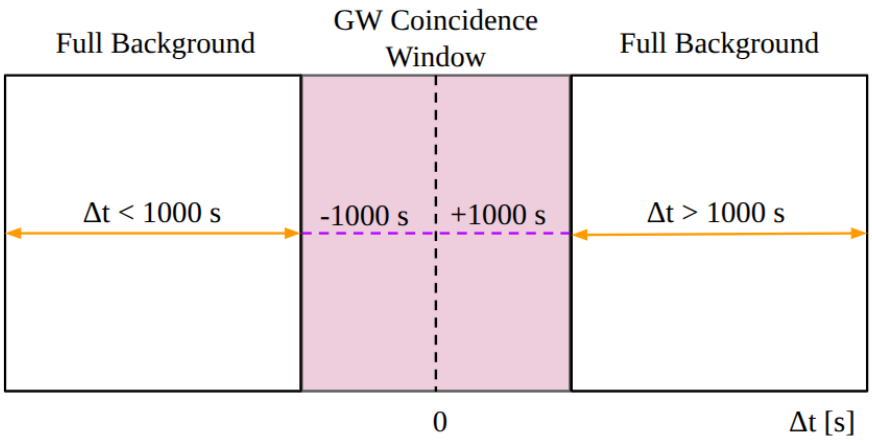


Figure 6.2: The ±1000 s coincidence window highlighted by the pink rectangle defines the signal region used to search for neutrinos temporally coincident with GW events.

Figure 6.2 illustrates the coincidence window structure. For the IBD case, a ±1000 s signal region is centered on the GW GPS trigger time. The ±50 s neutrino-proton coincidence window would follow the same structure. Following the Borexino analysis, a ±5000 s local window can also be defined, where the regions outside the central ±1000 s signal window provide two sidebands totaling 8000 s for estimating the local background. Borexino adopted this approach because the accidental background varied with time, making a local background estimate advantageous. In SNO+, however, the measured IBD background rate was found to be stable throughout the data-taking period. Consequently, the final background estimate is obtained from the full independent background dataset rather than from the local sidebands.

6.4 Monte Carlo Simulation

MC simulations are used throughout this analysis to model the detector response to neutrino interactions, determine the detection efficiencies, optimize the event selection criteria, and calculate upper limits on the neutrino fluence. Because the production spectrum of MeV neutrinos from compact binary mergers is currently unknown, simulated events are generated using a model-independent flat neutrino energy spectrum and subsequently reweighted to theoretical emission models.

6.4.1 Neutrino Emission Models

Unlike reactor neutrinos or CCSN neutrinos, the MeV-scale neutrino emission spectrum from compact binary mergers is not well established. No MeV neutrino counterpart to a compact binary merger has been observed, and theoretical predictions depend strongly on the merger type, remnant evolution, accretion disk properties, and surrounding environment.

Previous coincidence searches by Borexino, KamLAND, and Super-Kamiokande have adopted assumed neutrino spectra when calculating detection efficiencies and fluence limits [107–109]. These assumed spectra generally fall into two categories: model-independent spectra, such as monoenergetic or flat distributions, and model-dependent spectra motivated by thermal neutrino emission and CCSN.

Three spectra are considered in this work:

- A flat spectrum, which provides a model-independent benchmark and allows efficient reweighting to other spectra
- A pinched thermal Fermi-Dirac spectrum, representing thermal neutrino emission commonly adopted in previous coincidence searches
- Although compact binary mergers are not expected to exactly reproduce CCSN emission, the GKVM spectrum provides a standard candle-like benchmark for comparison with other MeV neutrino searches

This analysis starts with a flat neutrino spectrum for event generation. The flat sample provides a model-independent MC dataset that can be subsequently reweighted to represent different assumed emission models. Detector efficiencies and fluence limits are calculated using the original flat spectrum, as well as the reweighted pinched thermal Fermi-Dirac and GKVM CCSN-inspired spectra.

6.4.2 IBD Generator Improvements

The standard SNO+ IBD MC was originally developed for reactor antineutrino analyses. Consequently, it assumes a reactor antineutrino spectrum that falls rapidly above approximately 9 MeV in neutrino energy, making it unsuitable for the present search, which considers neutrino energies up to 50 MeV. Furthermore, the generator samples neutrino energies according to the product of the input neutrino fluence and the IBD interaction cross section.

The interaction rate is proportional to

$$R(E_\nu) \propto \Phi(E_\nu)\sigma_{\mathrm{IBD}}(E_\nu) \tag{6.3}$$

where $\Phi(E_\nu)$ is the neutrino fluence and $\sigma_{\mathrm{IBD}}(E_\nu)$ is the IBD cross section. Because the IBD cross section increases with neutrino energy, supplying a flat fluence spectrum does not produce a flat distribution of generated interactions. Higher-energy neutrinos are preferentially selected by the generator because they have a larger interaction probability. For this analysis, a locally modified version of the IBD generator was developed to generate a truly flat neutrino energy spectrum. Rather than sampling directly from the input fluence, the generator samples from a modified distribution:

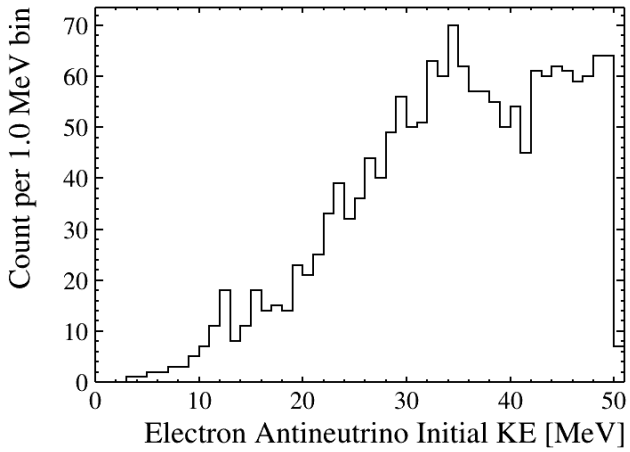
$$\Phi_{\mathrm{gen}}(E_\nu) \propto \frac{\Phi(E_\nu)}{\sigma_{\mathrm{IBD}}(E_\nu)} \tag{6.4}$$

The acceptance probability within the generator remains proportional to the IBD cross section, giving

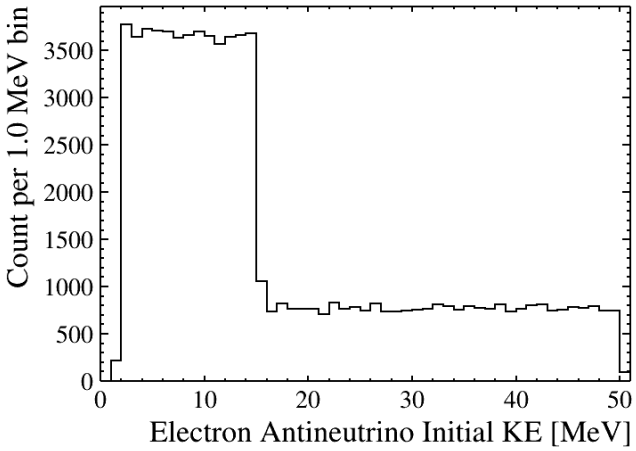
$$P(E_\nu) \propto \frac{dN}{dE_\nu} \propto \Phi_{\mathrm{gen}}(E_\nu)\,\sigma_{\mathrm{IBD}}(E_\nu) \propto \Phi(E_\nu) \tag{6.5}$$

Consequently, when the input fluence is flat, the accepted neutrino energies are also flat. This produces a single simulation sample that can subsequently be reweighted to different neutrino emission models. The effect of this modification is shown in Figure 6.3. The standard generator samples interactions according to the product of the input spectrum and the energy-dependent IBD cross section, producing a non-flat accepted neutrino distribution. The modified generator corrects for

this effect and produces a flat neutrino energy spectrum. The discontinuity at 15 MeV corresponds to the boundary between the independently generated low- and high-energy MC samples.



(a) IBD Generator



(b) Flat IBD Generator

Figure 6.3: Comparison of generated electron antineutrino energy distributions using the standard IBD generator (top) and the modified flat spectrum IBD generator developed for this analysis (bottom).

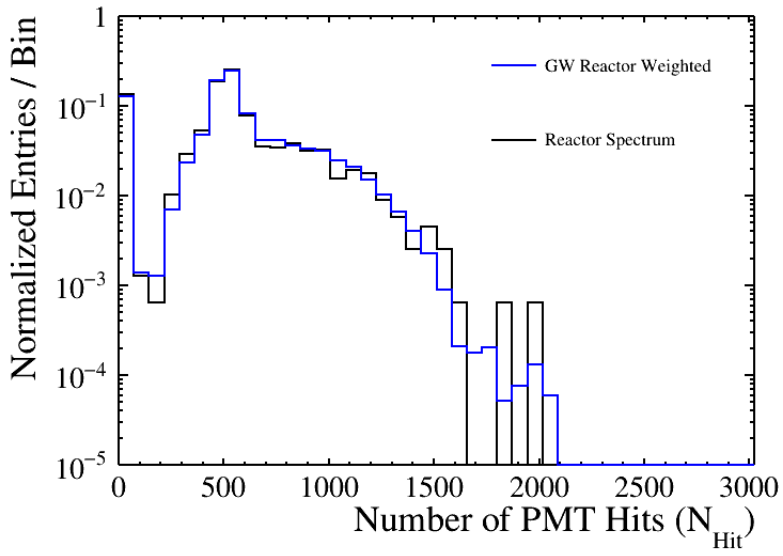
In addition to producing the desired energy distribution, the modified generator improved the efficiency of MC generation by reducing the oversampling of high-energy interactions and increasing

the available statistics in the lower-energy region.

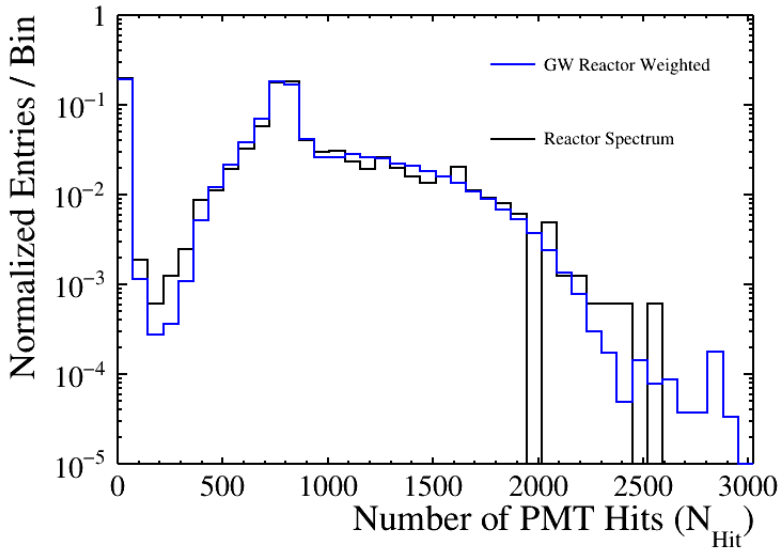
To further improve the statistical precision of the analysis, separate MC samples were generated for low-energy (1.7-15.0 MeV) and high-energy (15.0-50.1 MeV) neutrinos. Since detector backgrounds are higher at low energies, and detector thresholds, reconstruction effects, and selection efficiencies vary most rapidly in this region, additional MC statistics were generated at low energies. Each simulated detector run therefore contains approximately 45,000 low-energy events and 20,000 high-energy events, for a total of approximately 65,000 generated events per run.

To validate the modified generator, the reconstructed detector response was compared with the standard IBD MC sample. The flat spectrum events were reweighted by the reactor antineutrino flux and IBD cross section to reproduce the expected reactor antineutrino interaction spectrum.

This comparison verifies that modifying the generator sampling procedure does not introduce reconstruction artifacts or change the detector response. The PPO and bisMSB comparisons between the reweighted GW MC samples and the standard reactor IBD MC samples are shown in Figure 6.4.



(a) PPO



(b) BisMSB

Figure 6.4: RAT801 GW MC production with run 310048 (PPO–top) and run 355014 (bisMSB–bottom), reweighted using the reactor antineutrino spectrum (blue). Overlaying this with the analysis script using RAT801 SNO+ PPO MC production for the reactor IBD spectrum with the same runs (black).

Small residual differences remain between the two productions, consistent with differences in the complete production chain beyond the simplified reweighting procedure and due to low simulated statistics. Nevertheless, the agreement demonstrates that the modified generator introduces no significant reconstruction bias and is suitable for the present analysis.

All IBD signal MC samples presented in the remainder of this chapter were produced using this modified generator.

6.4.3 Neutrino-Proton ES Cross Section Correction

The neutrino-proton ES channel is sensitive to neutrinos of all flavors through the neutral current (NC) interaction and provides a complementary search channel to IBD. Since the calculated neutrino fluence limits depend sensitively on the assumed interaction cross section, the implementation of the ES event generator in RAT was independently validated before producing MC samples.

During this validation, a discrepancy was identified between the differential cross section implemented in `ProtonESgen.cc` and the analytic expression given by Dasgupta and Beacom [30]. The published differential cross section is

$$\frac{d\sigma}{dT} = \frac{G_F^2\, m_p}{\pi}\left[\left(1 - \frac{m_p\, T}{2E_\nu^2}\right) c_V^2 + \left(1 + \frac{m_p\, T}{2E_\nu^2}\right) c_A^2\right] \tag{6.6}$$

where T is the proton recoil kinetic energy, E_ν is the incident neutrino energy, and c_V and c_A are the weak vector and axial-vector couplings.

In contrast, the RAT implementation incorrectly evaluated the energy-dependent terms as

$$\frac{d\sigma}{dT} = \frac{G_F^2\, m_p}{\pi}\left[\left(\frac{1 - m_p\, T}{2} E_\nu^2\right) c_V^2 + \left(\frac{1 + m_p\, T}{2} E_\nu^2\right) c_A^2\right] \tag{6.7}$$

placing the neutrino energy out of the denominator. This changes the energy dependence of the differential cross section, producing increasingly large deviations at higher neutrino energies. The incorrect implementation placed the neutrino-energy dependence outside the dimensionless recoil correction term, producing an incorrect scaling with neutrino energy and substantially altering the

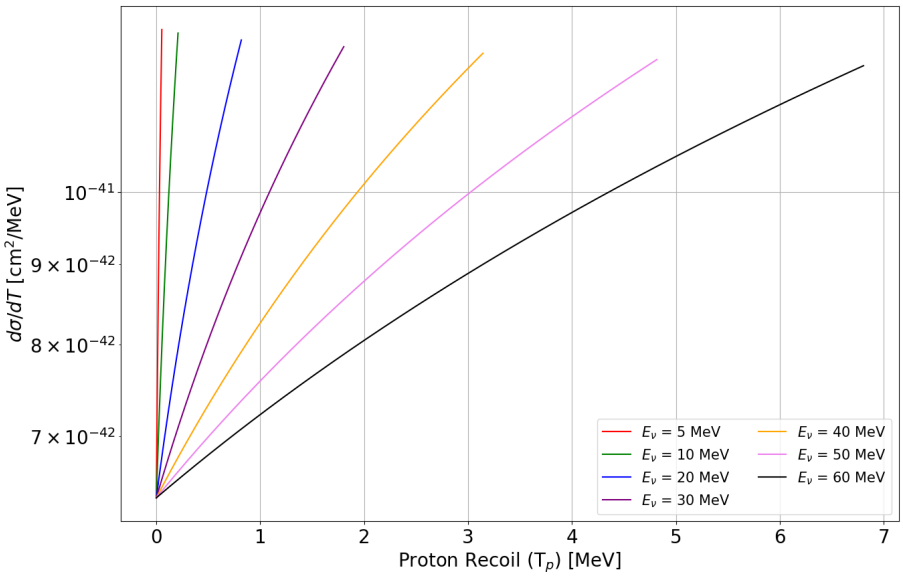


Figure 6.5: Differential neutrino-proton ES cross section calculated using the analytic expression of Dasgupta and Beacom [30] for representative neutrino energies.

predicted recoil spectrum.

Figures 6.5 and 6.6 are included to further show the difference in the expected cross section given Dasgupta and Beacom's analytic equation [30] and what was incorporated into RAT.

Figure 6.7 compares the original implementation with the corrected calculation in the MC simulation. The largest differences occur in the high-energy region relevant to this analysis, where the incorrect implementation overestimates the differential cross section.

The generator was updated to implement the correct analytic expression, and the correction was subsequently merged into the official RAT software repository for future neutrino-proton ES simulations [111]. All MC samples and fluence calculations presented in this dissertation use the corrected implementation.

6.5 GW Coincidence Analysis Framework

6.5.1 Timing and Livetime Validation

The event timing information in SNO+ is reconstructed using two detector clock systems. The 10 MHz clock system provides the absolute timing reference required to compare SNO+ events with

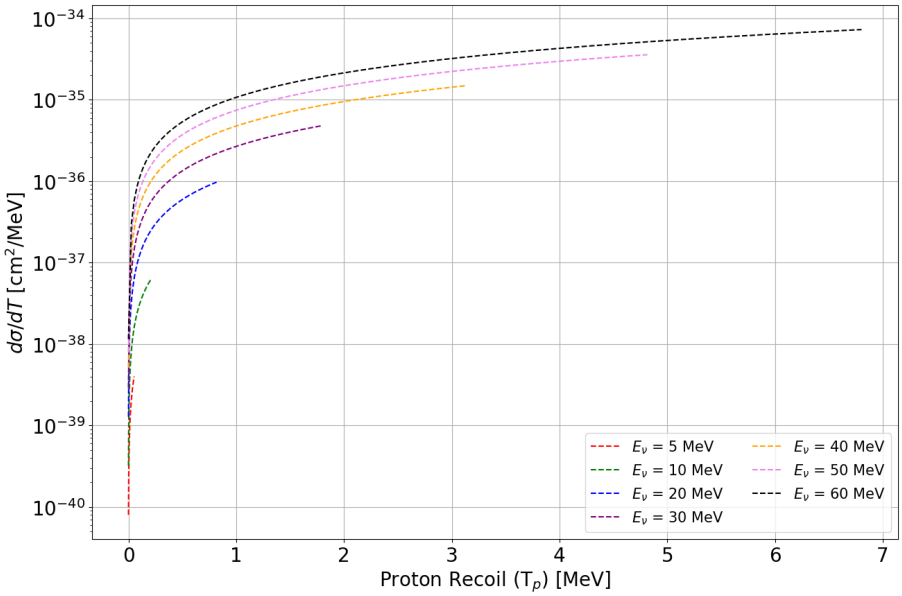


Figure 6.6: Differential neutrino-proton ES cross section implemented in the original RAT `ProtonESgen.cc` event generator.

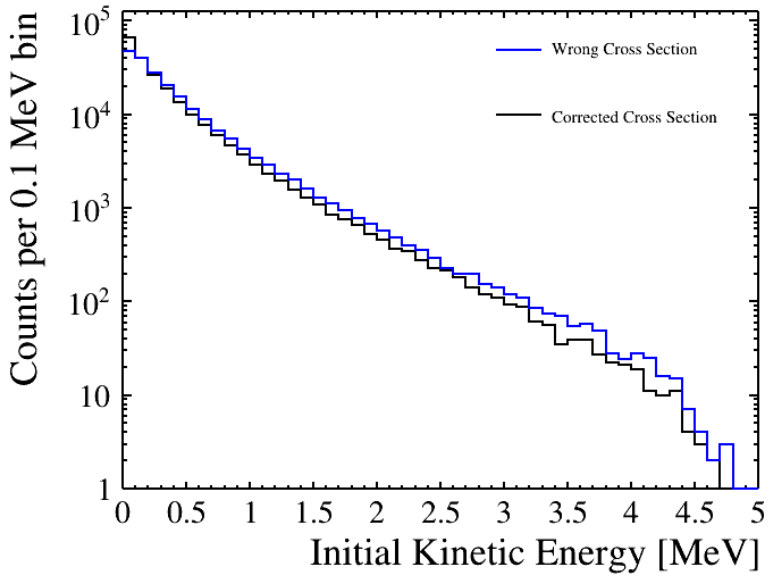


Figure 6.7: The "Wrong Cross Section" curve corresponds to the original RAT implementation, while the "Corrected Cross Section" curve uses the locally updated implementation matching the analytic expression from Dasgupta and Beacom [30].

external GW trigger times, while the 50 MHz clock is used for precise relative timing calculations within each run, including the prompt-delayed separation used in the IBD analysis.

The livetime is determined independently for each subrun using the detector clock information. The total exposure is obtained by summing the valid livetimes from all selected subruns passing the analysis requirements.

Agreement between the 10 MHz and 50 MHz livetime calculations was used as a timing consistency check. Table 6.2 lists the comparison of livetimes in the PPO+BHT and bisMSB phases for the full background-only datasets.

Dataset	10 MHz Livetime [s]	50 MHz Livetime [s]	Difference
PPO+BHT	4.204×10^6	4.204×10^6	$< 0.1\%$
bisMSB	3.872×10^7	3.886×10^7	0.36%

Table 6.2: Comparison of detector livetimes calculated using the 10 MHz and 50 MHz clock systems.

Accurate absolute timing is essential for the GW coincidence analysis because the signal window is defined relative to the GPS time reported for each GW event. A correction to an offset in the 10 MHz clock system was described in Chapter 3, Section 3.6.

During validation of the bisMSB dataset, an issue was identified with the reconstructed 10 MHz clock times. Beginning around run 353207, reconstructed event times exhibited large discontinuities, with offsets corresponding to nonphysical absolute timestamps far outside the data-taking period. This issue originated from the `reconstructClocks` processor, which relied on ClockJump corrections that produced incorrect absolute times. The affected clock reconstruction procedure was no longer used in later processed data beginning with run 367918.

Since the absolute event timing is required only to determine the position of the GW coincidence window, the underlying 50 MHz event timing information remained usable once a reliable run start time was provided. To recover the affected runs, the official run start times from the Run Selection database [106] were used as an external timing reference. These times originate from the `RUN.ratdb` tables and were verified to be unaffected by the reconstructed clock discontinuities. The run start

times were collected into a database file and implemented as a fallback reference whenever an invalid 10 MHz clock time was identified.

For affected runs, the corrected event time was therefore calculated by anchoring the relative 50 MHz clock information to the validated run start time:

$$t_{\text{corrected}} = t_{\text{run start}} + \Delta t_{50\,\text{MHz}} \tag{6.8}$$

where $\Delta t_{50\,\text{MHz}}$ is the relative event time measured from the start of the run.

This correction restored the expected run timing and allowed the GW coincidence windows used in both neutrino searches to be calculated correctly.

The search window for each GW candidate is defined using the absolute GPS time reported by LVK. The analysis is therefore anchored to the GW event time rather than to SNO+ run boundaries. A coincidence window is constructed around each GW trigger time, and all available SNO+ subruns overlapping this time interval are included. The IBD analysis uses a $\pm$1000 s window, while the neutrino-proton ES analysis uses a $\pm$50 s window as determined from the sensitivity optimization.

Since the coincidence window may span multiple subruns/runs or occur near the beginning or end of a run, the analysis does not assume continuous detector operation. If part of the coincidence window overlaps a detector downtime period or unavailable run, that period contributes zero livetime. This does not bias the search because all background expectations are normalized using the measured detector livetime.

GW candidates with insufficient temporal coverage, such as cases where only the pre-GW or post-GW portion of the coincidence window is available, are removed from the final analysis sample as described in Section 6.2.3.

6.6 Signal Channels

Liquid scintillator detectors are sensitive to several low-energy neutrino interaction channels. A summary of the expected event yields for various charged current (CC) and neutral current (NC)

interaction channels is shown in Table 6.3.

Supernova Neutrino Interaction Channels		
Channels	Weak Interaction Type	Event Yield
$\bar{\nu}_e + p \rightarrow e^+ + n$ (IBD)	CC	194.7 ± 1.0
$\nu_e + e^- \rightarrow \nu_e + e^-$	NC/CC	6.4
$\bar{\nu}_e + e^- \rightarrow \bar{\nu}_e + e^-$	NC	2.7
$\nu_x + e^- \rightarrow \nu_x + e^-$	NC	2.1
$\bar{\nu}_x + e^- \rightarrow \bar{\nu}_x + e^-$	NC	1.8
$\nu + p \rightarrow \nu + p$	NC	429.1 ± 12.0
$\nu_e + {}^{12}\mathrm{C} \rightarrow {}^{12}\mathrm{C} + \nu_e + e^- + e^+$	CC	2.7 ± 0.3
$\bar{\nu}_e + {}^{12}\mathrm{C} \rightarrow {}^{12}\mathrm{C} + \bar{\nu}_e + e^- + e^+$	CC	7.0 ± 0.7
$\nu + {}^{12}\mathrm{C} \rightarrow {}^{12}\mathrm{C} + \nu + \gamma$ (15.11 MeV)	NC	43.8 ± 8.7
$\nu_e + {}^{12}\mathrm{C} \rightarrow {}^{11}\mathrm{C} + e^- + p$	CC	0.16 ± 0.08
$\bar{\nu}_e + {}^{12}\mathrm{C} \rightarrow {}^{11}\mathrm{B} + e^+ + n$	CC	0.16 ± 0.08
$\nu + {}^{12}\mathrm{C} \rightarrow {}^{11}\mathrm{B} + \nu + p$	NC	1.6 ± 0.5
$\nu + {}^{12}\mathrm{C} \rightarrow {}^{11}\mathrm{C} + \nu + n$	NC	0.5 ± 0.16

Table 6.3: Interaction channels for supernova neutrinos in liquid scintillator with corresponding event yields estimated based on a CCSN at 10 kpc observed in SNO+, adapted from [3] and [4]. The errors on the event yields are derived from the uncertainties of the interaction cross sections. Note that the uncertainties of the electron scattering cross sections arising from Standard Model calculations are less than 1%, and are neglected in the yield count.

Here, ν_x denotes the heavy-flavor neutrinos (ν_μ and ν_τ), which are grouped together because they have similar interactions at MeV energies.

The events in Table 6.3 assume a standard supernova (SN) at 10 kpc with total energy 3×10^{53} erg equally partitioned among the three neutrino flavors and their corresponding antineutrinos with mean energies of 12 MeV for the electron neutrino, 15 MeV for the electron antineutrino, and 18 MeV for the heavier neutrino species. If a galactic CCSN occurs, the SNO+ detector will observe several hundred neutrinos in a short burst of about 10 seconds.

Of the available interaction channels, this analysis focuses on IBD and neutrino-proton ES. These channels were selected because they provide the largest expected event yields for MeV neutrinos, offer complementary flavor sensitivity, and represent the two most promising channels for a search for neutrinos from compact binary mergers. In particular, IBD provides a clean delayed-coincidence signature, while neutrino-proton ES is sensitive to all neutrino flavors through the NC interaction.

The event yields in Table 6.3 provide a reference benchmark for comparing interaction channels. Since this analysis considers alternative neutrino spectra, including a pinched thermal Fermi-Dirac spectrum and the GKVM CCSN model, the expected event yields are recalculated using the corresponding fluence models when evaluating detector performance.

6.6.1 IBD

The IBD interaction,

$$\bar{\nu}_e + p \rightarrow e^+ + n \tag{6.9}$$

is the primary detection channel for electron antineutrinos in liquid scintillator. In this interaction, an electron antineutrino interacts with a free proton in the scintillator, producing a positron and a neutron.

The reaction has a kinematic threshold because the final-state neutron and positron are more massive than the initial-state proton. For a proton initially at rest, the threshold neutrino energy is

$$E_\nu^{\text{thr}} = \frac{(m_n + m_e)^2 - m_p^2}{2m_p} \approx 1.806 \text{ MeV} \tag{6.10}$$

Therefore, IBD is sensitive to electron antineutrinos with energies above the interaction threshold of approximately 1.8 MeV.

The IBD signature consists of two correlated signals. The positron immediately deposits its kinetic energy in the liquid scintillator through ionization and excitation of the surrounding scintillator molecules. As these excited molecules return to their ground state, they emit visible scintillation photons that are detected by the SNO+ PMTs. The positron subsequently annihilates with an electron, producing two 0.511 MeV gammas, which also deposit their energy in the scintillator and contribute to the prompt scintillation signal.

The neutron, being electrically neutral, does not directly ionize the scintillator. Instead, it thermalizes through elastic scattering, primarily with hydrogen nuclei. These scatters produce low-energy proton recoils, which generate a small amount of scintillation light; however, this contribution is

heavily quenched and is much smaller than the prompt positron signal. Therefore, the neutron thermalization light does not form the primary IBD detection signature.

After thermalization, the neutron undergoes a random walk through the scintillator before being captured, predominantly on hydrogen. The capture reaction,

$$n + p \rightarrow d + \gamma(2.2 \text{ MeV}) \tag{6.11}$$

produces a 2.2 MeV gamma that Compton scatters in the scintillator, generating a second burst of scintillation light. This delayed signal occurs with a characteristic capture time of approximately 200 μs after the prompt positron interaction.

The prompt visible energy is related to the incident antineutrino energy by

$$E_{\text{prompt}} \simeq E_{\nu} - 0.78 \text{ MeV} \tag{6.12}$$

up to small corrections from neutron recoil and detector response. The delayed event is approximately fixed by the 2.2 MeV neutron capture gamma.

The IBD interaction provides one of the cleanest signatures in a liquid scintillator detector because the prompt positron signal and delayed neutron capture signal are correlated in both time and space. This delayed-coincidence topology strongly suppresses backgrounds. For this reason, IBD is the primary channel used in this search. The IBD cross section used in this analysis follows the Vogel and Beacom prescription implemented in RAT [112]. At MeV energies, IBD provides a relatively large and well-understood interaction cross section compared with other detectable channels in liquid scintillator.

6.6.2 Neutrino-Proton ES

The neutrino-proton ES interaction,

$$\nu + p \rightarrow \nu + p \tag{6.13}$$

is a NC process in which a neutrino scatters elastically from a free proton in the liquid scintillator. Unlike IBD, no charged lepton is produced in the final state. Instead, the neutrino transfers a fraction of its energy to the proton through the weak interaction and continues with reduced energy.

Because the interaction proceeds through the NC, all neutrino and antineutrino flavors contribute with approximately flavor-independent cross sections, up to differences from axial-vector interference terms and radiative corrections. Neutrino-proton ES provides sensitivity to the total neutrino flux rather than only the electron antineutrino component.

The recoiling proton loses its kinetic energy through ionization and excitation of the surrounding scintillator molecules, producing scintillation light that is detected by the SNO+ PMTs. Unlike relativistic electrons and positrons, however, protons have a much larger stopping power (dE/dx) and therefore experience significant ionization quenching, as described by Birks' law in Subsection 3.2.3. As a result, only a small fraction of the proton's kinetic energy is converted into visible scintillation light, causing the observed energies to be substantially lower than the true proton recoil energies.

Unlike IBD, neutrino-proton ES produces only a single prompt interaction and does not possess a delayed coincidence signature. Consequently, the analysis cannot exploit the powerful time and spatial correlations used for background rejection in the IBD channel. Instead, the search relies on identifying a statistical excess of low-energy proton recoils above the expected detector backgrounds within the GW coincidence window.

Although experimentally more challenging than IBD, neutrino-proton ES offers several important advantages. It is sensitive to all neutrino flavors, has the largest expected event yield for a CCSN in liquid scintillator (Table 6.3), and establishes corresponding all-flavor neutrino fluence limits. For these reasons, neutrino-proton ES serves as a valuable complement to the IBD search presented in this dissertation.

6.6.3 Reference CCSN Event Yields

Although this dissertation searches for neutrinos from compact binary mergers rather than CCSNe, reference CCSN spectra provide a useful benchmark for comparing detector sensitivity across different interaction channels. The MeV-scale neutrino emission from compact binary mergers is uncertain because it depends on the merger type, remnant lifetime, amount of neutron-rich ejecta, and accretion disk properties. Therefore, these event yields should be interpreted as detector-performance benchmarks rather than predictions for GW-associated neutrino signals. At the typical distances of GW sources considered in this analysis (hundreds of Mpc), CCSN-like neutrino emission would produce an expected number of detected events many orders of magnitude below one.

The event yields in Table 6.3 are calculated using the same reference SN model adopted in the SNO+ supernova sensitivity study. This model assumes a source distance of 10 kpc and a total gravitational binding energy release of 3×10^{53} erg (300 foe), emitted as neutrinos with the total energy approximately equipartitioned among all neutrino and antineutrino flavors.

Flavor transformation effects during propagation, including MSW and collective neutrino oscillation effects, depend on the SN environment, neutrino mass ordering, and oscillation model assumptions. These effects are not included in the event yields shown here; instead, the original model spectra are used directly to provide a detector-response benchmark.

To benchmark the expected number of neutrino interactions in SNO+, the model neutrino fluence at Earth was folded with the Vogel and Beacom analytic IBD cross section [112], which is used in RAT's IBD generator, and the number of protons in the scintillator in the 6 m fiducial volume (FV), which is 5.64×10^{31} [113]. The GKVM CCSN fluence is then used separately as the benchmark spectrum for evaluating the GW-analysis signal expectations.

The expected number of interactions for a given channel is calculated as

$$N_{\text{exp}} = N_{\text{targets}} \int \Phi(E_\nu)\sigma(E_\nu)\epsilon(E_\nu)dE_\nu \tag{6.14}$$

where N_{targets} is the number of available interaction targets (for example, free protons for IBD and neutrino-proton ES) in the scintillator, $\Phi(E_\nu)$ is the neutrino fluence at Earth, and $\sigma(E_\nu)$ is the energy-dependent interaction cross section. For the purpose of comparing intrinsic interaction yields, the detection efficiency is taken to be unity. Detector effects, including energy thresholds, reconstruction efficiencies, and event-selection efficiencies, are incorporated later through the MC simulation.

Since the fluence is provided in discrete energy bins from SNOwGLoBES [114], this integral is evaluated as a sum

$$N_{\text{exp}} \approx N_{\text{targets}} \sum_k \Phi_k \sigma(E_k) \epsilon(E_k) \tag{6.15}$$

where Φ_k is the fluence per bin and $\sigma(E_k)$ is the cross section evaluated at the bin center.

For the IBD channel, only the electron antineutrino component of the fluence contributes. For neutrino-proton ES, the contributions from all six neutrino and antineutrino flavors are included.

The reference SN yields discussed above provide a comparison with previous SNO+ sensitivity studies. For the GW analysis presented in this work, the same calculation is repeated using the GKVM CCSN spectrum, which is used as one of the benchmark emission models for the fluence-limit calculation.

Using the GKVM $\bar{\nu}_e$ fluence and the Vogel and Beacom implementation of the IBD cross section [112], the expected number of IBD interactions in the SNO+ detector for a source at 10 kpc (6 m FV, $N_p = 5.64 \times 10^{31}$) is found to be

$$N_{\text{IBD}}^{\text{exp}}(10 \text{ kpc}) = 134.0 \tag{6.16}$$

Similarly, the expected number of neutrino-proton ES interactions is

$$N_{\nu p}^{\text{exp}}(10 \text{ kpc}) = 223.2 \tag{6.17}$$

These values represent the total number of physical neutrino interactions in the detector prior to any detector effects, such as energy thresholds, quenching, reconstruction, or analysis selection cuts for a GKVM CCSN model instead of the reference SN model.

The GKVM event yields differ from those obtained using the reference SN model in the SNO+ sensitivity study [3, 4] in Table 6.3 because the underlying emission assumptions are different. First, the GKVM model assumes a total emitted neutrino energy of 185 foe rather than 300 foe, reducing the overall fluence. Second, the flavor-dependent spectral shapes differ from those of the reference model, particularly for the heavy-flavor neutrinos. Since neutrino-proton ES receives contributions from all neutrino flavors, these spectral differences reduce its expected yield more strongly than for the IBD channel, which is sensitive only to electron antineutrinos.

The uncertainties on the event yields are taken to arise from the theoretical uncertainties on the interaction cross sections. Since the predicted number of interactions depends linearly on the cross section, a fractional uncertainty on the cross section propagates directly to the same fractional uncertainty on the event yield

$$\frac{\Delta N}{N} = \frac{\Delta \sigma}{\sigma} \tag{6.18}$$

In the SNO+ SN sensitivity estimates, the quoted uncertainties correspond to fractional cross section uncertainties of approximately (0.5%) for IBD and (2.8%) for neutrino-proton ES (ν-p), as inferred from the reported event yields and uncertainties. These values reflect the relatively well-constrained theoretical description of the IBD cross section compared to the larger theoretical uncertainties associated with neutrino-proton ES scattering.

Applying these fractional cross section uncertainties to the calculated event yields gives

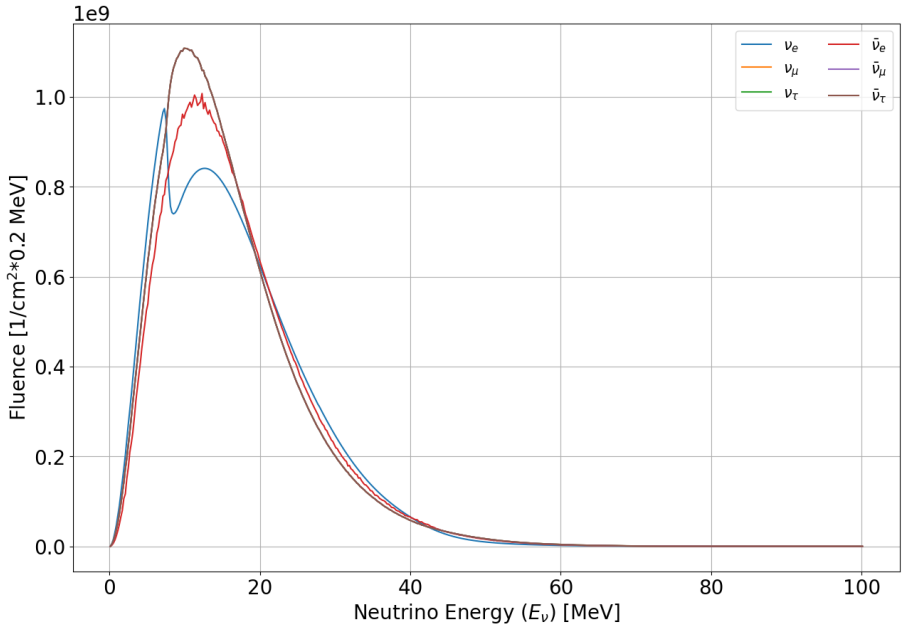
$$N_{\mathrm{IBD}}^{\mathrm{exp}}(10\ \mathrm{kpc}) = 134.0 \pm 0.7 \tag{6.19}$$

while for neutrino-proton ES,

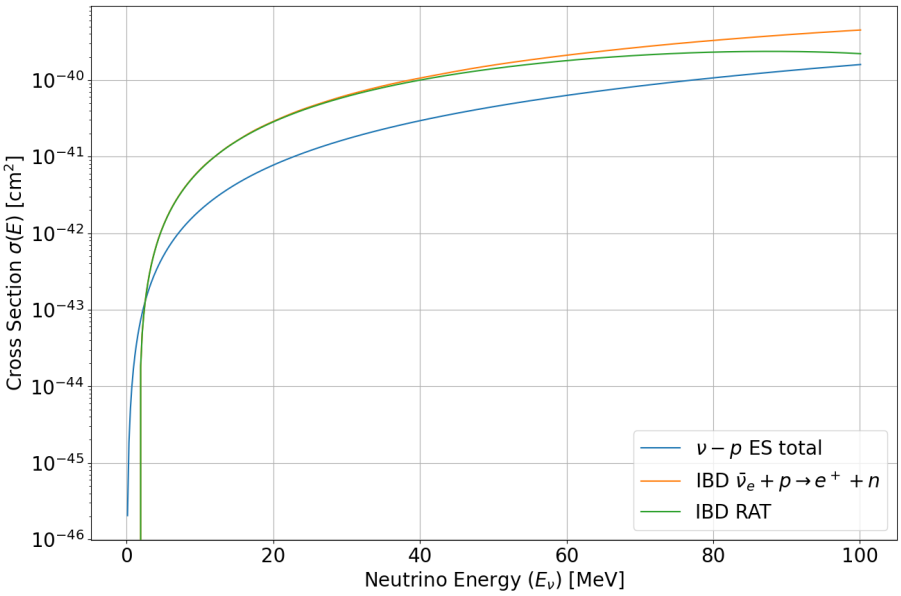
$$N_{\nu p}^{\mathrm{exp}}(10\ \mathrm{kpc}) = 223.2 \pm 6.2 \tag{6.20}$$

These uncertainties reflect only the interaction cross section contribution. Uncertainties associated with the assumed astrophysical emission model, such as the total emitted energy, spectral shape, and flavor composition, are not included because the purpose of this calculation is to compare detector interaction channels rather than predict the neutrino yield from a specific source. For the GW coincidence search, these cross section uncertainties are small compared with the dominant limitations arising from the unknown neutrino emission mechanism and the large distances of the GW sources.

Figure 6.8 depicts the GKVM CCSN fluence as a function of neutrino energy for all flavors (top) and the cross sections of the IBD and neutrino-proton ES channels, alongside another IBD cross section from SNOwGLoBES in orange (bottom) [114].



(a) GKVM Fluence



(b) Cross Sections

Figure 6.8: GKVM CCSN fluence as a function of neutrino energy for all flavors (left) and the cross sections of the IBD and neutrino-proton ES channels, alongside another IBD cross section from SNOwGLoBES in orange (right).

6.7 IBD Analysis

The IBD analysis follows the blind analysis procedure described in Section 6.1. The event selection, background estimation, sensitivity optimization, and fluence-limit calculations were finalized before examining the GW-coincident data. Validation was performed using background data and fake GW triggers prior to unblinding.

6.7.1 Event Selection

The data are analyzed on a run-by-run basis. For each run, all corresponding sub-run ntuples are combined into a single ROOT `TChain`, allowing the complete run to be processed with a consistent event selection.

The IBD selection criteria are summarized in Table 6.4.

Cuts	**Prompt**	**Delayed**
Energy [MeV]	0.9 – 50.0	1.85 – 2.5
Fiducial Volume [mm]	< 5700	
$\lvert\Delta\vec{r}\rvert$ [m]	< 2.5	
Δt [μs]	$400 < \Delta t < 2000$	
Data Cleaning	Pass	
Reconstruction Valid	True	

Table 6.4: IBD selection criteria applied to both data and MC analyses.

The selection criteria are designed to identify the characteristic IBD delayed-coincidence signature while suppressing accidental backgrounds and poorly reconstructed events. The data cleaning and reconstruction requirements remove instrumental backgrounds and events for which the position and energy reconstruction are unreliable. The FV requirement reduces backgrounds originating near the AV and external detector materials.

The prompt-delayed spatial and timing requirements exploit the correlation between the positron signal and subsequent neutron capture. The neutron capture time requirement is chosen to retain the majority of neutron captures on hydrogen while rejecting random coincidences between unrelated events. Similarly, the prompt-delayed spatial separation requirement suppresses accidental pairs while maintaining high IBD detection efficiency.

These selection criteria are based on the SNO+ reactor antineutrino analysis, with modifications motivated by the broader energy range expected for a potential astrophysical neutrino signal. The reactor antineutrino analysis uses an upper prompt energy of 9.0 MeV, while this analysis extends the prompt energy range to 50.0 MeV.

The same selection criteria are applied to both data and MC to ensure a consistent comparison between observed candidates, background estimates, and signal efficiencies.

The standard SNO+ data cleaning mask (0xD82100000162C6) was applied to all data events [115]. Additionally, both data and MC were processed using the radial-dependent energy correction developed by Daniel Cookman (`CalibrateEnergyRTF`, version 3 for PPO and bisMSB data [116]).

The treatment of event vetoes also differs from the reactor antineutrino analysis. Since the detailed neutrino emission properties of compact binary mergers are uncertain, the analysis avoids applying additional vetoes that could remove potential signal-like events beyond the standard data-quality requirements.

A multiplicity selection is therefore implemented as a tag rather than a veto. Events occurring close together in space and time are identified, allowing comparison with the reactor antineutrino candidate lists, but these events are not removed from the GW search sample. An IBD candidate pair receives a multiplicity tag if any additional event with reconstructed energy greater than 0.4 MeV occurs between the prompt and delayed candidates, or within ± 1 ms of either event, and is reconstructed within 2 m of either event.

This tag identifies multi-event topologies that may arise from correlated backgrounds, such as cosmogenic fast neutrons, or from multiple IBD-like interactions occurring close together in time. The low 0.4 MeV threshold increases sensitivity to low-energy activity, including proton recoils produced by fast neutrons entering the scintillator volume. Since the time structure and multiplicity of a potential compact binary merger neutrino signal are unknown, these events are retained in the final GW search sample.

Cosmic ray muons passing through or near the detector produce large amounts of scintillation and Cherenkov light and are therefore identified by their high N_{Hit}. Events with $N_{Hit} > 3000$ (roughly 9 MeV in bisMSB and 14 MeV in PPO) are tagged as muon candidates. Following an identified muon, events occurring within the subsequent 20 s are removed through the data cleaning mask in order to suppress cosmogenic backgrounds, including neutron production and long-lived radioactive isotopes.

The low cosmic ray muon rate at SNOLAB allows this conservative veto window while introducing only a small livetime reduction. For the background-only PPO+BHT dataset used in this analysis, 3758 muons were tagged, corresponding to a total vetoed time of 75160 s and a livetime loss of 1.8%. For the background-only bisMSB dataset, 32588 muons were tagged, corresponding to a total vetoed time of 651760 s and a livetime loss of 1.7%. The combination of the low muon rate, high tagging efficiency, and long veto window makes muon-induced backgrounds negligible, except for possible fast neutrons entering the scintillator from untagged external muons. Table 6.5 lists the tagged muons and livetime information for the PPO+BHT and bisMSB phases for the full background-only and GW coincidence windows.

Dataset	Muon Tags	Removed Livetime [s]	Livetime Loss
PPO+BHT background	3758	75160	1.79%
PPO+BHT GW windows	209	4180	1.83%
bisMSB background	32588	651760	1.68%
bisMSB GW windows	1508	30160	1.67%

Table 6.5: Livetime loss associated with the muon veto in the IBD analysis.

Atmospheric neutrinos are produced when cosmic rays interact with nuclei in the Earth's atmosphere, producing a flux of neutrinos extending from hundreds of MeV to the GeV energy scale [117]. Unlike cosmic ray muons, atmospheric neutrinos pass through the SNOLAB rock overburden and can interact inside the SNO+ detector. These interactions occur through both CC and NC processes and may produce secondary neutrons through interactions with carbon nuclei in the scintillator.

Such neutron-producing interactions are a potential background for IBD searches because multi-

ple neutron captures occurring close together in space and time can mimic the prompt-delayed coincidence signature.

Because atmospheric neutrino events are typically associated with higher-energy activity than reactor antineutrino events, an atmospheric neutrino selection is implemented as a tag rather than a veto. Events with high N_{Hit} and subsequent events occurring within 1 s are identified but retained in the final sample. Since the neutrino emission properties of compact binary mergers are unknown, removing these events could unnecessarily reduce sensitivity to a potential high-energy signal. The tag allows atmospheric-like candidates to be studied after unblinding while preserving compatibility with existing reactor antineutrino cross-checks.

6.7.2 Signal MC Efficiency

The IBD signal efficiency was evaluated using the flat spectrum IBD MC samples described in Section 6.4. Simulated events were generated throughout the full scintillator volume and processed using the same reconstruction and selection criteria applied to data.

Two efficiencies are considered. The full-volume efficiency includes the FV acceptance and is defined relative to all generated events within the AV:

$$\epsilon_{\mathrm{IBD}} = \frac{N_{\mathrm{pass}}}{N_{\mathrm{AV}}} \tag{6.21}$$

where N_{gen} is the number of generated IBD interactions and N_{pass} is the number of events passing the full IBD selection.

The selection efficiency is calculated only for events generated within the analysis FV:

$$\epsilon_{\mathrm{IBD}} = \frac{N_{\mathrm{pass}}}{N_{\mathrm{FV}}} \tag{6.22}$$

For events generated throughout the full scintillator volume using the PPO+BHT and bisMSB data combined, the efficiency is

$$\epsilon_{\mathrm{AV}} = 0.74 \tag{6.23}$$

Restricting to events generated within the FV gives

$$\epsilon_{\text{sel}} = 0.88 \tag{6.24}$$

The FV efficiency is used when calculating fluence limits because the number of target protons is calculated using the same FV.

MC Statistical Uncertainty

The uncertainty due to the finite size of the MC samples is calculated assuming binomial statistics,

$$\sigma_\epsilon = \sqrt{\frac{\epsilon(1-\epsilon)}{N_{\text{FV}}}} \tag{6.25}$$

Large MC samples were produced to ensure that the statistical uncertainty on the efficiency was small compared to variations associated with detector conditions.

Detector Configuration Stability

During the PPO phase, the detector configuration evolved as PMT crates were restored following damage to a full crate. Dedicated MC samples were generated to evaluate the dependence of the IBD selection efficiency on the number of active channels.

Two representative detector configurations were studied: run 309448, corresponding to four unavailable crates, and run 310637, corresponding to one unavailable crate. For 5000 generated IBD events, the measured efficiencies were

$$\epsilon_{1 \text{ crate off}} = 0.859 \pm 0.005 \tag{6.26}$$

$$\epsilon_{4 \text{ crates off}} = 0.847 \pm 0.005 \tag{6.27}$$

The difference between these configurations is

$$\Delta\epsilon = 0.859 - 0.847 = 0.012 \tag{6.28}$$

corresponding to a relative variation of approximately 1.2%.

The uncertainty on the difference:

$$\sigma_\Delta = \sqrt{\sigma_1^2 + \sigma_2^2} = 0.0071 \tag{6.29}$$

The MC statistical uncertainty is small compared with the observed run-to-run variations in detector response. Therefore, variations in the selection efficiency across detector configurations are treated as the dominant contribution to the efficiency uncertainty.

The run-to-run variation in efficiency across the PPO+BHT GW-coincident runs was evaluated using dedicated simulations. The RMS variation was found to be approximately 0.004, corresponding to a relative efficiency variation of 0.5%. For the bisMSB runs, the RMS was 0.003 with a relative efficiency variation of 0.3%. The combined PPO+BHT and bisMSB RMS and variation is 0.004 and 0.4%.

6.7.3 Background Estimation

The IBD background rate is estimated directly from data rather than from simulation. This data-driven approach uses data outside the GW coincidence windows as a representative sample of the detector conditions during the search. Applying the same IBD selection criteria to these periods provides a direct measurement of the expected number of accidental coincidences and true IBD backgrounds that could occur within a GW coincidence window.

Using data naturally incorporates detector conditions, reactor antineutrinos, geoneutrinos, cosmogenic backgrounds, radioactive backgrounds contributing to accidental coincidences, and other accidental event pairs present during the SNO+ scintillator phase.

To construct the background-only dataset, runs containing GW coincidence windows were excluded to ensure the background estimate remained statistically independent of the blinded search regions. For the final compact binary merger fluence analysis, this corresponds to 16 GW candidates in the PPO+BHT phase and 110 GW candidates in the bisMSB phase, after excluding candidates classified as terrestrial or unknown by LVK. The same IBD selection criteria described in Subsection 6.7.1 were then applied to the remaining data. The resulting number of IBD candidates was used to calculate a global background rate

$$R_{\mathrm{bkg}} = \frac{N_{\mathrm{IBD}}^{\mathrm{bkg}}}{T_{\mathrm{bkg}}} \tag{6.30}$$

where $N_{\mathrm{IBD}}^{\mathrm{bkg}}$ is the number of IBD candidates identified in the background-only dataset and T_{bkg} is the corresponding livetime in seconds.

For the LAB+PPO+BHT phase, the background-only dataset contains

$$T_{\mathrm{bkg}}^{\mathrm{PPO+BHT}} = 4.20 \times 10^{6}\ \mathrm{s} \tag{6.31}$$

of livetime after removing GW-coincident data. Applying the IBD selection gives 16 background IBD candidate pairs, corresponding to a background rate of

$$R_{\mathrm{bkg}}^{\mathrm{PPO+BHT}} = \frac{16}{4.20 \times 10^{6}} = (3.81 \pm 0.95) \times 10^{-6}\ \mathrm{pairs/s} \tag{6.32}$$

The expected number of IBD-like background candidates in a single ± 1000 s GW coincidence window is therefore

$$b_{\mathrm{GW}} = R_{\mathrm{bkg}} \Delta T \tag{6.33}$$

where $\Delta T = 2000$ s. For the PPO+BHT phase,

$$b_{\mathrm{GW}}^{\mathrm{PPO+BHT}} = (3.81 \times 10^{-6})(2000) = 7.62 \times 10^{-3} \tag{6.34}$$

The statistical uncertainty is propagated according to

$$\sigma_b = \sqrt{N_{\mathrm{bkg}}}\frac{T_{\mathrm{GW}}}{T_{\mathrm{bkg}}} \tag{6.35}$$

where T_{GW} is the total livetime contained within the GW coincidence windows.

For the 16 PPO+BHT GW coincidence windows used in the final analysis, this gives

$$b^{\mathrm{total}}_{\mathrm{PPO+BHT}} = 0.122 \pm 0.031 \tag{6.36}$$

expected background events.

The same procedure is applied independently to the bisMSB phase because the detector optical properties and corresponding datasets are different. The background-only dataset contains

$$T^{\mathrm{bisMSB}}_{\mathrm{bkg}} = 3.87 \times 10^7 \text{ s} \tag{6.37}$$

of livetime after removing GW-coincident data. Applying the IBD selection gives 200 background IBD candidate pairs, corresponding to a background rate of

$$R^{\mathrm{bisMSB}}_{\mathrm{bkg}} = \frac{200}{3.87 \times 10^7} = (5.16 \pm 0.36) \times 10^{-6} \text{ pairs/s} \tag{6.38}$$

The expected number of IBD-like background candidates in a single $\pm$1000 s GW coincidence window is therefore

$$b^{\mathrm{bisMSB}}_{\mathrm{GW}} = (5.16 \times 10^{-6})(2000) = 1.03 \times 10^{-2} \tag{6.39}$$

For the 110 bisMSB GW coincidence windows used in the final analysis, this gives

$$b^{\mathrm{total}}_{\mathrm{bisMSB}} = 1.13 \pm 0.08 \tag{6.40}$$

expected background events.

The final combined expected background is obtained by summing the PPO+BHT and bisMSB contributions:

$$b_{\text{total}} = b_{\text{PPO+BHT}} + b_{\text{bisMSB}} = 1.25 \pm 0.09 \tag{6.41}$$

Although the final IBD background normalization is determined directly from data, the expected physical composition of this background can be estimated using the SNO+ reactor antineutrino background model [47]. Scaling the expected components from the reactor antineutrino analysis to the total GW coincidence livetime gives an approximate total of 1.20 events, consistent with the data-driven expectation of 1.25 ± 0.09 events used in this analysis. The largest contributions are expected to come from reactor antineutrino IBD interactions and radiogenic (α, n) backgrounds, with smaller contributions from geoneutrinos, α-p coincidences, and atmospheric neutrino interactions.

Component	Approximate expected events in GW windows
Reactor $\bar{\nu}_e$ IBD	0.60
Geoneutrino IBD	0.16
(α, n) proton recoils	0.34
(α, n) other	0.05
α-p coincidences	0.03
Atmospheric ν	0.02
Approximate total	1.20
Data-driven total used in this analysis	1.25 ± 0.09

Table 6.6: Approximate composition of the IBD-like background expected in the GW coincidence windows, estimated by scaling the SNO+ reactor antineutrino background model to the total GW search livetime. The final background normalization used in this analysis is determined directly from the data-driven background measurement.

The data-driven approach naturally incorporates possible time variations in these components, including changes in reactor operation, detector conditions, and accidental coincidence rates. Radiogenic backgrounds are expected to be approximately stable within each scintillator phase, while reactor antineutrino rates vary slowly compared with the GW coincidence windows. Therefore, the measured background rate provides the most representative estimate of the expected background during the search period.

The measured PPO+BHT and bisMSB background rates are statistically compatible. The PPO+BHT

dataset contains only 16 IBD candidates, giving a rate uncertainty of approximately 25%, while the larger bisMSB dataset contains 200 candidates, reducing the rate uncertainty to approximately 7%. The two measured rates differ by approximately 1.3σ.

Although the fractional uncertainty on the measured background rate is limited by the number of IBD candidates in the background-only dataset, the uncertainty on the predicted number of events in the GW coincidence windows remains small. This is because the background measurement uses a much longer livetime than the total GW search window, so the statistical uncertainty is reduced when scaling the measured rate to the expected background contribution.

These values are summarized in Table 6.7.

Quantity	PPO+BHT	bisMSB	Combined
Background livetime [s]	4.20×10^6	3.87×10^7	—
Tagged IBD candidates	16	200	—
IBD background rate [s^{-1}]	$(3.81 \pm 0.95) \times 10^{-6}$	$(5.16 \pm 0.36) \times 10^{-6}$	—
GW coincidence windows	16	110	—
Expected background per GW window	$(7.62 \pm 1.90) \times 10^{-3}$	$(1.03 \pm 0.07) \times 10^{-2}$	—
Total expected background	0.122 ± 0.031	1.13 ± 0.08	1.25 ± 0.09

Table 6.7: Summary of the data-driven IBD background estimate for the PPO+BHT and bisMSB scintillator phases. The expected background is calculated from the measured IBD candidate rate in the background-only dataset and scaled to the total livetime contained within the ±1000 s GW coincidence windows. Uncertainties correspond to the statistical uncertainty from the number of IBD candidates observed in the background-only datasets.

As a cross-check, the local sideband background estimate, the approach used by Borexino in their analysis, was compared to the background rate measured using the full background-only dataset. The local sideband is defined using the ±5000 s region surrounding each GW trigger, excluding the central blinded ±1000 s signal window. This method provides a background estimate local to the GW events and is sensitive to possible time-dependent variations in the detector background.

Such variations could arise from changes in detector conditions, periods of increased cosmogenic activity, changes in detector noise rates, time-dependent radioactive backgrounds, or changes in reactor antineutrino flux. A local sideband approach is advantageous if these variations are significant

because the sideband samples detector conditions close in time to the GW coincidence window.

For a 10 day subset of the bisMSB background-only dataset, the local sideband contains six IBD candidates over a livetime of 911184 s, giving a background rate of

$$R_{\text{sideband}} = (6.58 \pm 2.69) \times 10^{-6} \text{ pairs/s} \tag{6.42}$$

The full background-only dataset contains 200 IBD candidates over a livetime of 3.89×10^7 s, corresponding to

$$R_{\text{full}} = (5.15 \pm 0.36) \times 10^{-6} \text{ pairs/s} \tag{6.43}$$

The compatibility between the two measurements is quantified using

$$Z = \frac{|R_{\text{sideband}} - R_{\text{full}}|}{\sqrt{\sigma^2_{\text{sideband}} + \sigma^2_{\text{full}}}} \tag{6.44}$$

This gives

$$Z = 0.53 \tag{6.45}$$

indicating that the two background estimates agree within one standard deviation. Therefore, no statistically significant variation in the IBD background rate is observed near the GW trigger times.

Although the two methods are consistent, the local sideband contains only six IBD candidates and is therefore statistically limited, with a fractional uncertainty of approximately

$$\frac{\sigma_R}{R} \approx \frac{1}{\sqrt{6}} \approx 41\% \tag{6.46}$$

In comparison, the full background-only dataset contains 200 candidates, reducing the statistical uncertainty to approximately 7%. The agreement between the local sideband and full-dataset measurements demonstrates that the IBD background rate is stable within the statistical precision

of the sideband test. Therefore, the full background-only dataset can be used without introducing evidence of a time-dependent bias, while providing a more precise estimate of the expected IBD background rate.

Appendix A contains the list of PPO+BHT and bisMSB background IBD candidates.

6.7.4 Sensitivity Optimization

The IBD selection criteria were optimized prior to unblinding by evaluating the expected sensitivity of the analysis under different cut configurations. A multi-dimensional scan was performed over the FV, prompt-delayed spatial separation, neutron capture time window, and prompt energy range. Since the expected signal rate from compact binary mergers is unknown, the optimization was performed assuming the background-only hypothesis. The goal was to determine the selection criteria that would provide the strongest expected upper limit on the neutrino fluence in the absence of a detected signal.

The optimized quantities were the FV radius, prompt-delayed spatial separation, neutron capture time window, and prompt energy range. The scanned parameters included variations around the nominal reactor antineutrino selection:

- FV radius (R_{FV})
- Prompt-delayed separation (Δr)
- Prompt-delayed coincidence time (Δt)
- Maximum prompt energy

For each selection configuration, the signal efficiency was determined using flat spectrum IBD MC simulations. The efficiency was calculated as

$$\epsilon = \frac{N_{\mathrm{pass}}}{N_{\mathrm{FV}}} \tag{6.47}$$

where N_{FV} is the number of generated IBD interactions with true positions inside the FV and N_{pass}

is the number satisfying the full delayed-coincidence selection.

The MC scan showed that the delayed-coincidence efficiency was largely unchanged between FVs of 5700 mm and 5800 mm, with efficiencies of approximately 87% for both selections. The efficiency reached a plateau for coincidence windows near 2000 μs and prompt-delayed spatial separations near 2500 mm, indicating that nearly all neutron captures were retained with these selections.

The expected background was evaluated using a 17-day background-only data subset from the PPO+BHT phase, with all GW-coincident runs removed. Accidental coincidences were estimated using a time-scrambling technique, where event times were randomized and the IBD selection was repeated over 50 iterations. This procedure preserves the single-event rates and energy distributions while removing physical time correlations between events.

For a fixed $\Delta r = 2500$ mm, the expected accidental background remained very small for all tested coincidence windows. Increasing the coincidence time from 1000 μs to 2000 μs increased the expected accidental rate only slightly, while improving the neutron capture efficiency. Therefore, the final selection uses

$$\Delta t < 2000 \ \mu\text{s} \tag{6.48}$$

Similarly, the spatial separation requirement

$$\Delta r < 2500 \text{ mm} \tag{6.49}$$

was retained because it provides high neutron capture efficiency while suppressing accidental coincidences.

The FV selection was evaluated by comparing the expected fluence sensitivity for different radii. For each configuration, the expected 90% confidence level event upper limit, N_{90}, was calculated using the Feldman-Cousins approach based on the expected background.

The sensitivity metric was proportional to

$$\Phi_{90} \propto \frac{N_{90}}{N_p \epsilon} \tag{6.50}$$

where N_p is the number of target protons inside the FV and ϵ is the signal efficiency.

A larger FV increases the number of target protons and therefore improves the statistical sensitivity. The 5800 mm FV was found to improve the expected fluence limit by approximately 5% due to the increased target mass. However, this improvement is comparable to the expected change in background rate and does not include additional systematic uncertainties associated with reconstruction near the AV.

Moving closer to the AV increases sensitivity to position reconstruction uncertainties and external backgrounds. Assuming an approximately uniform background distribution, the expected background scales with detector volume,

$$\frac{B_{5800}}{B_{5700}} \approx \left(\frac{5800}{5700}\right)^3 \approx 1.05 \tag{6.51}$$

corresponding to a 5% increase in background expectation.

Because the gain in expected sensitivity was small and the 5700 mm FV has stronger validation from the reactor antineutrino analysis, the final selection adopts

$$R_{\mathrm{FV}} < 5700 \text{ mm} \tag{6.52}$$

The same optimization procedure was repeated for the bisMSB dataset with a 10 day livetime and produced consistent results, so the same selection criteria are used for both detector phases.

The prompt energy range was extended relative to the reactor antineutrino selection because the neutrino energy spectrum from compact binary mergers is uncertain. Increasing the prompt energy upper bound to 50.0 MeV significantly improves the acceptance for higher-energy astrophysical

neutrinos while introducing a negligible increase in the observed IBD-like background rate.

6.8 IBD Results

After the event selection, background estimation procedure, and coincidence window construction were finalized, the analysis chain was validated using blinded data before examining the true GW-coincident windows. This section presents the final validation tests, the unblinded IBD search results, and the resulting neutrino fluence constraints.

6.8.1 Blind Analysis Validation

Before unblinding the true GW-coincident data, the complete analysis chain was validated using fake GW triggers. These tests were designed to verify every step of the search procedure, including coincidence window construction, IBD tagging, background estimation, Feldman-Cousins upper limit calculation, and conversion to a neutrino fluence limit.

A set of 12 runs from the PPO+BHT dataset were randomly selected from the run range 309448-310637. These runs did not contain any confirmed LVK GW candidates and were treated as fake GW-coincident runs. The selected validation runs were

309481, 309495, 309507, 309511, 309561, 309563,
309600, 309601, 309603, 309605, 309610, 309820

Since these runs were not associated with real GW events, artificial GW trigger times were assigned. The fake GW trigger time was chosen as the midpoint of each run to ensure maximal coverage of the coincidence window during validation.

For each fake GW trigger, a ± 1000 s coincidence window was constructed around the artificial GW trigger time. This represents the region where neutrino candidates would be searched for in the real analysis. The IBD selection described in Subsection 6.7.1 was then applied, and the number of observed IBD candidates inside the coincidence window was recorded.

The fake GW analysis was completed without identifying any IBD candidates inside the coincidence windows. The expected background contribution was calculated using the background-only dataset

described in Section 6.7.3. The observed number of events and expected background were then used to calculate the 90% CL upper limit on the number of signal events, N_{90}, using the same statistical procedure adopted for the final analysis.

The corresponding neutrino fluence upper limit was then calculated using the signal efficiency obtained from MC simulations. This validation confirmed that the event selection, statistical treatment, and fluence-limit calculation were functioning as expected before accessing the true GW-coincident data.

The same validation procedure was repeated for the bisMSB dataset with the following fake GW runs

354100, 355210, 357955, 358430, 359010, 360010,
361100, 362202, 363508, 364500, 366103, 370000

The fake trigger analysis again found no IBD candidates in the coincidence window, confirming that the pipeline was stable across both scintillator configurations.

After these validation tests, the analysis procedure was frozen and applied to the blinded GW-coincident datasets.

6.8.2 Single Run Unblinding

After validating the analysis chain using fake GW triggers, the first stage of unblinding was performed using individual GW-coincident runs. This provided a final verification that the coincidence window selection, background estimation, and fluence-limit calculation behaved as expected on real GW-coincident data before unblinding the remaining GW-coincident dataset.

The first unblinded run was PPO run 310048, corresponding to the GW candidate GW230609_010824 from the LVK O4a catalog. The same procedure developed using the fake GW studies was applied: a $\pm$1000 s coincidence window was constructed around the actual GW trigger time, the IBD selection was applied, and the number of observed candidates was compared to the expected background.

No IBD candidates were observed in the coincidence window. Therefore, the analysis chain proceeded through the final step and the fluence limit calculation procedure was verified.

The same validation was repeated for the bisMSB phase using run 355014. A validation of the corrected timing procedure detailed in Subsection 6.5.1 was also performed. The corrected timing procedure successfully reproduced the expected coincidence window, confirming the analysis workflow before unblinding the remaining GW-coincident data.

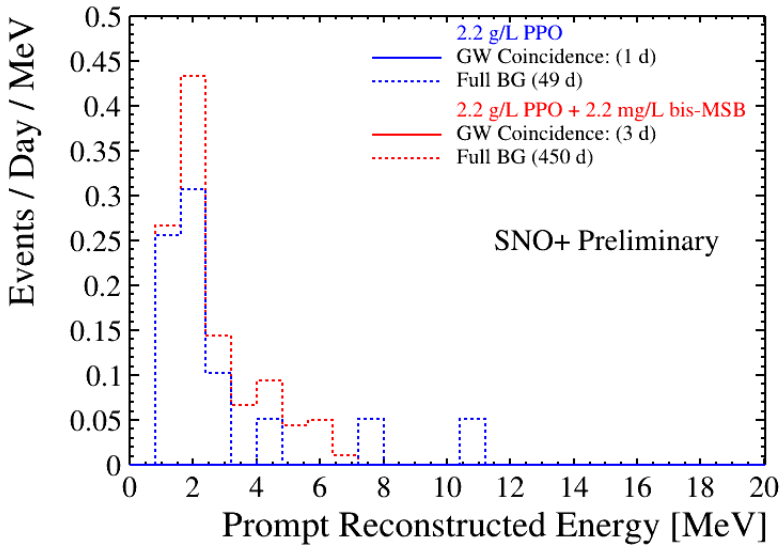
6.8.3 Full Unblinding

Following the single-run validation studies, the full GW-coincident dataset was unblinded. The full dataset consisted of 143 GW candidates overlapping stable SNO+ scintillator data-taking periods, including 25 candidates in the PPO+BHT phase and 118 candidates in the bisMSB phase. This sample includes 17 candidates classified by LVK as terrestrial or unknown, which were retained during unblinding but excluded from the final compact binary merger fluence calculation because no coincident neutrino excess was observed. The PPO+BHT and bisMSB detector configurations were analyzed independently due to their different optical responses, but the final results from both phases are combined after applying the corresponding detector efficiencies.

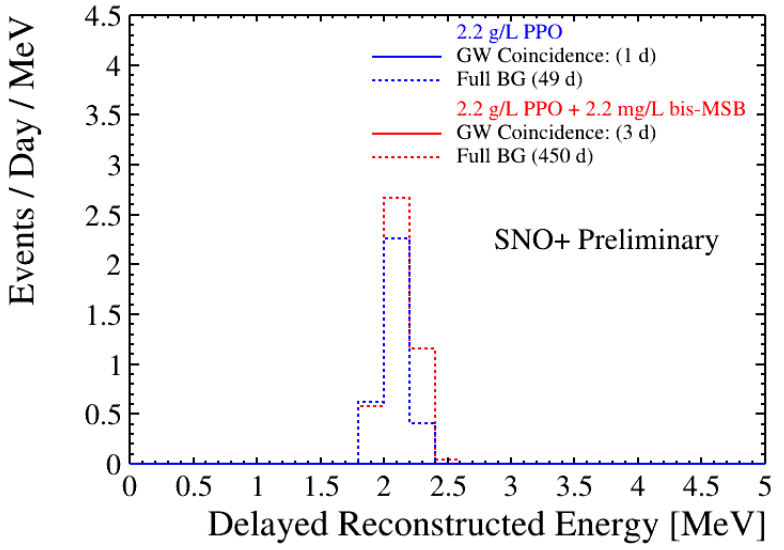
No IBD candidates were observed within any of the GW coincidence windows. The reconstructed prompt and delayed energy distributions for the GW-coincident and background-only runs are shown in Figure 6.9. The solid distributions correspond to events within the ±1000 s GW coincidence windows, while the dashed distributions show IBD candidates identified in the background-only dataset. This null observation is consistent with the expected background-only hypothesis. For the total expected background of 1.25 events across all GW coincidence windows, the probability of observing zero candidates is

$$P(0|1.25) = e^{-1.25} = 0.287 \tag{6.53}$$

Therefore, approximately 29% of background-only experiments would observe zero events. The observed result represents a modest downward fluctuation relative to the expected background of 1.25 events and is statistically compatible with the background-only hypothesis.



(a) Prompt Candidates



(b) Delayed Candidates

Figure 6.9: Reconstructed energy distributions of prompt (top) and delayed (bottom) IBD candidates. The dashed distributions correspond to IBD candidates identified in the background-only dataset, while the solid distributions correspond to candidates found within the ±1000 s GW coincidence windows. No IBD candidates were observed in the GW-coincident sample.

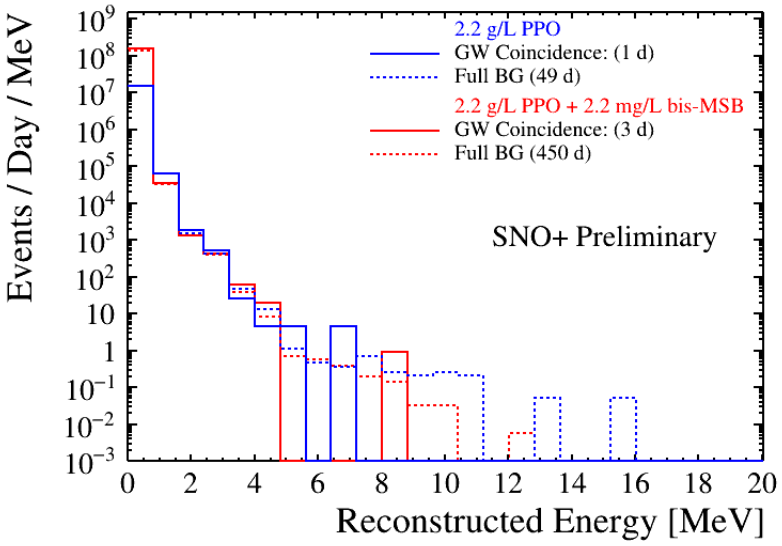


Figure 6.10: Singles distribution of events in the PPO+BHT (blue) and bisMSB (red) phases. The dashed distributions correspond to the background-only dataset, while the solid distributions show events within the ±1000 s GW coincidence windows.

In addition to the dedicated IBD coincidence search, the reconstructed energy distribution of all single events within the GW coincidence windows was compared with the corresponding background-only distribution, as shown in Figure 6.10. This provides a model-independent cross-check for possible excesses that may not satisfy the IBD delayed coincidence selection. Such events could arise from other neutrino interaction channels, including neutrino interactions on ^{12}C, which produce single-event signatures. No significant excess above the expected background distribution was observed.

The IBD candidates tagged in the full background-only windows in Figure 6.9 agree with the reactor antineutrino and solar analyses. The expected number of background events was calculated from the data-driven background rates described in Subsection 6.7.3. The final results are summarized in Table 6.8.

Dataset	GW Candidates	Background Expectation	Observed	N_{90}
PPO+BHT	16	0.12	0	–
bisMSB	110	1.13	0	–
Combined	126	1.25	0	1.47

Table 6.8: Summary of the final astrophysical GW candidate IBD unblinding results. The expected background is calculated using the data-driven IBD background rates scaled to the total GW coincidence livetime. The combined Feldman–Cousins 90% confidence level upper limit on the number of signal events is $N_{90} = 1.47$.

6.8.4 Fluence Upper Limits

The absence of observed IBD candidates in the GW coincidence windows is converted into an upper limit on the electron antineutrino fluence from compact binary mergers. The fluence calculation depends on the assumed neutrino emission spectrum, the IBD interaction cross section, the number of target protons in the FV, and the energy-dependent IBD selection efficiency determined from MC simulations.

For an individual GW candidate i and an assumed normalized neutrino spectrum $f(E_\nu)$, the 90% confidence level fluence upper limit is calculated as

$$\Phi_{90,i} = \frac{N_{90,i}}{N_p \int_{E_{\min}}^{E_{\max}} f(E_\nu)\sigma_{\mathrm{IBD}}(E_\nu)\epsilon_i(E_\nu)dE_\nu} \tag{6.54}$$

where $N_{90,i}$ is the upper limit on the number of signal events, N_p is the number of free protons in the FV, $f(E_\nu)$ is the normalized neutrino spectrum, $\sigma_{\mathrm{IBD}}(E_\nu)$ is the IBD cross section, and $\epsilon_i(E_\nu)$ is the run-dependent IBD selection efficiency. The spectrum is normalized such that

$$\int_{E_{\min}}^{E_{\max}} f(E_\nu)\, dE_\nu = 1 \tag{6.55}$$

For the model-independent fluence calculation, the flat spectrum MC sample is used to determine the energy-dependent detection efficiency. For a monoenergetic electron antineutrino spectrum,

Equation 6.54 reduces to

$$\Phi_{90,i}(E_\nu) = \frac{N_{90,i}}{N_p \sigma_{\mathrm{IBD}}(E_\nu)\epsilon_i(E_\nu)} \tag{6.56}$$

For the combined analysis, a common (average per-GW) fluence at Earth is assumed for each GW candidate. The expected signal contributions from the individual candidates are therefore summed, yielding a stacked upper limit on this common fluence. For a model spectrum, the stacked common-fluence upper limit is

$$\Phi_{90}^{\mathrm{stack}} = \frac{N_{90}^{\mathrm{stack}}}{N_p \sum_{i=1}^{N_{\mathrm{GW}}} \int_{E_{\mathrm{min}}}^{E_{\mathrm{max}}} f(E_\nu)\sigma_{\mathrm{IBD}}(E_\nu)\epsilon_i(E_\nu)dE_\nu} \tag{6.57}$$

For the monoenergetic case, this becomes

$$\Phi_{90}^{\mathrm{stack}}(E_\nu) = \frac{N_{90}^{\mathrm{stack}}}{N_p \sigma_{\mathrm{IBD}}(E_\nu) \sum_{i=1}^{N_{\mathrm{GW}}} \epsilon_i(E_\nu)} \tag{6.58}$$

The final combined fluence analysis uses the PPO+BHT and bisMSB datasets together, corresponding to the 126 astrophysical GW candidates. Since zero IBD candidates are observed with a nominal expected background of 1.25 events, the Feldman-Cousins method gives

$$N_{90}^{\mathrm{stack}} = 1.47 \tag{6.59}$$

The uncertainty on the expected background rate is not included in the Feldman-Cousins construction. From the statistical uncertainties on the PPO+BHT and bisMSB background measurements, the combined background expectation is $b = 1.25 \pm 0.09$. Variations within this uncertainty have a negligible impact on the resulting upper limit because the background uncertainty is small compared with the Poisson uncertainty associated with the low number of expected and observed events.

For the 5.7 m FV, the number of free protons is

$$N_p = 4.84 \times 10^{31} \tag{6.60}$$

The IBD cross section is taken from the Vogel and Beacom prescription implemented in RAT [112]. The selection efficiency is determined from the flat spectrum IBD MC simulation as

$$\epsilon(E_k) = \frac{N_{\text{pass}}(E_k)}{N_{\text{FV}}(E_k)} \tag{6.61}$$

where $N_{\text{FV}}(E_k)$ is the number of generated IBD interactions within the FV in energy bin k, and $N_{\text{pass}}(E_k)$ is the number passing the full IBD selection. The efficiency includes reconstruction, FV migration, and delayed-coincidence selection effects.

Equation 6.54 is evaluated for the Fermi-Dirac and GKVM spectra, while Equation 6.56 is evaluated at each neutrino energy using the flat spectrum MC simulation. The final limits are obtained by summing the run-dependent sensitivities according to Equations 6.57 and 6.58. The resulting spectrum-integrated stacked limits are summarized in Table 6.9, and selected monoenergetic stacked limits are shown in Table 6.10.

Spectrum Model	Mean ϵ_{pair}	Stacked (per-GW) Φ_{90} [cm^{-2}]	Single-GW Φ_{90} [cm^{-2}]
GKVM	0.8664 ± 0.0003	1.18×10^7	2.46×10^9
Fermi–Dirac	0.8696 ± 0.0003	1.92×10^7	4.04×10^9

Table 6.9: Mean spectrum-weighted IBD pair selection efficiencies and 90% confidence level fluence upper limits for the stacked analysis using all 126 GW candidates and for the individual GW candidate `S250206dm` (SNO+ run 366227). The stacked (average per-GW) common-fluence limits are calculated by summing the run-dependent sensitivities of all 126 GW candidates under the assumption of a common neutrino fluence at Earth, using $N_{90}^{\text{stack}} = 1.47$. The individual-GW limits use the single-window Feldman-Cousins upper limit of $N_{90} = 2.44$. The efficiency uncertainties include only MC statistical uncertainties.

The monoenergetic stacked (average per-GW) common-fluence limit is shown in Figure 6.11. The SNO+ result is obtained by summing the run-dependent sensitivities of all 126 astrophysical GW candidates under the assumption that each candidate produces the same electron antineutrino

E_ν [MeV]	Mean $\epsilon_{\text{pair}}(E_\nu)$	Stacked (per-GW) $\Phi_{90}(E_\nu)$ [cm^{-2}]	Single-GW $\Phi_{90}(E_\nu)$ [cm^{-2}]
2	0.882 ± 0.003	1.46×10^{10}	3.07×10^{12}
5	0.890 ± 0.001	2.28×10^{8}	4.73×10^{10}
10	0.881 ± 0.002	4.17×10^{7}	8.83×10^{9}
20	0.872 ± 0.004	9.90×10^{6}	2.08×10^{9}
40	0.852 ± 0.004	2.84×10^{6}	6.47×10^{8}
50	0.862 ± 0.004	1.98×10^{6}	4.19×10^{8}

Table 6.10: Selected monoenergetic IBD common-fluence upper limits for the stacked sample of 126 GW candidates. The listed efficiencies are the mean run-dependent pair selection efficiencies obtained from the flat spectrum MC simulation, whereas the stacked fluence limits use the summed sensitivity of all 126 GW candidates. The final column gives the individual-GW fluence limits for the GW candidate `S250206dm` (SNO+ run 366227), calculated using the single-window Feldman-Cousins upper limit of $N_{90} = 2.44$. The quoted efficiency uncertainties correspond to the binomial MC statistical uncertainty.

fluence at Earth. The resulting limit is therefore the average (per-GW) fluence constraint from the stacked sample following the convention adopted by Borexino [107] and should not be interpreted as the limit from one individual GW candidate.

To obtain the merger-classification limits, the expected background is also divided by detector phase and merger class. Since no IBD candidates are observed in either subset, the corresponding Feldman-Cousins upper limits are determined from the subset-specific background expectations. The values used in the fluence calculation are summarized in Table 6.11.

Sample	N_{GW}	n_{obs}	b	N_{90}
All	126	0	1.252	1.47
BBH	122	0	1.216	1.49
NSBH	4	0	0.0358	2.40

Table 6.11: Observed IBD candidate counts, expected backgrounds, and 90% confidence level Feldman-Cousins signal upper limits for the full GW sample and the merger-classification subsets. The background expectations are calculated separately for the PPO+BHT and bisMSB detector phases and then summed within each merger class.

The stacked calculation is also performed separately for the LVK merger classifications, as shown in Figure 6.12. For each classification, the run-dependent sensitivities of the candidates in that subset are summed, and the subset-specific Feldman-Cousins upper limit from Table 6.11 is used. The BBH sample gives the strongest limit because it contains 122 of the 126 selected GW candidates,

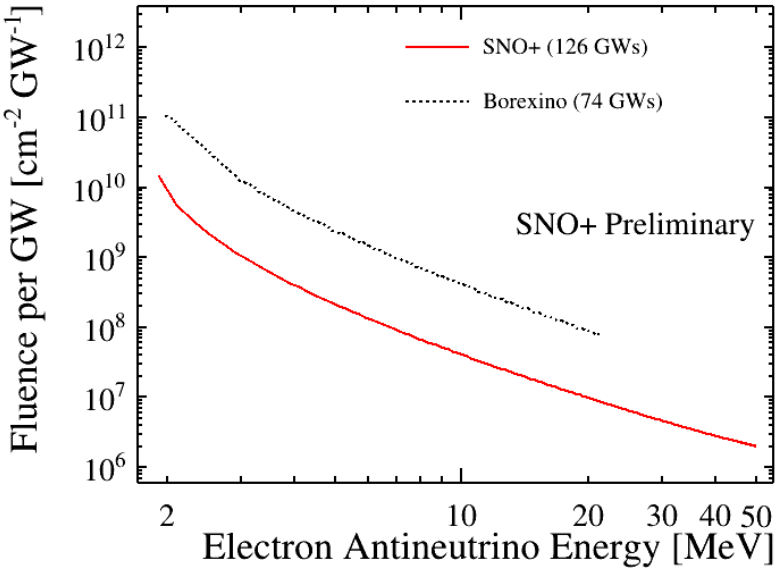


Figure 6.11: SNO+ 90% confidence level monoenergetic IBD stacked common-fluence upper limit obtained using all 126 GW candidates (red), compared with the stacked Borexino result using 74 GW candidates (black). Both analyses report stacked average (per-GW) fluence limits under the assumption that every GW candidate produces the same neutrino fluence at Earth.

whereas the NS-BH sample contains only four candidates. The smaller NS-BH background results in a larger value of N_{90}^{NSBH}, which further weakens the NS-BH fluence limit relative to the BBH limit. The difference between the curves primarily reflects the accumulated detector exposure and should not be interpreted as evidence that an individual BBH merger is more strongly constrained than an individual NS-BH merger.

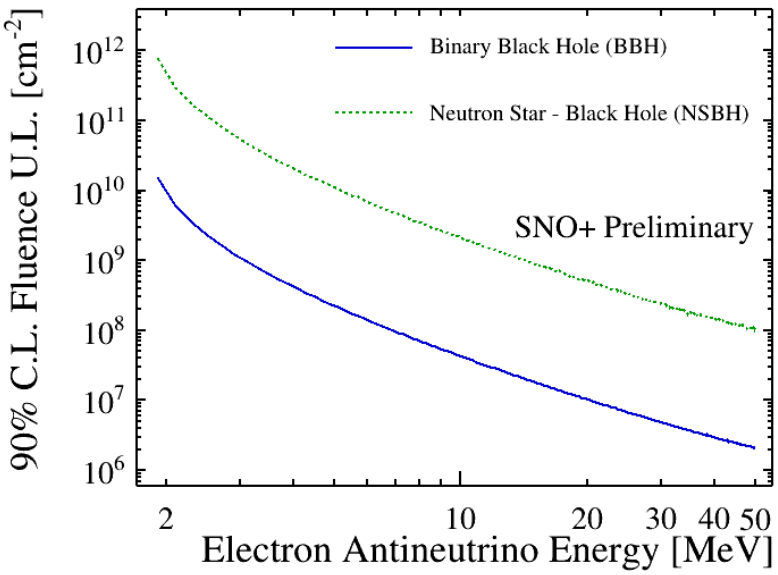


Figure 6.12: SNO+ 90% confidence level monoenergetic IBD stacked common-fluence upper limits separated by LVK merger classification. The BBH result combines 122 GW candidates and uses $N_{90}^{\mathrm{BBH}} = 1.49$, while the NS-BH result combines four candidates and uses $N_{90}^{\mathrm{NSBH}} = 2.40$.

Previous searches for MeV neutrinos in temporal coincidence with GW events have been performed by Borexino (2023), KamLAND (2020), and Super-Kamiokande (2021) [107–109]. In the absence of a coincident neutrino signal, these experiments placed upper limits on the neutrino fluence associated with individual GW candidates and stacked GW samples.

For comparison with published individual-event limits, an individual-GW SNO+ fluence limit is also calculated. The detector response corresponding to SNO+ run 366227, coincident with the NS-BH candidate `S250206dm`, is used, and the fluence curve is recalculated using the single-window Feldman-Cousins upper limit of $N_{90} = 2.44$, appropriate for zero observed events and negligible expected

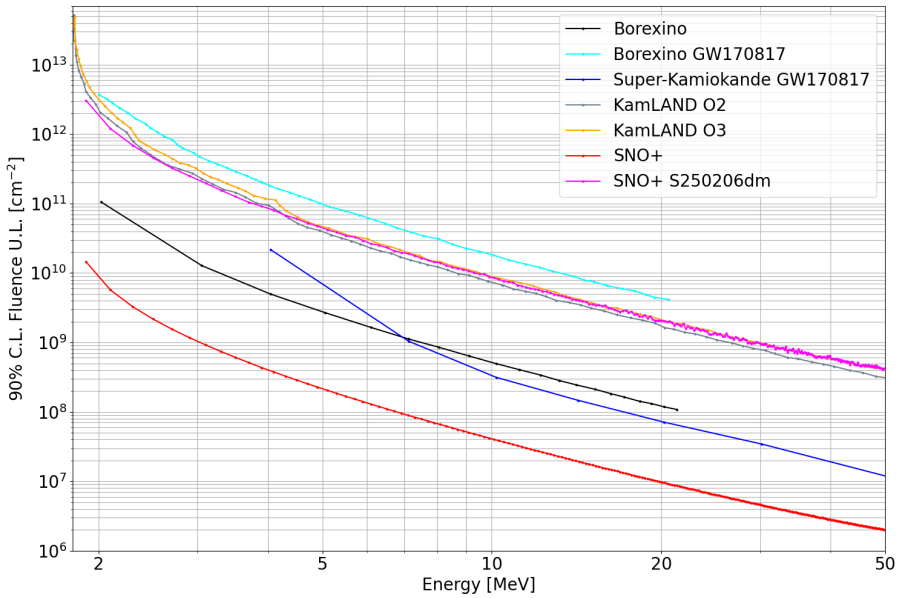


Figure 6.13: Comparison of 90% confidence level monoenergetic $\bar{\nu}_e$ fluence upper limits. The SNO+ result (red) is the stacked common-fluence limit from 126 GW candidates, and the Borexino result (black) is the corresponding stacked limit from 74 candidates. The SNO+ individual-GW result (magenta) is shown together with the published individual-event limits from Borexino (cyan), KamLAND (slate gray and orange), and Super-Kamiokande (blue).

background. Unlike the stacked common-fluence result, this curve represents the sensitivity of a single GW coincidence window and does not benefit from the summed exposure of the full 126-candidate sample.

Figure 6.13 compares both stacked and individual-event monoenergetic IBD fluence limits. The SNO+ and Borexino stacked (average per-GW) results combine 126 and 74 GW candidates, respectively, under a common-fluence assumption. The SNO+ individual curve is calculated for one selected GW coincidence window using its run-dependent detector efficiency and a single-window upper limit of $N_{90} = 2.44$. The Borexino, KamLAND, and Super-Kamiokande individual-event curves are shown for the corresponding published GW candidates. The stacked and individual curves represent different statistical hypotheses and are therefore compared separately.

All three experiments derive limits using the IBD interaction channel. Borexino and KamLAND report monoenergetic electron antineutrino fluence limits, while Super-Kamiokande reports limits over

a broad range of assumed neutrino energies. These model-independent limits provide a comparison of detector sensitivity without assuming a specific astrophysical emission spectrum. The Borexino stacked result previously provided the strongest constraints among previous GW-coincident MeV neutrino searches in the few-MeV energy region.

The improved low-energy sensitivity of SNO+ relative to previous searches arises from several factors. Compared with Borexino, SNO+ has a larger target mass, with a fiducial scintillator mass of approximately 668 tonnes compared with 145 tonnes in Borexino, corresponding to a target-mass ratio of approximately 4.6. The SNO+ stacked sample also contains 126 GW candidates compared with 74 in the Borexino sample, providing an additional exposure ratio of approximately 1.7 under the common-fluence assumption.

The inclusion of the measured background in the Feldman-Cousins construction further strengthens the numerical upper limit. SNO+ observes zero candidates with an expected background of 1.25 events, giving $N_{90}^{stack} = 1.47$, compared with $N_{90}^{stack} = 2.44$ for zero observed events and negligible background.

The IBD selection efficiencies are comparable between the two detectors, with SNO+ achieving an efficiency of approximately 88%.

Combining these effects gives an expected improvement in the stacked (average per-GW) common-fluence sensitivity of approximately

$$4.6 \times 1.7 \times \frac{2.44}{1.47} \times \frac{0.881}{0.842} \approx 14 \tag{6.62}$$

This simple scaling predicts approximately an order-of-magnitude improvement relative to the Borexino stacked fluence limits, consistent with the comparison shown in Figure 6.11. The scaling is intended only as an approximate estimate, since the final limits also depend on the detailed energy-dependent efficiencies and the distribution of GW candidates across detector run conditions.

The dependence of the final sensitivity on the observed number of coincident candidates was also

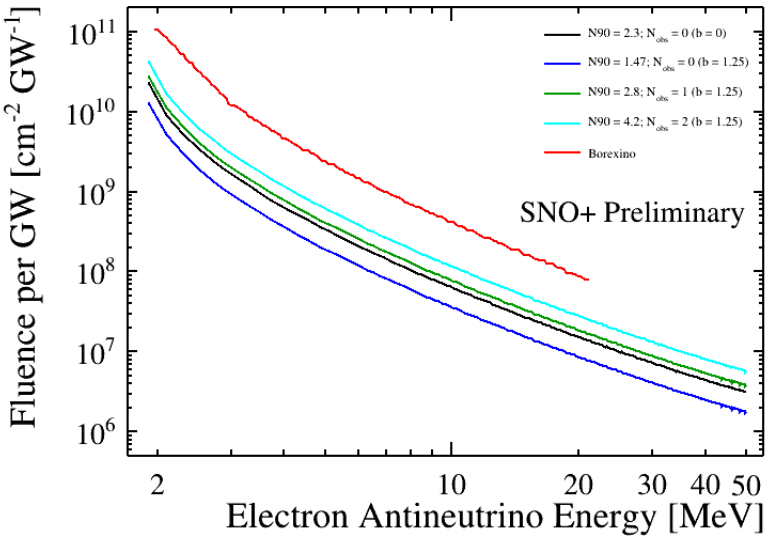


Figure 6.14: Effect of different possible unblinding outcomes on the SNO+ 90% confidence level IBD fluence upper limits. Curves correspond to different assumed numbers of observed events in the GW coincidence windows, with the upper limits calculated using the Feldman-Cousins approach.

evaluated. The original projected sensitivity assumed zero observed candidates and negligible background, corresponding to the standard Poisson upper limit of $N_{90} = 2.3$.

The final analysis instead uses the Feldman-Cousins construction with the measured background expectation. Figure 6.14 shows the resulting fluence limits for different possible unblinding outcomes. As expected, additional observed candidates increase the value of N_{90} and therefore weaken the resulting fluence constraints.

6.8.5 Neutrino Energy Constraints

The fluence upper limits calculated in Subsection 6.8.4 constrain the number of electron antineutrinos reaching Earth. To compare these limits with theoretical predictions, the model-dependent fluence constraints are converted into upper limits on the isotropic-equivalent energy emitted in electron antineutrinos.

For an individual GW candidate at luminosity distance d_i, the isotropic-equivalent energy limit is

$$E^{90}_{\mathrm{rad},i} = 4\pi d_i^2 \, \Phi_{90,i} \, \langle E_\nu \rangle \left(1.602 \times 10^{-6}\right) \tag{6.63}$$

where $\Phi_{90,i}$ is the model-integrated fluence upper limit in cm^{-2}, $\langle E_\nu \rangle$ is the mean electron-antineutrino energy in MeV, and the factor 1.602×10^{-6} converts MeV to erg.

The stacked fluence analysis instead assumes a common fluence at Earth for every candidate in a merger category. Since the stacked fluence limit already contains the summed sensitivity of the candidates in the sample, a normalized effective distance is used to convert the stacked fluence into a common isotropic-equivalent emitted-energy constraint:

$$D_{\mathrm{eff}} = \left(\frac{N_{\mathrm{GW}}}{\sum_{i=1}^{N_{\mathrm{GW}}} d_i^{-2}} \right)^{1/2} \tag{6.64}$$

This definition is matched to the stacked common-fluence normalization. For approximately equal detector sensitivity among GW candidates, it is algebraically equivalent to the source-class formulation used by KamLAND, in which the fluence is not first reduced by the number of candidates and the effective distance is defined without the N_{GW} factor. The two formulations give the same emitted-energy constraint when the fluence and effective-distance conventions are used consistently.

The normalized effective distance is an inverse-square-weighted characteristic distance of the sample. Nearby GW candidates receive greater weight through the inverse-square (d_i^{-2}) distance dependence. The normalization by N_{GW} prevents the number of candidates from being counted a second time after it has already entered the stacked fluence limit. The effective distances for the full, BBH, and NS-BH samples are approximately 926, 1106, and 291 Mpc, respectively, as shown in Figure 6.15.

Given the stacked model-dependent fluence upper limit $\Phi^{\mathrm{stack}}_{90}$ and the corresponding normalized effective distance, the upper limit on the common isotropic-equivalent energy emitted in electron

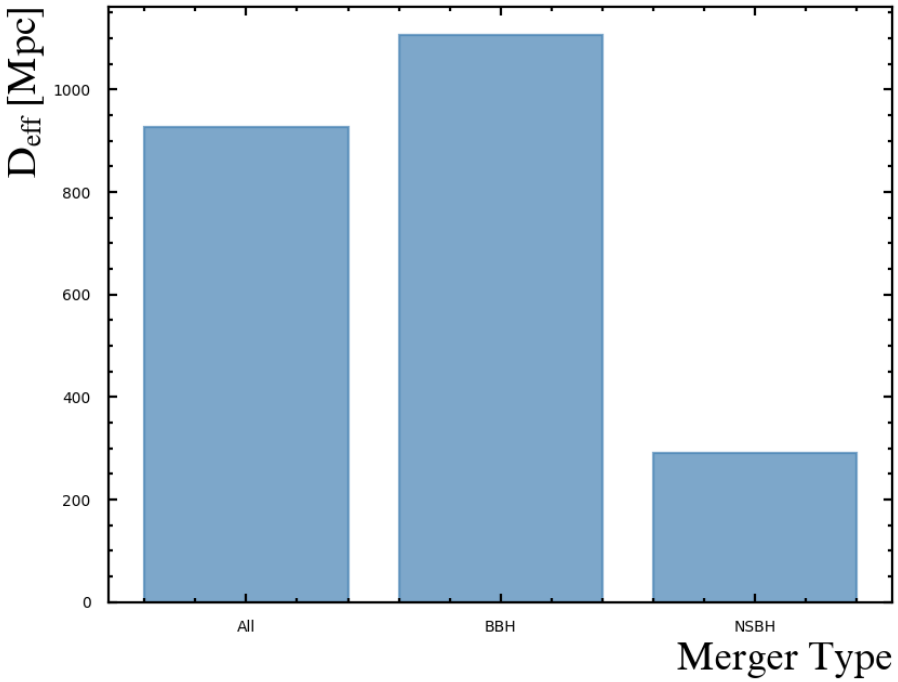


Figure 6.15: Normalized effective distances used to convert the stacked common-fluence limits into isotropic-equivalent emitted-energy constraints. The values are calculated using $D_{\rm eff}^2 = N_{\rm GW}/\sum_i d_i^{-2}$ for the full GW sample ("All", $N = 126$), the BBH sample ($N = 122$), and the NS-BH sample ($N = 4$). The relatively small NS-BH effective distance reflects the proximity of the four NS-BH candidates compared with the BBH population.

antineutrinos is

$$E_{\rm rad}^{90} = 4\pi D_{\rm eff}^2 \, \Phi_{90}^{\rm stack} \, \langle E_\nu \rangle \left(1.602 \times 10^{-6}\right) \tag{6.65}$$

where $\langle E_\nu \rangle$ is the mean antineutrino energy predicted by the assumed emission spectrum in MeV, and the factor 1.602×10^{-6} converts MeV to erg.

Two representative MeV electron-antineutrino spectra are considered: a Fermi-Dirac spectrum with $\langle E_\nu \rangle = 12.7$ MeV and the GKVM CCSN-inspired spectrum with $\langle E_\nu \rangle = 16.5$ MeV. The fluence limit is evaluated separately for each model because the IBD cross section and energy-dependent selection efficiency are weighted differently by the two spectral shapes.

The normalized effective distances and the corresponding stacked emitted-energy limits are summarized in Table 6.12. Figure 6.16 provides a graphical comparison of the results for the All, BBH, and NS-BH samples under the GKVM and Fermi-Dirac spectral assumptions.

Merger Type	$D_{\rm eff}$ [Mpc]	GKVM $E_{\rm rad}^{90}$ [erg]	FD $E_{\rm rad}^{90}$ [erg]
All	926	3.19×10^{58}	4.03×10^{58}
BBH	1106	4.76×10^{58}	6.02×10^{58}
NS-BH	291	1.63×10^{59}	2.06×10^{59}

Table 6.12: Upper limits on the isotropic-equivalent energy emitted in electron antineutrinos for the stacked GW samples under the GKVM and Fermi-Dirac spectral assumptions. The normalized effective distance is calculated using Equation 6.64, and the emitted-energy limits are obtained using Equation 6.65.

Figure 6.16 compares the stacked isotropic-equivalent emitted-energy limits for the three merger categories. The ordering is determined by the product $D_{\rm eff}^2 \Phi_{90}$ rather than by the effective distance alone. Although the NS-BH sample has the smallest effective distance, it has a substantially weaker stacked fluence limit because it contains only four GW candidates and uses the subset-specific Feldman-Cousins upper limit $N_{90}^{\rm NSBH} = 2.40$. This reduction in accumulated exposure outweighs the advantage of the smaller effective distance.

For a fixed merger category, the difference between the GKVM and Fermi-Dirac results arises from both the model-dependent fluence limit and the mean neutrino energy. The GKVM spectrum gives

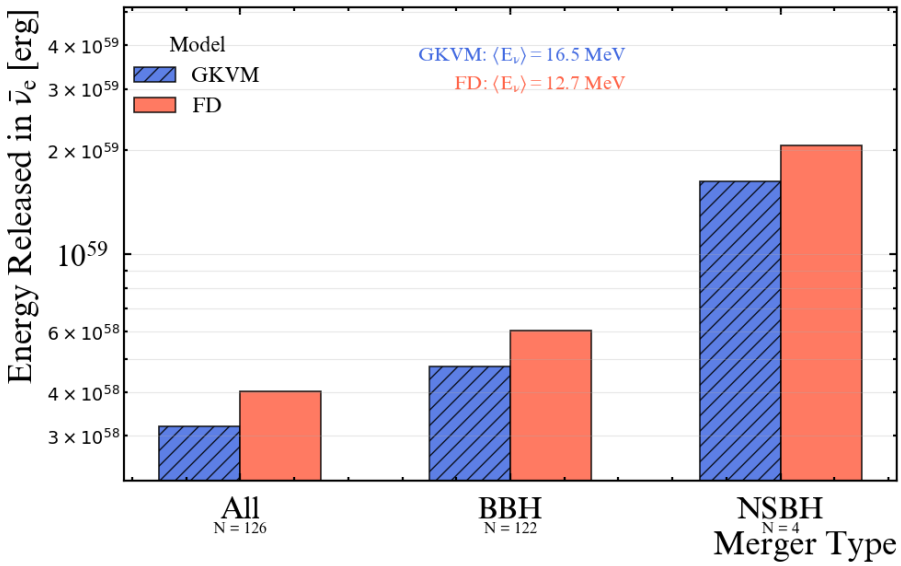


Figure 6.16: Upper limits on the common isotropic-equivalent energy emitted in electron antineutrinos for the full, BBH, and NS-BH stacked GW samples under the GKVM and Fermi-Dirac spectral assumptions. The limits use the stacked common-fluence constraints and the normalized effective distances defined in Equation 6.64.

the stronger energy constraint because its improved fluence sensitivity more than compensates for its larger mean neutrino energy.

An individual-source constraint is also calculated for the NS-BH candidate `S250206dm`, associated with SNO+ run 366227 and a reported luminosity distance of 349 Mpc. Using the individual-GW fluence limits and Equation 6.63, the resulting fluence and isotropic-equivalent emitted-energy limits are summarized in Table 6.13. Unlike the source-class limits, these values refer directly to one GW

Spectrum	Φ_{90} [cm^{-2}]	$E^{90}_{\rm rad}$ [erg]
GKVM	2.46×10^{9}	9.48×10^{59}
Fermi–Dirac	4.04×10^{9}	1.20×10^{60}

Table 6.13: Individual-GW fluence and isotropic-equivalent emitted-energy upper limits for the NS-BH candidate `S250206dm` (SNO+ run 366227, $d = 349$ Mpc).

candidate and do not depend on an effective-distance construction.

The resulting limits are many orders of magnitude larger than the approximately 10^{53} erg total neutrino energy released by a typical core-collapse supernova. They therefore do not constrain

standard CCSN-like neutrino emission from compact-binary mergers at the distances probed by the LVK O4 sample. This is expected because the GW candidates are typically located at distances of hundreds to thousands of Mpc, whereas current MeV neutrino detectors are sensitive to standard CCSN-like neutrino emission primarily from sources within the Local Group.

6.9 Neutrino-Proton ES Analysis

A complementary search was performed using neutrino-proton ES. Unlike the IBD channel, neutrino-proton ES is a NC interaction and therefore provides sensitivity to all neutrino flavors. However, the interaction produces only a single recoiling proton and does not have a delayed-coincidence signature. As a result, the analysis is limited by the significantly larger single-event background rate.

This search represents the first application of the neutrino-proton ES channel to a GW-coincident neutrino search. The goal of the analysis is to evaluate the achievable sensitivity using the existing scintillator dataset and establish the analysis framework for future searches.

The timing reconstruction, livetime calculation, and GW coincidence window construction are identical to those described in Section 6.5.1. Due to the higher background rate in the single-event sample, the optimized coincidence window was reduced from ± 1000 s to ± 50 s.

6.9.1 Event Selection and Optimization

Candidate neutrino-proton ES events are selected as single scintillation events in temporal coincidence with GW candidates. Events are required to pass the standard SNO+ data cleaning criteria and have valid energy and position reconstruction (described in Subsection 6.2.3).

The selection criteria were optimized using a subset of the background-only dataset with known GW-coincident periods removed. A 17 day PPO+BHT dataset and 14 day bisMSB dataset were used to scan combinations of FV, reconstructed energy range, and coincidence window size. The expected number of background events was calculated from the measured single-event background rate.

The expected Feldman-Cousins upper limit, $N_{90}(b)$, was then evaluated and the optimization parameter

$$\text{FOM} = \frac{N_{90}(b)}{N_p \epsilon} \tag{6.66}$$

was minimized. Here N_{90} is the expected Feldman-Cousins upper limit under the background-only hypothesis and ϵ is the signal efficiency.

This quantity is proportional to the expected fluence upper limit for a fixed neutrino energy, since

$$\Phi_{90}(E_\nu) = \frac{N_{90}}{N_p \sigma_{\nu p}(E_\nu) \epsilon(E_\nu)} \tag{6.67}$$

The optimized selection is summarized in Table 6.14:

Cuts	**Requirement**
Energy [MeV]	$0.5 < E_{\text{reco}} < 70$ MeV
Fiducial Volume [mm]	< 5500
Data Cleaning	Pass
Reconstruction Valid	True
BiPo Tagging & Applied	True

Table 6.14: Neutrino-proton ES selection criteria applied to both data and MC analyses.

The reconstructed energy range was chosen to maximize sensitivity to the quenched proton recoil spectrum expected from astrophysical neutrinos while removing low-energy radioactive backgrounds. The upper energy bound retains sensitivity to higher-energy neutrinos while introducing negligible additional background.

The coincidence window is reduced relative to the IBD analysis because the larger single-event background rate results in a stronger dependence on the searched livetime. A ± 50 s window provides the best expected sensitivity based on the optimization scan.

Additional rejection of radioactive backgrounds is achieved using BiPo tagging. This removes time-correlated decay sequences from the uranium and thorium chains that can produce low-energy backgrounds in the scintillator phase.

6.9.2 Signal Simulation and Efficiency

The neutrino-proton ES signal efficiency was evaluated using dedicated MC simulations. The simulation includes the neutrino-proton interaction, scintillation response, detector simulation, and event reconstruction.

A major difference between neutrino-proton ES and electron-like interactions is the effect of ionization quenching. Proton recoils have a large energy loss per unit distance, reducing the visible scintillation energy relative to the true recoil energy. This effect is modeled using Birks' law as described in Subsection 3.2.3.

Figure 6.17 shows the relationship between the incident neutrino energy and the reconstructed visible energy for simulated neutrino-proton ES events passing the analysis energy range. Because proton recoils are strongly quenched in liquid scintillator, the reconstructed visible energy is much lower than the incident neutrino energy. As a result, MeV-scale neutrinos populate the low reconstructed-energy region where single-event radioactive backgrounds are largest. Reaching a substantially cleaner reconstructed-energy region would require significantly higher incident neutrino energies.

The neutrino-proton ES generator was updated as part of this analysis to correct the implementation of the interaction cross section (described in Subsection 6.4.3). The corrected generator produces the expected proton recoil spectrum and allows the selection efficiency to be evaluated as a function of neutrino energy.

The signal efficiency is calculated using the fraction of generated events passing the complete analysis selection:

$$\epsilon(E_\nu) = \frac{N_{\text{pass}}(E_\nu)}{N_{\text{gen}}(E_\nu)} \tag{6.68}$$

where $N_{\text{gen}}(E_\nu)$ is the number of generated neutrino-proton ES events at neutrino energy E_ν, and $N_{\text{pass}}(E_\nu)$ is the number remaining after applying the energy, FV, data cleaning, reconstruction, and background tagging requirements.

The resulting efficiency includes losses from proton recoil quenching, detector threshold effects,

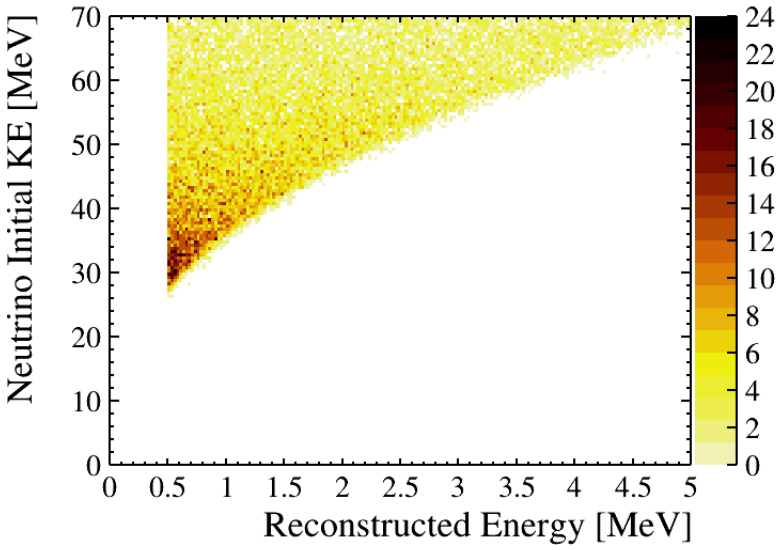


Figure 6.17: Simulated neutrino-proton ES reconstructed energy as a function of incident neutrino energy after applying the analysis energy range. The low reconstructed visible energies arise from ionization quenching of proton recoils in liquid scintillator.

reconstruction failures, and event selection cuts. These efficiencies are used when converting the observed number of events into neutrino fluence upper limits.

6.9.3 Background Estimation and Validation

Due to the large number of single events, the neutrino-proton ES background can be estimated using local sidebands around each GW trigger. The background was measured using the ±5000 s regions surrounding each GW event, excluding the central blinded ±50 s signal window.

This approach accounts for possible time-dependent variations in the single-event background rate from radioactive backgrounds, detector conditions, and scintillator stability.

The expected background in the GW coincidence windows is calculated by scaling the observed sideband event rate according to

$$B_{\text{exp}} = N_{\text{OFF}} \frac{T_{\text{ON}}}{T_{\text{OFF}}} \tag{6.69}$$

where N_{OFF} is the number of events observed in the sideband regions, T_{OFF} is the sideband livetime,

and T_{ON} is the total livetime contained within the GW coincidence windows.

The dominant uncertainty in the neutrino-proton ES background estimate arises from possible variations in the single-event background rate between the coincidence window and sideband regions rather than from the statistical uncertainty on the large sideband event sample.

The resulting background prediction is then compared with the observed number of events after unblinding.

6.10 Neutrino-Proton ES Results

After finalizing the selection criteria and background estimation procedure, the neutrino-proton ES search was unblinded. The initial unblinding sample included all 143 GW candidates passing detector-quality requirements, including candidates classified by LVK as terrestrial or unknown.

Dataset	N_{ON}	N_{OFF}	T_{ON} [s]	T_{OFF} [s]	B_{exp}	Excess
PPO+BHT	14159	1201801	2500	214170	$14051.2 \pm 13.1_{\mathrm{stat}} \pm 405.5_{\mathrm{syst}}$	107.8
bisMSB	94265	7514805	11002.9	874700	$94294.2 \pm 35.5_{\mathrm{stat}} \pm 672.8_{\mathrm{syst}}$	-29.2
Combined	108424	8716606	13502.876	1088869.992	$108345.4 \pm 37.8_{\mathrm{stat}} \pm 785.5_{\mathrm{syst}}$	78.6

Table 6.15: Neutrino-proton ES unblinding results comparing the observed candidates counts in the GW coincidence windows with the expected background estimated from the local sidebands. The ON-window corresponds to the optimized ±50 s GW coincidence windows, while the OFF-window corresponds to the local sideband regions used to estimate the background.

The reconstructed energy distribution of neutrino-proton ES candidates in the GW coincidence windows is compared with the scaled sideband background prediction in Figure 6.18. Both distributions are summed over all GW candidates and both scintillator phases. The agreement between the GW-coincident sample and the scaled sideband prediction shows no evidence for a localized excess in reconstructed energy.

The combined PPO+BHT and bisMSB dataset contains

$$N_{\mathrm{obs}} = 108424 \tag{6.70}$$

events within the optimized ±50 s coincidence windows. The expected background from the local

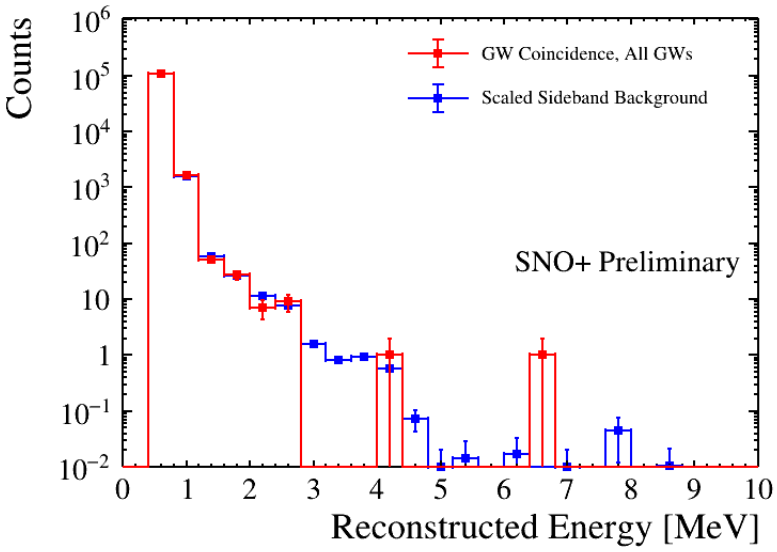


Figure 6.18: Reconstructed energy distribution of neutrino-proton ES candidates in the optimized ±50 s GW coincidence windows compared with the scaled sideband background prediction. Both distributions are summed over the GW candidates and scintillator phases. Error bars show the statistical uncertainties on the GW-coincident and scaled sideband samples.

sideband measurement is

$$b = 108345.4 \pm 37.8_{\text{stat}} \pm 785.5_{\text{syst}} \tag{6.71}$$

The observed difference is

$$N_{\text{obs}} - b = 78.6 \tag{6.72}$$

events, corresponding to a 0.24σ fluctuation. Therefore, no statistically significant excess of neutrino-proton ES candidates is observed. The results are summarized in Table 6.15.

As in the IBD analysis, terrestrial and unknown GW candidates are retained during unblinding as a validation of the coincidence search, but are removed from the final compact binary merger fluence calculation.

6.10.1 Fluence Upper Limits

The absence of a statistically significant neutrino-proton ES excess is converted into an upper limit on the all-flavor neutrino fluence from compact binary mergers. For the final fluence calculation, the 17 terrestrial and unknown candidates are excluded, leaving the same 126 astrophysical GW candidates used in the IBD analysis.

The fluence calculation follows the same procedure as the IBD analysis, with the IBD cross section replaced by the neutrino-proton ES cross section.

For an individual GW candidate i and a monoenergetic neutrino source, the fluence upper limit is

$$\Phi_{90,i}(E_\nu) = \frac{N_{90,i}}{N_p \sigma_{\nu p}(E_\nu) \epsilon_i(E_\nu)} \tag{6.73}$$

where $N_{90,i}$ is the Feldman-Cousins upper limit on the number of signal events, N_p is the number of target protons, $\sigma_{\nu p}(E_\nu)$ is the neutrino-proton ES cross section, and $\epsilon_i(E_\nu)$ is the run-dependent detection efficiency determined from MC simulations.

For the combined analysis, a common (average per-GW) neutrino fluence at Earth is assumed for every GW candidate. The expected signal contributions from the individual candidates are therefore summed, yielding a stacked upper limit on this common fluence. For the monoenergetic case, the stacked fluence upper limit is

$$\Phi_{90}^{\text{stack}}(E_\nu) = \frac{N_{90}^{\text{stack}}}{N_p \sigma_{\nu p}(E_\nu) \sum_{i=1}^{N_{\text{GW}}} \epsilon_i(E_\nu)} \tag{6.74}$$

For the final 126 candidate astrophysical GW sample, including the uncertainty on the expected background in the Feldman-Cousins construction gives a 90% confidence level stacked upper limit of

$$N_{90}^{\text{stack}} = 1479.6 \tag{6.75}$$

The larger value of N_{90}^{stack} compared with the IBD analysis reflects the higher single-event background rate associated with the absence of a delayed-coincidence signature.

This value is substituted into the stacked fluence expression above to calculate the final stacked (average per-GW) neutrino-proton ES fluence limits. The resulting monoenergetic neutrino-proton ES fluence limits are shown in Figure 6.19. The limits are reported using the same stacked (average per-GW) normalization convention as the IBD analysis. Although the neutrino-proton ES channel has a larger expected event yield for a nearby supernova-like burst, the GW-coincident fluence limits are weaker than the IBD limits due to the substantially larger single-event background and the reduced visible energy produced by quenched proton recoils.

Unlike IBD, which primarily constrains the electron antineutrino component, the neutrino-proton ES limits provide sensitivity to all neutrino flavors through the neutral current interaction.

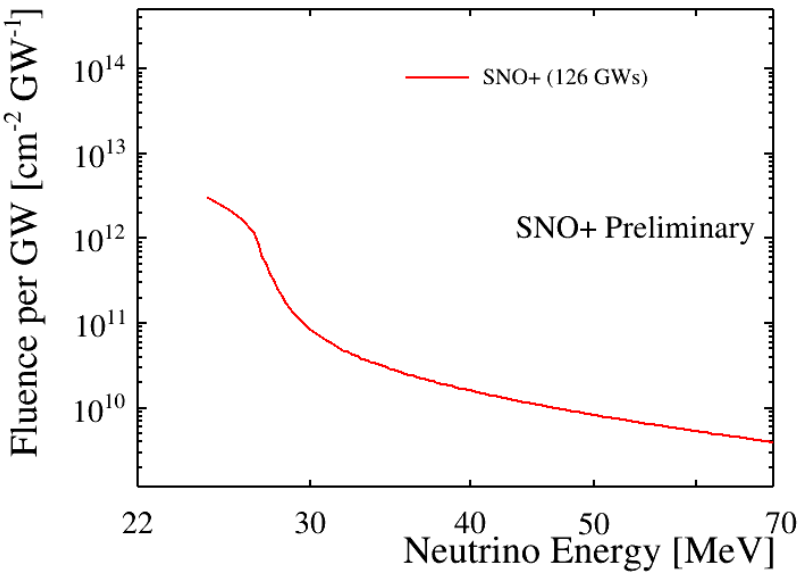


Figure 6.19: Combined SNO+ 90% confidence level stacked (average per-GW) monoenergetic neutrino-proton ES fluence upper limits using the final 126 astrophysical GW candidates. The limits assume a common neutrino fluence at Earth for every GW candidate and are reported using the same per-GW normalization convention as the IBD analysis.

The fluence calculation is also performed separately for each GW merger classification, as shown in

Figure 6.20. As with the IBD analysis, differences between classifications are driven primarily by the number of GW candidates contributing to each stacked (average per-GW) sample rather than by assumptions about different neutrino emission properties.

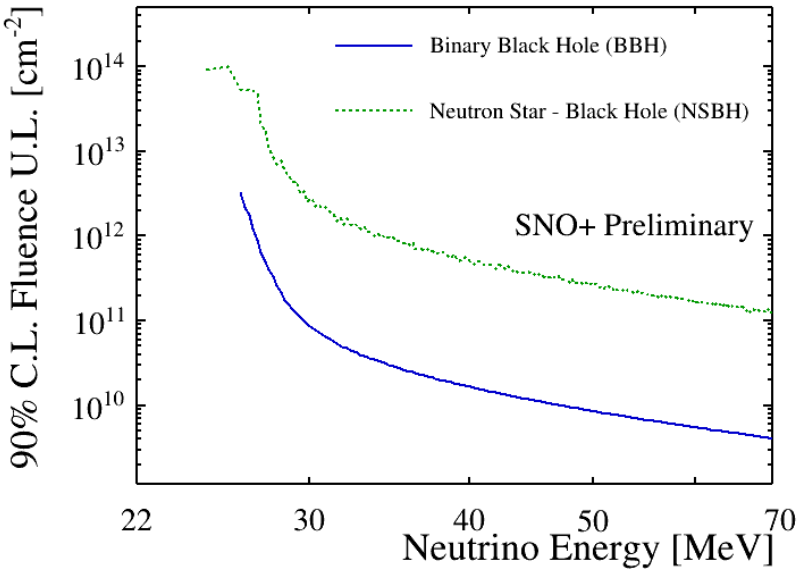


Figure 6.20: SNO+ 90% confidence level monoenergetic neutrino-proton ES fluence upper limits separated by GW merger classification.

6.11 Summary

This chapter presented the first SNO+ search for MeV neutrinos in temporal coincidence with GW events detected during LVK O4. Two complementary detection channels were investigated: IBD, which provides a distinctive delayed-coincidence signature for electron antineutrinos, and neutrino-proton ES, a NC interaction providing sensitivity to all neutrino flavors.

The analysis was performed using a blind approach. GW-coincident data were excluded while the event selection, background estimation, signal efficiency calculations, and statistical analysis procedure were developed and validated. Dedicated MC simulations were produced for both signal channels. For the IBD analysis, a modified generator was developed to produce a true flat neutrino energy spectrum extending up to 50 MeV. For the neutrino-proton ES analysis, the interaction cross section implemented in the simulation was corrected and validated against the analytic calculation.

These simulations were used to determine the energy-dependent detector efficiencies and calculate fluence limits for monoenergetic neutrinos and theoretical emission spectra.

For the IBD analysis, backgrounds were estimated directly from SNO+ data by removing periods containing GW coincidence windows and applying the same delayed-coincidence selection to the remaining dataset. The final astrophysical GW sample consisted of 126 compact binary merger candidates, with an expected background of 1.25 ± 0.09 events. After unblinding, no IBD candidates were observed within the ± 1000 s GW coincidence windows, consistent with the background-only expectation. Using the Feldman-Cousins approach, this corresponds to a 90% confidence level stacked upper limit of $N_{90}^{\text{stack}} = 1.47$ signal events, which is used to derive the stacked average (per-GW) fluence limits under the assumption of a common neutrino fluence at Earth for every GW candidate.

A complementary neutrino-proton ES search was performed using an optimized ± 50 s coincidence window. The background was estimated using local sidebands around each GW trigger to account for possible time-dependent variations in the single-event rate. No statistically significant excess was observed, with the measured event rate consistent with the background-only expectation. The resulting Feldman-Cousins stacked upper limit of $N_{90}^{\text{stack}} = 1479.6$ was used to calculate the first SNO+ stacked average (per-GW) GW-coincident neutrino-proton ES fluence limits.

The null results from both channels were used to place 90% confidence level stacked average (per-GW) upper limits on the neutrino fluence from compact binary mergers. The IBD limits constrain the electron antineutrino component, while the neutrino-proton ES limits provide complementary all-flavor sensitivity through the NC interaction. Limits were calculated for monoenergetic neutrinos and for model-dependent spectra, including Fermi-Dirac and GKVM CCSN-inspired emission models used as detector sensitivity benchmarks. The stacked average (per-GW) IBD fluence constraints improve upon previous low-energy GW-neutrino searches due to the increased number of GW candidates, larger fiducial target mass, and low background rate achieved in SNO+.

The stacked average (per-GW) IBD fluence limits were also converted into constraints on the com-

mon isotropic-equivalent energy emitted in electron antineutrinos using the GW source distances. Although the resulting limits remain several orders of magnitude above the energy scale associated with standard CCSN-like neutrino emission, they provide constraints on exceptionally energetic or non-standard neutrino emission scenarios from compact binary mergers.

The analysis framework developed here, including GW coincidence matching, blind analysis procedures, data-driven background estimation, simulation improvements, and fluence-limit calculations, establishes SNO+ as a sensitive detector for future multi-messenger searches. Continued data collection and the combination of multiple detection channels will improve sensitivity to weak MeV-scale neutrino signals associated with astrophysical transients.

CHAPTER 7

CONCLUSIONS

"Does anybody really know what time it is?
(Care) Does anybody really care?
(About time) you know, I can't imagine why
(Oh no, no) we've all got time enough to cry"
— "Does Anybody Really Know What Time It Is?," Chicago

This dissertation presented a search for MeV-scale neutrinos in temporal coincidence with GW events using the SNO+ liquid scintillator detector. The detection of GWs has opened a new era of multi-messenger astronomy, and the observation of coincident MeV neutrinos would provide direct information about particle production, energy transport, and the astrophysical environments surrounding compact binary mergers.

The analysis used GW candidates reported during the LVK O4 observing run and searched for coincident neutrino interactions in SNO+ scintillator data. Due to the uncertainty in the MeV neutrino emission expected from compact binary mergers, this work adopted both model-independent and model-dependent approaches. Dedicated MC simulations were generated using broad neutrino energy spectra to determine the detector response, and the resulting efficiencies were used to evaluate monoenergetic fluence limits and constraints based on theoretical emission spectra.

Several improvements to the SNO+ simulation framework were developed as part of this work. The IBD event generator was modified to efficiently produce model-independent neutrino samples extending to 50 MeV, enabling studies beyond the reactor antineutrino energy region. In addition, the neutrino-proton ES generator was independently validated, leading to a correction of the implemented cross section to ensure agreement with analytic calculations. These improvements provide validated simulation tools for future low-energy astrophysical neutrino searches in SNO+.

The primary search channel was IBD, which provides a distinctive delayed-coincidence signature

for identifying electron antineutrinos. A complementary search was also performed using neutrino-proton ES, a NC interaction sensitive to all neutrino flavors. The searches were performed as blind analyses, with event selection criteria, background estimation methods, and statistical procedures finalized before examining the GW-coincident data.

After unblinding, no IBD candidates were observed within the ±1000 s coincidence windows around the 126 astrophysical GW candidates. This result is consistent with the expected background of 1.25 ± 0.09 events. Using the Feldman-Cousins approach, a 90% confidence level stacked upper limit of $N_{90}^{\text{stack}} = 1.47$ signal events was obtained and used to calculate stacked average (per-GW) electron antineutrino fluence constraints under the assumption of a common neutrino fluence for all GW candidates.

The neutrino-proton ES search used an optimized ±50 s coincidence window to reduce the larger single-event background associated with the absence of a delayed-coincidence signature. No statistically significant excess was observed above the data-driven background expectation. The resulting Feldman-Cousins upper limit of $N_{90}^{\text{stack}} = 1479.6$ signal events was used to calculate the first SNO+ stacked average (per-GW) all-flavor neutrino-proton ES fluence limits associated with GW events.

The IBD stacked average (per-GW) IBD fluence limits improve upon previous low-energy liquid scintillator GW-neutrino searches by approximately an order of magnitude in the few-MeV energy region. This improvement results from the larger fiducial target mass, increased number of GW candidates, low background rate, and high detection efficiency achieved in SNO+. The neutrino-proton ES analysis establishes a complementary all-flavor approach for future transient searches.

Despite this improvement, the sensitivity of current MeV neutrino searches is limited primarily by the large distances of detected GW sources rather than detector performance. Compact binary mergers observed by the LVK network typically occur at distances of hundreds to thousands of Mpc, where standard CCSN-like neutrino emission would produce significantly less than one detectable interaction in SNO+.

This distance limitation can be illustrated by considering a CCSN-like neutrino burst with a total

emitted neutrino energy of approximately 3×10^{53} erg. For such a source, the expected number of detected IBD events scales approximately as

$$N_{\mathrm{IBD}}(D, M) \propto M \left(\frac{1}{D}\right)^2 \tag{7.1}$$

where M is the detector target mass and D is the source distance. Using the SNO+ scintillator mass and IBD detection efficiency, a Galactic-scale event would produce a detectable signal, while the expected event rate rapidly decreases for sources outside the Local Group. A source at the distance of the Large Magellanic Cloud would produce only a few IBD interactions, and an equivalent source in Andromeda would produce significantly less than one event.

Consequently, the absence of a detected signal is consistent with current theoretical expectations. Observing MeV neutrinos from compact binary mergers at typical LVK distances would require either substantially larger neutrino emission than standard CCSN expectations or next-generation detectors with much larger target masses.

The fluence limits were therefore converted into constraints on the isotropic-equivalent energy emitted in electron antineutrinos. Although these limits currently probe only exceptionally energetic or non-standard neutrino emission scenarios from compact binary mergers, they establish the strongest liquid scintillator constraints to date in the few-MeV energy range and provide an important experimental benchmark for future searches.

7.1 Future Work

Future improvements are expected as additional calibration data further constrain the detector response. During the PPO phase and early bisMSB data-taking period overlapping LVK O4, calibration coverage was limited compared with later SNO+ operations. Future calibration campaigns will improve modeling of the detector energy response, position reconstruction, and systematic uncertainties associated with the neutrino detection efficiency.

Continued LVK observing runs will increase the number of GW candidates available for stacking analyses, improving the achievable fluence sensitivity as additional independent sources are included.

Additional SNO+ livetime will also improve background characterization and provide larger datasets for rare-event searches.

Future improvements to the neutrino-proton ES analysis will focus on improved background modeling, lower detection thresholds, and optimized selection strategies. Although the observable signal is challenging due to proton quenching and the absence of a delayed-coincidence signature, neutrino-proton ES provides the largest expected event yield in liquid scintillator detectors for CCSN-like neutrino spectra and remains an important channel for all-flavor multi-messenger searches.

Improved detector calibrations and increased scintillator livetime will further constrain the low-energy detector response and reduce systematic uncertainties associated with proton recoil reconstruction and quenching models.

At lower detection thresholds, coherent elastic neutrino-nucleus scattering (CEνNS) provides another promising channel for future multi-messenger neutrino searches. In this interaction, the neutrino scatters coherently from the entire nucleus, causing the cross section to scale approximately with the square of the neutron number ($\sigma \propto N^2$). This coherent enhancement results in a much larger cross section compared with other low-energy neutrino interactions and provides sensitivity to all active neutrino flavors. However, the resulting nuclear recoil energies are very small, requiring detectors with extremely low energy thresholds. Dedicated CEνNS experiments may therefore provide complementary sensitivity to neutrinos from astrophysical transients.

Future large-scale hybrid detectors may further improve sensitivity to astrophysical neutrinos. Technologies such as dichroicons, designed to separate Cherenkov and scintillation photons, could combine the low energy threshold and high light yield of liquid scintillator detectors with the directional reconstruction capabilities of water Cherenkov detectors. Such developments would improve background rejection, particle identification, and event classification in future multi-messenger neutrino searches.

As GW observatories continue to identify new astrophysical transients, searches across complementary messengers and neutrino interaction channels will remain essential. The techniques developed

in this work establish the foundation for future SNO+ multi-messenger analyses and position the experiment to search for MeV neutrino counterparts to the growing population of gravitational wave sources observed by the LVK network.

APPENDIX A

BACKGROUND IBD CANDIDATE LISTS

Category	**Number of Candidates**	**Description**
Common candidates	9	Agreement with reactor $\bar{\nu}_e$ analysis
GW/solar energy extension	1	Prompt energy above reactor analysis range
BHT-specific candidates	3	Present only in GW analysis dataset
Rejected candidates	3	Removed by multiplicity/NHit vetoes
Total GW IBD candidates	16	Background-only sample

Table A.1: Summary of background-only IBD candidates identified in the LAB+PPO+BHT phase. The GW neutrino analysis selection is compared with the independent reactor antineutrino analysis. Green indicates candidates found by both analyses, magenta indicates candidates removed by reactor antineutrino vetoes, blue indicates candidates retained only by the GW/solar analyses due to the extended prompt energy range ($E_{\text{prompt}} > 9$ MeV), and white indicates runs not included in the reactor antineutrino dataset.

Category	**Number of Candidates**	**Description**
Common candidates	151	Agreement with reactor $\bar{\nu}_e$ analysis
Rejected candidates	47	Removed by multiplicity/NHit vetoes
Pedestal cut difference	2	Removed after additional pedestal cuts
Total GW IBD candidates	200	Background-only sample

Table A.2: Summary of background-only IBD candidates identified in the LAB+PPO+BHT+bisMSB phase. Candidates are compared with the independent reactor antineutrino analysis. Green/yellow candidates represent agreement between analyses, while magenta candidates are rejected by reactor antineutrino vetoes. Differences arise from analysis-specific vetoes and selection criteria.

Table A.3: Full list of background-only IBD candidates in the LAB + 2.2 g/L PPO + 6.5 mg/L BHT phase. The table compares the GW IBD selection with the independent reactor antineutrino candidate list. Green/yellow entries indicate agreement with the reactor antineutrino lists, magenta tag cells indicate candidates removed by reactor antineutrino vetoes, blue marks the GW/solar prompt energy extension, and white entries indicate candidates not included in the reactor antineutrino comparison dataset.

Δt [μs]	ΔR [mm]	E_d [MeV]	E_p [MeV]	Run	R_d [mm]	R_p [mm]	Prompt GTID	Delayed GTID	Pairs	Mult.	Atm.	Status	Note
906.4	754.442	2.10612	1.4163	309729	4028.85	4547.38	1287703	1287705	1	0	0	Agree	
158.22	327.556	2.12111	2.27958	309799	2684.26	2748.49	8412334	8412338	1	0	0	Agree	
35.64	359.829	2.02712	1.76171	309900	5004.32	4813.91	6220912	6220914	1	0	0	Agree	
486.7	630.629	2.13792	2.57141	309953	5697.85	5499.06	2082660	2082664	1	0	0	Agree	
29.88	850.223	2.03247	2.08773	310125	3717.8	3694.38	6352629	6352631	1	1	1	Reactor veto	
104.96	588.764	2.18209	1.1698	310209	4211.81	3699.56	2459319	2459321	1	0	0	Agree	
38.06	1813.12	1.93401	2.02404	310357	5233.2	5275.37	12706969	12706971	1	0	1	Reactor veto	
381.8	126.464	2.23575	7.70492	310455	5159.48	5197.09	8611655	8611657	1	0	0	Agree	
549.26	964.745	2.02907	2.04852	310457	1975.05	1249.8	7423225	7423227	1	0	1	Reactor veto	
468.98	182.404	2.07054	2.84915	310483	4817.43	4700.45	15802501	15802505	1	0	0	Agree	
603.64	914.568	1.93773	1.57884	310517	3294.23	3068.95	2738133	2738135	1	0	0	Agree	
80.5	473.786	2.14182	4.35294	310578	3898.4	4067.6	13093900	13093903	1	0	0	Agree	
43.7	549.521	2.08398	10.8985	310622	5206.88	5639.06	10289206	10289208	1	0	0	GW/solar: $E_p >$ 9 MeV	
177.56	1151.06	2.14266	1.91606	310951	3626.34	4220.78	1646275	1646277	1	0	0		Not in reactor dataset
52.12	735.98	1.99937	0.950941	311061	5594.73	4998.24	666999	667001	1	0	0		Not in reactor dataset
17.08	286.823	2.20859	1.58138	311239	5319.52	5213.69	1928097	1928099	1	0	0		Not in reactor dataset

Table A.4: Full list of background-only IBD candidates in the LAB+ 2.2 g/L PPO + 6.5 mg/L BHT + 2.2 mg/L bisMSB phase. The table compares the GW IBD selection with the independent reactor antineutrino candidate lists. Green/yellow entries indicate agreement with the reactor antineutrino lists, magenta tag cells indicate candidates removed by reactor antineutrino vetoes, and orange indicates candidates removed due to pedestal-cut.

Δt [μs]	ΔR [mm]	E_d [MeV]	E_p [MeV]	Run	R_d [mm]	R_p [mm]	Prompt GTID	Delayed GTID	Pairs	Mult.	Atm.	Status	Note
84.28	871.163	1.9817	2.06742	354125	3013.48	2562.78	5405030	5405032	1	1	1	Reactor veto	
10.44	508.723	2.0518	3.24674	354793	5306.78	5674.36	2332099	2332101	1	0	0	Agree	
161.24	482.693	2.17141	4.43865	354883	1825.77	1632.7	3676555	3676557	1	0	0	Agree	
7.96	899.39	2.25172	2.36581	354892	5417.7	5378.62	2137949	2137951	1	0	0	Agree	
93.22	719.658	2.16943	2.34662	354992	4130.97	4781.73	477248	477252	1	0	0	Agree	
22.42	1778.45	2.01854	2.90035	354996	4504.74	2833.06	1071133	1071135	1	0	0	Agree	
377.32	1100.88	1.95626	2.07471	355116	3868.38	3289.38	11700060	11700063	1	0	1	Reactor veto	
23.72	492.447	1.97921	2.17047	355527	4978.77	5418.07	12264977	12264979	1	0	0	Agree	
128.2	794.58	2.12064	1.34644	355533	2363.96	1735.05	15177013	15177015	1	0	0	Agree	
18.72	355.561	2.00041	5.51503	355550	2219.75	2455.72	2417367	2417370	1	0	0	Agree	
408.96	428.891	2.22902	2.16644	355584	4330.44	4097.23	15949918	15949924	1	0	0	Agree	
576.02	1424.39	1.94014	1.68104	355649	5540.47	4891.77	12665053	12665059	1	0	0	Agree/check note	Po-Wei cuts this with corrected accidental classifier
143.88	384.007	2.09648	2.27027	355674	4415.14	4197.16	4135574	4135576	1	0	0	Agree	
82.96	245.169	2.27098	1.39081	355798	3636.38	3481.1	4002803	4002806	1	0	0	Agree	
7.7	338.282	2.16492	4.13093	355843	3410.9	3524.61	15087301	15087303	1	0	0	Agree	
381.98	787.462	2.22955	1.25923	355859	4784.81	4870.08	12738939	12738941	1	0	0	Agree	
48.84	837.337	2.10258	5.7187	355867	5063.85	5215.05	134758	134760	1	0	0	Agree	
87.92	306.048	2.1854	1.16488	355906	4179	4013.42	4224975	4224977	1	0	0	Agree	
65.1	528.632	2.11228	1.67952	356016	3715.21	4059.18	4717020	4717023	1	0	0	Agree	
43.16	187.938	1.98646	6.5237	356029	3346.25	3228.77	6630171	6630173	1	0	0	Agree	
6.42	246.929	2.1154	1.33489	356556	4522	4405.02	13924385	13924387	1	0	0	Agree	
322.04	227.894	2.13755	4.4138	356575	3608.93	3714.68	15662811	15662818	1	0	0	Agree	
527.54	2336.71	1.88646	0.985591	356603	5631.19	3337.06	9699882	9699887	1	0	0	Agree/check note	Po-Wei tags and removes with accidental classifier
80.74	453.465	2.21336	3.1404	356644	4758.69	5086.38	7926855	7926858	1	0	0	Agree	
21.28	1199.04	1.97301	2.00965	356647	3229.74	3370.44	15443173	15443175	1	0	1	Reactor veto	
135.94	411.563	2.05677	2.00351	356988	3706.55	3595.03	12668586	12668588	1	0	0	Agree	
222.64	695.843	2.0741	2.13948	357031	3909.52	3952.8	1591763	1591765	1	0	1	Reactor veto	
173.5	434.415	2.12667	1.06976	357080	5001.32	5147.24	15756691	15756693	1	0	0	Agree	
208.28	210.971	2.23464	2.0994	357134	2290.01	2470.08	4377973	4377975	1	0	1	Reactor veto	

Continued on next page

Table A.4: Full list of background-only IBD candidates in the LAB+ 2.2 g/L PPO + 6.5 mg/L BHT + 2.2 mg/L bisMSB phase. The table compares the GW IBD selection with the independent reactor antineutrino candidate lists. Green/yellow entries indicate agreement with the reactor antineutrino lists, magenta tag cells indicate candidates removed by reactor antineutrino vetoes, and orange indicates candidates removed due to pedestal-cut (continued).

Δt [μs]	ΔR [mm]	E_d [MeV]	E_p [MeV]	Run	R_d [mm]	R_p [mm]	Prompt GTID	Delayed GTID	Pairs	Mult.	Atm.	Status	Note
220.82	1069.08	2.04821	2.03935	357199	3845.47	3740.84	3038750	3038752	1	0	1	Reactor veto	
98.44	1194.38	2.00925	1.91294	357282	4366.47	4515.99	4574053	4574055	1	0	1	Reactor veto	
126.62	1189.99	2.24014	2.12709	357340	5481.29	5445.97	6473849	6473851	1	0	1	Reactor veto	
78.88	262.746	2.13611	2.80877	357349	4652.19	4815.84	3194170	3194173	1	0	0	Agree	
89.26	469.294	2.35194	4.90876	357503	3350.02	3675.58	6049322	6049324	1	1	0	Reactor veto	
117.42	1238.16	2.09654	1.36378	357629	1051.66	1089.45	15821488	15821492	1	0	0	Agree	
17.86	374.878	2.09639	2.22747	357638	5072.69	5333.92	8594524	8594526	1	0	1	Reactor veto	
131.78	93.2698	2.11355	1.35779	357740	4032.41	4012.15	368441	368443	1	0	0	Agree	
14.76	803.519	2.03979	2.10737	357789	2443.23	3009.04	11365858	11365860	2	1	1	Reactor veto	
79.44	1110.9	2.17265	2.12374	357789	2443.53	3346.44	11365862	11365864	2	1	1	Reactor veto	
47.64	493.708	1.98454	1.81954	357797	5652.14	5264.58	2529989	2529991	1	1	1	Reactor veto	
145.06	588.649	1.94108	1.50036	357801	3698.55	3603.36	14377634	14377636	1	0	0	Agree	
65.7	220.152	2.11552	3.34108	357815	4480.14	4623.41	1985760	1985762	1	0	0	Agree	
7	513.247	1.8865	2.01334	357997	3668.11	3967.44	13597549	13597551	1	1	1	Reactor veto	
276.98	1237.41	2.07977	1.87795	358022	4854.22	5111.46	3797624	3797634	1	1	1	Reactor veto	
54.38	374.881	2.24825	1.5754	358086	2100.89	2319.23	2902121	2902123	1	0	0	Agree	
43.86	211.824	2.19158	2.55684	358156	4745.23	4687.62	11646244	11646246	1	0	0	Agree	
27.5	225.319	2.13639	2.87494	358189	4096.25	3873.25	11152417	11152419	1	0	0	Agree	
7.92	1491.9	1.9241	1.0353	358191	5662.12	5210.01	7774990	7774992	1	0	0	Agree	
29.14	187.857	2.23473	1.68819	358237	4765.55	4643.06	2648876	2648878	1	0	0	Agree	
70.02	59.7835	2.15841	1.11418	358262	5306.88	5326.55	9216387	9216389	1	0	0	Agree	
122.38	768.111	2.32378	1.41805	358300	1799.41	2449.78	334158	334160	1	0	0	Agree	
207.86	749.777	2.3291	2.74797	358338	5602.85	5000.25	9833852	9833854	1	0	0	Agree	
340.28	98.0161	2.19324	3.0482	358420	4710.33	4773.15	1593059	1593061	1	0	0	Agree	
34.1	773.926	2.01184	1.70684	358497	3960.05	4283.6	8607965	8607967	1	0	0	Agree	
170.78	788.964	2.17772	1.48393	359224	3582.01	4356.17	9314876	9314879	1	0	0	Agree	
210	777.744	2.22885	4.29119	359289	5420.35	4707.73	13332640	13332643	1	0	0	Agree	
351.94	317.675	2.12333	2.14897	359327	5081.38	4861.27	7733606	7733608	1	0	0	Agree	
184.66	863.342	2.33404	6.07489	359389	4892.58	4188.61	8336647	8336651	1	0	0	Agree	
12.58	521.023	2.23803	2.09849	359412	2238.46	2655.19	4439551	4439554	1	0	0	Agree	
85.84	415.251	2.16521	2.07223	359447	5680.75	5640.67	8610586	8610588	1	0	0	Agree	

Continued on next page

Table A.4: Full list of background-only IBD candidates in the LAB+ 2.2 g/L PPO + 6.5 mg/L BHT + 2.2 mg/L bisMSB phase. The table compares the GW IBD selection with the independent reactor antineutrino candidate lists. Green/yellow entries indicate agreement with the reactor antineutrino lists, magenta tag cells indicate candidates removed by reactor antineutrino vetoes, and orange indicates candidates removed due to pedestal-cut (continued).

Δt [μs]	ΔR [mm]	E_d [MeV]	E_p [MeV]	Run	R_d [mm]	R_p [mm]	Prompt GTID	Delayed GTID	Pairs	Mult.	Atm.	Status	Note
199.44	483	2.14995	1.22929	359483	4746.21	5083.9	14742949	14742952	1	0	0	Agree	
30.8	362.867	1.95824	2.0226	359616	1956.55	1720.33	10183670	10183672	1	0	1	Reactor veto	
27.78	1212.18	2.00713	1.9048	359788	4975.06	4471.91	2422943	2422945	2	1	1	Reactor veto	
132.76	1955.45	2.03892	1.84246	359788	4173.61	4305.43	2422947	2422949	2	1	1	Reactor veto	
158.68	398.256	2.13729	3.50822	359833	883.286	898.442	8735193	8735195	1	0	0	Agree	
770.64	179.579	2.24923	3.61118	359902	4961.38	4946.55	7177933	7177935	1	0	0	Agree	
467.86	1060.31	2.1533	4.46692	359953	5374.61	5102.61	15472137	15472140	1	0	0	Agree	
119.08	2447.53	2.16482	2.00318	359996	2899.68	3078.81	3869780	3869782	1	0	1	Reactor veto	
45.72	410.526	2.05502	4.5556	360055	4675.05	4271.92	16160405	16160407	1	0	0	Agree	
86.74	174.078	2.16142	3.10628	360091	2841.33	2865.79	1866031	1866033	1	0	0	Agree	
32.44	1564.77	2.02404	2.05522	360092	4645.02	3487.01	11089045	11089047	2	1	1	Reactor veto	
114.06	618.372	2.09596	2.16675	360092	3759.22	3387.76	11089049	11089051	2	1	1	Reactor veto	
234.34	443.64	2.12324	6.06346	360093	3111.4	3010.19	14836968	14836971	1	0	0	Agree	
387.72	235.391	2.25491	2.50596	360103	5601.93	5452.36	2417217	2417221	1	0	0	Agree	
44.04	267.232	2.29	2.52796	360365	4742.89	4899.19	5990030	5990032	1	0	0	Agree	
234.14	188.894	2.1582	4.4752	360493	3471.97	3431.23	12915495	12915497	1	0	0	Agree	
579.04	548.439	2.13514	1.24225	360506	2188.51	2675.69	8655933	8655938	1	0	0	Agree	
216.1	234.677	2.242	4.26217	360580	5191.63	5422.31	5913920	5913924	1	1	0	Reactor veto	
178.3	494.616	2.0466	3.24386	360715	3260.34	3466.68	10634862	10634865	1	0	0	Agree	
11.44	657.683	2.046	1.85686	360926	4914.01	5246.98	3865492	3865494	1	0	1	Reactor veto	
249.82	377.596	2.21491	2.92297	360993	5210.15	5471.85	7165615	7165618	1	0	0	Agree	
14.54	175.674	2.0334	5.20753	361109	2394.22	2483.79	5615243	5615246	1	0	0	Agree	
269.02	706.858	2.04526	5.18035	361155	4427.93	4397.12	7036197	7036201	1	0	0	Agree	
429.76	321.848	2.25401	2.36344	361208	4431.91	4187.94	8289348	8289352	1	0	0	Agree	
128.62	328.906	2.15243	1.51513	361225	5511.87	5395.63	12722926	12722929	1	0	0	Agree	
450.58	152.842	2.16397	4.49957	361252	4051.36	4185.93	13167618	13167621	1	0	0	Agree	
125.76	468.695	2.22552	2.93779	361652	4885.16	4465.01	15670212	15670214	1	0	0	Agree	
59.76	201.373	2.12949	2.93058	361795	4004.26	4016.11	6710042	6710044	1	0	0	Agree	
366.54	162.158	2.10651	4.54546	361807	5259.77	5289.24	634422	634427	1	0	0	Agree	
165.58	398.563	2.11593	2.1382	361823	3957.25	4215.39	1237136	1237140	1	0	0	Agree	

Continued on next page

Table A.4: Full list of background-only IBD candidates in the LAB+ 2.2 g/L PPO + 6.5 mg/L BHT + 2.2 mg/L bisMSB phase. The table compares the GW IBD selection with the independent reactor antineutrino candidate lists. Green/yellow entries indicate agreement with the reactor antineutrino lists, magenta tag cells indicate candidates removed by reactor antineutrino vetoes, and orange indicates candidates removed due to pedestal-cut (continued).

Δt [μs]	ΔR [mm]	E_d [MeV]	E_p [MeV]	Run	R_d [mm]	R_p [mm]	Prompt GTID	Delayed GTID	Pairs	Mult.	Atm.	Status	Note
262.16	164.261	2.08299	1.53778	361843	4425.37	4380.88	9605865	9605869	1	0	0	Agree/check note	Serena looked at this run b/c there was a noel server wet-end breakdown
255.76	503.127	2.20786	1.80391	361935	2911.1	3190.27	7104152	7104154	1	0	0	Agree	
77.8	586.981	2.49304	6.22986	362075	5642.15	5563.49	12756548	12756551	1	0	0	Agree	
54.64	327.937	1.90487	2.0921	362241	5173.63	5491.38	4008949	4008952	1	1	1	Reactor veto	
26.5	468.055	1.89525	1.9022	362247	3297.74	2986.39	14849233	14849235	1	0	1	Reactor veto	
192.18	209.366	2.11653	3.74998	362347	3608.28	3636.88	1534623	1534627	1	0	0	Agree	
734.12	106.487	2.16798	1.19614	362424	4975.63	5034.48	10433506	10433512	1	0	0	Agree	
292.82	330.47	2.16818	5.65078	362426	1199.82	1503.86	12477112	12477115	1	0	0	Agree	
7.42	712.663	2.11659	1.29157	362453	4592.33	4244.57	2051133	2051135	1	0	0	Agree	
556.72	166.159	2.09874	1.8803	362464	4515.66	4591.69	7948563	7948565	1	0	0	Agree	Ped cut (cut) (on reactor antinu list)
216.1	350.165	2.12105	5.0708	363075	3968.63	4305.92	283331	283333	1	0	0	Agree	
886.14	759.376	2.15612	1.89785	363163	4992.79	5625.83	7277751	7277756	1	0	0	Agree	
31.5	348.377	2.32935	1.81041	363226	5549.14	5429.72	14779530	14779532	1	0	0	Agree	
220.68	372.703	2.1879	2.86023	363265	3800.19	4070.44	6771424	6771428	1	0	0	Agree	
259.54	392.026	1.97142	1.29029	363424	4760.8	5151.57	12591034	12591037	1	0	0	Agree	
75.96	211.068	2.37893	4.30764	363477	2754.28	2876.39	14598377	14598380	1	0	0	Agree	
55.02	190.065	2.28416	6.11482	363584	5444.95	5277.34	3697631	3697637	1	1	0	Reactor veto	
4.7	503.414	2.1358	2.18805	363720	2822.3	3208.49	14248439	14248441	1	1	0	Reactor veto	
26.16	426.384	2.11679	1.23773	363742	4921.99	5288.61	15097813	15097815	1	0	0	Agree	
112.28	496.866	2.12804	1.69309	363759	5202.16	4754.96	7117233	7117235	1	0	0	Agree	
68.02	1456.38	2.05253	2.55642	363767	1389.28	1739.49	258065	258068	1	0	0	Agree	
784.16	290.175	2.1359	1.69295	363776	3343.3	3426.94	11660559	11660564	1	0	0	Agree	
4.18	193.973	2.22691	5.91923	363865	3089.48	3161.04	10617357	10617360	1	0	0	Agree	
124.92	1513.48	2.09972	1.96301	363913	3987.51	3991.11	1447375	1447378	1	0	1	Reactor veto	
277.12	715.316	2.11467	1.49896	363941	2049.6	2755.88	2180390	2180393	1	0	0	Agree	
263.86	1996.6	2.0218	1.97697	363960	4730.91	3540.46	7093615	7093617	2	1	1	Reactor veto	
38.56	818.768	2.02505	2.05796	363960	4398.41	4251.45	7093619	7093621	2	1	1	Reactor veto	
5.18	1271.75	2.13209	0.911122	364300	4485.7	4827.26	3167266	3167268	1	0	0	Agree	
31	930.237	1.88712	2.16161	364375	3371.57	3385.5	1547060	1547062	1	1	1	Reactor veto	
102.58	250.231	1.99343	2.09293	365059	5276.07	5518.15	3238499	3238501	1	0	1	Reactor veto	

Continued on next page

Table A.4: Full list of background-only IBD candidates in the LAB+ 2.2 g/L PPO + 6.5 mg/L BHT + 2.2 mg/L bisMSB phase. The table compares the GW IBD selection with the independent reactor antineutrino candidate lists. Green/yellow entries indicate agreement with the reactor antineutrino lists, magenta tag cells indicate candidates removed by reactor antineutrino vetoes, and orange indicates candidates removed due to pedestal-cut (continued).

Δt [μs]	ΔR [mm]	E_d [MeV]	E_p [MeV]	Run	R_d [mm]	R_p [mm]	Prompt GTID	Delayed GTID	Pairs	Mult.	Atm.	Status	Note
855.9	173.267	2.23236	4.05927	365067	4998.75	5048.24	9980918	9980923	1	0	0	Agree	
51.24	272.298	2.30867	2.05071	365150	5552.02	5533.82	3239588	3239590	1	0	0	Agree	
413.04	389.508	2.14466	4.1078	365200	5049.36	5144.35	14407502	14407505	1	1	0	Reactor veto	
89.14	323.654	2.08095	1.39154	365272	4976.21	5223.17	8188186	8188189	1	0	0	Agree	
122.34	512.318	2.23943	2.69735	365342	2457.31	2965.16	5153675	5153677	1	0	0	Agree	
170.12	226.861	2.25715	6.31157	365353	2355.55	2529.85	16647966	16647970	1	0	0	Agree	
151.02	285.921	2.21651	7.08623	365393	4909	5044.11	7978693	7978696	1	0	0	Agree	
171.86	489.721	2.17346	4.92236	365398	5285.24	5010.91	3556336	3556338	1	0	0	Agree	
117.6	186.21	1.9443	1.28001	365453	5429.07	5359.38	12737363	12737365	1	0	0	Agree	
210.54	884.17	2.20626	2.05188	365489	5538.19	5570.81	1424885	1424887	1	0	0	Agree	
337.7	1576.13	2.23079	1.88358	365650	3204.12	3913.18	1117145	1117149	1	0	0	Agree	
411.62	204.929	2.16602	2.76227	365651	4087.57	4240.87	5780244	5780249	1	0	0	Agree	
95.24	707.578	2.02801	1.29831	365782	2111.54	1737.84	10820554	10820556	1	0	0	Agree	
220.38	291.446	2.13869	1.95345	365802	4463.01	4665.19	16365005	16365009	1	0	0	Agree	
807.48	729.919	2.12593	1.42485	365815	4156.05	3758.42	7004079	7004085	1	0	0	Agree	
177.46	285.671	2.09489	2.63994	365845	4699.3	4828.4	10731914	10731916	1	0	0	Agree	
235.52	338.191	1.96404	3.11943	365850	5326.29	4992.49	11411636	11411638	1	0	0	Agree	
318.72	691.398	2.02243	2.10968	365906	3028.11	3219.47	15184924	15184938	1	0	1	Reactor veto	
83.56	673.592	2.17838	3.42949	365954	1284.36	678.468	2360399	2360401	1	0	0	Agree	
157.08	630.769	1.98365	1.84467	366027	5348.16	4985.01	10255584	10255588	1	1	1	Reactor veto	
941.4	255.49	2.15829	3.44551	366067	4318.87	4418.32	16013184	16013187	1	0	0	Agree	
134.3	124.058	2.16267	1.08377	366151	5513.08	5411.83	10462017	10462019	1	0	0	Agree	
351.42	337.481	2.17182	1.23702	366153	5113.73	5366.54	4491644	4491646	1	0	0	Agree/check note	Serena looked at this run b/c there was a noel server wet-end breakdown
50.64	442.323	2.03807	5.66641	366198	5229.18	4887.71	16098029	16098032	1	0	0	Agree	
381.3	290.247	2.28745	3.11358	366304	4457.82	4510.53	7612105	7612108	1	0	0	Agree	
94.26	130.562	2.27498	1.3351	366344	5366.99	5352.65	3770257	3770259	1	0	0	Agree	
379.36	733.814	2.2949	2.31691	366524	4473.93	4880.24	5189791	5189795	1	0	1	Reactor veto	
66.66	230.542	2.15561	1.44554	366534	2944.58	3167.09	13435384	13435387	1	0	0	Agree	
4.02	100.852	2.22559	1.71875	366668	3556.44	3579.14	11946399	11946401	1	0	0	Agree	
267.38	346.612	2.2105	1.12625	366787	3481.66	3687.61	11844304	11844307	1	0	0	Agree	

Continued on next page

Table A.4: Full list of background-only IBD candidates in the LAB+ 2.2 g/L PPO + 6.5 mg/L BHT + 2.2 mg/L bisMSB phase. The table compares the GW IBD selection with the independent reactor antineutrino candidate lists. Green/yellow entries indicate agreement with the reactor antineutrino lists, magenta tag cells indicate candidates removed by reactor antineutrino vetoes, and orange indicates candidates removed due to pedestal-cut (continued).

Δt [μs]	ΔR [mm]	E_d [MeV]	E_p [MeV]	Run	R_d [mm]	R_p [mm]	Prompt GTID	Delayed GTID	Pairs	Mult.	Atm.	Status	Note
416.4	635.956	2.32585	2.24131	366851	1300.4	1907	15658182	15658186	1	0	0	Agree	
2.86	135.701	2.10138	4.63274	366902	2994.71	2925.9	879420	879423	1	0	0	Agree	
62.38	669.95	1.97552	1.90174	366935	4620.34	5103.34	16307308	16307310	3	1	1	Reactor veto	
49.54	2145.32	1.92125	1.96778	366935	5077.22	4785.09	16307314	16307316	3	1	1	Reactor veto	
130.82	767.241	2.2505	1.89672	366935	5090.78	4525.62	16307318	16307321	3	1	1	Reactor veto	
82.6	532.25	1.96908	1.35685	366977	5616.3	5686.53	15619521	15619523	1	0	0	Agree	
753.38	355.004	2.32377	4.01883	366999	5447.01	5197.22	16661231	16661234	1	0	0	Agree	
21.16	50.7914	2.15535	2.04372	367083	5284.55	5245.23	7194095	7194098	1	1	0	Reactor veto	
40.78	901.404	2.1821	1.22649	367097	3850.85	3353.55	16161473	16161475	1	0	0	Agree	
508.7	348.647	2.04135	5.05856	367545	5460.84	5196.65	8002860	8002863	1	0	0	Agree	
7.7	523.038	2.02841	1.99057	367591	2987.24	3347.39	3216821	3216823	1	0	1	Reactor veto	
534.34	274.765	2.25182	1.79271	367659	4481.38	4258.99	3754674	3754677	1	0	0	Agree	
490.66	185.751	2.04917	3.02197	367818	4052.8	4097.25	4813944	4813947	1	0	0	Agree	
212.62	391.449	2.30409	4.51305	368002	3815.34	4202.07	472888	472891	1	0	0	Agree	
271.52	468.562	2.01695	1.99371	368006	5525.91	5462.91	11124152	11124156	2	1	1	Reactor veto	
276.82	1388.72	2.0696	1.79863	368006	4342.37	5678.12	11124154	11124158	2	1	1	Reactor veto	
1102.74	378.894	2.13557	3.36599	368054	5203.84	5545.9	10985725	10985731	1	0	0	Agree	
112.58	900.096	1.96171	1.97869	368081	2568.12	1869.03	9851991	9851994	1	1	1	Reactor veto	
178.72	242.22	2.01025	5.31397	368107	5607.23	5596.47	1658525	1658527	1	0	0	Agree	
392.64	799.692	2.13554	2.26677	368201	5468.48	5638.98	16391347	16391349	1	0	1	Reactor veto	
497.38	434.132	2.16441	2.55915	368223	4735.59	5055.1	11749780	11749782	1	0	0	Agree	
21.08	351.783	2.24812	1.52401	368482	5325.68	5300.38	6972646	6972648	1	0	0	Agree	
5.32	939.139	2.03465	1.94171	368555	2343.28	2159.59	13050966	13050968	1	1	1	Reactor veto	
295.28	740.77	2.15624	1.33325	368778	5343.26	5683.47	9850408	9850411	1	0	0	Agree	
159.68	1072.43	2.19338	2.52961	368835	4400.54	4853.63	11445421	11445424	1	0	0	Agree	
14.36	455.984	1.96688	2.06916	368913	3813.13	4022.34	94808	94810	1	0	0	Agree	
680.88	430.415	2.15835	1.28766	368914	2289.83	2444.51	7381721	7381724	1	0	0	Agree	
690.06	688.06	2.18093	0.928017	368963	5495.29	5500.04	1369937	1369940	1	0	0	Agree/check note	Serena looked at this run b/c there was a noel server wet-end breakdown
226.26	120.22	2.10272	3.49603	368985	2069.53	1953.53	5649801	5649803	1	0	0	Agree	
10.06	515.553	2.26823	1.38231	369204	4413.5	4788.56	8529075	8529077	1	0	0	Agree	

Continued on next page

Table A.4: Full list of background-only IBD candidates in the LAB+ 2.2 g/L PPO + 6.5 mg/L BHT + 2.2 mg/L bisMSB phase. The table compares the GW IBD selection with the independent reactor antineutrino candidate lists. Green/yellow entries indicate agreement with the reactor antineutrino lists, magenta tag cells indicate candidates removed by reactor antineutrino vetoes, and orange indicates candidates removed due to pedestal-cut (continued).

Δt [μs]	ΔR [mm]	E_d [MeV]	E_p [MeV]	Run	R_d [mm]	R_p [mm]	Prompt GTID	Delayed GTID	Pairs	Mult.	Atm.	Status	Note
117.66	1276.19	2.03443	2.07768	369318	3330.34	3011.21	1244529	1244531	1	0	1	Reactor veto	
507.96	218.621	2.24957	3.1816	369434	4251.56	4091.48	15499092	15499099	1	0	0	Agree	
263.06	1891.26	2.25251	2.06984	369572	1910.94	3215.34	16159229	16159231	1	1	1	Reactor veto	
655.96	134.78	2.1986	3.56585	369760	4265.37	4361.71	589941	589945	1	0	0	Agree	
3.22	451.314	2.03652	1.153	369768	3331.83	3135.14	5326936	5326938	1	0	0	Agree	
68.68	126.666	2.20309	1.55829	369853	2397.63	2443.05	535586	535588	1	0	0	Agree	
178.68	212.614	2.00231	1.46087	369931	5326.01	5293.35	7250621	7250624	1	0	0	Agree	
3.98	605.304	2.28505	4.70466	370018	5365.65	5330.8	15414558	15414560	1	0	0	Agree	
62.14	336.655	1.93091	2.0505	370086	4983.49	4960.2	7949940	7949943	2	1	1	Reactor veto	
130.46	587.698	2.06173	2.03022	370086	4962.92	4813.66	7949945	7949949	2	1	1	Reactor veto	
1013.72	156.402	2.42451	1.00255	370369	3201.61	3112.61	13291165	13291169	1	0	0	Agree/check note	Serena looked at this run b/c there was a noel server wet-end breakdown
185.18	324.642	2.10771	2.05511	370558	3079.17	3237.95	5128812	5128814	1	0	0	Agree	
308.32	319.696	2.26621	1.14204	370689	4517.67	4565.96	6775099	6775101	1	0	0	Agree	
120.12	220.42	2.19582	1.09124	370928	4091.36	4131.29	2641375	2641377	1	0	0	Agree	
121.9	174.353	2.15665	2.62274	370978	2382.27	2462.31	12311406	12311409	1	0	0	Agree	
466.62	450.338	2.19589	1.28566	370992	2900.53	2963.93	11256471	11256474	1	0	0	Agree	Ped cut (cut) (on reactor antinu list)
111.1	246.201	2.27459	3.90781	371134	4186.5	4290.32	13964569	13964571	1	0	0	Agree	
199.96	1163.99	2.18588	2.24413	371157	3279.01	4328.26	11124896	11124898	2	0	1	Reactor veto	Serena looked at this run b/c there was a noel server wet-end breakdown
412.28	113.84	2.18633	2.7116	371157	3715.76	3660.83	12637858	12637864	2	0	0	Agree	
147.12	1482.02	2.12848	2.10074	371197	3826.79	4946.78	2874583	2874587	1	0	1	Reactor veto	

APPENDIX B

GW-COINCIDENT CANDIDATE LISTS

Table B.1: O4a GW candidates used in the SNO+ coincidence search. The GW trigger time, corresponding SNO+ run, run duration, and GW GPS trigger time are shown.

GW Candidate	**GW UTC**	**Run**	**Duration (s)**	**GPS**
GW240109_050431	2024-01-09 05:04:31.800000+00:00	355462	3599.93	1388811890
GW240107_013215	2024-01-07 01:32:15.700000+00:00	355396	3600.24	1388626354
GW240105_151143	2024-01-05 15:11:43.200000+00:00	355353	3599.91	1388502721
GW231230_170116	2023-12-30 17:01:17+00:00	355200	3600.13	1387990895
GW231226_101520	2023-12-26 10:15:20.300000+00:00	355084	3600.13	1387620938
GW231224_024321	2023-12-24 02:43:22+00:00	355020	3600.17	1387421020
GW231223_202619	2023-12-23 20:26:19+00:00	355014	3600.18	1387398397
GW231221_135041	2023-12-21 13:50:41.300000+00:00	354944	3600.18	1387201859
GW231220_173406	2023-12-20 17:34:06.200000+00:00	354919	3374.94	1387128864
GW231206_233901	2023-12-06 23:39:01.500000+00:00	354126	3600.11	1385941160
GW231206_233134	2023-12-06 23:31:34.500000+00:00	354126	3600.11	1385940713
GW231206_010629	2023-12-06 01:06:29.200000+00:00	354104	3600.11	1385860007
GW230717_102139	2023-07-17 10:21:39.100000+00:00	311135	3601.12	1373624517
GW230712_090405	2023-07-12 09:04:05.900000+00:00	311006	3601.15	1373187864
GW230709_122727	2023-07-09 12:27:27.200000+00:00	310907	3601.13	1372940865
GW230709_063445	2023-07-09 06:34:45.100000+00:00	310902	3601.12	1372919703
GW230708_230935	2023-07-08 23:09:35.500000+00:00	310894	3601.15	1372892994
GW230708_071859	2023-07-08 07:18:59.400000+00:00	310876	3601.12	1372835957
GW230708_053705	2023-07-08 05:37:05.100000+00:00	310875	3601.17	1372829843
GW230706_104333	2023-07-06 10:43:33.200000+00:00	310825	3601.15	1372675431
GW230702_185453	2023-07-02 18:54:53.700000+00:00	310721	3601.16	1372359312
GW230702_162025	2023-07-02 16:20:25.900000+00:00	310719	3601.13	1372350044
GW230630_125806	2023-06-30 12:58:06.900000+00:00	310663	3601.15	1372165105
GW230630_070659	2023-06-30 07:06:59+00:00	310657	3601.14	1372144037

Continued on next page

GW Candidate	GW UTC	Run	Duration (s)	GPS
GW230628_231200	2023-06-28 23:12:00.400000+00:00	310620	3601.12	1372029138
GW230627_015337	2023-06-27 01:53:37.800000+00:00	310567	3601.14	1371866036
GW230625_211655	2023-06-25 21:16:55+00:00	310536	3601.16	1371763033
GW230624_113103	2023-06-24 11:31:03.700000+00:00	310501	3601.15	1371641482
GW230618_102550	2023-06-18 10:25:50+00:00	310347	3601.15	1371119168
GW230615_160825	2023-06-15 16:08:26+00:00	310237	3601.14	1370880524
GW230609_010824	2023-06-09 01:08:24.400000+00:00	310048	3601.13	1370308122
GW230608_205047	2023-06-08 20:50:47.200000+00:00	310044	3601.12	1370292665
GW230606_024545	2023-06-06 02:45:45.500000+00:00	309963	3601.13	1370054764
GW230605_065343	2023-06-05 06:53:43.500000+00:00	309923	3601.16	1369983242
GW230603_174756	2023-06-03 17:47:56.900000+00:00	309886	3601.12	1369849695
GW230601_224134	2023-06-01 22:41:34.100000+00:00	309843	3601.17	1369694512
GW230529_181500	2023-05-29 18:15:00.700000+00:00	309756	3601.12	1369419319

Table B.2: O4b GW candidates used in the SNO+ coincidence search. The GW trigger time, corresponding SNO+ run, run duration, and GW GPS trigger time are shown.

GW Candidate	GW UTC	Run	Duration (s)	GPS
S250119cv	2025-01-19 19:02:38.320000+00:00	365814	3601.15	1421348576
S250119ag	2025-01-19 02:51:38.780000+00:00	365798	3601.15	1421290317
S250118dp	2025-01-18 17:05:23.220000+00:00	365788	3601.15	1421255141
S250118az	2025-01-18 05:58:02.470000+00:00	365775	3601.12	1421215100
S250118t	2025-01-18 02:32:25.940000+00:00	365772	3601.13	1421202764
S250114ax	2025-01-14 08:22:03.220000+00:00	365734	3601.15	1420878141
S250109bi	2025-01-09 07:45:52.380000+00:00	365611	3601.16	1420443970
S250109f	2025-01-09 01:05:41.480000+00:00	365604	3601.14	1420419959
S250104v	2025-01-04 01:51:22.330000+00:00	365459	3601.13	1419990700
S250101k	2025-01-01 01:12:05.050000+00:00	365369	3601.13	1419729143
S241231bg	2024-12-31 05:41:33.610000+00:00	365349	3601.16	1419658912
S241230ev	2024-12-30 23:36:18.070000+00:00	365343	3601.12	1419636996
S241230bd	2024-12-30 08:45:04.540000+00:00	365327	3601.20	1419583523
S241225v	2024-12-25 08:28:15.650000+00:00	365206	3601.13	1419150514
S241225c	2024-12-25 04:25:53.250000+00:00	365202	3601.17	1419135971
S241127aj	2024-11-27 06:10:08.230000+00:00	364451	3601.13	1416723026
S241125n	2024-11-25 01:01:16.780000+00:00	364389	3601.12	1416531695
S241122a	2024-11-22 17:51:00.880000+00:00	364331	3601.17	1416333079
S241116cq	2024-11-16 15:17:53.680000+00:00	363892	3601.13	1415805492
S241114y	2024-11-14 02:47:11.780000+00:00	363798	3601.16	1415587650
S241111bn	2024-11-11 11:15:52.570000+00:00	363763	3601.13	1415358971
S241110br	2024-11-10 12:41:23.680000+00:00	363740	3601.12	1415277702
S241109bn	2024-11-09 11:59:24.900000+00:00	363716	3601.15	1415188783
S241109p	2024-11-09 03:33:18+00:00	363707	3601.15	1415158416

Continued on next page

GW Candidate	GW UTC	Run	Duration (s)	GPS
S241102br	2024-11-02 12:40:58.790000+00:00	363525	3601.29	1414586477
S241101ee	2024-11-01 22:05:23.060000+00:00	363510	3601.13	1414533941
S241009em	2024-10-09 22:04:55.520000+00:00	362893	3601.16	1412546714
S240925n	2024-09-25 00:58:09.990000+00:00	362521	3601.13	1411261108
S240924a	2024-09-24 00:03:16.550000+00:00	362491	3601.49	1411171415
S240923ct	2024-09-23 20:40:06.110000+00:00	362487	3601.17	1411159224
S240921cw	2024-09-21 20:18:35.790000+00:00	362438	3601.15	1410985134
S240920dw	2024-09-20 12:40:24.880000+00:00	362406	3601.13	1410871243
S240920bz	2024-09-20 07:34:24.480000+00:00	362401	3601.13	1410852882
S240919bn	2024-09-19 06:15:59.190000+00:00	362375	3601.13	1410761777
S240917cb	2024-09-17 13:02:37.720000+00:00	362328	3601.13	1410613376
S240915bd	2024-09-15 10:51:51.060000+00:00	362272	3601.32	1410432729
S240915b	2024-09-15 00:13:57.710000+00:00	362261	3601.14	1410394456
S240910ci	2024-09-10 10:35:35.490000+00:00	362113	3601.15	1409999753
S240908dg	2024-09-08 12:51:34.270000+00:00	362061	3601.15	1409835112
S240908bs	2024-09-08 08:26:28.410000+00:00	362057	3601.12	1409819206
S240907cg	2024-09-07 15:38:33.770000+00:00	362037	3601.16	1409758732
S240902bq	2024-09-02 14:33:06.760000+00:00	361883	3601.19	1409322805
S240830gn	2024-08-30 21:11:20.390000+00:00	361818	3601.13	1409087498
S240825ar	2024-08-25 05:51:46.980000+00:00	361669	3601.30	1408600325
S240807h	2024-08-07 21:45:59.200000+00:00	361224	3601.13	1407102377
S240716b	2024-07-16 03:49:00.510000+00:00	360631	3600.15	1405136959
S240705at	2024-07-05 05:32:15.920000+00:00	360354	3600.11	1404192754
S240703ad	2024-07-03 19:13:55.280000+00:00	360318	3600.13	1404069253
S240630t	2024-06-30 10:17:03.370000+00:00	360232	3600.15	1403777841
S240627by	2024-06-27 13:16:22.200000+00:00	360163	3601.13	1403529400
S240622h	2024-06-22 00:40:08.420000+00:00	360026	3601.15	1403052026

Continued on next page

GW Candidate	GW UTC	Run	Duration (s)	GPS
S240621em	2024-06-21 21:40:41.720000+00:00	360023	3601.12	1403041260
S240621eb	2024-06-21 20:09:35.530000+00:00	360021	3601.12	1403035794
S240621dy	2024-06-21 19:50:59.430000+00:00	360021	3601.12	1403034677
S240618ah	2024-06-18 07:16:27.150000+00:00	359929	3601.13	1402730205
S240615ea	2024-06-15 16:07:35.330000+00:00	359859	3601.15	1402502873
S240615dg	2024-06-15 11:36:20.720000+00:00	359855	3601.11	1402486599
S240601co	2024-06-01 23:10:04.030000+00:00	359510	3601.17	1401318622
S240601aj	2024-06-01 06:12:00.360000+00:00	359492	3601.34	1401257538
S240531bp	2024-05-31 07:52:48.460000+00:00	359469	3601.15	1401177186
S240530a	2024-05-30 01:24:17.950000+00:00	359437	3601.12	1401067476
S240527fv	2024-05-27 23:09:10.380000+00:00	359380	3601.15	1400886568
S240527en	2024-05-27 18:34:29.060000+00:00	359373	3601.14	1400870087
S240525p	2024-05-25 03:12:10.640000+00:00	359309	3601.13	1400641949
S240520cv	2024-05-20 21:36:16.970000+00:00	359192	3601.16	1400276195
S240515m	2024-05-15 00:53:01.110000+00:00	359054	3601.14	1399769599
S240514x	2024-05-14 12:17:13.720000+00:00	359025	3601.12	1399724252
S240514c	2024-05-14 08:03:21.050000+00:00	359017	3601.11	1399709019
S240513ei	2024-05-13 18:33:02.900000+00:00	359004	3348.49	1399660401
S240512r	2024-05-12 02:41:39.150000+00:00	358961	3601.13	1399516917
S240511i	2024-05-11 03:15:08+00:00	358938	3601.14	1399432526
S240507p	2024-05-07 04:16:32.350000+00:00	358631	3601.17	1399090610
S240505av	2024-05-05 13:35:52.580000+00:00	358592	3601.13	1398951371
S240501an	2024-05-01 03:35:34.920000+00:00	358477	3601.14	1398569753
S240428dr	2024-04-28 22:54:40.080000+00:00	358401	3601.18	1398380098
S240426dl	2024-04-26 15:18:03.770000+00:00	358345	3601.17	1398179902
S240426s	2024-04-26 03:14:51.980000+00:00	358333	3601.32	1398136510
S240421ar	2024-04-21 05:29:35.730000+00:00	358182	3601.13	1397712594

Continued on next page

GW Candidate	GW UTC	Run	Duration (s)	GPS
S240413p	2024-04-13 02:20:19.850000+00:00	357963	3601.13	1397010038

Table B.3: O4c GW candidates used in the SNO+ coincidence search. The GW trigger time, corresponding SNO+ run, run duration, and GW GPS trigger time are shown.

GW Candidate	GW UTC	Run	Duration (s)	GPS
S250727dc	2025-07-27 20:01:48.460000+00:00	371172	3601.19	1437681726
S250726ak	2025-07-26 08:28:15.370000+00:00	371135	3601.20	1437553713
S250725l	2025-07-25 04:20:50.940000+00:00	371102	3601.18	1437452469
S250725j	2025-07-25 04:09:44.250000+00:00	371102	3601.18	1437451802
S250712cd	2025-07-12 14:25:32.330000+00:00	370718	3601.13	1436365550
S250711q	2025-07-11 03:27:25.110000+00:00	370680	3601.11	1436239663
S250705cb	2025-07-05 16:29:56.840000+00:00	370533	3601.12	1435768215
S250704ab	2025-07-04 04:30:48.040000+00:00	370493	3601.15	1435638666
S250701bq	2025-07-01 23:17:46.930000+00:00	370423	3601.11	1435447085
S250701bp	2025-07-01 20:34:40.860000+00:00	370420	3601.14	1435437299
S250629bs	2025-06-29 12:13:04.380000+00:00	370351	3601.13	1435234402
S250629ae	2025-06-29 05:50:36.920000+00:00	370345	3601.17	1435211455
S250628am	2025-06-28 18:23:19.780000+00:00	370333	3601.13	1435170218
S250331o	2025-03-31 01:34:48.440000+00:00	367651	3601.13	1427420106
S250328ae	2025-03-28 05:40:27.420000+00:00	367584	3601.15	1427175645
S250326y	2025-03-26 01:54:06.150000+00:00	367528	3601.14	1426989264
S250319bu	2025-03-19 06:25:36.480000+00:00	367339	3601.14	1426400754
S250304cb	2025-03-04 06:22:45.570000+00:00	366931	3601.16	1425104584
S250227e	2025-02-27 00:12:45.470000+00:00	366804	3601.17	1424650383
S250226dl	2025-02-26 22:48:38.700000+00:00	366803	3601.17	1424645337
S250223dk	2025-02-23 12:01:15.360000+00:00	366702	3601.14	1424347293
S250211be	2025-02-11 04:35:43.150000+00:00	366341	3601.17	1423283761
S250211aa	2025-02-11 02:25:46.620000+00:00	366338	3601.14	1423275965
S250208ad	2025-02-08 03:51:06.790000+00:00	366265	3601.13	1423021885

Continued on next page

GW Candidate	GW UTC	Run	Duration (s)	GPS
S250206dm	2025-02-06 21:25:30.440000+00:00	366227	3601.13	1422912348
S250205bk	2025-02-05 10:35:41.580000+00:00	366181	3601.19	1422786960
S250202cu	2025-02-02 18:49:02.510000+00:00	366111	3601.17	1422557361

BIBLIOGRAPHY

[1] Andrea Giuliani and Alfredo Poves. Neutrinoless double-beta decay. *Adv. High Energy Phys.*, 2012. URL https://inspirehep.net/files/993c2d095c834c15d16db3e8dfbe5e55.

[2] Benjamin Tam and Amanda Bacon. SNO+ Scintillator (LAB + 2.2 g/L PPO) Light Yield Plot for approval. Technical report, SNO+, 2022.

[3] Belina Krosigk. *Measurement of Proton and α Particle Quenching in LAB Based Scintillators and Determination of Spectral Sensitivities to Supernova Neutrinos in the SNO+ Detector.* PhD thesis, Technischen Universität Dresden, 2015. Accessed: February 26, 2026.

[4] Jia-Shian Wang. *Supernova Neutrinos and Measurement of Liquid Scintillator Backgrounds in SNO+.* PhD thesis, University of Oxford, 2022. Accessed: February 26, 2026.

[5] Ossila enablind science. Beta Decay: Equations, Feynman Diagrams & Measurement, 2026. URL https://www.ossila.com/pages/introduction-to-beta-decay.

[6] Los Alamos Science. The Reines-Cowan Experiments: Detecting the Poltergeist, 1997.

[7] Wikipedia. Standard Model — Wikipedia, the free encyclopedia., 2026.

[8] Fermilab: All Things Neutrino. Which neutrino is the lightest?, 2026.

[9] Elisabetta Bossio and Matteo Agostini. Probing beyond the standard model physics with double-beta decays. *Journal of Physics G: Nuclear and Particle Physics*, 51(2):023001, dec 2023. doi: 10.1088/1361-6471/ad11f9. URL https://doi.org/10.1088/1361-6471/ad11f9.

[10] W. C. Haxton, R. G. Hamish Robertson, and Aldo M. Serenelli. Solar Neutrinos: Status and Prospects. *Ann. Rev. Astron. Astrophys.*, 51:21–61, 2013. doi: 10.1146/annurev-astro-081811-125539. URL https://www.annualreviews.org/content/journals/10.1146/annurev-astro-081811-125539.

[11] Q. R. Ahmad, R. C. Allen, T. C. Andersen, J. D.Anglin, J. C. Barton, E. W. Beier, M. Bercovitch, J. Bigu, S. D. Biller, R. A. Black, I. Blevis, R. J. Boardman, J. Boger, E. Bonvin, M. G. Boulay, M. G. Bowler, T. J. Bowles, S. J. Brice, M. C. Browne, T. V. Bullard, G. Bühler, J. Cameron, Y. D. Chan, H. H. Chen, M. Chen, X. Chen, B. T. Cleveland, E. T. H. Clifford, J. H. M. Cowan, D. F. Cowen, G. A. Cox, X. Dai, F. Dalnoki-Veress, W. F. Davidson, P. J. Doe, G. Doucas, M. R. Dragowsky, C. A. Duba, F. A. Duncan, M. Dunford, J. A. Dunmore, E. D. Earle, S. R. Elliott, H. C. Evans, G. T. Ewan, J. Farine, H. Fergani, A. P. Ferraris, R. J. Ford, J. A. Formaggio, M. M. Fowler, K. Frame, E. D. Frank, W. Frati, N. Gagnon, J. V. Germani, S. Gil, K. Graham, D. R. Grant, R. L. Hahn, A. L. Hallin, E. D. Hallman, A. S. Hamer, A. A. Hamian, W. B. Handler, R. U. Haq, C. K. Hargrove, P. J. Harvey, R. Hazama, K. M. Heeger, W. J. Heintzelman, J. Heise, R. L. Helmer, J. D. Hepburn,

H. Heron, J. Hewett, A. Hime, M. Howe, J. G. Hykawy, M. C. P. Isaac, P. Jagam, N. A. Jelley, C. Jillings, G. Jonkmans, K. Kazkaz, P. T. Keener, J. R. Klein, A. B. Knox, R. J. Komar, R. Kouzes, T. Kutter, C. C. M. Kyba, J. Law, I. T. Lawson, M. Lay, H. W. Lee, K. T. Lesko, J. R. Leslie, I. Levine, W. Locke, S. Luoma, J. Lyon, S. Majerus, H. B. Mak, J. Maneira, J. Manor, A. D. Marino, N. McCauley, A. B. McDonald, D. S. McDonald, K. McFarlane, G. McGregor, R. Meijer Drees, C. Mifflin, G. G. Miller, G. Milton, B. A. Moffat, M. Moorhead, C. W. Nally, M. S. Neubauer, F. M. Newcomer, H. S. Ng, A. J. Noble, E. B. Norman, V. M. Novikov, M. O'Neill, C. E. Okada, R. W. Ollerhead, M. Omori, J. L. Orrell, S. M. Oser, A. W. P. Poon, T. J. Radcliffe, A. Roberge, B. C. Robertson, R. G. H. Robertson, S. S. E. Rosendahl, J. K. Rowley, V. L. Rusu, E. Saettler, K. K. Schaffer, M. H. Schwendener, A. Schülke, H. Seifert, M. Shatkay, J. J. Simpson, C. J. Sims, D. Sinclair, P. Skensved, A. R. Smith, M. W. E. Smith, T. Spreitzer, N. Starinsky, T. D. Steiger, R. G. Stokstad, L. C. Stonehill, R. S. Storey, B. Sur, R. Tafirout, N. Tagg, N. W. Tanner, R. K. Taplin, M. Thorman, P. M. Thornewell, P. T. Trent, Y. I. Tserkovnyak, R. Van Berg, R. G. Van de Water, C. J. Virtue, C. E. Waltham, J.-X. Wang, D. L. Wark, N. West, J. B. Wilhelmy, J. F. Wilkerson, J. R. Wilson, P. Wittich, J. M. Wouters, and M. Yeh. Direct evidence for neutrino flavor transformation from neutral-current interactions in the sudbury neutrino observatory. *Phys. Rev. Lett.*, 89:011301, Jun 2002. doi: 10.1103/PhysRevLett.89.011301. URL https://link.aps.org/doi/10.1103/PhysRevLett.89.011301.

[12] M. Agostini, K. Altenmüller, S. Appel, V. Atroshchenko, Z. Bagdasarian, D. Basilico, G. Bellini, J. Benziger, D. Bick, G. Bonfini, D. Bravo, B. Caccianiga, F. Calaprice, A. Caminata, L. Cappelli, P. Cavalcante, F. Cavanna, A. Chepurnov, K. Choi, D. D'Angelo, S. Davini, A. Derbin, A. Di Giacinto, V. Di Marcello, X. F. Ding, A. Di Ludovico, L. Di Noto, I. Drachnev, G. Fiorentini, A. Formozov, D. Franco, F. Gabriele, C. Galbiati, M. Gschwender, C. Ghiano, M. Giammarchi, A. Goretti, M. Gromov, D. Guffanti, C. Hagner, E. Hungerford, Aldo Ianni, Andrea Ianni, A. Jany, D. Jeschke, S. Kumaran, V. Kobychev, G. Korga, T. Lachenmaier, T. Lasserre, M. Laubenstein, E. Litvinovich, P. Lombardi, I. Lomskaya, L. Ludhova, G. Lukyanchenko, L. Lukyanchenko, I. Machulin, F. Mantovani, G. Manuzio, S. Marcocci, J. Maricic, J. Martyn, E. Meroni, M. Meyer, L. Miramonti, M. Misiaszek, M. Montuschi, V. Muratova, B. Neumair, M. Nieslony, L. Oberauer, A. Onillon, V. Orekhov, F. Ortica, M. Pallavicini, L. Papp, Ö. Penek, L. Pietrofaccia, N. Pilipenko, A. Pocar, G. Raikov, M. T. Ranalli, G. Ranucci, A. Razeto, A. Re, M. Redchuk, B. Ricci, A. Romani, N. Rossi, S. Rottenanger, S. Schönert, D. Semenov, M. Skorokhvatov, O. Smirnov, A. Sotnikov, V. Strati, Y. Suvorov, R. Tartaglia, G. Testera, J. Thurn, E. Unzhakov, A. Vishneva, M. Vivier, R. B. Vogelaar, F. von Feilitzsch, M. Wojcik, M. Wurm, O. Zaimidoroga, S. Zavatarelli, K. Zuber, and G. Zuzel. Comprehensive geoneutrino analysis with borexino. *Phys. Rev. D*, 101:012009, Jan 2020. doi: 10.1103/PhysRevD.101.012009. URL https://link.aps.org/doi/10.1103/PhysRevD.101.012009.

[13] Georg G. Raffelt, Hans-Thomas Janka, and Damiano F. G. Fiorillo. Neutrinos from core-collapse supernovae. *arXiv*, 9 2025. URL https://arxiv.org/abs/2509.16306.

[14] The SNO+ collaboration, V. Albanese, R. Alves, M.R. Anderson, S. Andringa, L. Anselmo, E. Arushanova, S. Asahi, M. Askins, D.J. Auty, A.R. Back, S. Back, F. Barão, Z. Barnard,

A. Barr, N. Barros, D. Bartlett, R. Bayes, C. Beaudoin, E.W. Beier, G. Berardi, A. Bialek, S.D. Biller, E. Blucher, R. Bonventre, M. Boulay, D. Braid, E. Caden, E.J. Callaghan, J. Caravaca, J. Carvalho, L. Cavalli, D. Chauhan, M. Chen, O. Chkvorets, K.J. Clark, B. Cleveland, C. Connors, D. Cookman, I.T. Coulter, M.A. Cox, D. Cressy, X. Dai, C. Darrach, B. Davis-Purcell, C. Deluce, M.M. Depatie, F. Descamps, F. Di Lodovico, J. Dittmer, A. Doxtator, N. Duhaime, F. Duncan, J. Dunger, A.D. Earle, D. Fabris, E. Falk, A. Farrugia, N. Fatemighomi, C. Felber, V. Fischer, E. Fletcher, R. Ford, K. Frankiewicz, N. Gagnon, A. Gaur, J. Gauthier, A. Gibson-Foster, K. Gilje, O.I. González-Reina, D. Gooding, P. Gorel, K. Graham, C. Grant, J. Grove, S. Grullon, E. Guillian, S. Hall, A.L. Hallin, D. Hallman, S. Hans, J. Hartnell, P. Harvey, M. Hedayatipour, W.J. Heintzelman, J. Heise, R.L. Helmer, B. Hodak, M. Hodak, M. Hood, D. Horne, B. Hreljac, J. Hu, S.M.A. Hussain, T. Iida, A.S. Inácio, C.M. Jackson, N.A. Jelley, C.J. Jillings, C. Jones, P.G. Jones, K. Kamdin, T. Kaptanoglu, J. Kaspar, K. Keeter, C. Kefelian, P. Khaghani, L. Kippenbrock, J.R. Klein, R. Knapik, J. Kofron, L.L. Kormos, S. Korte, B. Krar, C. Kraus, C.B. Krauss, T. Kroupová, K. Labe, F. Lafleur, I. Lam, C. Lan, B.J. Land, R. Lane, S. Langrock, P. Larochelle, S. Larose, A. LaTorre, I. Lawson, L. Lebanowski, G.M. Lefeuvre, E.J. Leming, A. Li, O. Li, J. Lidgard, B. Liggins, P. Liimatainen, Y.H. Lin, X. Liu, Y. Liu, V. Lozza, M. Luo, S. Maguire, A. Maio, K. Majumdar, S. Manecki, J. Maneira, R.D. Martin, E. Marzec, A. Mastbaum, A. Mathewson, N. McCauley, A.B. McDonald, K. McFarlane, P. Mekarski, M. Meyer, C. Miller, C. Mills, M. Mlejnek, E. Mony, B. Morissette, I. Morton-Blake, M.J. Mottram, S. Nae, M. Nirkko, L.J. Nolan, V.M. Novikov, H.M. O'Keeffe, E. O'Sullivan, G.D. Orebi Gann, M.J. Parnell, J. Paton, S.J.M. Peeters, T. Pershing, Z. Petriw, J. Petzoldt, L. Pickard, D. Pracsovics, G. Prior, J.C. Prouty, S. Quirk, S. Read, A. Reichold, S. Riccetto, R. Richardson, M. Rigan, I. Ritchie, A. Robertson, B.C. Robertson, J. Rose, R. Rosero, P.M. Rost, J. Rumleskie, M.A. Schumaker, M.H. Schwendener, D. Scislowski, J. Secrest, M. Seddighin, L. Segui, S. Seibert, I. Semenec, F. Shaker, T. Shantz, M.K. Sharma, T.M. Shokair, L. Sibley, J.R. Sinclair, K. Singh, P. Skensved, M. Smiley, T. Sonley, A. Sörensen, M. St-Amant, R. Stainforth, S. Stankiewicz, M. Strait, M.I. Stringer, A. Stripay, R. Svoboda, S. Tacchino, B. Tam, C. Tanguay, J. Tatar, L. Tian, N. Tolich, J. Tseng, H.W.C. Tseung, E. Turner, R. Van Berg, E. Vázquez-Jáuregui, J.G.C. Veinot, C.J. Virtue, B. von Krosigk, J.M.G. Walker, M. Walker, J. Wallig, S.C. Walton, J. Wang, M. Ward, O. Wasalski, J. Waterfield, J.J. Weigand, R.F. White, J.R. Wilson, T.J. Winchester, P. Woosaree, A. Wright, J.P. Yanez, M. Yeh, T. Zhang, Y. Zhang, T. Zhao, K. Zuber, and A. Zummo. The sno+ experiment. *Journal of Instrumentation*, 16(08):P08059, aug 2021. doi: 10.1088/1748-0221/16/08/P08059. URL https://doi.org/10.1088/1748-0221/16/08/P08059.

[15] J Boger, R.L Hahn, J.K Rowley, A.L Carter, B Hollebone, D Kessler, I Blevis, F Dalnoki-Veress, A DeKok, J Farine, D.R Grant, C.K Hargrove, G Laberge, I Levine, K McFarlane, H Mes, A.T Noble, V.M Novikov, M O'Neill, M Shatkay, C Shewchuk, D Sinclair, E.T.H Clifford, R Deal, E.D Earle, E Gaudette, G Milton, B Sur, J Bigu, J.H.M Cowan, D.L Cluff, E.D Hallman, R.U Haq, J Hewett, J.G Hykawy, G Jonkmans, R Michaud, A Roberge, J Roberts, E Saettler, M.H Schwendener, H Seifert, D Sweezey, R Tafirout, C.J Virtue, D.N Beck, Y.D Chan, X Chen, M.R Dragowsky, F.W Dycus, J Gonzalez, M.C.P Isaac, Y Kajiyama, G.W Koehler, K.T Lesko, M.C Moebus, E.B Norman, C.E Okada, A.W.P Poon, P Purgalis, A Schuelke, A.R Smith, R.G Stokstad, S Turner, I Zlimen, J.M Anaya, T.J Bowles, S.J Brice,

Ernst-Ingo Esch, M.M Fowler, Azriel Goldschmidt, A Hime, A.F McGirt, G.G Miller, W.A Teasdale, J.B Wilhelmy, J.M Wouters, J.D Anglin, M Bercovitch, W.F Davidson, R.S Storey, S Biller, R.A Black, R.J Boardman, M.G Bowler, J Cameron, B Cleveland, A.P Ferraris, G Doucas, H Heron, C Howard, N.A Jelley, A.B Knox, M Lay, W Locke, J Lyon, S Majerus, M Moorhead, M Omori, N.W Tanner, R.K Taplin, M Thorman, D.L Wark, N West, J.C Barton, P.T Trent, R Kouzes, M.M Lowry, A.L Bell, E Bonvin, M Boulay, M Dayon, F Duncan, L.S Erhardt, H.C Evans, G.T Ewan, R Ford, A Hallin, A Hamer, P.M Hart, P.J Harvey, D Haslip, C.A.W Hearns, R Heaton, J.D Hepburn, C.J Jillings, E.P Korpach, H.W Lee, J.R Leslie, M.-Q Liu, H.B Mak, A.B McDonald, J.D MacArthur, W McLatchie, B.A Moffat, S Noel, T.J Radcliffe, B.C Robertson, P Skensved, R.L Stevenson, X Zhu, S Gil, J Heise, R.L Helmer, R.J Komar, C.W Nally, H.S Ng, C.E Waltham, R.C Allen, G Bühler, H.H Chen, G Aardsma, T Andersen, K Cameron, M.C Chon, R.H Hanson, P Jagam, J Karn, J Law, R.W Ollerhead, J.J Simpson, N Tagg, J.-X Wang, C Alexander, E.W Beier, J.C Cook, D.F Cowen, E.D Frank, W Frati, P.T Keener, J.R Klein, G Mayers, D.S McDonald, M.S Neubauer, F.M Newcomer, R.J Pearce, R.G.Van de Water, R.Van Berg, P Wittich, Q.R Ahmad, J.M Beck, M.C Browne, T.H Burritt, P.J Doe, C.A Duba, S.R Elliott, J.E Franklin, J.V Germani, P Green, A.A Hamian, K.M Heeger, M Howe, R.Meijer Drees, A Myers, R.G.H Robertson, M.W.E Smith, T.D Steiger, T.Van Wechel, and J.F Wilkerson. The sudbury neutrino observatory. *Nuclear Instruments and Methods in Physics Research Section A: Accelerators, Spectrometers, Detectors and Associated Equipment*, 449(1): 172–207, 2000. ISSN 0168-9002. doi: https://doi.org/10.1016/S0168-9002(99)01469-2. URL https://www.sciencedirect.com/science/article/pii/S0168900299014692.

[16] Iwan Morton-Blake. *First Measurement of Reactor Antineutrinos in Scintillator at SNO+ and Study of Alternative Designs for Large-Scale Liquid Scintillator Detectors*. PhD thesis, University of Oxford, 2021. Accessed: February 26, 2026.

[17] Department of Phyiscs, Duke University. Neutrinoless Double Beta Decay, 2017.

[18] Tanner Kaptanoglu. *REACTOR ANTINEUTRINOS IN THE SNO+ WATER PHASE AND DETECTOR R&D FOR LARGE-SCALE NEUTRINO DETECTORS*. PhD thesis, University of Pennsylvania, 2020. Accessed: February 26, 2026.

[19] Penn SNO Electronics. The SNO Front End Data Acquisition Electronics, 1998.

[20] Anthony Zummo. *MEASUREMENT OF REACTOR ANTINEUTRINO OSCILLATION WITH SNO+*. PhD thesis, University of Pennsylvania, 2024. Accessed: April 30, 2026.

[21] F. Mitch Newcomer Joshua Klein, Mark Neubauer and Rick Van Berg. The SNO Trigger System. Technical report, University of Pennsylvania, 1997. Internal document; accessed Feb 27, 2026.

[22] Rafael Hunt-Stokes. Calibration of the scintillation timing in sno+ using in-situ backgrounds, 2024. URL https://arxiv.org/abs/2403.19496.

[23] Tereza Kroupová. *Improving the Sensitivity to Neutrinoless Double Beta Decay in SNO+*. PhD thesis, University of Oxford, 2020. Accessed: February 26, 2026.

[24] B. P. Abbott, R. Abbott, T. D. Abbott, F. Acernese, K. Ackley, C. Adams, T. Adams, P. Addesso, R. X. Adhikari, V. B. Adya, C. Affeldt, M. Afrough, B. Agarwal, M. Agathos, K. Agatsuma, N. Aggarwal, O. D. Aguiar, L. Aiello, A. Ain, P. Ajith, B. Allen, G. Allen, A. Allocca, P. A. Altin, A. Amato, A. Ananyeva, S. B. Anderson, W. G. Anderson, S. V. Angelova, S. Antier, S. Appert, K. Arai, M. C. Araya, J. S. Areeda, N. Arnaud, K. G. Arun, S. Ascenzi, G. Ashton, M. Ast, S. M. Aston, P. Astone, D. V. Atallah, P. Aufmuth, C. Aulbert, K. AultONeal, C. Austin, A. Avila-Alvarez, S. Babak, P. Bacon, M. K. M. Bader, S. Bae, P. T. Baker, F. Baldaccini, G. Ballardin, S. W. Ballmer, S. Banagiri, J. C. Barayoga, S. E. Barclay, B. C. Barish, D. Barker, K. Barkett, F. Barone, B. Barr, L. Barsotti, M. Barsuglia, D. Barta, S. D. Barthelmy, J. Bartlett, I. Bartos, R. Bassiri, A. Basti, J. C. Batch, M. Bawaj, J. C. Bayley, M. Bazzan, B. Bécsy, C. Beer, M. Bejger, I. Belahcene, A. S. Bell, B. K. Berger, G. Bergmann, J. J. Bero, C. P. L. Berry, D. Bersanetti, A. Bertolini, J. Betzwieser, S. Bhagwat, R. Bhandare, I. A. Bilenko, G. Billingsley, C. R. Billman, J. Birch, R. Birney, O. Birnholtz, S. Biscans, S. Biscoveanu, A. Bisht, M. Bitossi, C. Biwer, M. A. Bizouard, J. K. Blackburn, J. Blackman, C. D. Blair, D. G. Blair, R. M. Blair, S. Bloemen, O. Bock, N. Bode, M. Boer, G. Bogaert, A. Bohe, F. Bondu, E. Bonilla, R. Bonnand, B. A. Boom, R. Bork, V. Boschi, S. Bose, K. Bossie, Y. Bouffanais, A. Bozzi, C. Bradaschia, P. R. Brady, M. Branchesi, J. E. Brau, T. Briant, A. Brillet, M. Brinkmann, V. Brisson, P. Brockill, J. E. Broida, A. F. Brooks, D. A. Brown, D. D. Brown, S. Brunett, C. C. Buchanan, A. Buikema, T. Bulik, H. J. Bulten, A. Buonanno, D. Buskulic, C. Buy, R. L. Byer, M. Cabero, L. Cadonati, G. Cagnoli, C. Cahillane, J. Calderón Bustillo, T. A. Callister, E. Calloni, J. B. Camp, M. Canepa, P. Canizares, K. C. Cannon, H. Cao, J. Cao, C. D. Capano, E. Capocasa, F. Carbognani, S. Caride, M. F. Carney, J. Casanueva Diaz, C. Casentini, S. Caudill, M. Cavaglià, F. Cavalier, R. Cavalieri, G. Cella, C. B. Cepeda, P. Cerdá-Durán, G. Cerretani, E. Cesarini, S. J. Chamberlin, M. Chan, S. Chao, P. Charlton, E. Chase, E. Chassande-Mottin, D. Chatterjee, K. Chatziioannou, B. D. Cheeseboro, H. Y. Chen, X. Chen, Y. Chen, H.-P. Cheng, H. Chia, A. Chincarini, A. Chiummo, T. Chmiel, H. S. Cho, M. Cho, J. H. Chow, N. Christensen, Q. Chu, A. J. K. Chua, S. Chua, A. K. W. Chung, S. Chung, and G. Ciani. Multi-messenger Observations of a Binary Neutron Star Merger. *The Astrophysical Journal Letters*, 848(2):L12, oct 2017. doi: 10.3847/2041-8213/aa91c9.

[25] B. P. Abbott et al. Observation of Gravitational Waves from a Binary Black Hole Merger. *Phys. Rev. Lett.*, 116(6):061102, 2016. doi: 10.1103/PhysRevLett.116.061102.

[26] LIGO Test Mass. LIGO Gallery, 2026.

[27] LIGO Observing Schedule. LIGO, VIRGO AND KAGRA OBSERVING RUN PLANS, 2025.

[28] Shanika Galaudage. Science Infographics, 2026.

[29] M. Favata and K. Thorne. Sounds of Spacetime, 2026.

[30] Basudeb Dasgupta and John F. Beacom. Reconstruction of supernova ν_μ, ν_τ, $\overline{\nu}_\mu$, and $\overline{\nu}_\tau$ neutrino spectra at scintillator detectors. *Phys. Rev. D*, 83:113006, Jun 2011. doi: 10.1103/PhysRevD.83.113006. URL https://link.aps.org/doi/10.1103/PhysRevD.83.113006.

[31] W. Pauli. Dear radioactive ladies and gentlemen. *Phys. Today*, 31N9:27, 1978.

[32] Enrico Fermi. Versuch einer theorie der β-strahlen. i. *Zeitschrift für Physik*, 1934. URL https://doi.org/10.1007/BF01351864.

[33] UCI. The singing UCI Nobel Laureate who nearly bombed Nevada, 2021. URL https://www.physics.uci.edu/node/14126. Accessed: February 26, 2026.

[34] Frederick Reines and Clyde L. Cowan. The neutrino. *Nature*, 178:446–449, 1956. doi: 10.1038/178446a0. URL https://www.nature.com/articles/178446a0.

[35] Ara Ioannisian and Stefan Pokorski. Three Neutrino Oscillations in Matter. *Phys. Lett. B*, 782:641–645, 2018. doi: 10.1016/j.physletb.2018.06.001. URL https://www.sciencedirect.com/science/article/pii/S0370269318304428?via%3Dihub.

[36] Himal Acharya et al. Sterile-neutrino search based on 259 days of KATRIN data. *Nature*, 648(8092):70–75, 2025. doi: 10.1038/s41586-025-09739-9. URL https://www.nature.com/articles/s41586-025-09739-9.

[37] S. P. Ahlen, A. Aviles, B. Cartwright, K. S. Croker, W. Elbers, D. Farrah, N. Fernandez, G. Niz, J. W. Rohlf, G. Tarlé, R. A. Windhorst, J. Aguilar, U. Andrade, D. Bianchi, D. Brooks, T. Claybaugh, A. de la Macorra, A. de Mattia, B. Dey, P. Doel, J. E. Forero-Romero, E. Gaztañaga, S. Gontcho A. Gontcho, G. Gutierrez, D. Huterer, M. Ishak, R. Kehoe, D. Kirkby, A. Kremin, O. Lahav, C. Lamman, M. Landriau, L. Le Guillou, M. E. Levi, M. Manera, R. Miquel, J. Moustakas, I. Pérez-Ràfols, F. Prada, G. Rossi, E. Sanchez, M. Schubnell, H. Seo, J. Silber, D. Sprayberry, M. Walther, B. A. Weaver, R. H. Wechsler, and H. Zou. Positive neutrino masses with desi dr2 via matter conversion to dark energy. *Phys. Rev. Lett.*, 135:081003, Aug 2025. doi: 10.1103/yb2k-kn7h. URL https://link.aps.org/doi/10.1103/yb2k-kn7h.

[38] T. M. C. Abbott, M. Aguena, A. Alarcon, A. Amon, D. Anbajagane, F. Andrade-Oliveira, S. Avila, S. S. Allam, D. Bacon, M. R. Becker, S. Bhargava, J. Blazek, S. Bocquet, D. Brooks, A. Carnero Rosell, J. Carretero, F. J. Castander, C. Chang, A. Choi, C. Conselice, M. Costanzi, M. Crocce, L. N. da Costa, M. E. S. Pereira, C. Doux, T. M. Davis, S. Desai, H. T. Diehl, S. Dodelson, P. Doel, J. Elvin-Poole, J. Esteves, S. Everett, A. Farahi, A. Ferté, B. Flaugher, J. García-Bellido, M. Gatti, G. Giannini, P. Giles, S. Grandis, D. Gruen, R. A. Gruendl, G. Gutierrez, I. Harrison, S. R. Hinton, D. L. Hollowood, K. Honscheid, N. Jeffrey, T. Jeltema, E. Krause, O. Lahav, S. Lee, C. Lidman, M. Lima, H. Lin, J. J. Mohr, J. L. Marshall, J. McCullough, J. Mena-Fern'andez, R. Miquel, J. Muir, J. Myles, R. L. C. Ogando, A. Palmese, M. Paterno, A. A. Plazas Malagón, A. Porredon, J. Prat, A. K. Romer, A. Roodman, E. Rozo, E. S. Rykoff, R. Rosenfeld, E. Sanchez, D. Sanchez Cid, I. Sevilla-Noarbe, M. Smith, E. Suchyta, Tae-hyeon Shin, G. Tarle, D. Thomas, Chun-

Hao To, M. A. Troxel, V. Vikram, A. R. Walker, David H. Weinberg, N. Weaverdyck, R. H. Wechsler, J. Weller, H.-Y. Wu, M. Yamamoto, B. Yanny, Y. Zhang, and C. Zhou. Dark energy survey year 3 results: Cosmological constraints from cluster abundances, weak lensing, and galaxy clustering. *Phys. Rev. D*, 112:083535, Oct 2025. doi: 10.1103/3dzh-d8f5. URL https://link.aps.org/doi/10.1103/3dzh-d8f5.

[39] Cheng Zhao et al. The completed SDSS-IV extended Baryon Oscillation Spectroscopic Survey: cosmological implications from multitracer BAO analysis with galaxies and voids. *Mon. Not. Roy. Astron. Soc.*, 511(4):5492–5524, 2022. doi: 10.1093/mnras/stac390. URL https://academic.oup.com/mnras/article/511/4/5492/6527584.

[40] Eleonora Di Valentino, Stefano Gariazzo, and Olga Mena. Most constraining cosmological neutrino mass bounds. *Phys. Rev. D*, 104:083504, Oct 2021. doi: 10.1103/PhysRevD.104.083504. URL https://link.aps.org/doi/10.1103/PhysRevD.104.083504.

[41] John N. Bahcall, M. H. Pinsonneault, and Sarbani Basu. Solar models: Current epoch and time dependences, neutrinos, and helioseismological properties. *Astrophys. J.*, 555:990–1012, 2001. doi: 10.1086/321493. URL https://iopscience.iop.org/article/10.1086/321493.

[42] J. N. Abdurashitov et al. Solar neutrino flux measurements by the Soviet-American Gallium Experiment (SAGE) for half the 22 year solar cycle. *J. Exp. Theor. Phys.*, 95:181–193, 2002. doi: 10.1134/1.1506424. URL https://link.springer.com/article/10.1134/1.1506424.

[43] W. Hampel et al. GALLEX solar neutrino observations: Results for GALLEX IV. *Phys. Lett. B*, 447:127–133, 1999. doi: 10.1016/S0370-2693(98)01579-2.

[44] M. Altmann et al. GNO solar neutrino observations: Results for GNO I. *Phys. Lett. B*, 490:16–26, 2000. doi: 10.1016/S0370-2693(00)00915-1. URL https://www.sciencedirect.com/science/article/pii/S0370269300009151?via%3Dihub.

[45] Y. Fukuda et al. Atmospheric muon-neutrino / electron-neutrino ratio in the multiGeV energy range. *Phys. Lett. B*, 335:237–245, 1994. doi: 10.1016/0370-2693(94)91420-6. URL https://www.sciencedirect.com/science/article/pii/0370269394914206?via%3Dihub.

[46] Y. Fukuda, T. Hayakawa, E. Ichihara, K. Inoue, K. Ishihara, H. Ishino, Y. Itow, T. Kajita, J. Kameda, S. Kasuga, K. Kobayashi, Y. Kobayashi, Y. Koshio, M. Miura, M. Nakahata, S. Nakayama, A. Okada, K. Okumura, N. Sakurai, M. Shiozawa, Y. Suzuki, Y. Takeuchi, Y. Totsuka, S. Yamada, M. Earl, A. Habig, E. Kearns, M. D. Messier, K. Scholberg, J. L. Stone, L. R. Sulak, C. W. Walter, M. Goldhaber, T. Barszczxak, D. Casper, W. Gajewski, P. G. Halverson, J. Hsu, W. R. Kropp, L. R. Price, F. Reines, M. Smy, H. W. Sobel, M. R. Vagins, K. S. Ganezer, W. E. Keig, R. W. Ellsworth, S. Tasaka, J. W. Flanagan, A. Kibayashi, J. G. Learned, S. Matsuno, V. J. Stenger, D. Takemori, T. Ishii, J. Kanzaki, T. Kobayashi, S. Mine, K. Nakamura, K. Nishikawa, Y. Oyama, A. Sakai, M. Sakuda, O. Sasaki, S. Echigo, M. Kohama, A. T. Suzuki, T. J. Haines, E. Blaufuss, B. K. Kim, R. Sanford, R. Svoboda, M. L. Chen, Z. Conner, J. A. Goodman, G. W. Sullivan, J. Hill, C. K. Jung, K. Martens, C. Mauger,

C. McGrew, E. Sharkey, B. Viren, C. Yanagisawa, W. Doki, K. Miyano, H. Okazawa, C. Saji, M. Takahata, Y. Nagashima, M. Takita, T. Yamaguchi, M. Yoshida, S. B. Kim, M. Etoh, K. Fujita, A. Hasegawa, T. Hasegawa, S. Hatakeyama, T. Iwamoto, M. Koga, T. Maruyama, H. Ogawa, J. Shirai, A. Suzuki, F. Tsushima, M. Koshiba, M. Nemoto, K. Nishijima, T. Futagami, Y. Hayato, Y. Kanaya, K. Kaneyuki, Y. Watanabe, D. Kielczewska, R. A. Doyle, J. S. George, A. L. Stachyra, L. L. Wai, R. J. Wilkes, and K. K. Young. Evidence for oscillation of atmospheric neutrinos. *Phys. Rev. Lett.*, 81:1562–1567, Aug 1998. doi: 10.1103/PhysRevLett.81.1562. URL https://link.aps.org/doi/10.1103/PhysRevLett.81.1562.

[47] M. Abreu et al. Measurement of reactor antineutrino oscillations with 1.46 ktonne-years of data at SNO+. *arXiv*, 11 2025. URL https://arxiv.org/abs/2511.11856.

[48] K. S. Hirata, T. Kajita, M. Koshiba, M. Nakahata, Y. Oyama, N. Sato, A. Suzuki, M. Takita, Y. Totsuka, T. Kifune, T. Suda, K. Takahashi, T. Tanimori, K. Miyano, M. Yamada, E. W. Beier, L. R. Feldscher, W. Frati, S. B. Kim, A. K. Mann, F. M. Newcomer, R. Van Berg, W. Zhang, and B. G. Cortez. Observation in the kamiokande-ii detector of the neutrino burst from supernova sn1987a. *Phys. Rev. D*, 38:448–458, Jul 1988. doi: 10.1103/PhysRevD.38.448. URL https://link.aps.org/doi/10.1103/PhysRevD.38.448.

[49] R. M. Bionta, G. Blewitt, C. B. Bratton, D. Casper, A. Ciocio, R. Claus, B. Cortez, M. Crouch, S. T. Dye, S. Errede, G. W. Foster, W. Gajewski, K. S. Ganezer, M. Goldhaber, T. J. Haines, T. W. Jones, D. Kielczewska, W. R. Kropp, J. G. Learned, J. M. LoSecco, J. Matthews, R. Miller, M. S. Mudan, H. S. Park, L. R. Price, F. Reines, J. Schultz, S. Seidel, E. Shumard, D. Sinclair, H. W. Sobel, J. L. Stone, L. R. Sulak, R. Svoboda, G. Thornton, J. C. van der Velde, and C. Wuest. Observation of a neutrino burst in coincidence with supernova 1987a in the large magellanic cloud. *Phys. Rev. Lett.*, 58:1494–1496, Apr 1987. doi: 10.1103/PhysRevLett.58.1494. URL https://link.aps.org/doi/10.1103/PhysRevLett.58.1494.

[50] E. N. Alekseev, L. N. Alekseeva, V. I. Volchenko, and I. V. Krivosheina. Possible Detection of a Neutrino Signal on 23 February 1987 at the Baksan Underground Scintillation Telescope of the Institute of Nuclear Research. *JETP Lett.*, 45:589–592, 1987.

[51] V. L. Dadykin et al. Detection of a Rare Event on 23 February 1987 by the Neutrino Radiation Detector Under Mont Blanc. *JETP Lett.*, 45:593–595, 1987.

[52] Nobel Prize Outreach. Nobel Prize in Physics 2015, 2015.

[53] B. Aharmim, S. N. Ahmed, T. C. Andersen, A. E. Anthony, N. Barros, E. W. Beier, A. Bellerive, B. Beltran, M. Bergevin, S. D. Biller, K. Boudjemline, M. G. Boulay, T. H. Burritt, B. Cai, Y. D. Chan, M. Chen, M. C. Chon, B. T. Cleveland, G. A. Cox-Mobrand, C. A. Currat, X. Dai, F. Dalnoki-Veress, H. Deng, J. Detwiler, P. J. Doe, R. S. Dosanjh, G. Doucas, P.-L. Drouin, F. A. Duncan, M. Dunford, S. R. Elliott, H. C. Evans, G. T. Ewan, J. Farine, H. Fergani, F. Fleurot, R. J. Ford, J. A. Formaggio, N. Gagnon, J. T. M. Goon, K. Graham, D. R. Grant, E. Guillian, S. Habib, R. L. Hahn, A. L. Hallin, E. D. Hallman, C. K. Hargrove, P. J. Harvey, R. Hazama, K. M. Heeger, W. J. Heintzelman, J. Heise, R. L. Helmer, R. J.

Hemingway, R. Henning, A. Hime, C. Howard, M. A. Howe, M. Huang, B. Jamieson, N. A. Jelley, J. R. Klein, M. Kos, A. Krüger, C. Kraus, C. B. Krauss, T. Kutter, C. C. M. Kyba, R. Lange, J. Law, I. T. Lawson, K. T. Lesko, J. R. Leslie, I. Levine, J. C. Loach, S. Luoma, R. MacLellan, S. Majerus, H. B. Mak, J. Maneira, A. D. Marino, R. Martin, N. McCauley, A. B. McDonald, S. McGee, C. Mifflin, M. L. Miller, B. Monreal, J. Monroe, A. J. Noble, N. S. Oblath, C. E. Okada, H. M. O'Keeffe, Y. Opachich, G. D. Orebi Gann, S. M. Oser, R. A. Ott, S. J. M. Peeters, A. W. P. Poon, G. Prior, K. Rielage, B. C. Robertson, R. G. H. Robertson, E. Rollin, M. H. Schwendener, J. A. Secrest, S. R. Seibert, O. Simard, J. J. Simpson, D. Sinclair, P. Skensved, M. W. E. Smith, T. J. Sonley, T. D. Steiger, L. C. Stonehill, N. Tagg, G. Tešić, N. Tolich, T. Tsui, R. G. Van de Water, B. A. VanDevender, C. J. Virtue, D. Waller, C. E. Waltham, H. Wan Chan Tseung, D. L. Wark, P. Watson, J. Wendland, N. West, J. F. Wilkerson, J. R. Wilson, J. M. Wouters, A. Wright, M. Yeh, F. Zhang, and K. Zuber. Measurement of the cosmic ray and neutrino-induced muon flux at the sudbury neutrino observatory. *Phys. Rev. D*, 80:012001, Jul 2009. doi: 10.1103/PhysRevD.80.012001. URL https://link.aps.org/doi/10.1103/PhysRevD.80.012001.

[54] M. Anderson, S. Andringa, E. Arushanova, S. Asahi, M. Askins, D. J. Auty, A. R. Back, Z. Barnard, N. Barros, D. Bartlett, F. Barão, R. Bayes, E. W. Beier, A. Bialek, S. D. Biller, E. Blucher, R. Bonventre, M. Boulay, D. Braid, E. Caden, E. J. Callaghan, J. Caravaca, J. Carvalho, L. Cavalli, D. Chauhan, M. Chen, O. Chkvorets, K. J. Clark, B. Cleveland, C. Connors, I. T. Coulter, D. Cressy, X. Dai, C. Darrach, B. Davis-Purcell, M. M. Depatie, F. Descamps, F. Di Lodovico, N. Duhaime, F. Duncan, J. Dunger, E. Falk, N. Fatemighomi, V. Fischer, E. Fletcher, R. Ford, N. Gagnon, K. Gilje, P. Gorel, K. Graham, C. Grant, J. Grove, S. Grullon, E. Guillian, A. L. Hallin, D. Hallman, S. Hans, J. Hartnell, P. Harvey, M. Hedayatipour, W. J. Heintzelman, J. Heise, R. L. Helmer, J. L. Hernández-Hernández, B. Hreljac, J. Hu, T. Iida, A. S. Inácio, C. M. Jackson, N. A. Jelley, C. J. Jillings, C. Jones, P. G. Jones, K. Kamdin, T. Kaptanoglu, J. Kaspar, K. Keeter, C. Kefelian, P. Khaghani, L. Kippenbrock, J. R. Klein, R. Knapik, J. Kofron, L. L. Kormos, B. Krar, C. Kraus, C. B. Krauss, T. Kroupova, K. Labe, I. Lam, C. Lan, B. J. Land, R. Lane, S. Langrock, A. LaTorre, I. Lawson, L. Lebanowski, G. M. Lefeuvre, E. J. Leming, A. Li, J. Lidgard, B. Liggins, X. Liu, Y. Liu, V. Lozza, M. Luo, S. Maguire, A. Maio, K. Majumdar, S. Manecki, J. Maneira, R. D. Martin, E. Marzec, A. Mastbaum, N. McCauley, A. B. McDonald, J. E. McMillan, P. Mekarski, M. Meyer, C. Miller, M. Mlejnek, E. Mony, I. Morton-Blake, M. J. Mottram, S. Nae, M. Nirkko, V. Novikov, H. M. O'Keeffe, E. O'Sullivan, G. D. Orebi Gann, M. J. Parnell, J. Paton, S. J. M. Peeters, T. Pershing, Z. Petriw, L. Pickard, D. Pracsovics, G. Prior, J. C. Prouty, S. Quirk, A. Reichold, R. Richardson, M. Rigan, A. Robertson, J. Rose, R. Rosero, P. M. Rost, J. Rumleskie, M. A. Schumaker, M. H. Schwendener, D. Scislowski, J. Secrest, M. Seddighin, L. Segui, S. Seibert, I. Semenec, T. Shantz, T. M. Shokair, L. Sibley, J. R. Sinclair, K. Singh, P. Skensved, T. Sonley, R. Stainforth, M. Strait, M. I. Stringer, R. Svoboda, A. Sörensen, B. Tam, J. Tatar, L. Tian, N. Tolich, J. Tseng, H. W. C. Tseung, E. Turner, R. Van Berg, J. G. C. Veinot, C. J. Virtue, B. von Krosigk, E. Vázquez-Jáuregui, J. M. G. Walker, M. Walker, J. Wang, O. Wasalski, J. Waterfield, J. J. Weigand, R. F. White, J. R. Wilson, T. J. Winchester, P. Woosaree, A. Wright, J. P. Yanez, M. Yeh, T. Zhao, K. Zuber, and A. Zummo. Search for invisible modes of nucleon decay in water with the sno+ detector. *Phys. Rev. D*, 99:032008, Feb 2019. doi: 10.1103/PhysRevD.99.032008. URL https://link.

aps.org/doi/10.1103/PhysRevD.99.032008.

[55] M. R. Anderson, S. Andringa, M. Askins, D. J. Auty, N. Barros, F. Barão, R. Bayes, E. W. Beier, A. Bialek, S. D. Biller, E. Blucher, R. Bonventre, M. Boulay, E. Caden, E. J. Callaghan, J. Caravaca, D. Chauhan, M. Chen, O. Chkvorets, B. Cleveland, M. A. Cox, M. M. Depatie, J. Dittmer, F. Di Lodovico, A. D. Earle, E. Falk, N. Fatemighomi, V. Fischer, E. Fletcher, R. Ford, K. Frankiewicz, K. Gilje, D. Gooding, C. Grant, J. Grove, A. L. Hallin, D. Hallman, S. Hans, J. Hartnell, P. Harvey, W. J. Heintzelman, R. L. Helmer, D. Horne, B. Hreljac, J. Hu, A. S. M. Hussain, A. S. Inácio, C. J. Jillings, T. Kaptanoglu, P. Khaghani, J. R. Klein, R. Knapik, L. L. Kormos, B. Krar, C. Kraus, C. B. Krauss, T. Kroupova, I. Lam, B. J. Land, A. LaTorre, I. Lawson, L. Lebanowski, E. J. Leming, A. Li, J. Lidgard, B. Liggins, Y. H. Lin, Y. Liu, V. Lozza, M. Luo, S. Maguire, A. Maio, S. Manecki, J. Maneira, R. D. Martin, E. Marzec, A. Mastbaum, N. McCauley, A. B. McDonald, P. Mekarski, M. Meyer, C. Mills, I. Morton-Blake, S. Nae, M. Nirkko, L. J. Nolan, H. M. O'Keeffe, G. D. Orebi Gann, M. J. Parnell, J. Paton, S. J. M. Peeters, T. Pershing, L. Pickard, G. Prior, A. Reichold, S. Riccetto, R. Richardson, M. Rigan, J. Rose, R. Rosero, P. M. Rost, J. Rumleskie, I. Semenec, F. Shaker, M. K. Sharma, K. Singh, P. Skensved, M. Smiley, M. I. Stringer, R. Svoboda, B. Tam, L. Tian, J. Tseng, E. Turner, R. Van Berg, J. G. C. Veinot, C. J. Virtue, E. Vázquez-Jáuregui, S. C. Walton, J. Wang, M. Ward, J. J. Weigand, J. R. Wilson, P. Woosaree, A. Wright, J. P. Yanez, M. Yeh, T. Zhang, Y. Zhang, K. Zuber, and A. Zummo. Measurement of neutron-proton capture in the SNO+ water phase. *Phys. Rev. C*, 102:014002, Jul 2020. doi: 10.1103/PhysRevC.102.014002. URL https://link.aps.org/doi/10.1103/PhysRevC.102.014002.

[56] SNO+ collaboration, M.R. Anderson, S. Andringa, M. Askins, D.J. Auty, F. Barão, N. Barros, R. Bayes, E.W. Beier, A. Bialek, S.D. Biller, E. Blucher, M. Boulay, E. Caden, E.J. Callaghan, J. Caravaca, M. Chen, O. Chkvorets, B. Cleveland, D. Cookman, J. Corning, M.A. Cox, C. Deluce, M.M. Depatie, F. Di Lodovico, J. Dittmer, E. Falk, N. Fatemighomi, V. Fischer, R. Ford, K. Frankiewicz, A. Gaur, K. Gilje, O.I. González-Reina, D. Gooding, C. Grant, J. Grove, A.L. Hallin, D. Hallman, J. Hartnell, W.J. Heintzelman, R.L. Helmer, J. Hu, R. Hunt-Stokes, S.M.A. Hussain, A.S. Inácio, C.J. Jillings, T. Kaptanoglu, P. Khaghani, H. Khan, J.R. Klein, L.L. Kormos, B. Krar, C. Kraus, C.B. Krauss, T. Kroupová, I. Lam, B.J. Land, A. LaTorre, I. Lawson, L. Lebanowski, C. Lefebvre, A. Li, J. Lidgard, Y.H. Lin, Y. Liu, V. Lozza, M. Luo, A. Maio, S. Manecki, J. Maneira, R.D. Martin, N. McCauley, A.B. McDonald, M. Meyer, C. Mills, I. Morton-Blake, S. Nae, M. Nirkko, L.J. Nolan, H.M. O'Keeffe, G.D. Orebi Gann, J. Page, W. Parker, J. Paton, S.J.M. Peeters, T. Pershing, L. Pickard, G. Prior, P. Ravi, A. Reichold, S. Riccetto, R. Richardson, M. Rigan, J. Rose, J. Rumleskie, I. Semenec, F. Shaker, M.K. Sharma, P. Skensved, M. Smiley, R. Stainforth, R. Svoboda, B. Tam, J. Tseng, E. Turner, S. Valder, E. Vázquez-Jáuregui, J.G.C. Veinot, C.J. Virtue, J. Wang, M. Ward, J.J. Weigand, J.R. Wilson, A. Wright, J.P. Yanez, M. Yeh, S. Yu, T. Zhang, Y. Zhang, K. Zuber, and A. Zummo. Optical calibration of the sno+ detector in the water phase with deployed sources. *Journal of Instrumentation*, 16(10):P10021, oct 2021. doi: 10.1088/1748-0221/16/10/P10021. URL https://doi.org/10.1088/1748-0221/16/10/P10021.

[57] M. Anderson, S. Andringa, S. Asahi, M. Askins, D. J. Auty, N. Barros, D. Bartlett, F. Barão, R. Bayes, E. W. Beier, A. Bialek, S. D. Biller, E. Blucher, R. Bonventre, M. Boulay, E. Caden,

E. J. Callaghan, J. Caravaca, D. Chauhan, M. Chen, O. Chkvorets, B. Cleveland, C. Connors, I. T. Coulter, M. M. Depatie, F. Di Lodovico, F. Duncan, J. Dunger, E. Falk, V. Fischer, E. Fletcher, R. Ford, N. Gagnon, K. Gilje, C. Grant, J. Grove, A. L. Hallin, D. Hallman, S. Hans, J. Hartnell, W. J. Heintzelman, R. L. Helmer, J. L. Hernández-Hernández, B. Hreljac, J. Hu, A. S. Inácio, C. J. Jillings, T. Kaptanoglu, P. Khaghani, J. R. Klein, R. Knapik, L. L. Kormos, B. Krar, C. Kraus, C. B. Krauss, T. Kroupova, I. Lam, B. J. Land, R. Lane, A. LaTorre, I. Lawson, L. Lebanowski, E. J. Leming, A. Li, J. Lidgard, B. Liggins, Y. Liu, V. Lozza, M. Luo, S. Maguire, A. Maio, S. Manecki, J. Maneira, R. D. Martin, E. Marzec, A. Mastbaum, N. McCauley, A. B. McDonald, P. Mekarski, M. Meyer, M. Mlejnek, I. Morton-Blake, S. Nae, M. Nirkko, H. M. O'Keeffe, G. D. Orebi Gann, M. J. Parnell, J. Paton, S. J. M. Peeters, T. Pershing, L. Pickard, D. Pracsovics, G. Prior, A. Reichold, R. Richardson, M. Rigan, J. Rose, R. Rosero, J. Rumleskie, I. Semenec, K. Singh, P. Skensved, M. I. Stringer, R. Svoboda, B. Tam, L. Tian, J. Tseng, E. Turner, R. Van Berg, J. G. C. Veinot, C. J. Virtue, E. Vázquez-Jáuregui, J. Wang, J. J. Weigand, J. R. Wilson, P. Woosaree, A. Wright, J. P. Yanez, M. Yeh, K. Zuber, and A. Zummo. Measurement of the ^{8}B solar neutrino flux in SNO+ with very low backgrounds. *Phys. Rev. D*, 99:012012, Jan 2019. doi: 10.1103/PhysRevD.99.012012. URL https://link.aps.org/doi/10.1103/PhysRevD.99.012012.

[58] A. Allega, M. R. Anderson, S. Andringa, J. Antunes, M. Askins, D. J. Auty, A. Bacon, N. Barros, F. Barão, R. Bayes, E. W. Beier, T. S. Bezerra, A. Bialek, S. D. Biller, E. Blucher, E. Caden, E. J. Callaghan, S. Cheng, M. Chen, B. Cleveland, D. Cookman, J. Corning, M. A. Cox, R. Dehghani, J. Deloye, C. Deluce, M. M. Depatie, J. Dittmer, K. H. Dixon, F. Di Lodovico, E. Falk, N. Fatemighomi, R. Ford, K. Frankiewicz, A. Gaur, O. I. González-Reina, D. Gooding, C. Grant, J. Grove, A. L. Hallin, D. Hallman, W. J. Heintzelman, R. L. Helmer, J. Hu, R. Hunt-Stokes, S. M. A. Hussain, A. S. Inácio, C. J. Jillings, S. Kaluzienski, T. Kaptanoglu, P. Khaghani, H. Khan, J. R. Klein, L. L. Kormos, B. Krar, C. Kraus, C. B. Krauss, T. Kroupová, I. Lam, B. J. Land, I. Lawson, L. Lebanowski, J. Lee, C. Lefebvre, J. Lidgard, Y. H. Lin, V. Lozza, M. Luo, A. Maio, S. Manecki, J. Maneira, R. D. Martin, N. McCauley, A. B. McDonald, C. Mills, I. Morton-Blake, S. Naugle, L. J. Nolan, H. M. O'Keeffe, G. D. Orebi Gann, J. Page, W. Parker, J. Paton, S. J. M. Peeters, L. Pickard, P. Ravi, A. Reichold, S. Riccetto, R. Richardson, M. Rigan, J. Rose, R. Rosero, J. Rumleskie, I. Semenec, P. Skensved, M. Smiley, R. Svoboda, B. Tam, J. Tseng, E. Turner, S. Valder, C. J. Virtue, E. Vázquez-Jáuregui, J. Wang, M. Ward, J. R. Wilson, J. D. Wilson, A. Wright, J. P. Yanez, S. Yang, M. Yeh, S. Yu, Y. Zhang, K. Zuber, and A. Zummo. Evidence of antineutrinos from distant reactors using pure water at SNO+. *Phys. Rev. Lett.*, 130:091801, Mar 2023. doi: 10.1103/PhysRevLett.130.091801. URL https://link.aps.org/doi/10.1103/PhysRevLett.130.091801.

[59] Charlie Mills. *Improved sensitivity to Δm^2_{21} by classification of the $^{13}C(\alpha, n)\,^{16}O$ background in the SNO+ antineutrino analysis.* PhD thesis, University of Sussex, 2022. Accessed: February 26, 2026.

[60] A. Allega et al. Initial measurement of reactor antineutrino oscillation at SNO+. *Eur. Phys. J. C*, 85(1):17, 2025. doi: 10.1140/epjc/s10052-024-13687-5. [Erratum: Eur.Phys.J.C 85, 296 (2025)].

[61] ISEGNIM. *High Precision Versatile High Voltage Module in NIM Standard*, 2026.

[62] WaveSurfer. *WaveSurfer 4000HD High Definition Oscilloscopes (200 MHz - 1 GHz) Datasheet*, 2023.

[63] Tony LaTorre. *LeCrunch Open Source Software*, 2013.

[64] Minfang Yeh. Improving light yield measurements for low-yield scintillators. Technical report, Brookhaven National Laboratory, 2019.

[65] Roland Winston and Jay M. Enoch. Retinal cone receptor as an ideal light collector. *Journal of the Optical Society of America*, 61 8:1120–2, 1971. URL https://api.semanticscholar.org/CorpusID:33459986.

[66] The SNO+ Collaboration. SNO+ Detector Operator Manual. Technical report, SNO+ Collaboration, 2019. Internal document; accessed Feb 27, 2026.

[67] C. J. Jillings, R. J. Ford, A. L. Hallin, P. J. Harvey, R. W. MacLeod, H. B. Mak, P. Skensved, and R. L. Stevenson. The photomultiplier tube testing facility for the Sudbury Neutrino Observatory. *Nuclear Instruments and Methods in Physics Research A*, 373(3):421–429, February 1996. doi: 10.1016/0168-9002(96)00067-8.

[68] Xilinx User Guide. *Xilinx UG080 ML401/ML402/ML403 User Guide*. AMD, 2006.

[69] Xilinx XC2C512 CoolRunner-II CPLD. *Xilinx XC2C512 CoolRunner-II CPLD*. AMD, 2007.

[70] S. Agostinelli et al. GEANT4 - A Simulation Toolkit. *Nucl. Instrum. Meth. A*, 506:250–303, 2003. doi: 10.1016/S0168-9002(03)01368-8. URL https://www.sciencedirect.com/science/article/pii/S0168900203013688.

[71] Stan Seibert. *RAT Documentation*, 2014. URL https://rat.readthedocs.io/en/latest/.

[72] Matt Mottram. Updated functional form energy reconstruction: EnergyRThetaFunctional. Technical report, SNO+, 2015. Internal document; accessed Feb 27, 2026.

[73] A. Allega, M. R. Anderson, S. Andringa, J. Antunes, M. Askins, D. J. Auty, A. Bacon, J. Baker, N. Barros, F. Barão, R. Bayes, E. W. Beier, T. S. Bezerra, A. Bialek, S. D. Biller, E. Blucher, E. Caden, E. J. Callaghan, M. Chen, S. Cheng, B. Cleveland, D. Cookman, J. Corning, M. A. Cox, R. Dehghani, J. Deloye, M. M. Depatie, F. Di Lodovico, J. Dittmer, K. H. Dixon, E. Falk, N. Fatemighomi, R. Ford, A. Gaur, O. I. González-Reina, D. Gooding, C. Grant, J. Grove, S. Hall, A. L. Hallin, W. J. Heintzelman, R. L. Helmer, C. Hewitt, B. Hreljac, V. Howard, J. Hu, R. Hunt-Stokes, S. M. A. Hussain, A. S. Inácio, C. J. Jillings, S. Kaluzienski, T. Kaptanoglu, P. Khaghani, H. Khan, J. R. Klein, L. L. Kormos, B. Krar, C. Kraus, C. B. Krauss, T. Kroupová, C. Lake, L. Lebanowski, J. Lee, C. Lefebvre, Y. H. Lin, V. Lozza, M. Luo, A. Maio, S. Manecki, J. Maneira, R. D. Martin, N. McCauley, A. B.

McDonald, C. Mills, G. Milton, I. Morton-Blake, M. Mubasher, A. Molina Colina, D. Morris, S. Naugle, L. J. Nolan, H. M. O'Keeffe, G. D. Orebi Gann, J. Page, K. Paleshi, W. Parker, J. Paton, S. J. M. Peeters, L. Pickard, P. Ravi, A. Reichold, S. Riccetto, M. Rigan, J. Rose, R. Rosero, J. Rumleskie, I. Semenec, P. Skensved, M. Smiley, J. Smith, R. Svoboda, B. Tam, J. Tseng, S. Valder, E. Vázquez-Jáuregui, C. J. Virtue, J. Wang, M. Ward, J. R. Wilson, J. D. Wilson, A. Wright, J. P. Yanez, S. Yang, M. Yeh, Z. Ye, S. Yu, Y. Zhang, K. Zuber, and A. Zummo. Event-by-event direction reconstruction of solar neutrinos in a high light-yield liquid scintillator. *Phys. Rev. D*, 109:072002, Apr 2024. doi: 10.1103/PhysRevD.109.072002. URL https://link.aps.org/doi/10.1103/PhysRevD.109.072002.

[74] A. Einstein. Die grundlage der allgemeinen relativitätstheorie. *Annalen der Physik*, 354(7): 769–822, 1916. doi: https://doi.org/10.1002/andp.19163540702. URL https://onlinelibrary.wiley.com/doi/abs/10.1002/andp.19163540702.

[75] B. P. Abbott et al. LIGO: The Laser interferometer gravitational-wave observatory. *Rept. Prog. Phys.*, 72:076901, 2009. doi: 10.1088/0034-4885/72/7/076901.

[76] J. Aasi et al. Advanced LIGO. *Class. Quant. Grav.*, 32:074001, 2015. doi: 10.1088/0264-9381/32/7/074001.

[77] E. Capote et al. Advanced LIGO detector performance in the fourth observing run. *Phys. Rev. D*, 111(6):062002, 2025. doi: 10.1103/PhysRevD.111.062002.

[78] T Accadia, F Acernese, M Alshourbagy, P Amico, F Antonucci, S Aoudia, N Arnaud, C Arnault, K G Arun, P Astone, S Avino, D Babusci, G Ballardin, F Barone, G Barrand, L Barsotti, M Barsuglia, A Basti, Th S Bauer, F Beauville, M Bebronne, M Bejger, M G Beker, F Bellachia, A Belletoile, J L Beney, M Bernardini, S Bigotta, R Bilhaut, S Birindelli, M Bitossi, M A Bizouard, M Blom, C Boccara, D Boget, F Bondu, L Bonelli, R Bonnand, V Boschi, L Bosi, T Bouedo, B Bouhou, A Bozzi, L Bracci, S Braccini, C Bradaschia, M Branchesi, T Briant, A Brillet, V Brisson, L Brocco, T Bulik, H J Bulten, D Buskulic, C Buy, G Cagnoli, G Calamai, E Calloni, E Campagna, B Canuel, F Carbognani, L Carbone, F Cavalier, R Cavalieri, R Cecchi, G Cella, E Cesarini, E Chassande-Mottin, S Chatterji, R Chiche, A Chincarini, A Chiummo, N Christensen, A C Clapson, F Cleva, E Coccia, P F Cohadon, C N Colacino, J Colas, A Colla, M Colombini, G Conforto, A Corsi, S Cortese, F Cottone, J P Coulon, E Cuoco, S D'Antonio, G Daguin, A Dari, V Dattilo, P Y David, M Davier, R Day, G Debreczeni, G De Carolis, M Dehamme, R Del Fabbro, W Del Pozzo, M del Prete, L Derome, R De Rosa, R DeSalvo, M Dialinas, L Di Fiore, A Di Lieto, M Di Paolo Emilio, A Di Virgilio, A Dietz, M Doets, P Dominici, A Dominjon, M Drago, C Drezen, B Dujardin, B Dulach, C Eder, A Eleuteri, D Enard, M Evans, L Fabbroni, V Fafone, H Fang, I Ferrante, F Fidecaro, I Fiori, R Flaminio, D Forest, L A Forte, J D Fournier, L Fournier, J Franc, O Francois, S Frasca, F Frasconi, A Freise, A Gaddi, M Galimberti, L Gammaitoni, P Ganau, C Garnier, F Garufi, M E Gáspár, G Gemme, E Genin, A Gennai, G Gennaro, L Giacobone, A Giazotto, G Giordano, L Giordano, C Girard, R Gouaty, A Grado, M Granata, V Granata, X Grave, C Greverie, H Groenstege, G M Guidi, S Hamdani, J F Hayau, S Hebri, A Heidmann, H Heitmann, P Hello, G Hemming, E Hennes, R Hermel, P Heusse, L Holloway,

D Huet, M Iannarelli, P Jaranowski, D Jehanno, L Journet, S Karkar, T Ketel, H Voet, J Kovalik, I Kowalska, S Kreckelbergh, A Krolak, J C Lacotte, B Lagrange, P La Penna, M Laval, J C Le Marec, N Leroy, N Letendre, T G F Li, B Lieunard, N Liguori, O Lodygensky, B Lopez, M Lorenzini, V Loriette, G Losurdo, M Loupias, J M Mackowski, T Maiani, E Majorana, C Magazzù, I Maksimovic, V Malvezzi, N Man, S Mancini, B Mansoux, M Mantovani, F Marchesoni, F Marion, P Marin, J Marque, F Martelli, A Masserot, L Massonnet, G Matone, L Matone, M Mazzoni, F Menzinger, C Michel, L Milano, Y Minenkov, S Mitra, M Mohan, J L Montorio, R Morand, F Moreau, J Moreau, N Morgado, A Morgia, S Mosca, V Moscatelli, B Mours, P Mugnier, F A Mul, L Naticchioni, I Neri, F Nocera, E Pacaud, G Pagliaroli, A Pai, L Palladino, C Palomba, F Paoletti, R Paoletti, A Paoli, S Pardi, G Parguez, M Parisi, A Pasqualetti, R Passaquieti, D Passuello, M Perciballi, B Perniola, G Persichetti, S Petit, M Pichot, F Piergiovanni, M Pietka, R Pignard, L Pinard, R Poggiani, P Popolizio, T Pradier, M Prato, G A Prodi, M Punturo, P Puppo, K Qipiani, O Rabaste, D S Rabeling, I Rácz, F Raffaelli, P Rapagnani, S Rapisarda, V Re, A Reboux, T Regimbau, V Reita, A Remilleux, F Ricci, I Ricciardi, F Richard, M Ripepe, F Robinet, A Rocchi, L Rolland, R Romano, D Rosińska, P Roudier, P Ruggi, G Russo, L Salconi, V Sannibale, B Sassolas, D Sentenac, S Solimeno, R Sottile, L Sperandio, R Stanga, R Sturani, B Swinkels, M Tacca, R Taddei, L Taffarello, M Tarallo, S Tissot, A Toncelli, M Tonelli, O Torre, E Tournefier, F Travasso, C Tremola, E Turri, G Vajente, J F J van den Brand, C Van Den Broeck, S van der Putten, M Vasuth, M Vavoulidis, G Vedovato, D Verkindt, F Vetrano, O Véziant, A Viceré, J Y Vinet, S Vilalte, S Vitale, H Vocca, R L Ward, M Was, K Yamamoto, M Yvert, J P Zendri, and Z Zhang. Virgo: a laser interferometer to detect gravitational waves. *Journal of Instrumentation*, 7(03):P03012, mar 2012. doi: 10.1088/1748-0221/7/03/P03012. URL https://doi.org/10.1088/1748-0221/7/03/P03012.

[79] F. Acernese et al. Advanced Virgo: a second-generation interferometric gravitational wave detector. *Class. Quant. Grav.*, 32(2):024001, 2015. doi: 10.1088/0264-9381/32/2/024001.

[80] KAGRA Collaboration, H Abe, R X Adhikari, T Akutsu, M Ando, A Araya, N Aritomi, H Asada, Y Aso, S Bae, Y Bae, R Bajpai, S W Ballmer, K Cannon, Z Cao, E Capocasa, M Chan, C Chen, D Chen, K Chen, Y Chen, C-Y Chiang, Y-K Chu, J C Driggers, S E Dwyer, A Effler, S Eguchi, M Eisenmann, Y Enomoto, R Flaminio, H K Fong, V V Frolov, Y Fujii, Y Fujikawa, Y Fujimoto, M Fukushima, D Gao, G-G Ge, S Ha, I P W Hadiputrawan, S Haino, W-B Han, K Hasegawa, K Hattori, H Hayakawa, K Hayama, Y Himemoto, N Hirata, C Hirose, T-C Ho, B-H Hsieh, H-F Hsieh, C Hsiung, H-Y Huang, P Huang, Y-C Huang, Y-J Huang, D C Y Hui, S Ide, B Ikenoue, K Inayoshi, Y Inoue, K Ito, Y Itoh, K Izumi, C Jeon, H-B Jin, K Jung, P Jung, K Kaihotsu, T Kajita, M Kakizaki, M Kamiizumi, N Kanda, T Kato, K Kawabe, K Kawaguchi, C Kim, J Kim, J C Kim, Y-M Kim, N Kimura, Y Kobayashi, K Kohri, K Kokeyama, A K H Kong, N Koyama, C Kozakai, J Kume, Y Kuromiya, S Kuroyanagi, K Kwak, E Lee, H W Lee, R Lee, M Leonardi, K L Li, P Li, L C-C Lin, C-Y Lin, E T Lin, F-K Lin, F-L Lin, H L Lin, G C Liu, L-W Luo, M Ma'arif, E Majorana, Y Michimura, N Mio, O Miyakawa, K Miyo, S Miyoki, Y Mori, S Morisaki, N Morisue, Y Moriwaki, A Mullavey, K Nagano, K Nakamura, H Nakano, M Nakano, Y Nakayama, T Narikawa, L Naticchioni, L Nguyen Quynh, W-T Ni, T Nishimoto, A Nishizawa, S Nozaki, Y Obayashi, Y Obuchi, W Ogaki, J J Oh, K Oh, M Ohashi, T Ohashi, M Ohkawa, H Ohta, Y Okutani, K Oohara,

S Oshino, S Otabe, K-C Pan, A Parisi, J Park, F E Peña Arellano, S Saha, S Saito, Y Saito, K Sakai, T Sawada, Y Sekiguchi, L Shao, Y Shikano, H Shimizu, R Shimizu, K Shimode, H Shinkai, T Shishido, A Shoda, K Somiya, I Song, R Sugimoto, J Suresh, T Suzuki, T Suzuki, T Suzuki, H Tagoshi, H Takahashi, R Takahashi, S Takano, H Takeda, M Takeda, M Tamaki, K Tanaka, T Tanaka, T Tanaka, S Tanioka, A Taruya, T Tomaru, T Tomura, L Trozzo, T Tsang, J-S Tsao, S Tsuchida, T Tsutsui, T Tsuzuki, D Tuyenbayev, N Uchikata, T Uchiyama, A Ueda, T Uehara, K Ueno, G Ueshima, F Uraguchi, T Ushiba, M H P M vanPutten, J Wang, T Washimi, C Wu, H Wu, T Yamada, K Yamamoto, T Yamamoto, K Yamashita, R Yamazaki, Y Yang, S-W Yeh, J Yokoyama, T Yokozawa, T Yoshioka, H Yuzurihara, S Zeidler, M Zhan, H Zhang, Y Zhao, and Z-H Zhu. Performance of the kagra detector during the first joint observation with geo600 (o3gk). *Progress of Theoretical and Experimental Physics*, 2023(10), October 2023. doi: 10.1093/ptep/ptac093. URL https://doi.org/10.1093/ptep/ptac093.

[81] T. Akutsu et al. KAGRA: 2.5 Generation Interferometric Gravitational Wave Detector. *Nature Astron.*, 3(1):35–40, 2019. doi: 10.1038/s41550-018-0658-y.

[82] Sean M. Carroll. *An Introduction to General Relativity Spacetime and Geometry.* Pearson Education, Inc., publishing as Addison Wesley, 2004.

[83] James B. Hartle. *Gravity An Introduction to Einstein's General Relativity.* Pearson Education, Inc., publishing as Addison Wesley, 2003.

[84] K.S. Thorne Charles W. Misner and J.A. Wheeler. *Gravitation.* W.H. Freeman, San Francisco, 1973.

[85] James Clerk Maxwell. *The Scientific Papers of James Clerk Maxwell.* Internet Archive, 1864.

[86] Oliver Heaviside. *From Oleg D. Jefimenko, Causality, Electromagnetic Induction, and Gravitation: A Different Approach to the Theory of Electromagnetic and Gravitational Fields.* Electret Scientific, Star City, 1893.

[87] R. A. Hulse and J. H. Taylor. Discovery of a pulsar in a binary system. *The Astrophysical Journal Letters*, 195:L51–L53, January 1975. doi: 10.1086/181708.

[88] Russell A. Hulse and Joseph H. Taylor Jr. Nobel Prize in Physics 1993, 1993. Accessed: February 26, 2026.

[89] B. P. Abbott, R. Abbott, T. D. Abbott, M. R. Abernathy, F. Acernese, K. Ackley, C. Adams, T. Adams, P. Addesso, R. X. Adhikari, V. B. Adya, C. Affeldt, M. Agathos, K. Agatsuma, N. Aggarwal, O. D. Aguiar, L. Aiello, A. Ain, P. Ajith, B. Allen, A. Allocca, P. A. Altin, S. B. Anderson, W. G. Anderson, K. Arai, M. A. Arain, M. C. Araya, C. C. Arceneaux, J. S. Areeda, N. Arnaud, K. G. Arun, S. Ascenzi, G. Ashton, M. Ast, S. M. Aston, P. Astone, P. Aufmuth, C. Aulbert, S. Babak, P. Bacon, M. K. M. Bader, P. T. Baker, F. Baldaccini, G. Ballardin, S. W. Ballmer, J. C. Barayoga, S. E. Barclay, B. C. Barish, D. Barker, F. Barone, B. Barr, L. Barsotti, M. Barsuglia, D. Barta, J. Bartlett, M. A. Barton, I. Bartos,

R. Bassiri, A. Basti, J. C. Batch, C. Baune, V. Bavigadda, M. Bazzan, B. Behnke, M. Bejger, C. Belczynski, A. S. Bell, C. J. Bell, B. K. Berger, J. Bergman, G. Bergmann, C. P. L. Berry, D. Bersanetti, A. Bertolini, J. Betzwieser, S. Bhagwat, R. Bhandare, I. A. Bilenko, G. Billingsley, J. Birch, I. A. Birney, O. Birnholtz, S. Biscans, A. Bisht, M. Bitossi, C. Biwer, M. A. Bizouard, J. K. Blackburn, C. D. Blair, D. G. Blair, R. M. Blair, S. Bloemen, O. Bock, T. P. Bodiya, M. Boer, G. Bogaert, C. Bogan, A. Bohe, P. Bojtos, C. Bond, F. Bondu, R. Bonnand, B. A. Boom, R. Bork, V. Boschi, S. Bose, Y. Bouffanais, A. Bozzi, C. Bradaschia, P. R. Brady, V. B. Braginsky, M. Branchesi, J. E. Brau, T. Briant, A. Brillet, M. Brinkmann, V. Brisson, P. Brockill, A. F. Brooks, D. A. Brown, D. D. Brown, N. M. Brown, C. C. Buchanan, A. Buikema, T. Bulik, H. J. Bulten, A. Buonanno, D. Buskulic, C. Buy, R. L. Byer, M. Cabero, L. Cadonati, G. Cagnoli, C. Cahillane, J. Calderón Bustillo, T. Callister, E. Calloni, J. B. Camp, K. C. Cannon, J. Cao, C. D. Capano, E. Capocasa, F. Carbognani, S. Caride, J. Casanueva Diaz, C. Casentini, S. Caudill, M. Cavaglià, F. Cavalier, R. Cavalieri, G. Cella, C. B. Cepeda, L. Cerboni Baiardi, G. Cerretani, E. Cesarini, R. Chakraborty, T. Chalermsongsak, S. J. Chamberlin, M. Chan, S. Chao, P. Charlton, E. Chassande-Mottin, H. Y. Chen, Y. Chen, C. Cheng, A. Chincarini, A. Chiummo, H. S. Cho, M. Cho, J. H. Chow, N. Christensen, Q. Chu, S. Chua, S. Chung, G. Ciani, F. Clara, J. A. Clark, F. Cleva, E. Coccia, P.-F. Cohadon, A. Colla, C. G. Collette, L. Cominsky, M. Constancio, A. Conte, L. Conti, D. Cook, T. R. Corbitt, N. Cornish, A. Corsi, S. Cortese, C. A. Costa, M. W. Coughlin, S. B. Coughlin, J.-P. Coulon, S. T. Countryman, P. Couvares, E. E. Cowan, D. M. Coward, M. J. Cowart, D. C. Coyne, R. Coyne, K. Craig, J. D. E. Creighton, T. D. Creighton, J. Cripe, S. G. Crowder, A. M. Cruise, A. Cumming, L. Cunningham, E. Cuoco, T. Dal Canton, S. L. Danilishin, S. D'Antonio, K. Danzmann, N. S. Darman, C. F. Da Silva Costa, V. Dattilo, I. Dave, H. P. Daveloza, M. Davier, G. S. Davies, E. J. Daw, R. Day, S. De, D. DeBra, G. Debreczeni, J. Degallaix, M. De Laurentis, S. Deléglise, W. Del Pozzo, T. Denker, T. Dent, H. Dereli, V. Dergachev, R. T. DeRosa, R. De Rosa, R. DeSalvo, S. Dhurandhar, M. C. Díaz, L. Di Fiore, M. Di Giovanni, A. Di Lieto, S. Di Pace, I. Di Palma, A. Di Virgilio, G. Dojcinoski, V. Dolique, F. Donovan, K. L. Dooley, S. Doravari, R. Douglas, T. P. Downes, M. Drago, R. W. P. Drever, J. C. Driggers, Z. Du, M. Ducrot, S. E. Dwyer, T. B. Edo, M. C. Edwards, A. Effler, H.-B. Eggenstein, P. Ehrens, J. Eichholz, S. S. Eikenberry, W. Engels, R. C. Essick, T. Etzel, M. Evans, T. M. Evans, R. Everett, M. Factourovich, V. Fafone, H. Fair, S. Fairhurst, X. Fan, Q. Fang, S. Farinon, B. Farr, W. M. Farr, M. Favata, M. Fays, H. Fehrmann, M. M. Fejer, D. Feldbaum, I. Ferrante, E. C. Ferreira, F. Ferrini, F. Fidecaro, L. S. Finn, I. Fiori, D. Fiorucci, R. P. Fisher, R. Flaminio, M. Fletcher, H. Fong, J.-D. Fournier, S. Franco, S. Frasca, F. Frasconi, M. Frede, Z. Frei, A. Freise, R. Frey, V. Frey, T. T. Fricke, P. Fritschel, V. V. Frolov, P. Fulda, M. Fyffe, H. A. G. Gabbard, J. R. Gair, L. Gammaitoni, S. G. Gaonkar, F. Garufi, A. Gatto, G. Gaur, N. Gehrels, G. Gemme, B. Gendre, E. Genin, A. Gennai, J. George, L. Gergely, V. Germain, Abhirup Ghosh, Archisman Ghosh, S. Ghosh, J. A. Giaime, K. D. Giardina, A. Giazotto, K. Gill, A. Glaefke, J. R. Gleason, E. Goetz, R. Goetz, L. Gondan, G. González, J. M. Gonzalez Castro, A. Gopakumar, N. A. Gordon, M. L. Gorodetsky, S. E. Gossan, M. Gosselin, R. Gouaty, C. Graef, P. B. Graff, M. Granata, A. Grant, S. Gras, C. Gray, G. Greco, A. C. Green, R. J. S. Greenhalgh, P. Groot, H. Grote, S. Grunewald, G. M. Guidi, X. Guo, A. Gupta, M. K. Gupta, K. E. Gushwa, E. K. Gustafson, R. Gustafson, J. J. Hacker, B. R. Hall, E. D. Hall, G. Hammond, M. Haney, M. M. Hanke, J. Hanks, C. Hanna, M. D. Hannam, J. Hanson, T. Hardwick, J. Harms, G. M. Harry, I. W.

Harry, M. J. Hart, M. T. Hartman, C.-J. Haster, K. Haughian, J. Healy, J. Heefner, A. Heidmann, M. C. Heintze, G. Heinzel, H. Heitmann, P. Hello, G. Hemming, M. Hendry, I. S. Heng, J. Hennig, A. W. Heptonstall, M. Heurs, S. Hild, D. Hoak, K. A. Hodge, D. Hofman, S. E. Hollitt, K. Holt, D. E. Holz, P. Hopkins, D. J. Hosken, J. Hough, E. A. Houston, E. J. Howell, Y. M. Hu, S. Huang, E. A. Huerta, D. Huet, B. Hughey, S. Husa, S. H. Huttner, T. Huynh-Dinh, A. Idrisy, N. Indik, D. R. Ingram, R. Inta, H. N. Isa, J.-M. Isac, M. Isi, G. Islas, T. Isogai, B. R. Iyer, K. Izumi, M. B. Jacobson, T. Jacqmin, H. Jang, K. Jani, P. Jaranowski, S. Jawahar, F. Jiménez-Forteza, W. W. Johnson, N. K. Johnson-McDaniel, D. I. Jones, R. Jones, R. J. G. Jonker, L. Ju, K. Haris, C. V. Kalaghatgi, V. Kalogera, S. Kandhasamy, G. Kang, J. B. Kanner, S. Karki, M. Kasprzack, E. Katsavounidis, W. Katzman, S. Kaufer, T. Kaur, K. Kawabe, F. Kawazoe, F. Kéfélian, M. S. Kehl, D. Keitel, D. B. Kelley, W. Kells, R. Kennedy, D. G. Keppel, J. S. Key, A. Khalaidovski, F. Y. Khalili, I. Khan, S. Khan, Z. Khan, E. A. Khazanov, N. Kijbunchoo, C. Kim, J. Kim, K. Kim, Nam-Gyu Kim, Namjun Kim, Y.-M. Kim, E. J. King, P. J. King, D. L. Kinzel, J. S. Kissel, L. Kleybolte, S. Klimenko, S. M. Koehlenbeck, K. Kokeyama, S. Koley, V. Kondrashov, A. Kontos, S. Koranda, M. Korobko, W. Z. Korth, I. Kowalska, D. B. Kozak, V. Kringel, B. Krishnan, A. Królak, C. Krueger, G. Kuehn, P. Kumar, R. Kumar, L. Kuo, A. Kutynia, P. Kwee, B. D. Lackey, M. Landry, J. Lange, B. Lantz, P. D. Lasky, A. Lazzarini, C. Lazzaro, P. Leaci, S. Leavey, E. O. Lebigot, C. H. Lee, H. K. Lee, H. M. Lee, K. Lee, A. Lenon, M. Leonardi, J. R. Leong, N. Leroy, N. Letendre, Y. Levin, B. M. Levine, T. G. F. Li, A. Libson, T. B. Littenberg, N. A. Lockerbie, J. Logue, A. L. Lombardi, L. T. London, J. E. Lord, M. Lorenzini, V. Loriette, M. Lormand, G. Losurdo, J. D. Lough, C. O. Lousto, G. Lovelace, H. Lück, A. P. Lundgren, J. Luo, R. Lynch, Y. Ma, T. MacDonald, B. Machenschalk, M. MacInnis, D. M. Macleod, F. Magaña Sandoval, R. M. Magee, M. Mageswaran, E. Majorana, I. Maksimovic, V. Malvezzi, N. Man, I. Mandel, V. Mandic, V. Mangano, G. L. Mansell, M. Manske, M. Mantovani, F. Marchesoni, F. Marion, S. Márka, Z. Márka, A. S. Markosyan, E. Maros, F. Martelli, L. Martellini, I. W. Martin, R. M. Martin, D. V. Martynov, J. N. Marx, K. Mason, A. Masserot, T. J. Massinger, M. Masso-Reid, F. Matichard, L. Matone, N. Mavalvala, N. Mazumder, G. Mazzolo, R. McCarthy, D. E. McClelland, S. McCormick, S. C. McGuire, G. McIntyre, J. McIver, D. J. McManus, S. T. McWilliams, D. Meacher, G. D. Meadors, J. Meidam, A. Melatos, G. Mendell, D. Mendoza-Gandara, R. A. Mercer, E. Merilh, M. Merzougui, S. Meshkov, C. Messenger, C. Messick, P. M. Meyers, F. Mezzani, H. Miao, C. Michel, H. Middleton, E. E. Mikhailov, L. Milano, J. Miller, M. Millhouse, Y. Minenkov, J. Ming, S. Mirshekari, C. Mishra, S. Mitra, V. P. Mitrofanov, G. Mitselmakher, R. Mittleman, A. Moggi, M. Mohan, S. R. P. Mohapatra, M. Montani, B. C. Moore, C. J. Moore, D. Moraru, G. Moreno, S. R. Morriss, K. Mossavi, B. Mours, C. M. Mow-Lowry, C. L. Mueller, G. Mueller, A. W. Muir, Arunava Mukherjee, D. Mukherjee, S. Mukherjee, N. Mukund, A. Mullavey, J. Munch, D. J. Murphy, P. G. Murray, A. Mytidis, I. Nardecchia, L. Naticchioni, R. K. Nayak, V. Necula, K. Nedkova, G. Nelemans, M. Neri, A. Neunzert, G. Newton, T. T. Nguyen, A. B. Nielsen, S. Nissanke, A. Nitz, F. Nocera, D. Nolting, M. E. N. Normandin, L. K. Nuttall, J. Oberling, E. Ochsner, J. O'Dell, E. Oelker, G. H. Ogin, J. J. Oh, S. H. Oh, F. Ohme, M. Oliver, P. Oppermann, Richard J. Oram, B. O'Reilly, R. O'Shaughnessy, C. D. Ott, D. J. Ottaway, R. S. Ottens, H. Overmier, B. J. Owen, A. Pai, S. A. Pai, J. R. Palamos, O. Palashov, C. Palomba, A. Pal-Singh, H. Pan, Y. Pan, C. Pankow, F. Pannarale, B. C. Pant, F. Paoletti, A. Paoli, M. A. Papa, H. R. Paris, W. Parker, D. Pascucci, A. Pasqualetti, R. Passaquieti, D. Pas-

suello, B. Patricelli, Z. Patrick, B. L. Pearlstone, M. Pedraza, R. Pedurand, L. Pekowsky, A. Pele, S. Penn, A. Perreca, H. P. Pfeiffer, M. Phelps, O. Piccinni, M. Pichot, M. Pickenpack, F. Piergiovanni, V. Pierro, G. Pillant, L. Pinard, I. M. Pinto, M. Pitkin, J. H. Poeld, R. Poggiani, P. Popolizio, A. Post, J. Powell, J. Prasad, V. Predoi, S. S. Premachandra, T. Prestegard, L. R. Price, M. Prijatelj, M. Principe, S. Privitera, R. Prix, G. A. Prodi, L. Prokhorov, O. Puncken, M. Punturo, P. Puppo, M. Pürrer, H. Qi, J. Qin, V. Quetschke, E. A. Quintero, R. Quitzow-James, F. J. Raab, D. S. Rabeling, H. Radkins, P. Raffai, S. Raja, M. Rakhmanov, C. R. Ramet, P. Rapagnani, V. Raymond, M. Razzano, V. Re, J. Read, C. M. Reed, T. Regimbau, L. Rei, S. Reid, D. H. Reitze, H. Rew, S. D. Reyes, F. Ricci, K. Riles, N. A. Robertson, R. Robie, F. Robinet, A. Rocchi, L. Rolland, J. G. Rollins, V. J. Roma, J. D. Romano, R. Romano, G. Romanov, J. H. Romie, D. Rosińska, S. Rowan, A. Rüdiger, P. Ruggi, K. Ryan, S. Sachdev, T. Sadecki, L. Sadeghian, L. Salconi, M. Saleem, F. Salemi, A. Samajdar, L. Sammut, L. M. Sampson, E. J. Sanchez, V. Sandberg, B. Sandeen, G. H. Sanders, J. R. Sanders, B. Sassolas, B. S. Sathyaprakash, P. R. Saulson, O. Sauter, R. L. Savage, A. Sawadsky, P. Schale, R. Schilling, J. Schmidt, P. Schmidt, R. Schnabel, R. M. S. Schofield, A. Schönbeck, E. Schreiber, D. Schuette, B. F. Schutz, J. Scott, S. M. Scott, D. Sellers, A. S. Sengupta, D. Sentenac, V. Sequino, A. Sergeev, G. Serna, Y. Setyawati, A. Sevigny, D. A. Shaddock, T. Shaffer, S. Shah, M. S. Shahriar, M. Shaltev, Z. Shao, B. Shapiro, P. Shawhan, A. Sheperd, D. H. Shoemaker, D. M. Shoemaker, K. Siellez, X. Siemens, D. Sigg, A. D. Silva, D. Simakov, A. Singer, L. P. Singer, A. Singh, R. Singh, A. Singhal, A. M. Sintes, B. J. J. Slagmolen, J. R. Smith, M. R. Smith, N. D. Smith, R. J. E. Smith, E. J. Son, B. Sorazu, F. Sorrentino, T. Souradeep, A. K. Srivastava, A. Staley, M. Steinke, J. Steinlechner, S. Steinlechner, D. Steinmeyer, B. C. Stephens, S. P. Stevenson, R. Stone, K. A. Strain, N. Straniero, G. Stratta, N. A. Strauss, S. Strigin, R. Sturani, A. L. Stuver, T. Z. Summerscales, L. Sun, P. J. Sutton, B. L. Swinkels, M. J. Szczepańczyk, M. Tacca, D. Talukder, D. B. Tanner, M. Tápai, S. P. Tarabrin, A. Taracchini, R. Taylor, T. Theeg, M. P. Thirugnanasambandam, E. G. Thomas, M. Thomas, P. Thomas, K. A. Thorne, K. S. Thorne, E. Thrane, S. Tiwari, V. Tiwari, K. V. Tokmakov, C. Tomlinson, M. Tonelli, C. V. Torres, C. I. Torrie, D. Töyrä, F. Travasso, G. Traylor, D. Trifirò, M. C. Tringali, L. Trozzo, M. Tse, M. Turconi, D. Tuyenbayev, D. Ugolini, C. S. Unnikrishnan, A. L. Urban, S. A. Usman, H. Vahlbruch, G. Vajente, G. Valdes, M. Vallisneri, N. van Bakel, M. van Beuzekom, J. F. J. van den Brand, C. Van Den Broeck, D. C. Vander-Hyde, L. van der Schaaf, J. V. van Heijningen, A. A. van Veggel, M. Vardaro, S. Vass, M. Vasúth, R. Vaulin, A. Vecchio, G. Vedovato, J. Veitch, P. J. Veitch, K. Venkateswara, D. Verkindt, F. Vetrano, A. Viceré, S. Vinciguerra, D. J. Vine, J.-Y. Vinet, S. Vitale, T. Vo, H. Vocca, C. Vorvick, D. Voss, W. D. Vousden, S. P. Vyatchanin, A. R. Wade, L. E. Wade, M. Wade, S. J. Waldman, M. Walker, L. Wallace, S. Walsh, G. Wang, H. Wang, M. Wang, X. Wang, Y. Wang, H. Ward, R. L. Ward, J. Warner, M. Was, B. Weaver, L.-W. Wei, M. Weinert, A. J. Weinstein, R. Weiss, T. Welborn, L. Wen, P. Weßels, T. Westphal, K. Wette, J. T. Whelan, S. E. Whitcomb, D. J. White, B. F. Whiting, K. Wiesner, C. Wilkinson, P. A. Willems, L. Williams, R. D. Williams, A. R. Williamson, J. L. Willis, B. Willke, M. H. Wimmer, L. Winkelmann, W. Winkler, C. C. Wipf, A. G. Wiseman, H. Wittel, G. Woan, J. Worden, J. L. Wright, G. Wu, J. Yablon, I. Yakushin, W. Yam, H. Yamamoto, C. C. Yancey, M. J. Yap, H. Yu, M. Yvert, A. Zadrożny, L. Zangrando, M. Zanolin, J.-P. Zendri, M. Zevin, F. Zhang, L. Zhang, M. Zhang, Y. Zhang, C. Zhao, M. Zhou, Z. Zhou, X. J. Zhu, M. E. Zucker, S. E. Zuraw, and J. Zweizig. Observation of gravitational waves from a binary black

hole merger. *Phys. Rev. Lett.*, 116:061102, Feb 2016. doi: 10.1103/PhysRevLett.116.061102. URL https://link.aps.org/doi/10.1103/PhysRevLett.116.061102.

[90] J. Weber. Evidence for discovery of gravitational radiation. *Phys. Rev. Lett.*, 22:1320–1324, Jun 1969. doi: 10.1103/PhysRevLett.22.1320. URL https://link.aps.org/doi/10.1103/PhysRevLett.22.1320.

[91] Seiji Kawamura and TAMA Collaboration. Laser interferometer gravitational wave detector: The current status of the tama project. *Progress of Theoretical Physics Supplement*, 136: 72–86, 04 1999. ISSN 0375-9687. doi: 10.1143/PTPS.136.72. URL https://doi.org/10.1143/PTPS.136.72.

[92] H Lück and the GEO600 Team. The geo600 project. *Classical and Quantum Gravity*, 14(6): 1471, jun 1997. doi: 10.1088/0264-9381/14/6/012. URL https://doi.org/10.1088/0264-9381/14/6/012.

[93] LIGO Collaboration. LASER INTERFEROMETER GRAVITATIONAL WAVE OBSERVATORY – LIGO -. Technical report, California Institute of Technology, 2006.

[94] Katerina Chatziioannou et al. On the properties of the massive binary black hole merger GW170729. *Phys. Rev. D*, 100(10):104015, 2019. doi: 10.1103/PhysRevD.100.104015.

[95] GraceDB. The gravitational wave candidate event database, Accessed: April 3, 2026. URL https://gracedb.ligo.org/superevents/public/O4a/.

[96] GWOSC. The gravitational wave open science cente, Accessed: April 3, 2026. URL https://gwosc.org/eventapi/html/GWTC-4.0/.

[97] A. G. Abac et al. GWTC-4.0: Methods for Identifying and Characterizing Gravitational-wave Transients. *arXiv*, 8 2025.

[98] Matthew Ball, Raymond Frey, and Kara Merfeld. Prospects for neutron star parameter estimation using gravitational waves from f modes associated with magnetar flares. *Monthly Notices of the Royal Astronomical Society*, 533(3):3090–3097, 09 2024. ISSN 0035-8711. doi: 10.1093/mnras/stae1987. URL https://doi.org/10.1093/mnras/stae1987.

[99] J. Abadie, B. P. Abbott, R. Abbott, R. Adhikari, P. Ajith, B. Allen, G. Allen, E. Amador Ceron, R. S. Amin, S. B. Anderson, W. G. Anderson, M. A. Arain, M. Araya, Y. Aso, S. Aston, P. Aufmuth, C. Aulbert, S. Babak, P. Baker, S. Ballmer, D. Barker, B. Barr, P. Barriga, L. Barsotti, M. A. Barton, I. Bartos, R. Bassiri, M. Bastarrika, B. Behnke, M. Benacquista, M. F. Bennett, J. Betzwieser, P. T. Beyersdorf, I. A. Bilenko, G. Billingsley, R. Biswas, E. Black, J. K. Blackburn, L. Blackburn, D. Blair, B. Bland, O. Bock, T. P. Bodiya, R. Bondarescu, R. Bork, M. Born, S. Bose, P. R. Brady, V. B. Braginsky, J. E. Brau, J. Breyer, D. O. Bridges, M. Brinkmann, M. Britzger, A. F. Brooks, D. A. Brown, A. Bullington, A. Buonanno, O. Burmeister, R. L. Byer, L. Cadonati, J. Cain, J. B. Camp, J. Can-

nizzo, K. C. Cannon, J. Cao, C. Capano, L. Cardenas, S. Caudill, M. Cavaglià, C. Cepeda, T. Chalermsongsak, E. Chalkley, P. Charlton, S. Chatterji, S. Chelkowski, Y. Chen, N. Christensen, S. S. Y. Chua, C. T. Y. Chung, D. Clark, J. Clark, J. H. Clayton, R. Conte, D. Cook, T. R. C. Corbitt, N. Cornish, D. Coward, D. C. Coyne, J. D. E. Creighton, T. D. Creighton, A. M. Cruise, R. M. Culter, A. Cumming, L. Cunningham, K. Dahl, S. L. Danilishin, K. Danzmann, B. Daudert, G. Davies, E. J. Daw, T. Dayanga, D. DeBra, J. Degallaix, V. Dergachev, R. DeSalvo, S. Dhurandhar, M. Díaz, F. Donovan, K. L. Dooley, E. E. Doomes, R. W. P. Drever, J. Driggers, J. Dueck, I. Duke, J.-C. Dumas, S. Dwyer, M. Edgar, M. Edwards, A. Effler, P. Ehrens, T. Etzel, M. Evans, T. Evans, S. Fairhurst, Y. Faltas, Y. Fan, D. Fazi, H. Fehrmann, L. S. Finn, K. Flasch, S. Foley, C. Forrest, N. Fotopoulos, M. Frede, M. Frei, Z. Frei, A. Freise, R. Frey, T. T. Fricke, D. Friedrich, P. Fritschel, V. V. Frolov, P. Fulda, M. Fyffe, J. A. Garofoli, S. Ghosh, J. A. Giaime, S. Giampanis, K. D. Giardina, E. Goetz, L. M. Goggin, G. González, S. Goßler, A. Grant, S. Gras, C. Gray, R. J. S. Greenhalgh, A. M. Gretarsson, R. Grosso, H. Grote, S. Grunewald, E. K. Gustafson, R. Gustafson, B. Hage, J. M. Hallam, D. Hammer, G. D. Hammond, C. Hanna, J. Hanson, J. Harms, G. M. Harry, I. W. Harry, E. D. Harstad, K. Haughian, K. Hayama, T. Hayler, J. Heefner, I. S. Heng, A. Heptonstall, M. Hewitson, S. Hild, E. Hirose, D. Hoak, K. A. Hodge, K. Holt, D. J. Hosken, J. Hough, E. Howell, D. Hoyland, B. Hughey, S. Husa, S. H. Huttner, D. R. Ingram, T. Isogai, A. Ivanov, W. W. Johnson, D. I. Jones, G. Jones, R. Jones, L. Ju, P. Kalmus, V. Kalogera, S. Kandhasamy, J. Kanner, E. Katsavounidis, K. Kawabe, S. Kawamura, F. Kawazoe, W. Kells, D. G. Keppel, A. Khalaidovski, F. Y. Khalili, R. Khan, E. Khazanov, H. Kim, P. J. King, J. S. Kissel, S. Klimenko, K. Kokeyama, V. Kondrashov, R. Kopparapu, S. Koranda, D. Kozak, V. Kringel, B. Krishnan, G. Kuehn, J. Kullman, R. Kumar, P. Kwee, P. K. Lam, M. Landry, M. Lang, B. Lantz, N. Lastzka, A. Lazzarini, P. Leaci, M. Lei, N. Leindecker, I. Leonor, H. Lin, P. E. Lindquist, T. B. Littenberg, N. A. Lockerbie, D. Lodhia, M. Lormand, P. Lu, M. Lubinski, A. Lucianetti, H. Lück, A. Lundgren, B. Machenschalk, M. MacInnis, M. Mageswaran, K. Mailand, C. Mak, I. Mandel, V. Mandic, S. Márka, Z. Márka, A. Markosyan, J. Markowitz, E. Maros, I. W. Martin, R. M. Martin, J. N. Marx, K. Mason, F. Matichard, L. Matone, R. A. Matzner, N. Mavalvala, R. McCarthy, D. E. McClelland, S. C. McGuire, G. McIntyre, D. J. A. McKechan, M. Mehmet, A. Melatos, A. C. Melissinos, G. Mendell, D. F. Menéndez, R. A. Mercer, L. Merrill, S. Meshkov, C. Messenger, M. S. Meyer, H. Miao, J. Miller, Y. Mino, S. Mitra, V. P. Mitrofanov, G. Mitselmakher, R. Mittleman, O. Miyakawa, B. Moe, S. D. Mohanty, S. R. P. Mohapatra, G. Moreno, K. Mors, K. Mossavi, C. MowLowry, G. Mueller, H. Müller-Ebhardt, S. Mukherjee, A. Mullavey, J. Munch, P. G. Murray, T. Nash, R. Nawrodt, J. Nelson, G. Newton, E. Nishida, A. Nishizawa, J. O'Dell, B. O'Reilly, R. O'Shaughnessy, E. Ochsner, G. H. Ogin, R. Oldenburg, D. J. Ottaway, R. S. Ottens, H. Overmier, B. J. Owen, A. Page, Y. Pan, C. Pankow, M. A. Papa, P. Patel, D. Pathak, M. Pedraza, L. Pekowsky, S. Penn, C. Peralta, A. Perreca, M. Pickenpack, I. M. Pinto, M. Pitkin, H. J. Pletsch, M. V. Plissi, F. Postiglione, M. Principe, R. Prix, L. Prokhorov, O. Puncken, V. Quetschke, F. J. Raab, D. S. Rabeling, H. Radkins, P. Raffai, Z. Raics, M. Rakhmanov, V. Raymond, C. M. Reed, T. Reed, H. Rehbein, S. Reid, D. H. Reitze, R. Riesen, K. Riles, P. Roberts, N. A. Robertson, C. Robinson, E. L. Robinson, S. Roddy, C. Röver, J. Rollins, J. D. Romano, J. H. Romie, S. Rowan, A. Rüdiger, K. Ryan, S. Sakata, L. Sammut, L. Sancho de la Jordana, V. Sandberg, V. Sannibale, L. Santamaría, G. Santostasi, S. Saraf, P. Sarin, B. S. Sathyaprakash, S. Sato, M. Satterthwaite, P. R. Saulson, R. Savage, R. Schilling, R. Schnabel, R. Schofield, B. Schulz,

B. F. Schutz, P. Schwinberg, J. Scott, S. M. Scott, A. C. Searle, F. Seifert, D. Sellers, A. S. Sengupta, A. Sergeev, B. Shapiro, P. Shawhan, D. H. Shoemaker, A. Sibley, X. Siemens, D. Sigg, A. M. Sintes, G. Skelton, B. J. J. Slagmolen, J. Slutsky, J. R. Smith, M. R. Smith, N. D. Smith, K. Somiya, B. Sorazu, F. Speirits, A. J. Stein, L. C. Stein, S. Steplewski, A. Stochino, R. Stone, K. A. Strain, S. Strigin, A. Stroeer, A. L. Stuver, T. Z. Summerscales, M. Sung, S. Susmithan, P. J. Sutton, G. P. Szokoly, D. Talukder, D. B. Tanner, S. P. Tarabrin, J. R. Taylor, R. Taylor, K. A. Thorne, K. S. Thorne, A. Thüring, C. Titsler, K. V. Tokmakov, C. Torres, C. I. Torrie, G. Traylor, M. Trias, L. Turner, D. Ugolini, K. Urbanek, H. Vahlbruch, M. Vallisneri, C. Van Den Broeck, M. V. van der Sluys, A. A. van Veggel, S. Vass, R. Vaulin, A. Vecchio, J. Veitch, P. J. Veitch, C. Veltkamp, A. Villar, C. Vorvick, S. P. Vyachanin, S. J. Waldman, L. Wallace, A. Wanner, R. L. Ward, P. Wei, M. Weinert, A. J. Weinstein, R. Weiss, L. Wen, S. Wen, P. Wessels, M. West, T. Westphal, K. Wette, J. T. Whelan, S. E. Whitcomb, B. F. Whiting, C. Wilkinson, P. A. Willems, H. R. Williams, L. Williams, B. Willke, I. Wilmut, L. Winkelmann, W. Winkler, C. C. Wipf, A. G. Wiseman, G. Woan, R. Wooley, J. Worden, I. Yakushin, H. Yamamoto, K. Yamamoto, D. Yeaton-Massey, S. Yoshida, M. Zanolin, L. Zhang, Z. Zhang, C. Zhao, N. Zotov, M. E. Zucker, J. Zweizig, and S. Buchner. Search for gravitational waves associated with the august 2006 timing glitch of the vela pulsar. *Phys. Rev. D*, 83:042001, Feb 2011. doi: 10.1103/PhysRevD.83.042001. URL https://link.aps.org/doi/10.1103/PhysRevD.83.042001.

[100] R. Abbott, T. D. Abbott, S. Abraham, F. Acernese, K. Ackley, A. Adams, C. Adams, R. X. Adhikari, V. B. Adya, C. Affeldt, D. Agarwal, M. Agathos, K. Agatsuma, N. Aggarwal, O. D. Aguiar, L. Aiello, A. Ain, P. Ajith, T. Akutsu, K. M. Aleman, G. Allen, A. Allocca, P. A. Altin, A. Amato, S. Anand, A. Ananyeva, S. B. Anderson, W. G. Anderson, M. Ando, S. V. Angelova, S. Ansoldi, J. M. Antelis, S. Antier, S. Appert, Koya Arai, Koji Arai, Y. Arai, S. Araki, A. Araya, M. C. Araya, J. S. Areeda, M. Arène, N. Aritomi, N. Arnaud, S. M. Aronson, H. Asada, Y. Asali, G. Ashton, Y. Aso, S. M. Aston, P. Astone, F. Aubin, P. Auclair, P. Aufmuth, K. AultONeal, C. Austin, S. Babak, F. Badaracco, M. K. M. Bader, S. Bae, Y. Bae, A. M. Baer, S. Bagnasco, Y. Bai, L. Baiotti, J. Baird, R. Bajpai, M. Ball, G. Ballardin, S. W. Ballmer, M. Bals, A. Balsamo, G. Baltus, S. Banagiri, D. Bankar, R. S. Bankar, J. C. Barayoga, C. Barbieri, B. C. Barish, D. Barker, P. Barneo, S. Barnum, F. Barone, B. Barr, L. Barsotti, M. Barsuglia, D. Barta, J. Bartlett, M. A. Barton, I. Bartos, R. Bassiri, A. Basti, M. Bawaj, J. C. Bayley, A. C. Baylor, M. Bazzan, B. Bécsy, V. M. Bedakihale, M. Bejger, I. Belahcene, V. Benedetto, D. Beniwal, M. G. Benjamin, T. F. Bennett, J. D. Bentley, M. BenYaala, F. Bergamin, B. K. Berger, S. Bernuzzi, D. Bersanetti, A. Bertolini, J. Betzwieser, R. Bhandare, A. V. Bhandari, D. Bhattacharjee, S. Bhaumik, J. Bidler, I. A. Bilenko, G. Billingsley, I. A. Birney, O. Birnholtz, S. Biscans, M. Bischi, S. Biscoveanu, A. Bisht, B. Biswas, M. Bitossi, M.-A. Bizouard, J. K. Blackburn, J. Blackman, C. D. Blair, D. G. Blair, R. M. Blair, F. Bobba, N. Bode, M. Boer, G. Bogaert, M. Boldrini, F. Bondu, E. Bonilla, R. Bonnand, P. Booker, B. A. Boom, R. Bork, V. Boschi, N. Bose, S. Bose, V. Bossilkov, V. Boudart, Y. Bouffanais, A. Bozzi, C. Bradaschia, P. R. Brady, A. Bramley, A. Branch, M. Branchesi, M. Breschi, T. Briant, J. H. Briggs, A. Brillet, M. Brinkmann, P. Brockill, A. F. Brooks, J. Brooks, D. D. Brown, S. Brunett, G. Bruno, R. Bruntz, J. Bryant, A. Buikema, T. Bulik, H. J. Bulten, A. Buonanno, R. Buscicchio, D. Buskulic, L. Cadonati, M. Caesar, G. Cagnoli, C. Cahillane, H. W. Cain, J. Calderón Bustillo, J. D. Callaghan,

T. A. Callister, E. Calloni, J. B. Camp, M. Canepa, M. Cannavacciuolo, K. C. Cannon, H. Cao, J. Cao, Z. Cao, E. Capocasa, E. Capote, G. Carapella, F. Carbognani, J. B. Carlin, M. F. Carney, M. Carpinelli, G. Carullo, T. L. Carver, J. Casanueva Diaz, C. Casentini, G. Castaldi, S. Caudill, M. Cavaglià, F. Cavalier, R. Cavalieri, G. Cella, P. Cerdá-Durán, E. Cesarini, W. Chaibi, K. Chakravarti, B. Champion, C.-H. Chan, C. Chan, C. L. Chan, M. Chan, K. Chandra, P. Chanial, S. Chao, P. Charlton, E. A. Chase, E. Chassande-Mottin, D. Chatterjee, M. Chaturvedi, K. Chatziioannou, A. Chen, C. Chen, H. Y. Chen, J. Chen, K. Chen, X. Chen, Y.-B. Chen, Y.-R. Chen, Z. Chen, H. Cheng, C. K. Cheong, H. Y. Cheung, H. Y. Chia, F. Chiadini, C-Y. Chiang, R. Chierici, A. Chincarini, M. L. Chiofalo, A. Chiummo, G. Cho, H. S. Cho, S. Choate, R. K. Choudhary, S. Choudhary, N. Christensen, H. Chu, Q. Chu, Y-K. Chu, S. Chua, K. W. Chung, G. Ciani, P. Ciecielag, M. Cieślar, M. Cifaldi, A. A. Ciobanu, R. Ciolfi, F. Cipriano, A. Cirone, F. Clara, E. N. Clark, J. A. Clark, L. Clarke, P. Clearwater, S. Clesse, F. Cleva, E. Coccia, P.-F. Cohadon, D. E. Cohen, L. Cohen, M. Colleoni, C. G. Collette, M. Colpi, C. M. Compton, M. Constancio, L. Conti, S. J. Cooper, P. Corban, T. R. Corbitt, I. Cordero-Carrión, S. Corezzi, K. R. Corley, N. Cornish, D. Corre, A. Corsi, S. Cortese, C. A. Costa, R. Cotesta, M. W. Coughlin, S. B. Coughlin, J.-P. Coulon, S. T. Countryman, B. Cousins, P. Couvares, P. B. Covas, D. M. Coward, M. J. Cowart, D. C. Coyne, R. Coyne, J. D. E. Creighton, T. D. Creighton, A. W. Criswell, M. Croquette, S. G. Crowder, J. R. Cudell, T. J. Cullen, A. Cumming, R. Cummings, E. Cuoco, M. Curyło, T. Dal Canton, G. Dálya, A. Dana, L. M. DaneshgaranBajastani, B. D'Angelo, S. L. Danilishin, S. D'Antonio, K. Danzmann, C. Darsow-Fromm, A. Dasgupta, L. E. H. Datrier, V. Dattilo, I. Dave, M. Davier, G. S. Davies, D. Davis, E. J. Daw, R. Dean, M. Deenadayalan, J. Degallaix, M. De Laurentis, S. Deléglise, V. Del Favero, F. De Lillo, N. De Lillo, W. Del Pozzo, L. M. DeMarchi, F. De Matteis, V. D'Emilio, N. Demos, T. Dent, A. Depasse, R. De Pietri, R. De Rosa, C. De Rossi, R. DeSalvo, R. De Simone, S. Dhurandhar, M. C. Díaz, M. Diaz-Ortiz, N. A. Didio, T. Dietrich, L. Di Fiore, C. Di Fronzo, C. Di Giorgio, F. Di Giovanni, T. Di Girolamo, A. Di Lieto, B. Ding, S. Di Pace, I. Di Palma, F. Di Renzo, A. K. Divakarla, A. Dmitriev, Z. Doctor, L. D'Onofrio, F. Donovan, K. L. Dooley, S. Doravari, I. Dorrington, M. Drago, J. C. Driggers, Y. Drori, Z. Du, J.-G. Ducoin, P. Dupej, O. Durante, D. D'Urso, P.-A. Duverne, S. E. Dwyer, P. J. Easter, M. Ebersold, G. Eddolls, B. Edelman, T. B. Edo, O. Edy, A. Effler, S. Eguchi, J. Eichholz, S. S. Eikenberry, M. Eisenmann, R. A. Eisenstein, A. Ejlli, Y. Enomoto, L. Errico, R. C. Essick, H. Estellés, D. Estevez, Z. Etienne, T. Etzel, M. Evans, T. M. Evans, B. E. Ewing, V. Fafone, H. Fair, S. Fairhurst, X. Fan, A. M. Farah, S. Farinon, B. Farr, W. M. Farr, N. W. Farrow, E. J. Fauchon-Jones, M. Favata, M. Fays, M. Fazio, J. Feicht, M. M. Fejer, F. Feng, E. Fenyvesi, D. L. Ferguson, A. Fernandez-Galiana, I. Ferrante, T. A. Ferreira, F. Fidecaro, P. Figura, I. Fiori, M. Fishbach, R. P. Fisher, J. M. Fishner, R. Fittipaldi, V. Fiumara, R. Flaminio, E. Floden, E. Flynn, H. Fong, J. A. Font, B. Fornal, P. W. F. Forsyth, A. Franke, S. Frasca, F. Frasconi, C. Frederick, Z. Frei, A. Freise, R. Frey, P. Fritschel, V. V. Frolov, G. G. Fronzé, Y. Fujii, Y. Fujikawa, M. Fukunaga, M. Fukushima, P. Fulda, M. Fyffe, H. A. Gabbard, B. U. Gadre, S. M. Gaebel, J. R. Gair, J. Gais, S. Galaudage, R. Gamba, D. Ganapathy, A. Ganguly, D. Gao, S. G. Gaonkar, B. Garaventa, C. García-Núñez, C. García-Quirós, F. Garufi, B. Gateley, S. Gaudio, V. Gayathri, G. Ge, G. Gemme, A. Gennai, J. George, L. Gergely, P. Gewecke, S. Ghonge, Abhirup. Ghosh, Archisman Ghosh, Shaon Ghosh, Shrobana Ghosh, Sourath Ghosh, B. Giacomazzo, L. Giacoppo, J. A. Giaime, K. D. Giardina, D. R. Gib-

son, C. Gier, M. Giesler, P. Giri, F. Gissi, J. Glanzer, A. E. Gleckl, P. Godwin, E. Goetz, R. Goetz, N. Gohlke, B. Goncharov, G. González, A. Gopakumar, M. Gosselin, R. Gouaty, B. Grace, A. Grado, M. Granata, V. Granata, A. Grant, S. Gras, P. Grassia, C. Gray, R. Gray, G. Greco, A. C. Green, R. Green, A. M. Gretarsson, E. M. Gretarsson, D. Griffith, W. Griffiths, H. L. Griggs, G. Grignani, A. Grimaldi, E. Grimes, S. J. Grimm, H. Grote, S. Grunewald, P. Gruning, J. G. Guerrero, G. M. Guidi, A. R. Guimaraes, G. Guixé, H. K. Gulati, H.-K. Guo, Y. Guo, Anchal Gupta, Anuradha Gupta, P. Gupta, E. K. Gustafson, R. Gustafson, F. Guzman, S. Ha, L. Haegel, A. Hagiwara, S. Haino, O. Halim, E. D. Hall, E. Z. Hamilton, G. Hammond, W.-B. Han, M. Haney, J. Hanks, C. Hanna, M. D. Hannam, O. A. Hannuksela, H. Hansen, T. J. Hansen, J. Hanson, T. Harder, T. Hardwick, K. Haris, J. Harms, G. M. Harry, I. W. Harry, D. Hartwig, K. Hasegawa, B. Haskell, R. K. Hasskew, C.-J. Haster, K. Hattori, K. Haughian, H. Hayakawa, K. Hayama, F. J. Hayes, J. Healy, A. Heidmann, M. C. Heintze, J. Heinze, J. Heinzel, H. Heitmann, F. Hellman, P. Hello, A. F. Helmling-Cornell, G. Hemming, M. Hendry, I. S. Heng, E. Hennes, J. Hennig, M. H. Hennig, F. Hernandez Vivanco, M. Heurs, S. Hild, P. Hill, Y. Himemoto, A. S. Hines, Y. Hiranuma, N. Hirata, E. Hirose, S. Hochheim, D. Hofman, J. N. Hohmann, A. M. Holgado, N. A. Holland, I. J. Hollows, Z. J. Holmes, K. Holt, D. E. Holz, Z. Hong, P. Hopkins, J. Hough, E. J. Howell, C. G. Hoy, D. Hoyland, A. Hreibi, B. Hsieh, Y. Hsu, G-Z. Huang, H-Y. Huang, P. Huang, Y-C. Huang, Y.-J. Huang, Y.-W. Huang, M. T. Hübner, A. D. Huddart, E. A. Huerta, B. Hughey, D. C. Y. Hui, V. Hui, S. Husa, S. H. Huttner, R. Huxford, T. Huynh-Dinh, S. Ide, B. Idzkowski, A. Iess, B. Ikenoue, S. Imam, K. Inayoshi, H. Inchauspe, C. Ingram, Y. Inoue, G. Intini, K. Ioka, M. Isi, K. Isleif, K. Ito, Y. Itoh, B. R. Iyer, K. Izumi, V. JaberianHamedan, T. Jacqmin, S. J. Jadhav, S. P. Jadhav, A. L. James, A. Z. Jan, K. Jani, K. Janssens, N. N. Janthalur, P. Jaranowski, D. Jariwala, R. Jaume, A. C. Jenkins, C. Jeon, M. Jeunon, W. Jia, J. Jiang, H.-B. Jin, G. R. Johns, A. W. Jones, D. I. Jones, J. D. Jones, P. Jones, R. Jones, R. J. G. Jonker, L. Ju, K. Jung, P. Jung, J. Junker, K. Kaihotsu, T. Kajita, M. Kakizaki, C. V. Kalaghatgi, V. Kalogera, B. Kamai, M. Kamiizumi, N. Kanda, S. Kandhasamy, G. Kang, J. B. Kanner, Y. Kao, S. J. Kapadia, D. P. Kapasi, C. Karathanasis, S. Karki, R. Kashyap, M. Kasprzack, W. Kastaun, S. Katsanevas, E. Katsavounidis, W. Katzman, T. Kaur, K. Kawabe, K. Kawaguchi, N. Kawai, T. Kawasaki, F. Kéfélian, D. Keitel, J. S. Key, S. Khadka, F. Y. Khalili, I. Khan, S. Khan, E. A. Khazanov, N. Khetan, M. Khursheed, N. Kijbunchoo, C. Kim, J. C. Kim, J. Kim, K. Kim, W. S. Kim, Y.-M. Kim, C. Kimball, N. Kimura, P. J. King, M. Kinley-Hanlon, R. Kirchhoff, J. S. Kissel, N. Kita, H. Kitazawa, L. Kleybolte, S. Klimenko, A. M. Knee, T. D. Knowles, E. Knyazev, P. Koch, G. Koekoek, Y. Kojima, K. Kokeyama, S. Koley, P. Kolitsidou, M. Kolstein, K. Komori, V. Kondrashov, A. K. H. Kong, A. Kontos, N. Koper, M. Korobko, K. Kotake, M. Kovalam, D. B. Kozak, C. Kozakai, R. Kozu, V. Kringel, N. V. Krishnendu, A. Królak, G. Kuehn, F. Kuei, A. Kumar, P. Kumar, Rahul Kumar, Rakesh Kumar, J. Kume, K. Kuns, C. Kuo, H-S. Kuo, Y. Kuromiya, S. Kuroyanagi, K. Kusayanagi, K. Kwak, S. Kwang, D. Laghi, E. Lalande, T. L. Lam, A. Lamberts, M. Landry, B. B. Lane, R. N. Lang, J. Lange, B. Lantz, I. La Rosa, A. Lartaux-Vollard, P. D. Lasky, M. Laxen, A. Lazzarini, C. Lazzaro, P. Leaci, S. Leavey, Y. K. Lecoeuche, H. K. Lee, H. M. Lee, H. W. Lee, J. Lee, K. Lee, R. Lee, J. Lehmann, A. Lemaître, E. Leon, M. Leonardi, N. Leroy, N. Letendre, Y. Levin, J. N. Leviton, A. K. Y. Li, B. Li, J. Li, K. L. Li, T. G. F. Li, X. Li, C-Y. Lin, F-K. Lin, F-L. Lin, H. L. Lin, L. C.-C. Lin, F. Linde, S. D. Linker, J. N. Linley, T. B. Littenberg, G. C. Liu, J. Liu, K. Liu, X. Liu, M. Llorens-Monteagudo, R. K. L. Lo,

A. Lockwood, M. L. Lollie, L. T. London, A. Longo, D. Lopez, M. Lorenzini, V. Loriette, M. Lormand, G. Losurdo, J. D. Lough, C. O. Lousto, G. Lovelace, H. Lück, D. Lumaca, A. P. Lundgren, L.-W. Luo, R. Macas, M. MacInnis, D. M. Macleod, I. A. O. MacMillan, A. Macquet, I. Magaña Hernandez, F. Magaña Sandoval, C. Magazzù, R. M. Magee, R. Maggiore, E. Majorana, I. Maksimovic, S. Maliakal, A. Malik, N. Man, V. Mandic, V. Mangano, J. L. Mango, G. L. Mansell, M. Manske, M. Mantovani, F. Marchesoni, M. Marchio, F. Marion, Z. Mark, S. Márka, Z. Márka, C. Markakis, A. S. Markosyan, A. Markowitz, E. Maros, A. Marquina, S. Marsat, F. Martelli, I. W. Martin, R. M. Martin, M. Martinez, V. Martinez, K. Martinovic, D. V. Martynov, E. J. Marx, H. Masalehdan, K. Mason, E. Massera, A. Masserot, T. J. Massinger, M. Masso-Reid, S. Mastrogiovanni, A. Matas, M. Mateu-Lucena, F. Matichard, M. Matiushechkina, N. Mavalvala, J. J. McCann, R. McCarthy, D. E. McClelland, P. McClincy, S. McCormick, L. McCuller, G. I. McGhee, S. C. McGuire, C. McIsaac, J. McIver, D. J. McManus, T. McRae, S. T. McWilliams, D. Meacher, M. Mehmet, A. K. Mehta, A. Melatos, D. A. Melchor, G. Mendell, A. Menendez-Vazquez, C. S. Menoni, R. A. Mercer, L. Mereni, K. Merfeld, E. L. Merilh, J. D. Merritt, M. Merzougui, S. Meshkov, C. Messenger, C. Messick, P. M. Meyers, F. Meylahn, A. Mhaske, A. Miani, H. Miao, I. Michaloliakos, C. Michel, Y. Michimura, H. Middleton, L. Milano, A. L. Miller, M. Millhouse, J. C. Mills, E. Milotti, M. C. Milovich-Goff, O. Minazzoli, Y. Minenkov, N. Mio, Ll. M. Mir, A. Mishkin, C. Mishra, T. Mishra, T. Mistry, S. Mitra, V. P. Mitrofanov, G. Mitselmakher, R. Mittleman, O. Miyakawa, A. Miyamoto, Y. Miyazaki, K. Miyo, S. Miyoki, Geoffrey Mo, K. Mogushi, S. R. P. Mohapatra, S. R. Mohite, I. Molina, M. Molina-Ruiz, M. Mondin, M. Montani, C. J. Moore, D. Moraru, F. Morawski, A. More, C. Moreno, G. Moreno, Y. Mori, S. Morisaki, Y. Moriwaki, B. Mours, C. M. Mow-Lowry, S. Mozzon, F. Muciaccia, Arunava Mukherjee, D. Mukherjee, Soma Mukherjee, Subroto Mukherjee, N. Mukund, A. Mullavey, J. Munch, E. A. Muñiz, P. G. Murray, R. Musenich, S. L. Nadji, K. Nagano, S. Nagano, K. Nakamura, H. Nakano, M. Nakano, R. Nakashima, Y. Nakayama, I. Nardecchia, T. Narikawa, L. Naticchioni, B. Nayak, R. K. Nayak, R. Negishi, B. F. Neil, J. Neilson, G. Nelemans, T. J. N. Nelson, M. Nery, A. Neunzert, K. Y. Ng, S. W. S. Ng, C. Nguyen, P. Nguyen, T. Nguyen, L. Nguyen Quynh, W.-T. Ni, S. A. Nichols, A. Nishizawa, S. Nissanke, F. Nocera, M. Noh, M. Norman, C. North, S. Nozaki, L. K. Nuttall, J. Oberling, B. D. O'Brien, Y. Obuchi, J. O'Dell, W. Ogaki, G. Oganesyan, J. J. Oh, K. Oh, S. H. Oh, M. Ohashi, N. Ohishi, M. Ohkawa, F. Ohme, H. Ohta, M. A. Okada, Y. Okutani, K. Okutomi, C. Olivetto, K. Oohara, C. Ooi, R. Oram, B. O'Reilly, R. G. Ormiston, N. D. Ormsby, L. F. Ortega, R. O'Shaughnessy, E. O'Shea, S. Oshino, S. Ossokine, C. Osthelder, S. Otabe, D. J. Ottaway, H. Overmier, A. E. Pace, G. Pagano, M. A. Page, G. Pagliaroli, A. Pai, S. A. Pai, J. R. Palamos, O. Palashov, C. Palomba, K. Pan, P. K. Panda, H. Pang, P. T. H. Pang, C. Pankow, F. Pannarale, B. C. Pant, F. Paoletti, A. Paoli, A. Paolone, A. Parisi, J. Park, W. Parker, D. Pascucci, A. Pasqualetti, R. Passaquieti, D. Passuello, M. Patel, B. Patricelli, E. Payne, T. C. Pechsiri, M. Pedraza, M. Pegoraro, A. Pele, F. E. Peña Arellano, S. Penn, A. Perego, A. Pereira, T. Pereira, C. J. Perez, C. Périgois, A. Perreca, S. Perriès, J. Petermann, D. Petterson, H. P. Pfeiffer, K. A. Pham, K. S. Phukon, O. J. Piccinni, M. Pichot, M. Piendibene, F. Piergiovanni, L. Pierini, V. Pierro, G. Pillant, F. Pilo, L. Pinard, I. M. Pinto, B. J. Piotrzkowski, K. Piotrzkowski, M. Pirello, M. Pitkin, E. Placidi, W. Plastino, C. Pluchar, R. Poggiani, E. Polini, D. Y. T. Pong, S. Ponrathnam, P. Popolizio, E. K. Porter, J. Powell, M. Pracchia, T. Pradier, A. K. Prajapati, K. Prasai, R. Prasanna, G. Pratten, T. Prestegard,

M. Principe, G. A. Prodi, L. Prokhorov, P. Prosposito, L. Prudenzi, A. Puecher, M. Punturo, F. Puosi, P. Puppo, M. Pürrer, H. Qi, V. Quetschke, P. J. Quinonez, R. Quitzow-James, F. J. Raab, G. Raaijmakers, H. Radkins, N. Radulesco, P. Raffai, S. X. Rail, S. Raja, C. Rajan, K. E. Ramirez, T. D. Ramirez, A. Ramos-Buades, J. Rana, P. Rapagnani, U. D. Rapol, B. Ratto, V. Raymond, N. Raza, M. Razzano, J. Read, L. A. Rees, T. Regimbau, L. Rei, S. Reid, D. H. Reitze, P. Relton, P. Rettegno, F. Ricci, C. J. Richardson, J. W. Richardson, L. Richardson, P. M. Ricker, G. Riemenschneider, K. Riles, M. Rizzo, N. A. Robertson, R. Robie, F. Robinet, A. Rocchi, J. A. Rocha, S. Rodriguez, R. D. Rodriguez-Soto, L. Rolland, J. G. Rollins, V. J. Roma, M. Romanelli, R. Romano, C. L. Romel, A. Romero, I. M. Romero-Shaw, J. H. Romie, C. A. Rose, D. Rosińska, S. G. Rosofsky, M. P. Ross, S. Rowan, S. J. Rowlinson, Santosh Roy, Soumen Roy, D. Rozza, P. Ruggi, K. Ryan, S. Sachdev, T. Sadecki, J. Sadiq, N. Sago, S. Saito, Y. Saito, K. Sakai, Y. Sakai, M. Sakellariadou, Y. Sakuno, O. S. Salafia, L. Salconi, M. Saleem, F. Salemi, A. Samajdar, E. J. Sanchez, J. H. Sanchez, L. E. Sanchez, N. Sanchis-Gual, J. R. Sanders, A. Sanuy, T. R. Saravanan, N. Sarin, B. Sassolas, H. Satari, S. Sato, T. Sato, O. Sauter, R. L. Savage, V. Savant, T. Sawada, D. Sawant, H. L. Sawant, S. Sayah, D. Schaetzl, M. Scheel, J. Scheuer, A. Schindler-Tyka, P. Schmidt, R. Schnabel, M. Schneewind, R. M. S. Schofield, A. Schönbeck, B. W. Schulte, B. F. Schutz, E. Schwartz, J. Scott, S. M. Scott, M. Seglar-Arroyo, E. Seidel, T. Sekiguchi, Y. Sekiguchi, D. Sellers, A. S. Sengupta, N. Sennett, D. Sentenac, E. G. Seo, V. Sequino, Y. Setyawati, T. Shaffer, M. S. Shahriar, B. Shams, L. Shao, S. Sharifi, A. Sharma, P. Sharma, P. Shawhan, N. S. Shcheblanov, H. Shen, S. Shibagaki, M. Shikauchi, R. Shimizu, T. Shimoda, K. Shimode, R. Shink, H. Shinkai, T. Shishido, A. Shoda, D. H. Shoemaker, D. M. Shoemaker, K. Shukla, S. ShyamSundar, M. Sieniawska, D. Sigg, L. P. Singer, D. Singh, N. Singh, A. Singha, A. M. Sintes, V. Sipala, V. Skliris, B. J. J. Slagmolen, T. J. Slaven-Blair, J. Smetana, J. R. Smith, R. J. E. Smith, S. N. Somala, K. Somiya, E. J. Son, K. Soni, S. Soni, B. Sorazu, V. Sordini, F. Sorrentino, N. Sorrentino, H. Sotani, R. Soulard, T. Souradeep, E. Sowell, V. Spagnuolo, A. P. Spencer, M. Spera, A. K. Srivastava, V. Srivastava, K. Staats, C. Stachie, D. A. Steer, J. Steinlechner, S. Steinlechner, D. J. Stops, M. Stover, K. A. Strain, L. C. Strang, G. Stratta, A. Strunk, R. Sturani, A. L. Stuver, J. Südbeck, S. Sudhagar, V. Sudhir, R. Sugimoto, H. G. Suh, T. Z. Summerscales, H. Sun, L. Sun, S. Sunil, A. Sur, J. Suresh, P. J. Sutton, Takamasa Suzuki, Toshikazu Suzuki, B. L. Swinkels, M. J. Szczepańczyk, P. Szewczyk, M. Tacca, H. Tagoshi, S. C. Tait, H. Takahashi, R. Takahashi, A. Takamori, S. Takano, H. Takeda, M. Takeda, C. Talbot, H. Tanaka, Kazuyuki Tanaka, Kenta Tanaka, Taiki Tanaka, Takahiro Tanaka, A. J. Tanasijczuk, S. Tanioka, D. B. Tanner, D. Tao, A. Tapia, E. N. Tapia San Martin, E. N. Tapia San Martin, J. D. Tasson, S. Telada, R. Tenorio, L. Terkowski, M. Test, M. P. Thirugnanasambandam, M. Thomas, P. Thomas, J. E. Thompson, S. R. Thondapu, K. A. Thorne, E. Thrane, Shubhanshu Tiwari, Srishti Tiwari, V. Tiwari, K. Toland, A. E. Tolley, T. Tomaru, Y. Tomigami, T. Tomura, M. Tonelli, A. Torres-Forné, C. I. Torrie, I. Tosta e Melo, D. Töyrä, A. Trapananti, F. Travasso, G. Traylor, M. C. Tringali, A. Tripathee, L. Troiano, A. Trovato, L. Trozzo, R. J. Trudeau, D. S. Tsai, D. Tsai, K. W. Tsang, T. Tsang, J-S. Tsao, M. Tse, R. Tso, K. Tsubono, S. Tsuchida, L. Tsukada, D. Tsuna, T. Tsutsui, T. Tsuzuki, M. Turconi, D. Tuyenbayev, A. S. Ubhi, N. Uchikata, T. Uchiyama, R. P. Udall, A. Ueda, T. Uehara, K. Ueno, G. Ueshima, D. Ugolini, C. S. Unnikrishnan, F. Uraguchi, A. L. Urban, T. Ushiba, S. A. Usman, A. C. Utina, H. Vahlbruch, G. Vajente, A. Vajpeyi, G. Valdes, M. Valentini, V. Valsan, N. van Bakel, M. van Beuzekom, J. F. J. van den Brand, C. Van

Den Broeck, D. C. Vander-Hyde, L. van der Schaaf, J. V. van Heijningen, M. H. P. M. van Putten, N. van Remortel, M. Vardaro, A. F. Vargas, V. Varma, M. Vasúth, A. Vecchio, G. Vedovato, J. Veitch, P. J. Veitch, K. Venkateswara, J. Venneberg, G. Venugopalan, D. Verkindt, Y. Verma, D. Veske, F. Vetrano, A. Viceré, A. D. Viets, V. Villa-Ortega, J.-Y. Vinet, S. Vitale, T. Vo, H. Vocca, E. R. G. von Reis, C. Vorvick, S. P. Vyatchanin, L. E. Wade, M. Wade, K. J. Wagner, R. C. Walet, M. Walker, G. S. Wallace, L. Wallace, S. Walsh, J. Wang, J. Z. Wang, W. H. Wang, R. L. Ward, J. Warner, M. Was, T. Washimi, N. Y. Washington, J. Watchi, B. Weaver, L. Wei, M. Weinert, A. J. Weinstein, R. Weiss, C. M. Weller, F. Wellmann, L. Wen, P. Weßels, J. W. Westhouse, K. Wette, J. T. Whelan, D. D. White, B. F. Whiting, C. Whittle, D. Wilken, D. Williams, M. J. Williams, A. R. Williamson, J. L. Willis, B. Willke, D. J. Wilson, W. Winkler, C. C. Wipf, T. Wlodarczyk, G. Woan, J. Woehler, J. K. Wofford, I. C. F. Wong, J. Wrangel, C. Wu, D. S. Wu, H. Wu, S. Wu, D. M. Wysocki, L. Xiao, W-R. Xu, T. Yamada, H. Yamamoto, Kazuhiro Yamamoto, Kohei Yamamoto, T. Yamamoto, K. Yamashita, R. Yamazaki, F. W. Yang, L. Yang, Yang Yang, Yi Yang, Z. Yang, M. J. Yap, D. W. Yeeles, A. B. Yelikar, M. Ying, K. Yokogawa, J. Yokoyama, T. Yokozawa, A. Yoon, T. Yoshioka, Hang Yu, Haocun Yu, H. Yuzurihara, A. Zadrożny, M. Zanolin, S. Zeidler, T. Zelenova, J.-P. Zendri, M. Zevin, M. Zhan, H. Zhang, J. Zhang, L. Zhang, R. Zhang, T. Zhang, C. Zhao, G. Zhao, Yue Zhao, Yuhang Zhao, Z. Zhou, X. J. Zhu, Z.-H. Zhu, M. E. Zucker, and J. Zweizig. Constraints on cosmic strings using data from the third advanced ligo–virgo observing run. *Phys. Rev. Lett.*, 126:241102, Jun 2021. doi: 10.1103/PhysRevLett.126.241102. URL https://link.aps.org/doi/10.1103/PhysRevLett.126.241102.

[101] Albert Sneppen, Darach Watson, Andreas Bauswein, Oliver Just, Rubina Kotak, Ehud Nakar, Dovi Poznanski, and Stuart Sim. Spherical symmetry in the kilonova AT2017gfo/GW170817. *Nature*, 614(7948):436–439, 2023. doi: 10.1038/s41586-022-05616-x.

[102] Anthony L. Piro, Bruno Giacomazzo, and Rosalba Perna. The fate of neutron star binary mergers. *The Astrophysical Journal Letters*, 844(2):L19, jul 2017. doi: 10.3847/2041-8213/aa7f2f. URL https://doi.org/10.3847/2041-8213/aa7f2f.

[103] Joshua R Klein and Aaron Roodman. Blind analysis in nuclear and particle physics. *Annual Review of Nuclear and Particle Science*, 55(Volume 55, 2005):141–163, 2005. ISSN 1545-4134. doi: https://doi.org/10.1146/annurev.nucl.55.090704.151521. URL https://www.annualreviews.org/content/journals/10.1146/annurev.nucl.55.090704.151521.

[104] M. Abreu et al. Measurement of Reactor Antineutrino Oscillation at SNO+. *Phys. Rev. Lett.*, 135(12):121801, 2025. doi: 10.1103/gypt-lc9v.

[105] Runs Page. Runs Page, 2026.

[106] Run Selection. Run Selection, 2026.

[107] D. Basilico, G. Bellini, J. Benziger, R. Biondi, B. Caccianiga, F. Calaprice, A. Caminata, A. Chepurnov, D. D'Angelo, A. Derbin, A. Di Giacinto, V. Di Marcello, X. F. Ding, A. Di Ludovico, L. Di Noto, I. Drachnev, D. Franco, C. Galbiati, C. Ghiano, M. Giammarchi,

A. Goretti, M. Gromov, D. Guffanti, Aldo Ianni, Andrea Ianni, A. Jany, V. Kobychev, G. Korga, S. Kumaran, M. Laubenstein, E. Litvinovich, P. Lombardi, I. Lomskaya, L. Ludhova, I. Machulin, J. Martyn, E. Meroni, L. Miramonti, M. Misiaszek, V. Muratova, R. Nugmanov, L. Oberauer, V. Orekhov, F. Ortica, M. Pallavicini, L. Pelicci, Ö. Penek, L. Pietrofaccia, N. Pilipenko, A. Pocar, G. Raikov, M. T. Ranalli, G. Ranucci, A. Re, N. Rossi, S. Schönert, D. Semenov, G. Settanta, M. Skorokhvatov, A. Singhal, O. Smirnov, A. Sotnikov, R. Tartaglia, G. Testera, E. Unzhakov, A. Vishneva, R. B. Vogelaar, F. von Feilitzsch, M. Wojcik, M. Wurm, S. Zavatarelli, K. Zuber, and G. Zuzel. Borexino's search for low-energy neutrinos associated with gravitational wave events from gwtc-3 database: Borexino collaboration. *The European Physical Journal C*, 83(6), June 2023. ISSN 1434-6052. doi: 10.1140/epjc/s10052-023-11688-4. URL http://dx.doi.org/10.1140/epjc/s10052-023-11688-4.

[108] S. Abe, S. Asami, A. Gando, Y. Gando, T. Gima, A. Goto, T. Hachiya, K. Hata, S. Hayashida, K. Hosokawa, K. Ichimura, S. Ieki, H. Ikeda, K. Inoue, K. Ishidoshiro, Y. Kamei, N. Kawada, Y. Kishimoto, T. Kinoshita, M. Koga, N. Maemura, T. Mitsui, H. Miyake, K. Nakamura, K. Nakamura, R. Nakamura, H. Ozaki, T. Sakai, H. Sambonsugi, I. Shimizu, J. Shirai, K. Shiraishi, A. Suzuki, Y. Suzuki, A. Takeuchi, K. Tamae, K. Ueshima, Y. Wada, H. Watanabe, Y. Yoshida, S. Obara, A. Kozlov, D. Chernyak, Y. Takemoto, S. Yoshida, S. Umehara, K. Fushimi, A. K. Ichikawa, K. Z. Nakamura, M. Yoshida, B. E. Berger, B. K. Fujikawa, J. G. Learned, J. Maricic, S. N. Axani, L. A. Winslow, Z. Fu, J. Ouellet, Y. Efremenko, H. J. Karwowski, D. M. Markoff, W. Tornow, A. Li, J. A. Detwiler, S. Enomoto, M. P. Decowski, C. Grant, T. O'Donnell, and S. Dell'Oro. Search for low-energy electron antineutrinos in kamland associated with gravitational wave events. *The Astrophysical Journal*, 909(2):116, March 2021. ISSN 1538-4357. doi: 10.3847/1538-4357/abd5bc. URL http://dx.doi.org/10.3847/1538-4357/abd5bc.

[109] K. Abe, C. Bronner, Y. Hayato, M. Ikeda, S. Imaizumi, J. Kameda, Y. Kanemura, Y. Kataoka, S. Miki, M. Miura, S. Moriyama, Y. Nagao, M. Nakahata, S. Nakayama, T. Okada, K. Okamoto, A. Orii, G. Pronost, H. Sekiya, M. Shiozawa, Y. Sonoda, Y. Suzuki, A. Takeda, Y. Takemoto, A. Takenaka, H. Tanaka, S. Watanabe, T. Yano, S. Han, T. Kajita, K. Okumura, T. Tashiro, R. Wang, J. Xia, G. D. Megias, D. Bravo-Berguño, L. Labarga, Ll. Marti, B. Zaldivar, B. W. Pointon, F. d. M. Blaszczyk, E. Kearns, J. L. Raaf, J. L. Stone, L. Wan, T. Wester, J. Bian, N. J. Griskevich, W. R. Kropp, S. Locke, S. Mine, M. B. Smy, H. W. Sobel, V. Takhistov, P. Weatherly, J. Hill, J. Y. Kim, I. T. Lim, R. G. Park, B. Bodur, K. Scholberg, C. W. Walter, L. Bernard, A. Coffani, O. Drapier, S. El Hedri, A. Giampaolo, M. Gonin, Th. A. Mueller, P. Paganini, B. Quilain, T. Ishizuka, T. Nakamura, J. S. Jang, J. G. Learned, L. H. V. Anthony, D. G. R. Martin, A. A. Sztuc, Y. Uchida, V. Berardi, M. G. Catanesi, E. Radicioni, N. F. Calabria, L. N. Machado, G. De Rosa, G. Collazuol, F. Iacob, M. Lamoureux, N. Ospina, L. Ludovici, Y. Maekawa, Y. Nishimura, S. Cao, M. Friend, T. Hasegawa, T. Ishida, M. Jakkapu, T. Kobayashi, T. Matsubara, T. Nakadaira, K. Nakamura, Y. Oyama, K. Sakashita, T. Sekiguchi, T. Tsukamoto, Y. Kotsar, Y. Nakano, H. Ozaki, T. Shiozawa, A. T. Suzuki, Y. Takeuchi, S. Yamamoto, A. Ali, Y. Ashida, J. Feng, S. Hirota, T. Kikawa, M. Mori, T. Nakaya, R. A. Wendell, K. Yasutome, P. Fernandez, N. McCauley, P. Mehta, A. Pritchard, K. M. Tsui, Y. Fukuda, Y. Itow, H. Menjo, T. Niwa, K. Sato, M. Tsukada, P. Mijakowski, J. Jiang, C. K. Jung, C. Vilela, M. J. Wilking, C. Yanagisawa,

K. Hagiwara, M. Harada, T. Horai, H. Ishino, S. Ito, Y. Koshio, H. Kitagawa, W. Ma, N. Piplani, S. Sakai, Y. Kuno, G. Barr, D. Barrow, L. Cook, A. Goldsack, S. Samani, C. Simpson, D. Wark, F. Nova, T. Boschi, F. Di Lodovico, J. Migenda, S. Molina Sedgwick, M. Taani, S. Zsoldos, J. Y. Yang, S. J. Jenkins, M. Malek, J. M. McElwee, O. Stone, M. D. Thiesse, L. F. Thompson, H. Okazawa, S. B. Kim, I. Yu, K. Nishijima, M. Koshiba, K. Iwamoto, Y. Nakajima, N. Ogawa, M. Yokoyama, K. Martens, M. R. Vagins, S. Izumiyama, M. Kuze, M. Tanaka, T. Yoshida, M. Inomoto, M. Ishitsuka, H. Ito, R. Matsumoto, K. Ohta, M. Shinoki, J. F. Martin, H. A. Tanaka, T. Towstego, R. Akutsu, M. Hartz, A. Konaka, P. de Perio, N. W. Prouse, S. Chen, B. D. Xu, M. Posiadala-Zezula, D. Hadley, B. Richards, B. Jamieson, J. Walker, A. Minamino, K. Okamoto, G. Pintaudi, S. Sano, R. Sasaki, A. K. Ichikawa, and K. Nakamura. Search for neutrinos in coincidence with gravitational wave events from the ligo–virgo o3a observing run with the super-kamiokande detector. *The Astrophysical Journal*, 918(2):78, September 2021. ISSN 1538-4357. doi: 10.3847/1538-4357/ac0d5a. URL http://dx.doi.org/10.3847/1538-4357/ac0d5a.

[110] Bruny Baret, Imre Bartos, Boutayeb Bouhou, Alessandra Corsi, Irene Di Palma, Corinne Donzaud, Véronique Van Elewyck, Chad Finley, Gareth Jones, Antoine Kouchner, Szabolcs Márka, Zsuzsa Márka, Luciano Moscoso, Eric Chassande-Mottin, Maria Alessandra Papa, Thierry Pradier, Peter Raffai, Jameson Rollins, and Patrick Sutton. Bounding the time delay between high-energy neutrinos and gravitational-wave transients from gamma-ray bursts. *Astroparticle Physics*, 35(1):1–7, 2011. ISSN 0927-6505. doi: https://doi.org/10.1016/j.astropartphys.2011.04.001. URL https://www.sciencedirect.com/science/article/pii/S0927650511000776.

[111] Amanda Bacon. Pr3203, 2026. URL https://github.com/snoplus/rat/pull/3203.

[112] P. Vogel and J. F. Beacom. Angular distribution of neutron inverse beta decay, $\overline{\nu}_e + \overrightarrow{p} \; e^+ + n$. *Phys. Rev. D*, 60:053003, Jul 1999. doi: 10.1103/PhysRevD.60.053003. URL https://link.aps.org/doi/10.1103/PhysRevD.60.053003.

[113] Benjamin Tam. Mass Spectroscopy Analysis for SNO+ Scintillator. Technical report, University of Oxford, 2025.

[114] Kate Scholberg. SNOwGLoBES, Accessed: April 3, 2026.

[115] Serena Ricetto. DC Mask Update rat801, 2024.

[116] Daniel Cookman. PR3151, 2025.

[117] Carlo Giunti and Chung W. Kim. *Fundamentals of Neutrino Physics and Astrophysics*. Oxford University Press, 2007. ISBN 978-0-19-850871-7. doi: 10.1093/acprof:oso/9780198508717.001.0001.